

DOCTORAL THESIS

Investigating Fish Hydrodynamic Sensing: An Integrated Approach Utilizing Numerical and Experimental Methods

Ali Hassan Khan

TALLINN UNIVERSITY OF TECHNOLOGY
DOCTORAL THESIS
8/2025

Investigating Fish Hydrodynamic Sensing: An Integrated Approach Utilizing Numerical and Experimental Methods

ALI HASSAN KHAN



TALLINN UNIVERSITY OF TECHNOLOGY
School of Information Technologies
Department of Computer Systems

The dissertation was accepted for the defense of the Doctor of Philosophy (Computer Systems and Engineering) degree on January 15, 2025.

Supervisor: Assoc. Prof. Jeffrey A. Tuhtan,
Department of Computer Systems, School of Information Technologies,
Tallinn University of Technology,
Tallinn, Estonia

Co-supervisors: Prof. Maarja Kruusmaa,
Department of Computer Systems, School of Information Technologies,
Tallinn University of Technology,
Tallinn, Estonia

Dr. Stefan Hoerner, Maître de Conférences,
Laboratoire des Écoulements Géophysiques et Industriels,
CNRS, Grenoble-INP, Université Grenoble-Alpes,
Grenoble, France

Opponents: Assoc. Prof. Costantino Manes,
Department of Environment, Land and Infrastructure Engineering,
Politecnico di Torino,
Torino, Italy

Prof. Catherine Anna Wilson,
School of Engineering,
Cardiff University,
Cardiff, United Kingdom

Defence of the thesis: January 20, 2025, Tallinn

Declaration:

Hereby I declare that this doctoral thesis, my original investigation and achievement, submitted for the doctoral degree at Tallinn University of Technology, has not been submitted for any academic degree elsewhere.

Ali Hassan Khan

signature



Copyright: Ali Hassan Khan, 2025

ISSN 2585-6901 (PDF)

ISBN 978-9916-80-254-0 (PDF)

DOI <https://doi.org/10.23658/taltech.8/2025>

Khan, A. H. (2025). *Investigating Fish Hydrodynamic Sensing: An Integrated Approach Utilizing Numerical and Experimental Methods* [TalTech Press]. <https://doi.org/10.23658/taltech.8/2025>

TALLINNA TEHNIKAÜLIKOOL
DOKTORITÖÖ
8/2025

**Kalade hüdrodünaamilise tunnetuse
uurimine: numbrilisi ja
eksperimentaalseid meetodeid kasutav
integreeritud lähenemisviis**

ALI HASSAN KHAN





This project has received funding from the European Union Horizon 2020 Research and Innovation Programme under the Marie Skłodowska-Curie Actions, Grant Agreement No. 860800.

Acknowledgements

I would like to express my sincere gratitude and appreciation to several individuals who have played a significant role in the successful completion of my Ph.D. journey. First and foremost, I would like to extend my heartfelt thanks to **Assoc. Prof. Jeffrey Andrew Tuhtan** for his unwavering support and guidance throughout my research. His expertise, valuable insights, and continuous encouragement have been instrumental in shaping the direction of my work. His dedication to my academic and personal growth has been truly remarkable. I also would like to acknowledge the invaluable support by **Dr. Stefan Hoerner**. His expertise in the field of numerical and experimental fluid dynamics has been crucial in overcoming various challenges and ensuring the smooth progress of my research. His willingness to share knowledge and provide assistance has been greatly appreciated. I am grateful to **Prof. Maarja Kruusmaa** for her thorough proofreading and insightful feedback on my articles and dissertation. Her meticulous attention to detail and constructive suggestions have significantly improved the quality and clarity of my written work. Additionally, her guidance and mentorship were immensely valuable throughout my Ph.D. journey.

Furthermore, I express my thanks to the entire team of the Centre for Biorobotics and Centre for Environmental Intelligence and Sensing for creating a conducive environment for research and providing access to the necessary resources and facilities. I am honored and privileged to have had the opportunity to work with such reputable individuals who have contributed significantly to my academic and personal growth. Your guidance, support, and expertise have been invaluable during the past four years.

Lastly, I would like to express my deepest appreciation to my family and loved ones, especially my wife, for their unwavering support, encouragement, and understanding throughout this challenging but rewarding endeavor. Their constant belief in my abilities has been a tremendous source of motivation.

Ali Hassan Khan
January 17, 2025

Abstract

Investigating Fish Hydrodynamic Sensing: An Integrated Approach Utilizing Numerical and Experimental Methods

Many aquatic vertebrates, including fish, use hydrodynamic stimuli to detect water displacement caused by obstacles or nearby swimming animals. In bony fish, these hydrodynamic stimuli are perceived through the lateral line organs. The lateral line system of fish is directly exposed to the surrounding water through its sensory hair-like structures called neuromasts. These highly sensitive mechanoreceptors are typically distributed over the head and body, and can also continue into the tail. Biophysical studies of the lateral line indicate that fish can sense the pressure, flow velocity, and acceleration of the near-body flow field, as well as their gradients, typically at rates between 20 and 400 Hz. This allows fish to perceive minute changes in the hydrodynamic environment with the efficacy of filtering out the self-induced water displacements produced during locomotion. The undulatory motion of the fish during the normal gait cycle sets up a flow field around it, caused by the displacement of water at the head and suction at the tail. These flow fields are significantly dependent on a fish's swimming speed and its body shape. The fluid moving around the body of the fish forms a thin layer called the boundary layer (BL) as a result of friction on the surface of the fish and the viscous effects of the fluid. Previous studies show that the boundary layer around the fish filters the hydrodynamic signals due to its damping properties. Therefore, the thickness of the boundary layer is crucial to evaluate the hydrodynamic signal perceived on the surface of the fish. However, there are significant research gaps in fish and flow interaction studies, such as the importance of realistic fish body shape in setting up surrounding flow fields, the absence of benchmarking computational fluid dynamics (CFD) studies, the lack of experimental metadata for validation, and largely unknown spatial relationships between the flow field properties and the locations of the lateral line sensory units. These research gaps leave us with an insufficient understanding of how fish perceive hydrodynamic stimuli. To address these gaps, this work conducted a comprehensive experimental analysis measuring the flow fields around various stationary fish models. Simultaneously, numerical models were developed and validated with experimental data for the investigation of spatially distributed flow fields (i.e. velocity, pressure, and shear stresses) and to examine their correspondence to fish body geometry. The results of this investigation provide insights into the hydrodynamic sensing capabilities of fish, thereby enriching the understanding of researchers and practitioners. This improved knowledge can be instrumental in recognizing the significance of fish-flow interactions in influencing fish behavior, and in developing new and more effective river management strategies for fish conservation. In addition, this research contributes significantly to the ecohydraulics community by offering open access measurement data and numerical models. In doing so, it is the author's hope that this will facilitate future research efforts and allow other scientists and researchers to build on, validate, and compare the findings of this study with the latest advances in ecohydraulic research.

Kokkuvõte

Kalade hüdrodünaamilise tunnetuse uurimine: Numbrilisi ja eksperimentaalseid meetodeid kasutav integreeritud lähenemisiis

Paljud vees elavad selgroogsed, sealhulgas kalad, kasutavad hüdrodünaamilisi stiimuleid vee takistuse või lähedal ujuvate loomade tuvastamiseks. Luukalad tajuvad hüdrodünaamilisi stiimuleid küljejoone kaudu. Kalade küljejoon puutub otse ümbritseva veega kokku läbi tundlike juuksekarva-sarnaste struktuuride, mida nimetatakse neuromastideks. Need mehhanoretseptorid asetsevad pikki kala pead ja keha külgi ning võivad jätkuda ka saba suunas. Küljejoone biofüüsikalised uuringud näitavad, et kalad suudavad tajuda lähedal asuva veekihi rõhku, voolukiirust ja kiirendust, samuti nende gradienti sagedusega 20 kuni 400 Hz. See võimaldab kaladel tajuda väikseid muutusi hüdrodünaamilises keskkonnas, filtreerides efektiivselt välja kalade enda tekitatud veeliikumise. Kalade liikumistsükli jooksul tekib nende ümber vooluväli, mille põhjustab laineline liikumine vee väljatõrjumisest peaosas ja imemisest sabaosas. Tekitatud veevool sõltub oluliselt kalade ujumiskiirusest ja keha kujust. Hõõrdumise ja vedeliku viskoosete mõjude tulemusena kala kehapiinal, moodustub kala keha ümber õhuke kiht, mida nimetatakse piirikihiks. Varasemad uuringud näitavad, et kalade ümber olev piirikiht filtreerib hüdrodünaamilisi signaale piirikihi summutavate omaduste tõttu. Seega on piirikihi paksus oluline hüdrodünaamiliste signaalide analüüsimisel, mida kala kehapiinal tajutakse. Kalavoogude interaktsiooni uuringutes on olulisi uurimislünki nagu realistliku kala kehakuju tähtsus ümbritsevate voogude tekitamisel, puuduvad mõõdetavate arvutuslike vedelike dünaamika uuringud, eksperimentaalsete metaandmete puudumine valideerimiseks ja füüsiliste suhete tunnustamine ruumiliselt jaotunud vooluväljade ning küljejoone organi vahel. Kõik need lüngad tekitavad ebapiisava arusaama sellest, kuidas kalad tajuvad hüdrodünaamilisi stiimuleid turbulentsetes tingimustes. Nende uurimislünkade lahendamiseks viidi selles töös läbi põhjalik eksperimentaalne analüüs, mõõtes vooluvälju erinevate statsionaarsete kalamakettide ümber. Samal ajal arendati välja numbrilised mudelid ja need kinnitati eksperimentaalsete andmetega, et uurida ruumiliselt jaotunud vooluvälju (nt kiirus, rõhk ja nihked) ja nende vastavust kala keha geomeetrialet. Selle uurimise tulemused annavad ülevaate kalade hüdrodünaamilistest tajumisvõimetest, rikastades sellega teadlaste ja praktikute arusaama. Need paremad teadmised võivad olla abiks kalade ja voolu koostoime tähtsuse äratundmisel kalade käitumise mõjutamiseks ja uuenduslike jõgede majandamisstrateegiatega väljatöötamiseks kalade kaitseks. Lisaks aitab see uurimus oluliselt kaasa ökoloogiakogukonnale, pakkudes avatud juurdepääsu nii eksperimentaalsetele andmetele kui ka välja töötatud numbrilistele mudelitele. Selle eesmärk on hõlbustada tulevasi teadusuuringuid, võimaldades teistel teadlastel ja uurijatel tugineda käesoleva uuringu tulemustele, neid valideerida ning võrrelda.

Contents

Acknowledgements	5
Abstract.....	6
Kokkuvõte	7
List of Publications	10
Author's Contributions to the Publications	11
Abbreviations.....	12
Symbols.....	13
Introduction	14
Problem Statement.....	16
1 Background	18
1.1 Hydrodynamic Flow Stimuli.....	18
1.2 Fish Lateral-line System	19
1.3 Experimental Methods for Flow Field Measurement.....	20
1.4 Numerical Modeling of Flow Fields	20
1.5 Research Gaps.....	21
1.6 Research Questions	22
2 Research Method.....	23
2.1 Acoustic Doppler Velocimetry	25
2.2 Laser Doppler Anemometry	25
2.3 Computational Fluid Dynamics	27
3 Physical Experiments	29
3.1 ADV Velocity Measurements	29
3.2 LDA Velocity Measurements	30
3.2.1 Flume Measurements of Brown trout.....	30
3.2.2 Swim Tunnel Measurements of Gudgeon	31
4 Numerical Modeling of Fish-Shaped Bodies.....	33
4.1 Numerical Modeling Framework	33
4.1.1 3D Fish Models	33
4.1.2 Boundary Conditions	35
4.1.3 Mesh Sensitivity Analysis	35
4.2 Turbulence Modeling	36
4.2.1 Reynolds Averaged Navier Stokes Equations.....	38
4.2.2 Standard $k - \varepsilon$ Model	39
4.2.3 $k - \omega$ SST Model.....	39
4.2.4 Spalart-Allmaras Model	39
4.3 Boundary Layer and Near-Wall Treatment	40
4.4 Validation of Numerical Model	41

5	Results and Discussions	43
5.1	Significance of Fish Body Shape	43
5.2	RANS Turbulence Model	43
5.3	Lateral Line Receptors and Flow Fields	44
5.4	Implication for Fish Conservation and Fish Passage	46
6	Conclusions and Outlook	48
6.1	Limitations of this Work	49
6.2	Future Outlook	50
	List of Figures	51
	List of Tables	52
	References	53
	Appendix 1	61
	Appendix 2	75
	Appendix 3	91
	Appendix 4	109
	Appendix 5	119
	Curriculum Vitae	133
	Elulookirjeldus	135

List of Publications

The present Ph.D. thesis is based on the following publications that are referred to in the text by Roman numbers.

- I A. H. Khan, K. R. Hussmann, D. Powalla, S. Hoerner, M. Kruusmaa, and J. A. Tuhtan, "An open 3D CFD model for the investigation of flow environments experienced by freshwater fish," *Ecological Informatics*, vol. 69, p. 101652, 2022
- II K. Bensing, J. A. Tuhtan, G. Toming, A. H. Khan, and B. Lehmann, "Fish body geometry reduces the upstream velocity profile in subcritical flowing waters," *Aquatic Sciences*, vol. 84, no. 3, p. 32, 2022
- III A. H. Khan, S. Hoerner, G. Tomming, M. Kruusmaa, and J. A. Tuhtan, "3D CFD analysis of pressure, boundary layer and shear stresses on a gudgeon (*Gobio gobio*)," *Journal of Ecohydraulics*, pp. 1-15, 2024
- IV A. H. Khan, K. R. Hussmann, D. Powalla, S. Hoerner, M. Kruusmaa, and J. A. Tuhtan, "Benchmarking 3D CFD for studies on turbulent flow around fish-shaped bodies," in *Proceedings of the 14th International Symposium on Ecohydraulics*, International Association for Hydro-Environment Engineering and Research, 2022
- V A. H. Khan, G. Toming, S. Hoerner, and J. A. Tuhtan, "Comparison of near-body flow fields of a Gudgeon and NACA0013 profile," in *Advances in Hydraulic Research* (M. B. Kalinowska, M. M. Mrokowska, and P. M. Rowiński, eds.), pp. 231-242, Springer Nature Switzerland, 2024

Author's Contributions to the Publications

- I In [Publication I], I contributed as a main author. I conceptualized and formulated the analysis, developed the numerical models, collected pertinent data, performed the data analysis, and composed the manuscript.
- II In [Publication II], I served as a co-author. My contributions included establishing the experimental setup, performing the experiments, collecting the data, and reviewing the manuscript.
- III In [Publication III], I worked as principal author, carrying out responsibilities that involved conceptualizing and designing the analysis, conducting experiments, developing numerical models, accumulating experimental and numerical data, performing data analysis, and composing the manuscript.
- IV In [Publication IV], I am the main author. I conceived and designed the analysis, developed numerical models, collected the data, performed the analysis, and wrote the article.
- V In [Publication V], I am the main author of this research article. Contributions include designing the analysis, developing CFD models, collecting the sampling data, performing comparative analysis, and compiling the script.

Abbreviations

EU	European Union
WFD	Water Framework Directive
ETNs	European Training Networks
RIBES	River flow regulation fish behavior and status
HPC	High-Performance Computing
CFD	Computational Fluid Dynamics
SN	Superficial Neuromasts
CN	Canal Neuromasts
PIV	Particle-Image Velocimetry
LLP	Lateral-line Probe
NACA	National Advisory Committee for Aeronautics
RANS	Reynolds-Averaged Navier-Stokes
SA	Spalart Allmaras
RNG	Re-Normalization Group
DNS	Direct Numerical Simulation
LES	Large Eddy Simulation
SIMPLE	Semi-Implicit Method for Pressure Linked Equations
AUVs	Autonomous Underwater Vehicles
ADV	Acoustic Doppler velocimetry
LDA	Laser-Doppler Anemometry
SNR	Signal-to-Noise Ratio
FSI	Fluid-Structure Interaction
FVM	Finite Volume Method
CAD	Computer-Aided Design
GCI	Grid Convergence Index
BL	Boundary layer
FS	Fish sensor
TI	Turbulence Intensity

Symbols

u_x	m/s	Velocity component in the streamwise direction (x-axis)
u_y	m/s	Velocity component in the lateral direction (y-axis)
u_z	m/s	Velocity component in the vertical direction (z-axis)
\bar{u}	m/s	Mean velocity
u'	m/s	Fluctuating velocity
u_d	m/s	Velocity at distance
U_{Diff}	m/s	Absolute velocity difference
U_{lda}	m/s	LDA measured velocity
U_{sim}	m/s	Simulated velocity
P	Pa	Pressure
ρ	m^3/s	Density of a fluid
k	m^2/s^2	Turbulent kinetic energy
ε	m^2/s^3	Turbulence dissipation
ω	$1/s$	Specific turbulence dissipation rate
t	s	Time
L	m	Length
W	m	Width
H	m	Height
d	m	Distance
d_h	m	Hydraulic diameter
C_d	-	Drag coefficient
C_p	-	Pressure coefficient
F_d	N	Drag force
A	m^2	Surface area
P_a	-	Order of accuracy
r_{ji}	-	Ratio of mesh size j to i
\ln	-	Natural logarithm
δ_{ij}	m/s	Kronecker delta
y^+	-	Dimensionless wall distance
u_t	m/s	Friction velocity
μ	m^2/s	Kinematic viscosity
δ	m	Boundary layer thickness
δ_i	m	Boundary layer thickness at specific velocity
τ	Pa	Shear stress
Re	-	Reynolds number
Fr	-	Froude number
Δ	-	Difference
C	m/s	Speed of sound
f_{source}	Hz	transmitted frequency
f_D	Hz	Doppler frequency
η_i	-	Weighting factor
σ^2	-	Variance
σ	-	Standard Deviation

Introduction

Hydrodynamic sensing is the ability of fish and amphibians to detect and respond to fluid motion, typically water currents and pressure changes in underwater environments [6]. Fish possess a multi-modal sensory system including the auditory, visual, olfactory, and mechanoreceptory systems with which they sense and navigate in underwater environments [7]. In fish, hydrodynamic sensing is facilitated by the mechanoreceptory system known as the lateral line which helps fish locate food (prey), avoid predators, navigate complex environments, and interact with their surroundings [8]. For all these activities, fish have to migrate through different habitats that can be crucial to the survival and prosperity of fish communities [9]. However, human activities and developments have disrupted the migration patterns of fish [10].

Since 1970, the population of migratory freshwater fish in Europe has plummeted by 93% [11]. The main factors driving this decline include river fragmentation, habitat loss, overfishing, overexploitation, and eutrophication [12]. Among these, river fragmentation is an important driver behind significant changes within the freshwater ecosystem, resulting in substantial ecological, hydrological, and geomorphological changes [13]. The alteration of natural flow regimes reduced the habitat connectivity and led to the fragmentation of aquatic populations [14]. As a result, fish populations, particularly migratory species, faced significant declines due to disrupted spawning habitats, reduced food availability, and barriers to movement, further threatening the stability of the ecosystem [15]. Given the changing nature of hydrodynamic regimes in freshwater ecosystems, fish flow sensing is influenced by both ontogenetic changes in the morphology of the lateral line system and the dynamic environmental conditions in which developing fish live [16].

Fish subjected to heterogeneous flows are required to maintain stability by continuously adjusting their body posture and fin movements to counteract the variable forces and maintain their orientation and position in the water [17]. Fish passages were designed to help migrate the fish upstream to their spawning grounds by overcoming the obstructions [18]. These structures contain distinct hydraulic conditions (varying flow velocity, high turbulence levels) based on their design [19], which can attract the targeted fish of a certain size and length [20]. Factors such as velocity and turbulence impact variations in swimming behavior, influenced by the fish's size, sex, and parasite intensity [21]. Adult fish are capable of surviving in high-velocity areas within vertical slot fishways [22] and can efficiently harness the energy from turbulent eddies for swimming [23]. In contrast, smaller fish face greater challenges when navigating through regions with higher flow velocities [22], ultimately decreasing the overall efficiency of the fishways. Alternative approaches to enhance fish migration, such as river restoration initiatives, have been implemented globally [24]. The European Union (EU) Water Framework Directive (WFD) is one such initiative, aimed at advancing the restoration of freshwater ecosystems. The commission initiated the Biodiversity Strategy 2030, Barrier Removal for the River Restoration Program [25] with the mandate of making at least 25,000 km of free-flowing rivers by eliminating obsolete barriers and restoring flood plains and wetlands by 2030. In Europe, more than 1400 river restoration projects have been carried out across 31 countries over the past 30 years. However, many river restoration projects have failed to deliver the anticipated recovery of fish communities, raising global concerns about their effectiveness [24, 26]. A key factor behind the failure of many restoration efforts is the degradation of hydrodynamic regimes [27]. Therefore, to restore the biodiversity in freshwater ecology, the relationship between fluvial hydraulics and fish behavior must be taken into account [28]. The fish behavioral choices in fish passages or habitat restoration efforts are far more complex and require more considerations beyond simple body movements and metabolic activi-

ties [29]. A fundamental approach to understanding fish behavior is by delving into their sensory ecology, i.e. how they sense and process information from their environment.

To explore the intricate nexus that links hydrodynamic flow regimes and fish's behavioral response, numerous European Training Networks (ETNs) such as MSCA-RIBES (River flow regulation, fish BEhaviour and Status), and related projects, e.g. FIThydro etc. were initiated. The overarching objective of these projects was to find innovative solutions to protect freshwater fish and restore river continuity in anthropogenically altered rivers through fundamental research. The work presented in this dissertation represents a contribution to the ETN MSCA-RIBES program. Specifically, it focuses on fish hydrodynamic sensing, examining how fish perceive hydrodynamic signatures in turbulent environments commonly found in freshwater ecosystems, and how their body morphology influences this perception. It will help determine the spatial hydrodynamic image produced by the fish in its surroundings used for passive sensing. Any changes in the self-induced flow fields are perceived by the fish as hydrodynamic stimuli that govern their behavioral response, triggering further actions. Therefore, analyzing flow fields and understanding the functional principles of fish hydrodynamic sensing can aid in refining current methodologies to better support and enhance the diversity of freshwater fauna.

Fish use a combination of sensory signals through different sensory mechanisms to acquire environmental information and guide their behavior. A concurrent and equivalent overlapping role of the inner ear and lateral line system of a fish has been identified in the detection of certain hydrodynamic stimuli [30]. However, the lateral line array mechanoreceptor system distinguishes itself significantly from other sensing modalities. This specialized system, which consists of a network of fluid-filled canals and sensory cells, enables the fish to detect tiny displacements and vibrations in the water. It enables fish to navigate through turbulent and turbid environments where vision is less effective. Swimming fish in an underwater environment develop a flow field around their body due to displacement of water in their head and suction in the tail region [31] (see Fig. 1). Subtle changes in the flow field from an obstacle or a predator-prey interaction can be passively sensed by the fish with the help of a lateral line system in fine spatial and temporal resolution. The flow field produced by the fish itself depends on the shape of the fish's body and its acceleration [32].

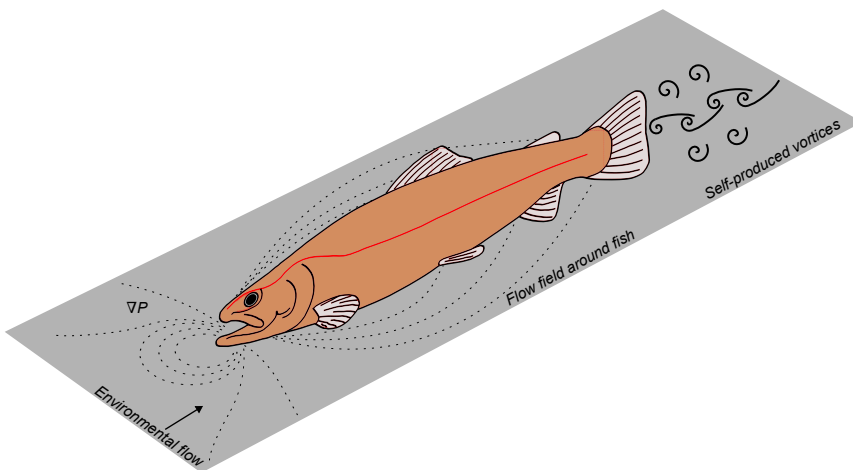


Figure 1: Self-induced flow fields around fish during the swimming gait cycle. The red line on the surface of the fish represents the lateral line sensing array.

Although research on passive sensing through the lateral line system is still in its early stages, the available knowledge about the spatial and temporal resolution of flow fields remains limited. Therefore, the current study investigates fish flow fields in spatial resolution and the impact of fish body morphology on self-induced flow fields. This work examines the self-induced flow fields around multiple freshwater fish models at fine spatial resolution. These fish models were kept rigid and stationary, consistent with previous research on fish hydrodynamic sensing which predominantly utilized stationary fish models [33, 34]. The rigid and stationary fish approach serves to simplify the analysis by providing a controlled framework for investigating fish-flow interactions, assuming that the fish filters the unsteady effects. Additionally, within the context of fish hydrodynamic sensing, it was observed that the lateral line detection array effectively senses the anterior 20% of the body length [35].

The flow fields around three-dimensional models of various fish were physically and numerically analyzed to improve our understanding of fish flow interactions and to acknowledge the importance of complex fish body shapes in producing the spatial velocity and pressure gradients that act as hydrodynamic stimuli. Due to advancements in high-performance computing (HPC) resources, physical phenomena such as flow fields around complex three-dimensional bodies can be simulated numerically. These numerical models can incorporate viscous effects and resolve the flow inside the boundary layer, providing a more realistic solution to the physical model deficient in prior research. Another significant contribution of this work is that it utilizes realistic fish body shapes with dorsal, pectoral, and anal fins. The use of realistic fish body shapes distinguishes this work from other studies incorporating simplified fish analogies. Ultimately, spatially distributed flow fields are correlated with the approximate positioning of the neuromasts on the surface of the fish. The findings of this research work will provide engineers and practitioners with a better understanding of the underlying principles in the surrounding flow fields of fish that act as hydrodynamic stimuli and contribute to fish behavior. Moreover, understanding and exploring the hydrodynamic sensing of freshwater fish will pave the way for bio-inspired designs in underwater robotics.

Problem Statement

Fish behavior is contingent on a multitude of factors. Among these, a significant contributing factor is the hydraulic environment, the velocities, pressures, shear stresses, and turbulence intensities, that a fish encounters in the wild. During upstream and downstream migration, fish encounter a variety of hydraulic conditions influencing their behavior; therefore, fish flow interactions require significant consideration. The operational mechanisms of fish mechanoreceptor organs in perceiving external stimuli have been explored in the past. However, the fish's self-induced flow fields that act as a medium in stimuli perception are overlooked and require further knowledge to understand their relationship to the lateral line sensing array. Enhancing our knowledge about fish flow interactions will ultimately help us understand, predict, and model fish behaviors.

In a nutshell, this research will address fundamental issues related to the fish flow interaction, such as the effect of the fish's body morphology on self-induced flow fields and the affiliation of the spatially distributed flow fields to the lateral line sensory units. These objectives are achieved by implementing state-of-the-art numerical modelling techniques, i.e. Computational Fluid Dynamics (CFD), in bridging the existing gaps in fish flow interaction while incorporating the biological aspects of fish sensing. Furthermore, the implications of the findings of this study for engineering applications are also discussed (see Fig. 2).

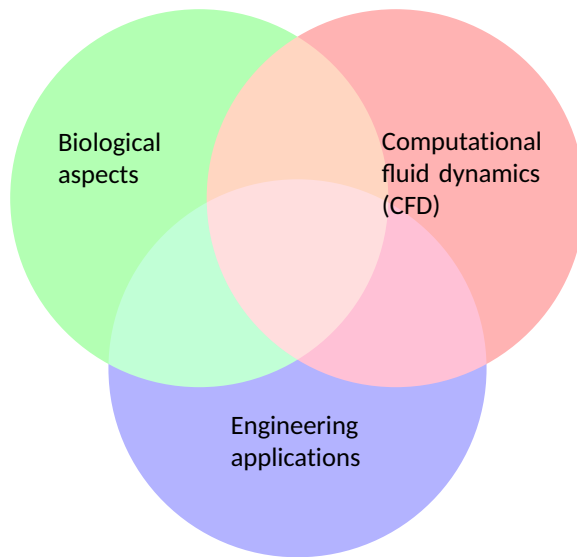


Figure 2: Overview of the synergistic impact of biological aspects, CFD, and engineering applications in this dissertation for improved understanding of fish flow interactions.

1 Background

This chapter provides an overview of existing research and knowledge in the field of fish flow interactions. It delves into an in-depth examination of previous approaches used in analyzing the flow fields around fish bodies and identifies the research gaps by highlighting the issues that require further investigation. The chapter starts with the theoretical background of the hydrodynamic flow stimuli and the lateral line system of fish, elucidating its intricate functionality to the stimuli. The following headings systematically outline the background of the study.

1.1 Hydrodynamic Flow Stimuli

Fish and other aquatic amphibians can sense moving objects or obstacles around their bodies through damming phenomena, which was first observed by [36]. Damming phenomena consist of the local displacement of water and the local rise of pressure in front of a moving fish to create space for it. This results in a self-induced flow field around the fish, which serves as hydrodynamic stimuli for the sensory units. A follow-up study of experimental research described the physiological and biological functioning of the lateral line system in fish [6]. The mechanoreceptor organ, i.e. the lateral line, was found to be sensitive to spatial derivatives of the local flow fields generated around the body of fish. Hydrodynamic stimuli alter local flow fields that are perceived and recognized by fish. In some cases, fish can even create spatial maps of their environment [37, 38]. The strength of the hydrodynamic stimulus signal perceived by the lateral line is attenuated proportionally to the distance from its source, particularly within a range of a few body lengths [8].

However, physiological investigations substantiate the pronounced contribution of the lateral line sensory system to stimulus detection within the central nervous system [39]. Earlier behavioral studies showed that lateral line array sensors mediate rheotaxis in fish [40] and, in addition to analyzing body kinematics, they also help determine hydrodynamic habitat [41]. The mechanosensory organs are sensitive to the temporal and spatial variations of both velocity and pressure [31]. Mathematical derivations of the velocity and pressure distribution on the surface of a fish in glide motion past an obstacle provide clear evidence that alterations in water displacement, resulting from both the movement of the fish and the presence of the obstacle, serve as stimuli for the lateral line sensory system [42]. The velocity distribution alterations appear inconsequential when approaching an obstacle head-on. In free stream flow, the resulting velocity distributions generated by the fish during swimming depend primarily on the morphology of the fish body [43]. These low-order simplified models utilized simplified 2D and 3D fish-shaped models, employing the potential flow assumption, which ignored the viscous effects. However, viscous effects are important because they generate a boundary layer around the surface of the fish due to its relative motion to the surrounding fluid [44]. The boundary layer around a swimming fish shows a fair trade-off between thrust production, separation control, and friction drag in undulatory motion [45]. However, the viscous boundary layer around the fish alters the amplitude and phase of the vibrating lateral line stimuli and influences the pressure fields, specifically at low frequencies [46]. In the case of an oscillating viscous boundary layer, it changes the velocity fields [47] that act on the superficial neuromasts, which at the receptor level interpret signals mediated by viscosity [48]. Flow fields, in particular, velocity, acceleration, pressure gradient, and shear stress on the fish surface, can all act as potential stimuli [49].

1.2 Fish Lateral-line System

The lateral line system is a sensory adaptation found in many aquatic vertebrates, including fish and some amphibians. It allows organisms to perceive and interpret hydrodynamic signals in their surrounding environment. The lateral line is a series of mechanoreceptors distributed throughout the bodies of these animals, allowing them to sense water movement, pressure changes, and velocity fluctuations [50]. The anatomical structure of the lateral line system exhibits considerable variation between and within different species. Somehow, these variations reflect the adaptations to the hydrodynamic conditions that fish encounter. However, a general description of the lateral line system reveals that it is composed of specialized sensory cells known as neuromasts. Based on physical positioning and functional objectives, neuromasts are classified into two categories: superficial neuromasts (SN) and canal neuromasts (CN). Superficial neuromasts are elongated hair-shaped structures known as cupulas, on the surface of fish projected into water [51, 52]. However, canal neuromasts are ovoid-shaped structure located within fluid-filled canals between cranial bones and fish scales [51, 53]. Generally, a single canal neuromast is placed equidistantly between two consecutive pores [54]. The sensory epithelium of a neuromast comprises hair cells similar to those found in vertebrates' auditory and vestibular systems. The ciliary bundles of these hair cells extend into a gelatinous cupula, establishing a connection between the hair cells and the fluid that envelopes the neuromast. Based on the morphological distinctions between superficial and canal neuromasts, the population of hair cells is typically limited to 10 in superficial neuromasts, whereas canal neuromasts exhibit a considerably larger count, typically ranging from hundreds to thousands of such cells. These hair cells are directional sensitive, and when viscous drag forces cause deflection of the cupula, it results in the generation of an opposite signal response. The morphology and functioning of the lateral line are illustrated in Fig. 3.

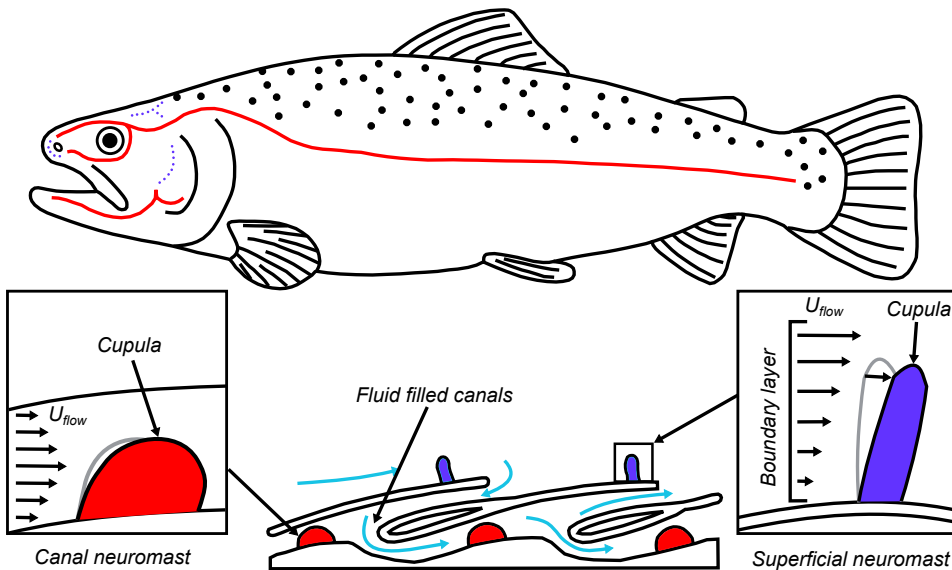


Figure 3: a) Illustration depicting the spatial arrangement of the superficial and canal neuromasts on a rainbow trout. b) Cross-sectional view of the lateral line above and below the scales, showing the canal pores and positioning of the cupula (adopted from [55]).

1.3 Experimental Methods for Flow Field Measurement

Moving or stationary objects generate hydrodynamic stimuli, providing external information to swimming fish [32]. The spatial location and distance estimation of objects approaching the fish are derived by analyzing the distorted flow fields. Experimental studies show that during a fish swimming gait cycle, a high-pressure region is generated around the nose of the fish, and a low-pressure region is generated around the widest part of the body with a thick boundary layer down the body [33]. Applying the basic Bernoulli principle, it is evident that the velocity is lowest in the high-pressure region and highest in the low-pressure region along the fish body. As both velocity and pressure are related, they act as hydrodynamic stimuli for sensory neurons. Several experimental techniques, such as particle image velocimetry (PIV) [33, 56] and lateral line probe (LLP) [57], have previously been used to analyze distorted velocity and pressure fields around a fish. For example, [33] used a PIV method to investigate the flow fields around blind Mexican cave-fish that glide towards a wall [33] and parallel to the wall [34]. These investigations revealed that hydrodynamic stimuli to the lateral line were observed within the local flow field when the fish was approximately at a distance of 0.20 body lengths of a wall. Similarly, the fluid-body interaction of a swimming Rainbow trout (*Oncorhynchus mykiss*) was investigated employing a PIV setup [56]. This study illustrates the characteristics of the boundary layer along the body length of the fish during a swimming gait cycle. Furthermore, it indicates that hydrodynamic perturbations generated by the fish body result in unsteadiness of the boundary layer leading to flow separation. The reversed flow in the unstable boundary layer could be interpreted by the superficial neuromasts in the form of a time-shifted irregular pattern of neuronal signal. Particle Image Velocimetry (PIV) is a non-intrusive technique used to measure flow velocity, offering accurate and precise velocity field measurements. However, it is a laborious and expensive method with limitations in terms of spatial resolution accessibility. Alternatively, pressure transducer sensors were used in [35] (replicating canal neuromasts) embedded in a rigid model of Rainbow trout (*Oncorhynchus mykiss*) measuring the pressure field on the surface of the fish. The main findings of this study show that regions experiencing the highest pressure variations along the body of fish (such as the head region) exhibit the highest concentration of canal neuromasts. The arrangement of the neuromasts was found to be in line with the pressure gradients on the surface of the rainbow trout. The principles of canal neuromast operation to external pressure changes have been extensively examined in the past and implemented to develop lateral line probes (LLP) for current velocity estimation [57, 58] or turbulence metrics [59]. Although these techniques are robust and provide a reasonable estimate of the velocity or pressure field around fish-shaped bodies, they lack precision and accuracy.

Among the above-mentioned flow field measurement techniques, non-intrusive techniques such as PIV provide an accurate measurement of the velocity fields around fish. However, the current issue with these studies is the lack of open access to experimental data for future research. There are no openly available flow field data for any fish species that can be used for validation and comparison, which poses a challenge in the advancement of studies on fish flow interactions. This potential issue is identified as a research gap and is addressed in this study.

1.4 Numerical Modeling of Flow Fields

Investigation into simulating the flow fields around fish-shaped bodies started in the late 1990s. Earlier studies carried out mathematical 2D calculations of the flow around fish

using potential flow theory [31] that delineate that the current velocity profiles and pressure distribution around a swimming fish that glides through a stationary cylinder become altered, which may serve as stimuli for the lateral line system of fish. Furthermore, it also highlights the difference between the current velocity profiles obtained from the fish-like cross-section and those of cylindrical or elliptical cross-sections. Following this, further research was carried out on three-dimensional flow field analysis of fish-like bodies that glide along or toward a plane surface [42, 43]. With advances in computer architecture and enhanced computing resources, CFD became popular in evaluating fish flow interactions, including fish swimming kinematics and fish hydrodynamics [60, 61]. A pioneering work in CFD conducted by [47] showed that using Reynolds-averaged Navier-Stokes (RANS) models, the 2D simulations around a molten Sculpin in the presence of a vibrating dipole do not produce realistic flow fields as in the 3D model. The 3D CFD simulation also showed that the presence of fish perturbed the dipole-sourced pressure field around the fish body. The vibrating sphere affected the velocity fields on the surface of the fish due to the resulting oscillatory boundary layer. Therefore, the boundary layer near the fish's surface plays a crucial role in sensing hydrodynamic cues.

In CFD particularly, [33] employed the incompressible Navier-Stokes equation and simulated flow fields around a blind Mexican cavefish model swimming using an arbitrary Lagrangian-Eulerian (ALE) method on an unstructured Voronoi finite-volume mesh. Later studies on fish modelling revealed that the flow distribution is greatly influenced by the body morphology of the fish [62]. The 3D isosurfaces from CFD of the distorted velocity fields around the head region are smaller for the pike-like morphotype as compared to the generalist body shape, i.e., rainbow trout. This study used the RANS $k - \omega$ SST model in the OpenFOAM framework while analyzing the velocity fields around the fish models.

However, there exist substantial gaps in simulating the fish flow interaction numerically. The previously developed CFD models are not openly available for further development. These investigations predominantly relied on simplified 2D numerical modeling methods to explore the spatial and temporal aspects of flow fields, which are imprecise, since fish possess complex 3D body shapes. Furthermore, there is a lack of benchmark studies specifically identifying the appropriate turbulence model to analyze fish-flow interactions. Although previous research has emphasized the importance of the boundary layer [56], a comprehensive investigation into the boundary layer through CFD concerning fish hydrodynamic sensing is adequately addressed. Therefore, this study aims to address these issues and bridge the identified gaps in the numerical modeling of fish bodies.

1.5 Research Gaps

The background studies encompassing the numerical or experimental methods used in the exploration of flow fields around fish bodies highlighted the following potential research gaps that hinder researchers, engineers, biologists and practitioners in assessing the swimming behavior of fish.

RG 1. Lack of openly available experimental metadata for validation: The lack of accessibility to experimental data hampers the ability of researchers to effectively validate and verify their computational models or theoretical frameworks. In scientific research, especially in fields such as CFD modeling of ecological flows, validation against experimental data is essential to ensure the accuracy and reliability of the results [63]. The unavailability of such data not only limits the scope for rigorous scientific scrutiny, but also impedes collaborative efforts and the advancement of knowledge in the field. Generating such data will promote transparency, repro-

ducibility, and progress in scientific research.

RG2. Absence of benchmarking CFD studies around fish bodies: While developing numerical models for fish bodies, it is crucial to select the appropriate turbulence model and near-wall modeling approach to ensure accurate simulations that realistically represent fish flow interactions. Given the variety of turbulence models designed for different applications [64], it is necessary to evaluate their performance specifically around fish bodies, followed by thorough validation and benchmarking. Such a process will significantly enhance the accuracy and applicability of future Computational Fluid Dynamics (CFD) models in the realms of ecological and environmental research.

RG 3. Neglecting to incorporate realistic fish bodies into numerical simulations: The substitution of fish bodies with simplified fish replicas to reduce computational complexity has been previously observed in many studies [42, 33]. However, simplified fish analogies overlook critical aspects of the three-dimensional shape of the fish body and its hydrodynamics. Little is known about the significance of the shape of the body of fish in self-induced flow fields compared to these analogies. Therefore, a comparative study is needed to analyze the flow fields around both and highlight critical aspects. This will improve the fidelity and applicability of future studies in aquatic biology, environmental science, and ecological conservation.

RG 4. Physical relationships between the spatial distribution of self-induced flow fields and the sensory units of the lateral line remain unclear: The lateral line system detects spatial and temporal gradients of the flow fields. The spatial distribution of self-induced flow fields is incorporated into the masking effect. Previous research has established that the body of the fish perturbs the pressure fields generated by external stimuli [47]. However, there remains a significant gap in understanding the correlation between specific patterns of self-induced flow fields generated by the fish body shape and the positioning of lateral line units, i.e. neuromasts. Addressing this research gap may lead to a better understanding of fish behavior, advancing the field of sensing technology toward the development of new hydrodynamic sensors in underwater robots and autonomous underwater vehicles (AUVs).

1.6 Research Questions

In pursuit of addressing the problem statement (discussed in the previous chapter) and bridging the research gaps identified regarding fish-flow interactions, the following research questions aim to ascertain the significance of fish body morphology and its influence on self-induced flow fields.

RQ 1. How significant is the fish's body shape and what is its influence on the surrounding flow fields? (**RG 3**)

RQ 2. Do the Reynolds Averaged Navier Stokes (RANS) turbulence models provide a good estimate of near-body flow fields around a fish-shaped body? (**RG 1, RG 2**)

RQ 3. Is there a spatial concordance between the near-body flow fields and the estimated neuromast locations on fish bodies? (**RG 4**)

In this study, the research questions are explored using both qualitative and quantitative approaches. The upcoming chapter will provide a thorough discussion of the research methodology chosen to tackle these questions.

2 Research Method

This chapter presents the research methodology used to address existing research gaps within the domain of self-induced fish flow fields. The aim is to obtain fresh insights into the physical characteristics of fish bodies and their impact on the surrounding flow fields. The study encompasses fundamental/basic research with the objective of better understanding the fish flow interactions in underwater environments (see Fig. 4). Furthermore, it establishes a foundation for potential engineering applications in the development of hydrodynamic sensors. The investigation of fish flow interaction was carried out using experimental and numerical methods. The experiments provided on-site measurements of the velocity fields surrounding the static fish models, which were subsequently used in the validation of numerical models. Later, these numerical models were used in the exploration of different flow field variables such as velocity (U), pressure (P), boundary layer thickness (δ), and shear stresses (τ), which are challenging to measure experimentally. An advantage of adopting the anticipated research approach is that it facilitates open access to the measured or simulated flow field data that can be used for future research endeavors.

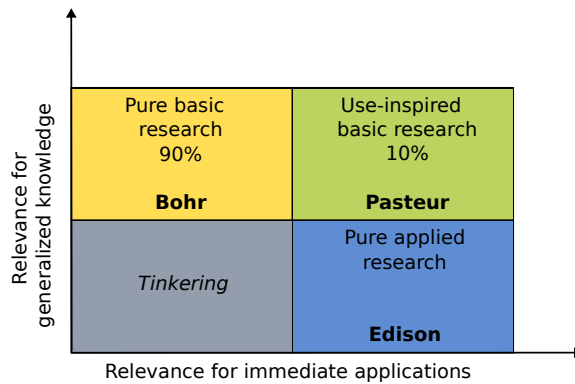


Figure 4: Pasteur's Quadrants [65] representing the contribution of type of research i.e. basic science (Bohr), use-inspired (Pasteur) and applied science (Edison).

Fish exhibit distinct flow patterns around their bodies during rheotaxis. These self-induced flow patterns are recognized and filtered by the fish. To investigate the relationship between the fish's body shape and the surrounding self-induced flow fields, two different experimental techniques, i.e., the Acoustic Doppler Velocimetry (ADV) and Laser Doppler Anemometry (LDA), were employed to measure the velocity fields around specific fish configurations. Subsequently, numerical models were developed using an open-source framework to simulate the flow around these fish configurations. The data obtained from both experimental and numerical methods were subjected to quantitative analysis, including statistical analysis and qualitative analysis, which involved examining the flow patterns around the fish models.

Within the scope of this work, nine different species of freshwater fish were selected (see Tab. 1). The selection of these species was based on common freshwater fish found in European rivers. It is important to note that no live fish were used in any of these experiments. Instead, physical models of these fish species were used. These physical models were either cast or 3D printed as rigid bodies. Cast models were utilized in the initial experiments employing the ADV measuring device. However, 3D-printed rigid models were employed in subsequent LDA experiments.

Table 1: List of fish species under observation and their geometric configurations

No.	Fish species	Body measurements		
		Body length [cm]	Body height [cm]	Body width [cm]
1.	Brown trout (<i>Salmo trutta</i>)	36.6	7.50	4.90
2.	Gudgeon (<i>Gobio gobio</i>)	15	2.70	1.95
3.	Perch (<i>Perca fluviatilis</i>)	20	5.80	3.20
4.	Roach (<i>Rutilus rutilus</i>)	20	6.00	2.80
5.	Nase (<i>Chondrostoma nasus</i>)	25	5.50	3.00
6.	Burbot (<i>Lota lota</i>)	25	4.25	4.25
7.	Chub (<i>Squalius cephalus</i>)	25	6.00	3.75
8.	Barbel (<i>Barbus barbus</i>)	30	5.70	3.60
9.	Bream (<i>Abramus brama</i>)	30	10.20	3.00
10.	Chub (<i>Squalius cephalus</i>)	40	9.60	6.00

The experimental setups to measure the flow fields around the physical fish models were deployed in the laboratory flumes and swim tunnels. Using the ADV and LDA devices, the time-averaged and instantaneous velocity fields at different flow rates were measured. The experimental and numerical methods used to study the flow fields around each fish model corresponding to the research question are summarized in Figure 5.

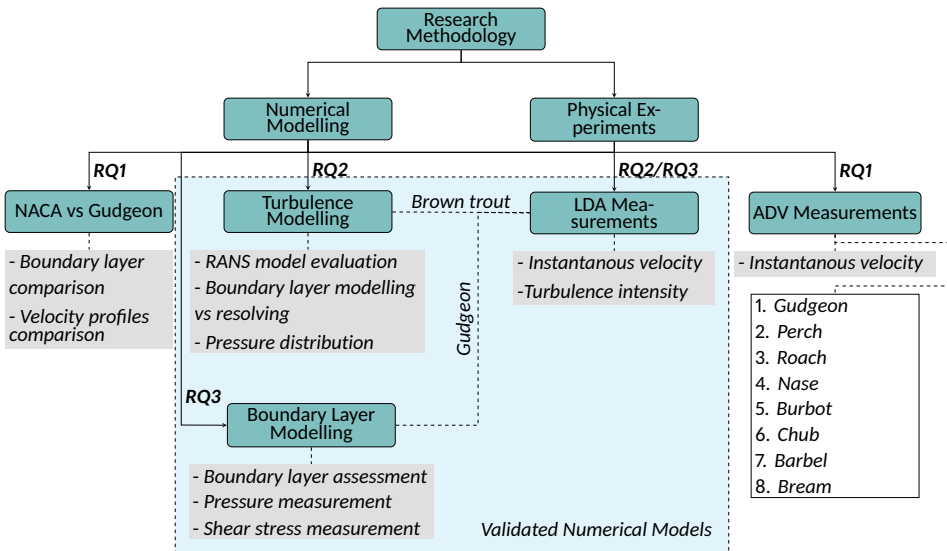


Figure 5: Synopsis of the research methodology adopted in this research work. The figure illustrates methods undertaken to analyse the freshwater fish species. The numerical models were validated using the laboratory LDA velocity measurements.

A brief overview of the measurement techniques and equipment used in this research is provided below.

2.1 Acoustic Doppler Velocimetry

Velocity measurements were recorded using a commercial ADV device by Vectrino Standard, Nortek AS, Norway. The device operates on the principle of the Doppler shift effect. It records 3D velocity vectors at a frequency of 1-25 Hz, with measurements taken at a distance of 5 cm below the transmitter (see Fig. 6). The sampling volume in which the velocity of the fluid is measured is less than 1 cm^3 . An acoustic signal transmitter is located at the center of the device that emits two ultrasonic pulses with a known time offset. The two transmitted pulses refer to the pulse-to-pulse coherent method [66], through which the mean water velocity and turbulence are calculated. Tracer particles in the flow reflect the incoming pulses that are detected by the four receivers and processed. The three components of the velocity (u_x , u_y , u_z) are calculated from the respective phase difference ($\Delta\phi_x$, $\Delta\phi_y$, $\Delta\phi_z$) between the pulses, using the following expression.

$$u = \frac{\Delta\phi C}{4\pi f_{source}\Delta t} \quad (1)$$

Where f_{source} is the transmitted frequency and Δt is the time difference between two consecutive pulses. The recorded velocity is scaled to the speed of sound through the particular fluid (C). The received signal is processed and visualized by *Vectrino+* software. The quality of the signal received by the receivers depends on the amount of tracer particles in the fluid, the flow velocity, and the position of the ADV device in the channel. In general, ADVs are capable of providing highly accurate and fine spatial measurement data that cause minimal disturbance to flow. Moreover, it is a robust technique that can be used in open fields and laboratory setups with minimal setup time.

2.2 Laser Doppler Anemometry

LDA is a non-intrusive and directional sensitive technique to measure velocity vectors in Cartesian coordinates (u_x , u_y , and u_z) of a moving fluid. Velocity measurements are performed with high spatial and temporal resolution without the requirement of a priori calibration. The functional principle of an LDA is based on the Doppler shift of scattered laser light from neutrally buoyant tracer particles added to the fluid [67]. The LDA device itself is comprised of a brag cell that splits a laser beam, a laser transmitter and receiver, a photo-detector, and a corresponding software i.e. *BSA Flow Software*, to process the collected data (see Fig. 7). The two intersecting laser beams focused by a focusing lens onto the measuring point inside the flowing fluid encompass a small volume (a few millimeters long and roughly some tenth of a millimeter in width), called probe volume, in which tracer particles interact with the laser light and scatter the light in different direc-

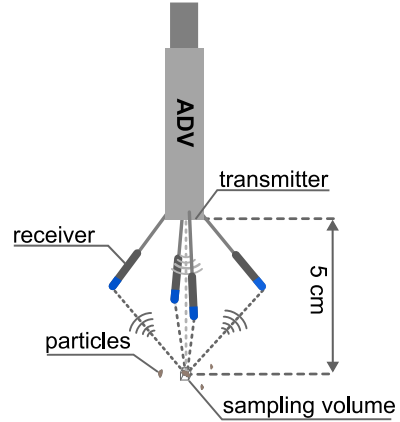


Figure 6: Velocity measurement of fluid particles using Acoustic Doppler principle.

tions. This results in parallel planes of high light intensity called fringes inside the probe volume. The fringe distance d_f depends on the wavelength of the laser light λ and the angle θ between the two laser beams.

$$d_f = \frac{\lambda}{2 \times \sin(\theta/2)} \quad (2)$$

The scattered laser light with a frequency shift is detected by the photo-detector, through which the particle velocity u is derived through the following expression.

$$u = d_f \cdot f_D \quad (3)$$

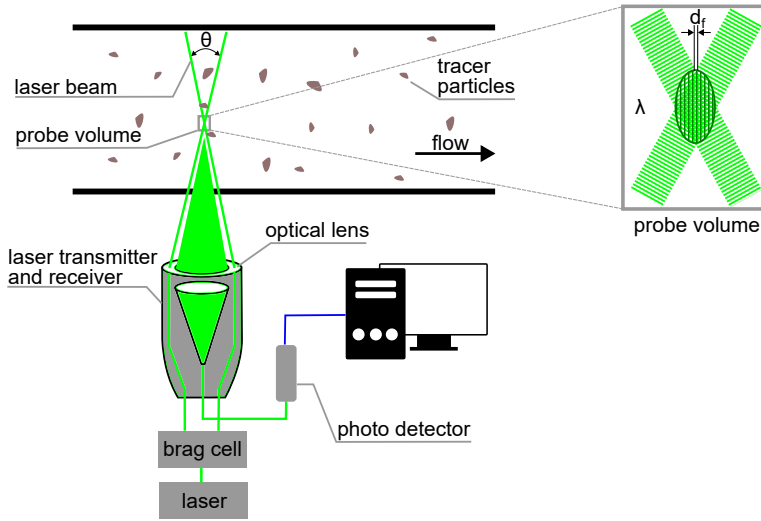


Figure 7: LDA measurement principle and its components.

The mean velocity \bar{u} and turbulence intensity is calculated from the obtained velocity components u_i from each laser over the number of samples N using the following expressions. Where η_i represents the weighting factor equivalent to $\eta_i = 1/N$, σ^2 represents the variance, and σ as the root mean square.

Mean velocity:

$$\bar{u} = \sum_{i=0}^{N-1} \eta_i \cdot u_i \quad (4)$$

Variance of the velocity samples:

$$\sigma^2 = \sum_{i=0}^{N-1} \eta_i \cdot (u_i - \bar{u})^2 \quad (5)$$

Standard deviation of the velocity samples:

$$\sigma = \sqrt{\sigma^2} \quad (6)$$

Turbulence intensity:

$$TI = \frac{\sigma}{\bar{u}} \quad (7)$$

The LDA experiments conducted in this work used an LDA device by Dantec Dynamics, Denmark. During measurements, two different focusing lenses were used i.e. 500 mm and 750 mm, to get optical access in different configuration setups. In our measurements, the two laser beams emitted by the laser transmitter were continuous and unsynchronized, aiming to attain higher sample rates. The laser head was mounted on a three-axis traversal system to achieve optical access within the test section from the bottom and side of the test section. The coordinate system of the traversal system was ensured to coincide with the coordinate system of the fish model located at the nose tip of the mounted fish. This was achieved through small iterative movement steps of the traversal system with the laser beams intersecting close to the nose tip of the fish model until it touched the nose. To achieve an optimal signal-to-noise ratio (SNR), it is essential to introduce a sufficient amount of tracer particles into the fluid, ensuring that the fluid maintains good transparency. In this study, only two Cartesian velocity components u_x and u_y were measured, ignoring the u_z component due to its negligible effect on mean flow.

2.3 Computational Fluid Dynamics

Computational fluid dynamics (CFD) is an advanced tool for quantitative prediction of fluid flow phenomena based on the conservation laws that govern fluid movement. It solves complex physical phenomena, i.e. turbulence modelling, fluid-structure interaction (FSI), etc. using numerical solution methods with the assistance of digital computers. The components of the numerical solution method are the mathematical model, discretization method, numerical grid, solving scheme, and convergence criteria [63]. It is crucial to choose an appropriate approach for each component based on the problem specifications because, in numerical modeling, the solution is always an approximation of the exact solution, and significant numerical errors can further exacerbate the discrepancy from the exact solution. In general, the mathematical model is the set of partial differential or integro-differential equations along with the boundary conditions. An incompressible, turbulent, and three-dimensional flow employs a set of governing equations, i.e. Navier-Stokes equations and continuity equation as a mathematical model. These governing equations can be solved directly without any modeling assumptions, a method known as Direct Numerical Simulation (DNS). Alternatively, they can be partially modeled, as in Large Eddy Simulation (LES), or fully modeled, as in Reynolds-Averaged Navier-Stokes (RANS) simulations. Discretization methods involve approximating differential equations through a set of algebraic equations. Among various discretization methods, the most frequently employed include finite difference, finite element, and finite volume methods. The finite-volume method (FVM) is commonly chosen for representing the three-dimensional computational domain. In FVM, the computational domain is divided into contiguous control volumes in which conservation equations are solved. This discretization method is useful for complex geometries such as fish, as it can accommodate any type of grid. The numerical grid is a set of discrete locations in the computational domain at which the flow variables are calculated. It can be structured, unstructured, or hybrid, depending on how complex the geometry is. The solving scheme addresses the set of linear or non-linear algebraic equations derived from the discretization method. The discretized equations are solved by an iterative technique that involves guessing the solution until it reaches the convergence of results. For convergence, normally the con-

vergence criteria are provided to the numerical method, in which the residual values of variables are defined. Although with advances in computing, the accuracy of numerical solutions has improved; however, approximate solutions are never exact. Certain potential sources of error such as discretization error, modeling error, etc. might affect the numerical solution, and thus be carefully handled. For example, mesh grid independence studies are conducted to decrease the discretization error. Similarly, the appropriate initial and boundary conditions with the correct input data are the key factors in reducing such errors.

The numerical models developed in this work were built in an open-source framework called OpenFOAM. OpenFOAM is a collection of C++ libraries and applications for continuum mechanics and multiphysics simulations. This particular framework was selected because of its extensive use in both academic and industrial sectors to simulate fluid dynamics and heat transfer problems. Another advantage of using OpenFOAM is that its libraries are openly available and can be customized according to the problem specification. It also provides an opportunity to discretize the 3D computational domain into hexahedral and polyhedral mesh elements using built-in utilities. In this research, three distinct numerical models were established, each designed to achieve specific objectives. For example, the first numerical model was designed to assess the performance of the turbulence model in estimating near-body flow fields around a brown trout model. The second CFD model was designed to assess the thickness of the boundary layer and to analyze the pressure field and shear stress around a gudgeon model. Ultimately, the third numerical model was developed to investigate the significance of the shape of the fish body in the self-induced flow fields around it. It was a comparative study between a three-dimensional model of a gudgeon and a NACA0013 hydrofoil. The specific procedure and settings of the numerical models are outlined in subsequent chapters.

3 Physical Experiments

This section presents an overview of the physical experiments conducted to address the research questions. In this study, three different experimental setups were established, each with its own unique configuration and measurement technique. The first experiment involved the use of an ADV measurement device in a laboratory flume to measure the velocity fields upstream of the fish. The second and third experiments utilized an LDA measurement device in two different environments, namely, a laboratory flume and a swimming tunnel. The choice of measurement facility depended on the spatial distance between the physical model of the fish and the measurement point. Since there was no existing data available, preliminary experiments were conducted in a large measurement facility (i.e., laboratory flume) that allowed for broader spatial measurements around the fish model. These measurements were taken at distances ranging from a few centimeters to a hundred centimeters in both the lateral and longitudinal directions. On the other hand, the swim tunnel provided a smaller measurement range with a finer resolution of 0.5 mm to 5 mm. Table 2 provides an overview of the experimental setups and their respective configurations.

Table 2: Experimental setup configurations and the measuring techniques employed

Exp. Setup	Measuring Technique	Recorded Variable	Measurement Facility	Measurement Resolution	Fish Specie Studied	Research Question
1	Acoustic Doppler Velocimeter (ADV)	Velocity (u_x, u_y, u_z)	Lab. flume (LxWxH) 40x2x1.4 m	1 cm	Eight species (see Fig. 5)	RQ1
2	Laser Doppler Anemometer (LDA)	Velocity (u_x, u_y)	Lab. flume (LxWxH) 10x1.2x0.8 m	3 mm	Brown trout	RQ2
3	Laser Doppler Anemometer (LDA)	Velocity (u_x, u_y)	Swim tunnel (LxWxH) 0.28x0.075x0.075 m	0.5 mm	Gudgeon	RQ3

3.1 ADV Velocity Measurements

In the initial experiments, an Acoustic Doppler Velocimeter (ADV) was used to measure the flow velocity upstream of the physical fish models. The experiments were carried out in the Laboratory of Hydraulics of the Technical University of Darmstadt, Germany. Physical 3D fish-shaped models of nine different species of fish, including two species of Chub (*Squalius cephalus*) were mounted in a 40 m long flume. These physical models were developed at the Centre for Environmental Intelligence and Sensing of Tallinn University of Technology (see Fig. 3). The dimensional parameters of the model and the composition construction features are described in detail in [68]. The anterior 1/3 of the fish models were made rigid to mount them to the moving frame, whereas the remaining posterior 2/3 body was cast of flexible silicon with a Shore hardness of 8. An ADV device was mounted on a robotic gantry in the flume together with the fish models (see Fig. 8). The upstream distance between the ADV probe and the fish model could be adjusted according to the requirements. Physical experiments were conducted in two steps. In the first step, a pilot study was carried out using three fish; Gudgeon, Nase, and Chub, to determine the consistent measurement time (5 mins), frequency (25 Hz), and the incremental distance (1-10 cm). The final step recorded the measurements for the evaluated time and distances considering the eight species of fish (Publication II).

The velocity vectors (u_x , u_y and u_z) in the Cartesian plane were recorded in a linear profile starting at the fish's nose (1 cm) up to 50 cm upstream. The incremental distance between 1 cm to 10 cm was kept at 1 cm, after that the increment distance was increased

to 10 cm until 50 cm. Experiments were carried out under three hydraulic conditions with different mean flow rates (0.35, 0.48, and 0.63 m/s) at the test section. To adapt conditions similar in the flume to the rheotactic alignment of fish, a velocity above 0.3 m/s with a middle velocity of 0.48 m/s was chosen for the experiments.

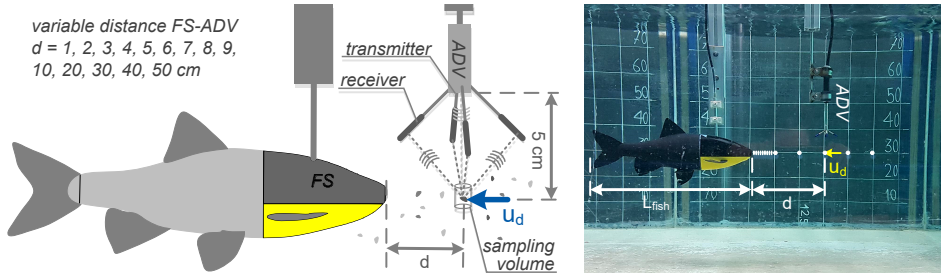


Figure 8: Overview of the ADV experimental setup procedure measuring the freestream velocity upstream of physical fish models in the large 40 m flume (adapted from Publication II)

3.2 LDA Velocity Measurements

Subsequently, two LDA experimental configurations were set up to measure the 2D planar velocity around a brown trout (*Salmo trutta*) and a gudgeon (*Gobio gobio*) fish model. The first experimental setup was built to measure the 2D velocity vectors (u_x and u_y) around the physical model of brown trout, which were used to validate the numerical model developed for the evaluation of the performance of RANS turbulence models in modelling the time-averaged flow fields. Similarly, the second set-up was also built to obtain the 2D velocity vectors (u_x and u_y) around a physical model of the gudgeon that was used to validate the numerical model developed to estimate the boundary layer thickness, pressure distribution, and shear stresses at the surface of fish. A detailed overview of both experimental configurations is provided in the following sections.

3.2.1 Flume Measurements of Brown trout

A laboratory setup was configured for the measurement of the 2D velocity (u_x and u_y) around a rigid 3D model of brown trout (Publication I). The 3D rigid model of the fish was based on the realistic body geometry of brown trout with a total body length of 35 cm [69]. Experiments were carried out in an open-channel laboratory flume at the Otto-von-Guericke University in Magdeburg, Germany (Fig. 9). Details of the flume dimensions are provided in Table 2. A honeycomb structure was used upstream of the test section to generate a rectilinear flow by directing the fluid in the main flow direction. Throughout the experiments, the depth of the water was maintained at 0.68 meters. The laser Doppler anemometry system (LDA) was strategically placed below the flume to facilitate optical access, covering a measurement volume of 0.6 m in length, 0.53 m in width, and 0.26 m in height, as shown in Fig. 10. Measurements were carried out at a mean stream velocity of 0.54 m/s, indicative of a fully turbulent flow regime with a Reynolds number (Re) of 6.8×10^5 based on the hydraulic diameter (d_h) of the flume.

$$d_h = \frac{4 \cdot b \cdot h}{b + 2 \cdot h} \quad (8)$$

Within the measurement domain, 253 probe locations were recorded to obtain the average and instantaneous velocity. The probe locations were categorized into three groups

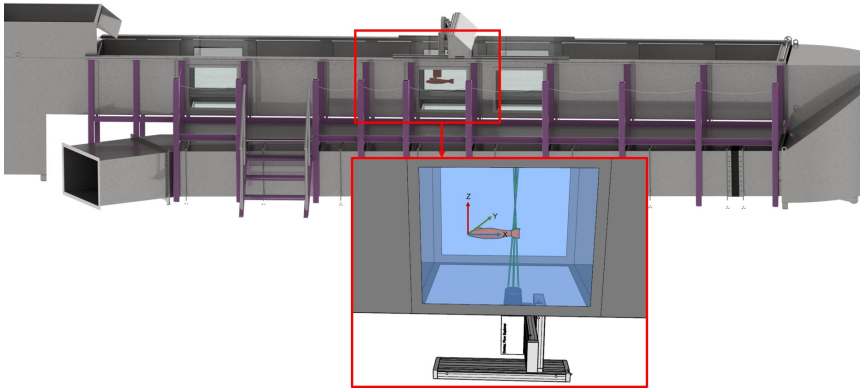


Figure 9: Overview of the LDA experimental setup with the 3D model of Brown trout placed in the measurement section of 10 m long flume. (Adapted from Publication I)

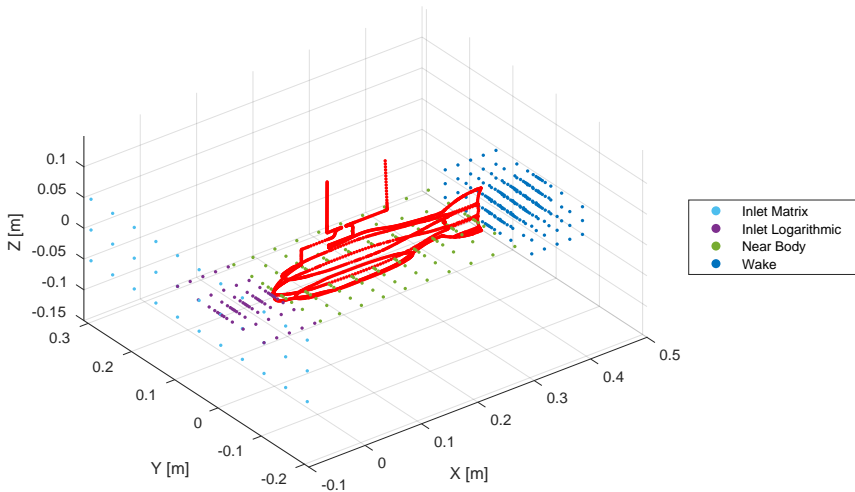


Figure 10: Positioning of measurement points around the Brown trout within the experimental domain.

based on their positioning around the fish, that is, upstream, body, and wake. The distance between the two probe locations was selected based on the lateral distance from the fish. This means that the density of the probe locations increased in the vicinity of the fish and decreased with increasing lateral distance from the fish. The closest measurement probe in the vicinity of the fish surface was located at a distance of 3 mm. The data obtained from the LDA measurements was post-processed and stored with the commercial software BSA Flow using a Dantec Flow Explorer DPSS 300 2D. The signal quality received through the software was optimized to achieve a good signal-to-noise (SNR) ratio of 70.1%. The experimental data were later used to validate the numerical models that were further investigated in the exploration of fish flow interaction.

3.2.2 Swim Tunnel Measurements of Gudgeon

The second LDA set-up used in this study used a 3D printed model of a bottom-dwelling fish gudgeon (*gobio gobio*) in a commercial swimming tunnel (185 L, Loligo Systems, Den-

mark) (see Fig. 11). Swim tunnels are widely used in studying fish swimming kinematics, energy expenditure, and swimming performance, and they have previously been used in a study of the swimming performance of a gudgeon with a similar size. The 2D velocity (u_x and u_y) was recorded in two perpendicular planes, i.e. the vertical plane (YZ) that is situated 0.048 m upstream of the fish body and the mid-dorsal ventral plane (XY) (Fig.12) at the tip of the nose of the fish ($Z = 0$). The reason for measuring the velocity in the vertical plane is to perform a quantitative analysis of the incoming flow, which was subsequently used as an input boundary condition in the numerical model. Additionally, due to the presence of guide vanes before the honeycomb structure, non-homogeneous flow distribution and high turbulence intensities were anticipated in the test section. To address this, a new honeycomb was modeled and 3D printed with a smaller orifice diameter (3 mm) to achieve a rectilinear flow.

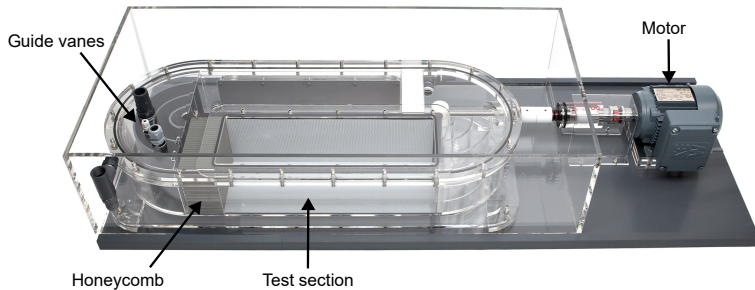


Figure 11: Swim tunnel by Loligo systems used in LDA experiments around Gudgeon.

In the vertical plane, there were 35 probe locations, each positioned at a clearance distance of 7.5 mm from the walls. Meanwhile, at the mid-dorsal ventral plane, velocity measurements were taken at 264 probe locations. In total, two sets of measurements were collected for two different hydraulic conditions i.e., at 0.25 m/s and 0.55 m/s, inside the swim tunnel test section (Publication III). The complete configuration of the swim tunnel with the gudgeon inside is shown in Fig. 12.

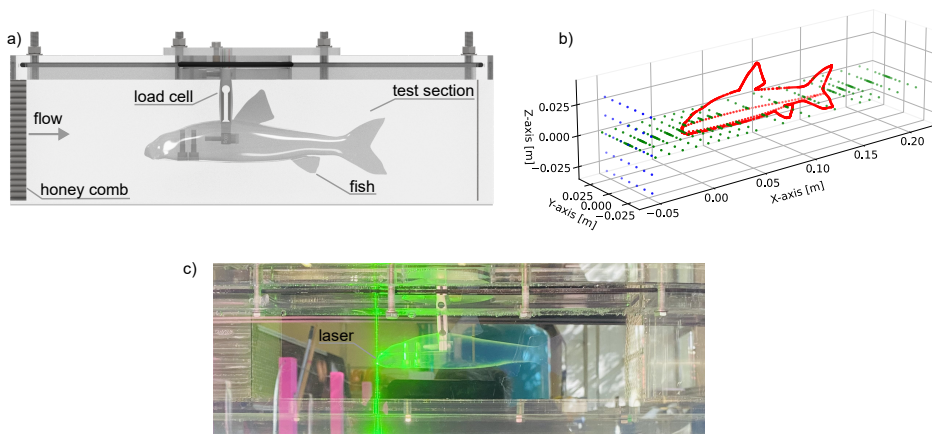


Figure 12: LDA measurements in the test section of swim tunnel. Left: 3D model of the gudgeon mounted into the swim tunnel with a load cell. Right: Location of the measurement probes inside the swim tunnel upstream around and in the wake of the fish. (adapted from Publication III)

4 Numerical Modeling of Fish-Shaped Bodies

The primary objective of this research is to conduct a thorough examination of the flow fields around the fish bodies. In pursuit of this objective, numerical simulations were conducted in conjunction with the experimental analysis for detailed scrutiny. To achieve this, three distinct numerical models were developed. The first model aimed to evaluate the performance of RANS turbulence models in estimating the self-induced velocity and pressure gradients around fish-shaped bodies. The second model analyzed the boundary layer thickness, pressure distribution, and shear stress along the body of the fish as a result of viscous effects. The third model compared the velocity field around a Gudgeon and a NACA profile, to examine potential differences in flow fields between both geometries. The numerical framework and the settings used in all three numerical models are presented in the following sections.

4.1 Numerical Modeling Framework

The numerical simulations around the fish-shaped bodies were performed in an open-source framework OpenFOAM-v2112 (see Section 2.3). The crucial steps in pre-processing such as geometry processing and mesh generation were carried out using extensive OpenFOAM utilities. Due to the significant distance between the free water surface and the fish model in flume experiments, the impact of surface fluctuations on the model was deemed negligible. Therefore, a single-phase solver for incompressible turbulent flow was preferred, offering substantial computational cost savings. An incompressible transient solver, *'pimpleFoam'* was initially employed (in Model I), anticipating unsteady behavior in the tail region of the flow. However, observations revealed that the flow remained steady prompting the use of a steady-state solver, i.e. *'simpleFoam'* in the subsequent simulations. The transport equation was solved iteratively by employing first-order numerical schemes for the gradients. A brief overview of the numerical simulation setups used in this realm is provided in Tab. 3.

Moreover, the numerical simulations were performed using parallel computing, allowing the simulations to execute on multiple processors, resulting in a significant reduction in simulation time. The Brown trout simulations were conducted on the Otto-von-Guericke University (OVGU) Neumann cluster, while the gudgeon simulations were carried out on a standalone machine (AMD EYPC 7713P processor) provided by the Centre for Environmental Sensing and Intelligence at Taltech. In the current work, each numerical simulation was executed in parallel on a maximum of 16 processors. For graphical representation, as well as post-processing and sampling of simulation data, the multiplatform data analysis and visualization tool *ParaView v5.10*, was used.

4.1.1 3D Fish Models

The numerical models incorporated 3D Computer-Aided Design (CAD) models of fish in the simulations. The 3D models of the fish, as well as the axis-symmetric NACA profile, were generated in CAD software SolidWorks. The first numerical model used a slightly abstracted 3D CAD model of a trout fish constructed based on the realistic body shape of a Brown trout (*Salmo trutta*). This design was adopted from the work of [69], which focused on the development of kinematics for robotic fish, utilizing Brown trout's physical characteristics as a reference. The second numerical model used a 3D CAD model of a Gudgeon (*Gobio gobio*) fish, constructed using three-dimensional representations of real fish. The 3D fish models parameters (except for trout) were provided by Dosch Design Kommunikationsagentur GmbH (*Marktheidenfeld, Germany*) and were derived from images

Table 3: Numerical setups configurations for all numerical models

	Numerical model I (Brown trout)	Numerical model II (Gudgeon)	Numerical model III (NACA)
Research Questions	<i>RQ2</i>	<i>RQ3</i>	<i>RQ1</i>
Numerical Framework	OpenFOAM-v2112	OpenFOAM-v2112	OpenFOAM-v2112
Solver	pimpleFoam	simpleFoam	simpleFoam
Characteristics	Incompressible, unsteady, turbulence	Incompressible, steady-state, turbulence	Incompressible, steady-state, turbulence
Temporal discretization			
Accuracy	First order	First order	First order
Timestep	10^{-3}	1	1
Spatial discretization			
Mesh type	Hybrid (Hexahedral & polyhedral)	Hybrid (Hexahedral, polyhedral)	Hybrid (Hexahedral, polyhedral)
Max cell size	0.0125 m	0.004 m	0.0035 m
Min cell size	0.001 m	0.00004 m	0.00004 m
Total number of cells	4.2 M	5.8 M	4.7 M
Turbulence model	$k - \epsilon$, $k - \omega$ SST, Spalart Allmaras	Spalart Allmaras	Spalart Allmaras
Wall treatment	Wall functions (unresolved) Calculated (resolved)	Fully resolved (Calculated)	Fully resolved (Calculated)
Convergence criteria			
Residuals	$U=10^{-4}$, $P=10^{-5}$	$U=10^{-5}$, $P=10^{-5}$	$U=10^{-5}$, $P=10^{-5}$
Relaxation factors	$U=0.7$, $P=0.6$	$U=0.7$, $P=0.7$	$U=0.7$, $P=0.7$
Total simulation time	384 CPUh	80 CPUh	76 CPUh

captured from live specimens. Modifications were made to these models to align them with the morphometric ratios outlined in [70]. This approach ensured a more accurate and representative model for the current research objectives. Lastly, for the comparative study between the gudgeon fish and the NACA profile, a 2D NACA0013 airfoil profile (coordinates retrieved from the UIUC Airfoil Coordinates Database [71]) was revolved around its longitudinal axis in SolidWorks to create a 3D streamlined and rotationally symmetric shape. The geometric dimensions of the corresponding CAD models are provided in Fig. 13.

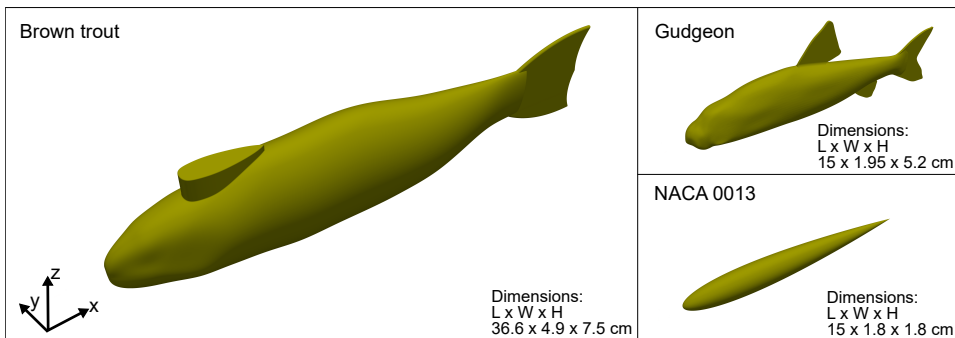


Figure 13: Isometric view of 3D models of the Rainbow trout, Gudgeon, and an axis-symmetric NACA profile. The brown trout model has an airfoil shape mounting at the top to hinge it to the mounting assembly.

The 3D CAD models of fish were imported into OpenFOAM as STL files which were castellated into the background mesh using a *cfMesh* utility in OpenFOAM. *cfMesh* is an advanced tool that discretizes the computational domain into small hexahedral mesh ele-

ments (in the free stream) and polyhedral mesh elements (close to the surface of fish) of the size specified in the dictionary. The detailed overview of mesh discretization in each numerical model with the total number of elements in the computational domain is provided in Tab. 3.

4.1.2 Boundary Conditions

The computational domain assigned in the numerical models varied for each setup, tailored to suit the specific measurement scale. However, the boundary conditions implemented at the domains were largely similar. For validation, numerical models of the Brown trout and the Gudgeon were developed with a mapped inlet velocity boundary condition. This condition was executed using a second-order polynomial expression derived from the LDA measurements recorded upstream of the fish close to the inlet of the channel. On the contrary, the numerical models used for the comparative study between the Gudgeon model and the NACA profile were set with a uniform inlet velocity condition. The surface of the fish and the boundary walls of the domain were assigned a non-slip velocity condition ($U = 0$). For pressure settings in all models, a Neumann boundary condition ($\nabla P = 0$) was specified at the inlet, while a Dirichlet boundary condition ($P = 0$) was employed at the outlet. The computational domain with the respective boundary condition are illustrated in Fig. 14.

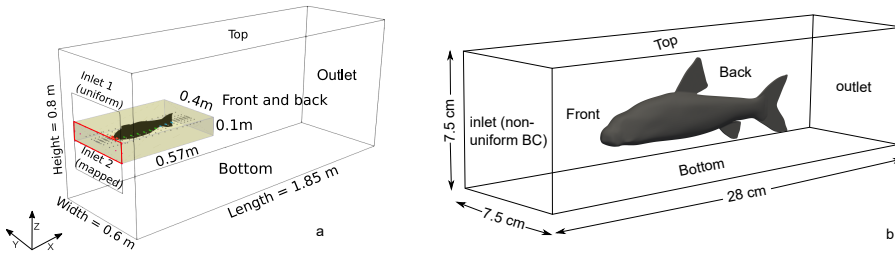


Figure 14: Computational domains of the numerical models along with the boundary conditions. a) Computational domain representing a section of the lab flume with a brown trout model. The highlighted region indicates the measurement area within the actual domain. b) Computational domain of the gudgeon inside the swim tunnel.

4.1.3 Mesh Sensitivity Analysis

It is imperative to ensure that the flow fields predicted through numerical modeling are independent of the size of the mesh grid to guarantee the integrity and accuracy of the simulation results. The accuracy and efficiency of numerical models are influenced by the size of discretized elements in the computational domain. Therefore, all developed numerical models were analyzed using a Grid Convergence Index (GCI) method, a standardized procedure introduced by [72], to estimate and report the uncertainty between the different sizes of the mesh elements. For each model, five meshes with different mesh cell sizes (coarse to fine) were generated. As a standard practice, an evaluation metric (in this case, the drag coefficient C_d) was selected to analyze the influence of the grid size on the estimated results. The drag coefficient was calculated using the following expression.

$$C_d = \frac{2F_d}{\rho u^2 A} \quad (9)$$

Where F_d is the drag force acting on the body surface area A , inside a fluid of density ρ

flowing with a mean velocity of U . In particular, the area of the fish or the 3D NACA0013 profile was calculated by multiplying the total length by the width of the object ($L \times W$). The difference in the measured drag coefficient value was reported as the error between successive meshes. Thus, the final mesh chosen for the simulations was determined through the iterative convergence of relative errors between the mesh. A detailed overview of the mesh statistics is provided in Tab. 4. Following the criteria proposed in [72], the ratio of each successive mesh size r_{ji} was calculated to determine the apparent order p_a of the method. The r_{ji} values were based on the largest mesh size within the computational domain in particular close to the boundaries, as the mesh size around the fish was fully resolved.

$$p_a = \frac{1}{\ln(r_{ji})} \left| \ln \left| \frac{E_{kj}}{E_{ji}} \right| + q(p_a) \right| \quad (10)$$

where $E_{kj} = C_{d_k} - C_{d_j}$ and $E_{ji} = C_{d_j} - C_{d_i}$.

$$q(p_a) = \ln \left[\frac{r_{ji}^{p_a} - s}{r_{kj}^{p_a} - s} \right] \quad (11)$$

$$s = 1. \text{sgn}(E_{kj}/E_{ji}) \quad (12)$$

The extrapolated values of the drag coefficient were calculated as:

$$C_{d_{ext}}^{ji} = (r_{ji}^{p_a} C_{d_i} - C_{d_j}) / (r_{ji}^{p_a} - 1) \quad (13)$$

The approximated relative error, (e_a^{ji}) between each consecutive mesh was calculated along with the grid convergence index (GCI) using the following expressions:

$$e_a^{ji} = \left| \frac{C_{d_i} - C_{d_j}}{C_{d_i}} \right| \quad (14)$$

$$GCI_{fine}^{ji} = \frac{1.25 e_a^{ji}}{r_{ji}^{p_a} - 1} \quad (15)$$

4.2 Turbulence Modeling

The flow observed in the flume test section ($Re=6.8 \times 10^5$) and the swim tunnel (Re ranges from $Re=1.87 \times 10^4$ to $Re=9.36 \times 10^4$), was completely turbulent, necessitating the use of turbulence models to effectively simulate the evolution of the flow within the test section. The Reynolds number is based on the hydraulic diameter, d_h , of the flume and swim tunnel. Rectilinear flow generated by the honeycomb structure breaks down large turbulent structures to the scale of the honeycombs and allows for faster dissipation of the turbulent energy and the reduction of the turbulent intensity. In the case of the swim tunnel, the turbulent intensity remained high (i.e. from 7 to 40%) due to the small distance from the honeycomb to the fish model and a high overall turbulent intensity of the system due to moderate rectification of the flow in the propulsion system. However, the flume measurements showed relatively low turbulent intensity (i.e. 3.5 to 4.5 %) in the test section. The reduced turbulent intensity in the flume is the result of using a secondary honeycomb structure along with a grid that could not be applied in the swim tunnel due to spatial constraints.

Table 4: Mesh sensitivity analysis conducted for the numerical models with GCI method

Parameters	Grid Convergence Index (GCI) Method		
	Brown trout model	Gudgeon model	NACA model
N_1, N_2, N_3, N_4, N_5	47 K, 107 K, 700 K, 4.2 M, 5.5 M	172 K, 0.65 M, 1.0 M, 5.8 M, 7.9 M	50 K, 1.2 M, 2.4 M, 4.7 M, 6.6 M
$y_1^+, y_2^+, y_3^+, y_4^+, y_5^+$	3.9, 2.7, 1.4, 0.7, 0.5	4.0, 0.40, 0.46, 0.65, 0.09	2.7, 2.12, 1.08, 0.15, 0.55
$C_{d1}, C_{d2}, C_{d3}, C_{d4}, C_{d5}$	0.0417, 0.0367, 0.0320, 0.0282, 0.0285	0.07087, 0.07431, 0.06947, 0.06389, 0.06354	0.03132, 0.03065, 0.03151, 0.03204, 0.03175
p_{avg}	1.49	3.632	2.354
$C_{d_{ext}}^{21}, C_{d_{ext}}^{32}, C_{d_{ext}}^{43}, C_{d_{ext}}^{54}$	0.0467, 0.0414, 0.0358, 0.1116	0.07546, 0.05011, 0.05831, 0.06319	0.03231, 0.03323, 0.03572, 0.03002
$e_a^{21}, e_a^{32}, e_a^{43}, e_a^{54}$	11.99%, 12.80%, 11.87%, 1.06%	4.63%, 6.96%, 8.73%, 0.55%	2.11%, 2.79%, 1.67%, 0.89%
GCI_{coarse}^{21}	14.98%	1.92%	3.96%
GCI^{32}	16.00%	34.83%	10.50%
GCI^{43}	14.84%	10.91%	16.67%
GCI_{fine}^{54}	5.30%	0.68%	7.86%

A suitable turbulence modeling approach is necessary to account for the turbulence characteristics in the numerical setup. To achieve this, three primary methods can be used to simulate turbulent flow in the test section: DNS, LES, and RANS. Direct Numerical Simulation (DNS) is the most accurate method for resolving turbulence. It solves the Navier-Stokes equation directly, encompassing the entire spectrum of turbulence, from the smallest eddies of Kolmogorov scales to the largest eddies of integral length scales. DNS resolves the spatial and temporal scales of the turbulence and is therefore computationally expensive even at low Reynolds numbers. This is why it is widely used for fundamental research on turbulence rather than as a general-purpose design tool. However, large-eddy simulation (LES) is a hybrid approach that resolves only large-scale turbulent structures while modeling the effects of smaller unresolved scales. It employs a spatial filter on the governing equations, allowing it to resolve significant turbulent features. The resolved scales are directly solved, whereas the unresolved filtered scales are modeled using subgrid-scale (SGS) models. The accuracy and efficiency of the LES simulations are heavily dependent on the choice of subgrid-scale (SGS) models, which are developed based on various assumptions and approaches. A simple and computationally affordable approach is Reynolds-averaged Navier-Stokes (RANS) modeling, which focuses on estimating the time-averaged flow fields. The RANS governing equations numerically solve the mean flow, representing turbulence properties with an additional term known as Reynolds stresses, which are modeled using turbulence models. These turbulence models provide closure to the RANS equations by expressing Reynolds stresses in terms of mean flow properties.

This study focuses on providing a cost-effective benchmarking case using RANS which are commonly used as substitutes as they are fast, i.e. providing a time-averaged solution, and are computationally moderate. Although the lateral line system of fish is highly sensitive to instantaneous flow fields, it is assumed that the spatial distribution of the flow from the fish bodies can be evaluated based on time-averaged values.

4.2.1 Reynolds Averaged Navier Stokes Equations

The Reynolds Averaged Navier Stokes Equations (RANS) are time-averaged equations of fluid moving through the domain. According to Reynolds' decomposition, the instantaneous quantity of the velocity is represented as the sum of the time-averaged and instantaneous fluctuation quantities. RANS simulations allow for a sufficient representation of the physical flow conditions in many applications in science and engineering and are widely employed in academics and industry. However, the system of RANS equations is not closed due to unknown variables, and thus a huge amount of closure models, also known as turbulence models, are developed over time within the framework of RANS. These closure models are non-universal and have semi-empirical characters, including submodels with constants. Most of these turbulence models are based on the Boussinesq hypothesis, which takes the assumption that Reynolds stresses are proportional to mean deformation rates [73]. Using Reynolds decomposition, the Navier-Stokes momentum equation is written as:

$$\rho \frac{\partial u_i}{\partial t} + \rho \frac{\partial}{\partial x_j} (u_i u_j) = -\frac{\partial p}{\partial x_i} + \frac{\partial}{\partial x_j} (2\mu S_{ij} - \rho \overline{u_i' u_j'}) \quad (16)$$

where u is velocity, t is time, p is pressure, μ is the dynamic viscosity, S_{ij} is the mean strain rate tensor, u' is the fluctuating velocity component and $\overline{u_i' u_j'}$ are the mean velocity gradients. The Boussinesq approach fundamentally relates the Reynolds stresses to the

mean velocity gradients, which are expressed as:

$$-\overline{\rho u_i' u_j'} = \mu_t \left(\frac{\partial u_i}{\partial x_j} + \frac{\partial u_j}{\partial x_i} \right) - \frac{2}{3} \left(\rho k + \mu_t \frac{\partial u_k}{\partial x_k} \right) \delta_{ij} \quad (17)$$

where δ_{ij} is the Kronecker delta with orthogonal coordinate indices i and j . An advantage of modeling Reynolds stresses with the Boussinesq hypothesis is the decrease in computational cost associated with the use of turbulent viscosity μ_t . The Boussinesq hypothesis fundamentally assumes μ_t to be a scalar quantity. Among the different RANS turbulence models, the ones most frequently used include the standard $k - \varepsilon$, $k - \omega$ SST, and *Spalart-Allmaras* models, each known for their suitability in different applications.

4.2.2 Standard $k - \varepsilon$ Model

The standard $k - \varepsilon$ model is one of the most widely used in RANS simulations. It is a two-equation model that solves the turbulent kinetic energy k and turbulent dissipation ε , which approximates the turbulence in the averaged flow field calculated by the RANS approach [74]. The $k - \varepsilon$ model is known to perform well in free shear flows, where pressure gradients tend to be small [75, 76]. Currently, there are multiple extensions of the standard model available, including the realizable $k - \varepsilon$ model and the re-normalization group (RNG) $k - \varepsilon$ model [77] etc. The difference between the standard model and its extensions is the capability of modeling the specific flow conditions, e.g. rotating flows and flow anisotropy, with enhanced accuracy. The standard $k - \varepsilon$ model is effective for high Reynolds numbers and fully turbulent flows.

4.2.3 $k - \omega$ SST Model

The issues related to the $k - \varepsilon$ model were resolved by introducing a hybrid turbulence model $k - \omega$ SST model. It is a two-equation model that combines the advantages of the $k - \omega$ model [78] i.e. better performance in transitional flows and flows with adverse pressure gradients and the $k - \varepsilon$ model. The $k - \omega$ SST model is well suited for wall-bounded and unbounded flows [79], where the transport of shear stress is included in the turbulent viscosity to improve the prediction of flow separation on smooth surfaces with adverse pressure gradients. A turbulent prediction limiter was added by [80] to avoid overprediction of turbulent kinetic energy in stagnation regions without influencing shear layers. Due to the importance of the near-body flow fields around fish, this model was taken into account, as it incorporates a blended function that determines the position and activates the required turbulence model. The value of the blended function goes to zero far from the wall, applying $k - \varepsilon$, and remains unity within the boundary layer where $k - \omega$ is used. In this study, the model was executed with the default values of the model constants presented in [80].

4.2.4 Spalart-Allmaras Model

The Spalart-Allmaras model is a single equation approach that implements linear eddy viscosity. The model was first introduced by [81] and developed for modeling airfoils with adverse pressure gradients, which are geometrically similar to 2D fish-shaped bodies. This model in particular lacks the turbulence kinetic energy and therefore while estimating the Reynolds stresses the last term in Eq. 17 is ignored and the kinematic eddy viscosity is calculated through the use of closure functions [82].

4.3 Boundary Layer and Near-Wall Treatment

The flow in all numerical simulations was fully turbulent and strongly influenced by the presence of the fish body. Closer to the surface of the fish, the fluid's viscosity is considered to satisfy the no-slip wall condition, which takes care of the velocity transition from a finite value close to the surface to zero directly at the surface of the fish. At a high Reynolds number, this transition occurs in a thin layer called the boundary layer (*BL*). In general, the flow can be classified into the bulk flow region, where viscous effects give rise to dissipation, and the boundary layer region, where the viscosity should be handled carefully to truly represent the velocity gradients.

The flow inside the boundary layer region can either be modelled or resolved depending on the significance of the problem. In the case of modelling, the mesh grid around the surface of the fish is coarse enough that the first mesh node lies in the log-law or a fully turbulent region (preferably $30 < y^+ < 300$). This is accompanied by the application of wall functions, which are empirical formulations to satisfy the physics of flow in the near-wall region. An advantage of using the wall function is that it does not require an abundant mesh near the surface of the fish. However, to resolve the boundary layer, modified turbulence models are used to allow the viscosity-affected region to be resolved with fine mesh on the surface of the fish, including the viscous sublayer, which requires a very fine mesh resolution (e.g. $y^+ < 1$).

$$y^+ = \frac{y u_\tau}{\mu} \quad (18)$$

Where y is the absolute distance from the wall, u_τ is the frictional velocity and μ is the dynamic viscosity. Considering the universal law of the wall the distribution of velocity in the inner layer (i.e. boundary layer region) and the outer layer (i.e. bulk flow region) is illustrated in Fig. 15. The initial numerical models developed to evaluate the RANS turbulence model performance employed both the modelled and resolved boundary layer approaches. Based on the findings from the initial models the latter models were developed using the resolved approach only.

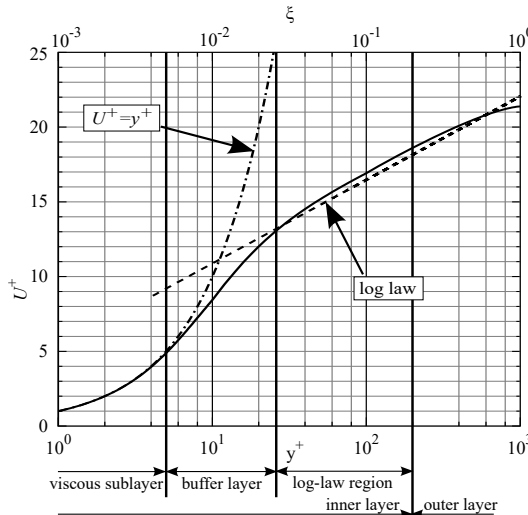


Figure 15: Velocity distribution in the turbulent boundary layer across different regions near the wall. (adapted from [83])

4.4 Validation of Numerical Model

The numerical models developed in this study were simultaneously validated with the experimental data (from section 3.2) to ensure the reliability of the model. For validation, it was important to achieve similar flow conditions in the computational domain as observed in the experimental measurements. Therefore, the time-averaged velocity measured in the YZ plane upstream of the fish for both brown trout and gudgeon near the honeycomb structure was mapped into the numerical model as an inlet boundary condition. The measured velocity was converted into a second-order polynomial derived from the linear regression of the velocity values at the measured locations. Although the experimental measurements encompassed the turbulence properties of the flow such as the turbulence intensities (TI), they could not be mapped in OpenFOAM due to the limitations of the single-equation turbulence model, i.e. Spalart Allmaras.

It is known that turbulence dissipates rapidly in RANS models and that a negligible effect on the fish is expected. Therefore, the estimated time-averaged velocity in the mid-dorsal ventral plane of the fish was validated with the experimentally recorded data. The validations were carried out on a 1:1 scale by plotting linear contour plots for the numerical and experimental velocity values. For the brown trout model, the validation of the estimated numerical velocity with the experimental data was selected as an assessment tool to evaluate the performance of the RANS turbulence models (see Fig. 20). However, for the gudgeon model, the estimated velocity was validated with experimental data to ensure the model's accuracy, which is later used to investigate pressure, boundary layer thickness, and shear stresses at the surface of the fish model.

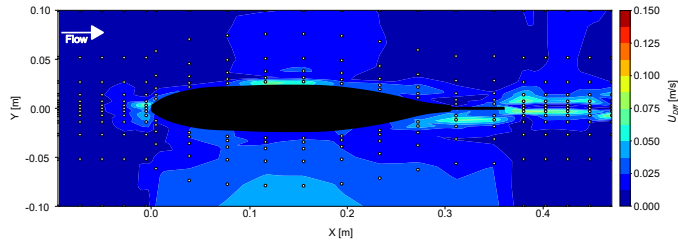


Figure 16: Absolute velocity difference between the estimated numerical velocity and the LDA recorded velocity around the Brown trout fish model with Spalart Allmaras (SA) model at the mean velocity $U_{mean} = 0.55$ m/s (Publication I).

The gudgeon fish model encountered major challenges during the validation process. The large curvature of the guide vanes before the honeycomb mesh structure resulted in a non-homogeneous flow with high turbulence levels inside the test section. The high levels of turbulence led to notable fluctuations in mean velocity measurements. Given these issues, validation of only the near-body velocity fields around the gudgeon fish was performed with experimental data, selectively excluding the upstream and downstream regions. Furthermore, at certain locations, the optical access of the LDA also deteriorated as a result of scratches on the walls of the acrylic swimming tunnel.

At these specific point locations, the measurement data was withdrawn. These locations were identified (see Fig. 18) by plotting a Bland-Altman plot [84] between the experimentally recorded velocity measurements and the simulated velocity estimates. Probe locations located within the gray-hashed area were considered outliers, as they exhibited the maximum difference between recorded and simulated velocity measurements and consequently were excluded from the analysis to maintain data integrity (Publication III). This approach ensured a more accurate validation of the model under the constraints

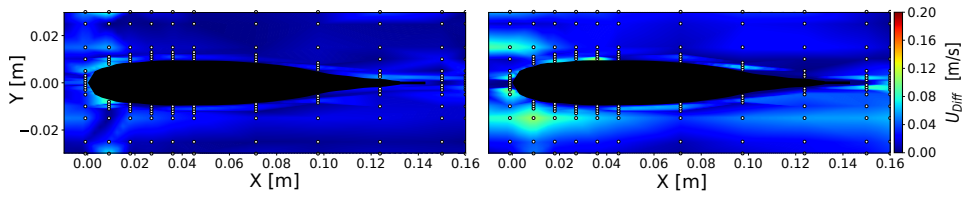


Figure 17: Absolute velocity difference between the estimated numerical velocity and the LDA recorded velocity around the gudgeon fish model with at the mean velocity $U_{mean} = 0.25$ m/s and $U_{mean} = 0.55$ m/s at mid-dorsal-ventral plane (Publication III).

imposed by the experimental setup.

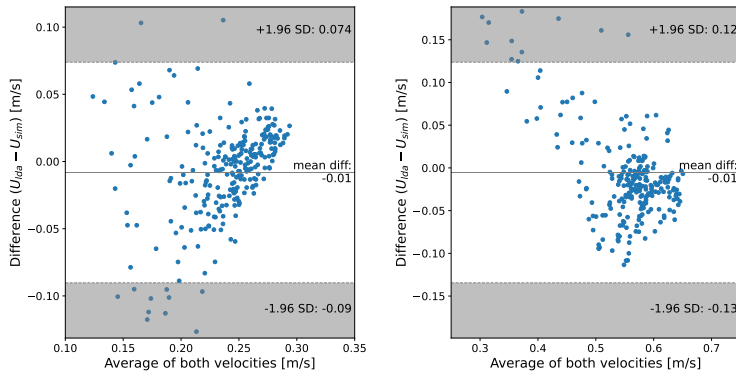


Figure 18: Difference between the estimated and measured velocity values using Bland-Altman plot for 0.25 m/s (left) and 0.55 m/s (right).

5 Results and Discussions

The chapter begins with a discussion of each research question followed by a critical discussion of the implications of the research findings on fish conservation. It offers a detailed understanding of the importance of body geometry in self-induced flow fields and its relationship with the sensory array of mechanoreceptors. Each section of the chapter corresponds to one of the research questions.

5.1 Significance of Fish Body Shape

RQ1. *How significant is the fish's body shape and what is its influence on the surrounding flow fields?*

Our investigations provide clear evidence that the 3D fish's complex body shape generates specific flow fields. The comparative study of velocity fields between a 3D NACA0013 profile and a gudgeon fish revealed only minor differences in boundary layer thickness (Publication V). Whereas, the pressure fields showed significant variations. Both the gudgeon and the NACA0013 profile exhibited high-pressure gradients in the head region and relatively low-pressure gradients along the body. However, a detailed analysis revealed that the fish's distinct body shape suppresses secondary gradients (Publication III) in the normalized pressure coefficient (C_p) around the head region (see Fig. 19). Previous studies calculated 2D velocity and normalized pressure coefficient around a NACA0013 profile and a simplified fish shape using low-order mathematical models [42, 43], revealing only marginal differences between the two. In contrast, our 3D model, incorporating a more realistic fish body shape, shows that the fish generates secondary fluctuations in the normalized pressure coefficient around the head region, specifically at 6% and 14% of the total body length of a gudgeon fish—a phenomenon absent in earlier studies [33, 34].

Furthermore, ADV experiments conducted to measure the velocity fields upstream of nine different physical fish models demonstrated that the fish's body shape significantly influences the depletion of incoming flow velocity. Though the streamlined body of the fish minimizes this depletion, variations were observed across the fish models. The longest fish body caused the highest velocity depletion, while the shortest body caused the least depletion (Publication II). Although velocity measurements were limited to the upstream region, they highlight the role of fish body shape in shaping the surrounding flow fields. The velocity depletion for each fish can be observed in Fig. 19.

The significance of fish body shape is intriguing, as it influences the surrounding flow fields and, as previous studies suggest, self-induced flow fields play a crucial role in enabling fish to perceive hydrodynamic stimuli [32]. Fish species have evolved their distinct body shapes relative to their specific environments and ecological niches. Numerical studies on 2D fish-like bodies have demonstrated that variations in body shape lead to changes in the surrounding velocity and pressure fields [42, 43]. However, modeling the flow fields around the complex 3D shapes of fish posed significant challenges, such as laborious meshing and high computational demands. To address these challenges, previous studies investigating fish-flow interactions often relied on fish analogies or over-simplified body shapes [33, 34] to reduce computational costs. Nevertheless, the use of over-simplified body shapes may compromise the accuracy and reliability of research findings.

5.2 RANS Turbulence Model

RQ2. *Do the Reynolds Averaged Navier Stokes (RANS) turbulence models provide a good estimate of near-body flow fields around a fish-shaped body?*

Within the scope of this work, three different RANS turbulence models were employed on

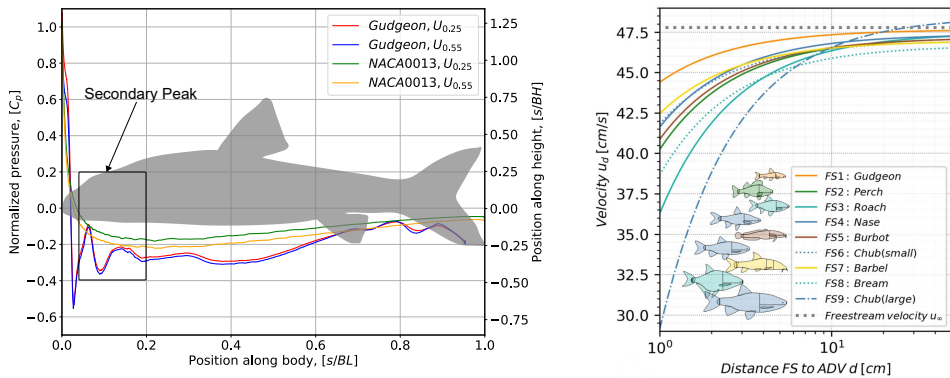


Figure 19: Left: Normalised pressure coefficient (C_p) comparison between a bottom-oriented Gudgeon fish and NACA0013 axis-symmetric profile at the mid-dorsal ventral plane. Right: Flow velocity reduction upstream of the fish for eight different fish species representing the lowest distortion for the smallest and highest distortion for the longest fish (adapted from Publication II).

a brown trout fish model to evaluate their performance in estimating the average velocity fields (Publication I). All turbulence models performed well in simulating the physical models of fish with minor differences. The standard model $k - \epsilon$ failed to estimate the velocity around the head region with adverse pressure gradients. Whereas the $k - \omega$ SST and Spalart Allmaras (SA) model performed nearly equally in the head region. Similar trends were observed along the body of the fish. The tail region is an important region where the flow becomes more turbulent. In this region, the SA model estimated the velocity field with the highest overall accuracy, both near the surface of the fish and away from the free stream. Furthermore, the resolved near-wall regions in all turbulence models provided better results than the non-resolved models. Hence, the resolved RANS turbulence models offer a reliable estimate of flow fields around fish-shaped bodies. Among RANS, the Spalart Allmaras (SA) model demonstrates comparatively better performance in predicting the flow fields.

5.3 Lateral Line Receptors and Flow Fields

RQ3. *Is there a spatial concordance between the near-body flow fields and the estimated neuromast locations on fish bodies?*

The distribution of lateral-line receptors along the fish body is adaptively evolved and could reflect the spatially distributed flow fields. The findings of this study revealed that the approximate positioning of the neuromasts does reflect the spatially distributed shear stresses along the body of the fish. The anterior 20% body length of the fish contained above 47% of the total number of superficial neuromasts, and within this region, the coefficient of skin friction also showed notable gradients as shown in Fig. 21 (Publication III). The validated numerical model of the gudgeon fish was mapped with the approximate positioning of the neuromasts (as described in [85]) and the boundary layer thickness, pressure, and shear stresses were correlated to the known positioning of neuromasts (Publication III). The boundary layer thickness calculated around the surface of a gudgeon fish showed that, regardless of the flow rate, the anterior head region exhibits a thinner boundary layer thickness while it increases along the body length and reaches maximum thickness in the tail region. Moreover, the anterior part of the fish experiences a laminar

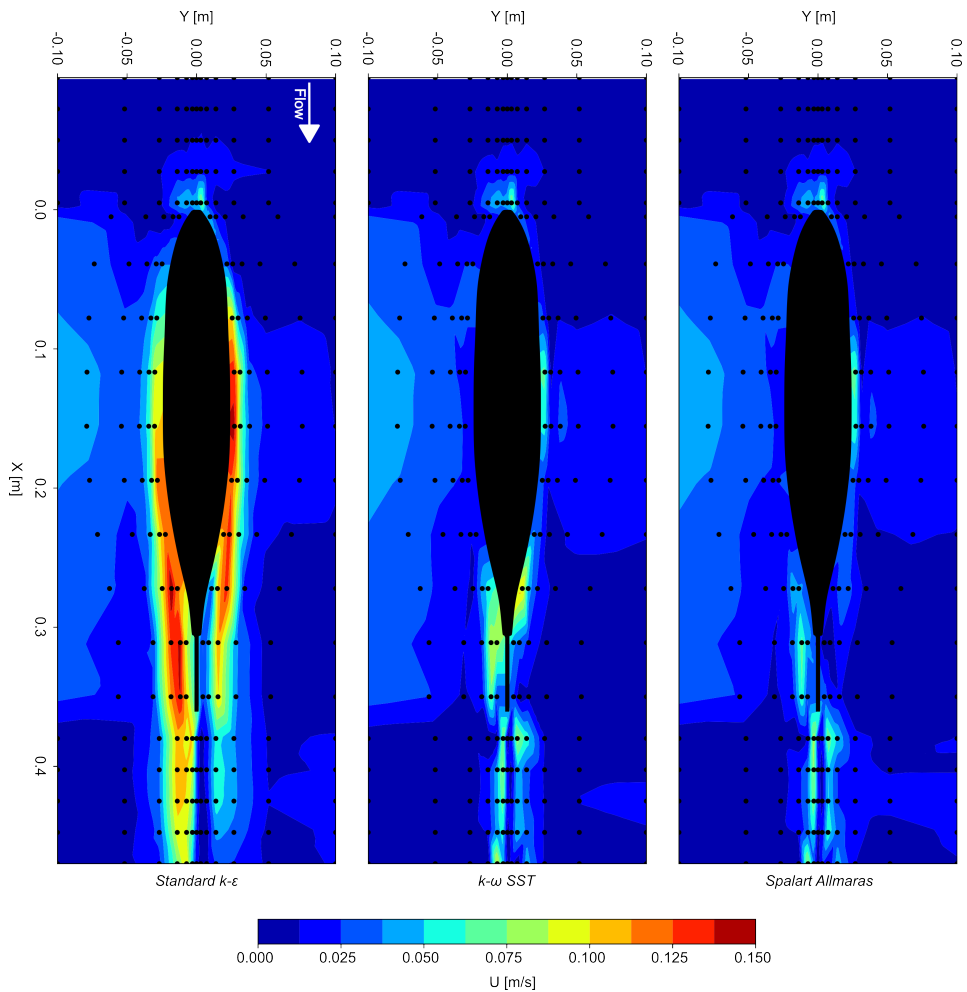


Figure 20: Absolute velocity difference between the LDA measured and simulated velocity for various turbulence models enacted in this study (adapted from Publication 1).

boundary layer, whereas in the tail region, it becomes more turbulent. With increasing Reynolds numbers, the thickness of the boundary layer started to decrease (see Fig. 22). The decrease in the thickness of the boundary layer at higher speeds was obvious which might limit the perception of hydrodynamic stimuli during fast manoeuvres and sprints, such as during predator-prey interactions. As is known, the canal neuromasts are embedded in the upper dermal layer and superficial neuromasts are suspended in the flow, both reside within the boundary layer. From the literature, it is evident that the anterior 20% of the fish body length contains a higher concentration of neuromasts [35]. However, the positioning and number of neuromasts on the surface of fish vary across species. Due to the uncertain precise placement of neuromasts, it was difficult to establish a correlation with the spatially distributed flow fields at specific body locations in earlier studies.

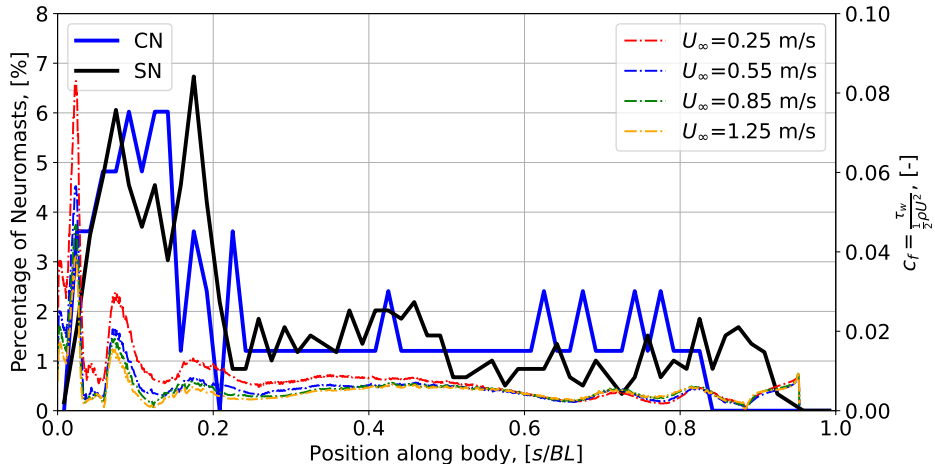


Figure 21: Dimensionless shear stress along the body of the gudgeon (right vertical axis) in relation to the distribution of neuromasts (left vertical axis) expressed as the percentage of canal neuromasts (CN) and superficial neuromasts (SN). The percentages were calculated based on biological observations from [85] (Adapted from Publication III).

5.4 Implication for Fish Conservation and Fish Passage

The results of this research offer valuable information on the fluid-body interactions that fish experience in turbulent regimes, commonly encountered in river ecosystems. Validated CFD models simulated the flow fields around the physical models of the fish, providing hydrodynamic signatures of pressure, velocity, and shear stresses at the surface of the fish. These hydrodynamic signatures assist the fish in the classification of flows in fish passages, ultimately contributing to the selection of the hydrodynamic preference [86]. The successful migration of fish, both upstream and downstream, hinges on the fish's ability to grapple with these structures, which is greatly influenced by the hydraulic conditions inside them. Therefore, assessing how fish perceive hydraulic conditions such as velocity, pressure, and turbulence intensity in their immediate surroundings was essential. Recognizing and classifying the different hydrodynamic signatures surrounding fish have the potential to understand their behavior and promote the development of more fish-friendly infrastructure. The findings of this study suggest that the body morphology of fish plays a crucial role in their hydrodynamic sensing. Larger fish, such as chub, create more significant flow depletion (Publication II), resulting in an expanded hydrodynamic image around them and possibly enhancing their sensing range. Secondly, the flow fields around a fish body correlate with the approximate positioning of neuromasts (Publication III). Understanding how fish perceive the hydrodynamic signatures can also be used to evaluate flow fields that attract or repel fish [87], linking hydrodynamics with fish behavior [88]. The knowledge of these hydrodynamic signatures can then be incorporated into the design and improvement of fish guidance systems and river restoration efforts.

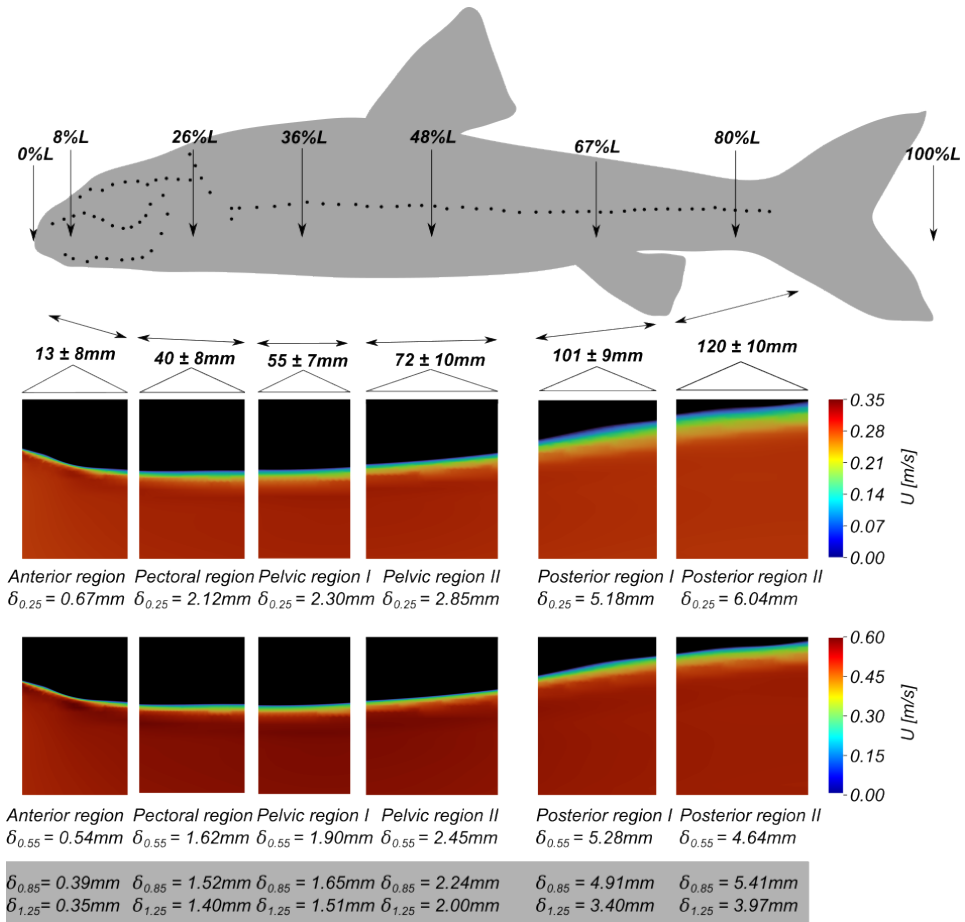


Figure 22: Boundary layer thickness along the body length of a Gudgeon at 0.25, 0.55, 0.85 and 1.25 m/s at the mid-dorsal ventral plane (adapted from Publication III).

6 Conclusions and Outlook

This work was motivated by emerging research in the field of fish hydrodynamic sensing. The literature study showed that during undulatory motion, the fish establish a surrounding flow field around their body depending on flow velocity and their body shape [32]. However, to date, there is no information on the contribution of three-dimensional complex fish body shapes to the surrounding flow fields. These flow fields act as hydrodynamic stimuli for the sensory neuromasts of the lateral line system [49]. The fluid-structure interaction and the boundary layer produced by viscous effects serve as a mechanical filter for superficial neuromasts [89] attenuating the stimuli signal. The characteristics of the boundary layer and the flow fields resulting from the fluid-body interaction around different fish models were thus explored to understand the contribution of fish body morphology to the fish's hydrodynamic sensing. We investigated the flow fields around fish models through experiments and numerical modelling. The numerical models were first validated with experimental data and then used to investigate the 2D and 3D distributions of the velocity field, the boundary layer thickness, the shear stresses, and the pressure fields. The main contributions of this work are the incorporation of realistic fish models and the open access to numerical and experimental data for future research. The careful analysis brought us to the following conclusions concerning each research question.

RQ 1. The complex 3D fish body shape produces flow field gradients in its surroundings that are greatly influenced by the fish body shape (Publication II). Incoming flow distortion becomes more pronounced as the body length of the fish increases, and, on the contrary, a decrease in body length results in a milder flow distortion. The velocity distributions around a three-dimensional fish-shaped body and the commonly used analogy (i.e. 3D axisymmetric NACA0013) exhibit similarities (Publication V), although there is a disparity in the normalized pressure coefficient (C_p) between the two configurations (see Fig. 19). These findings address the potential research gap (**RG3**) evident in fish hydrodynamic investigations, particularly regarding the utilization of simplified geometries in simulating flow fields similar to those of fish.

RQ 2. Reynolds-averaged Navier-Stokes (RANS) turbulence models provided a good estimate of the flow fields around fish-shaped bodies. The benchmark study conducted to analyze the performance of the turbulence model showed that among RANS the Spalart Allmaras turbulence model simulated the best overall estimate of streamwise and lateral velocity, especially in critical regions such as in the tail or wake where the boundary layer becomes more turbulent (Publication I). Furthermore, the resolved boundary layer case with low Reynolds wall functions provided better velocity fields close to the surface of the fish compared to the measured data. Therefore, the Spalart-Allmaras (SA) turbulence model with a resolved boundary layer is recommended for studies employing RANS turbulence models in fish-flow interactions. These imperative findings address **RG2**, highlighting the lack of Computational Fluid Dynamics (CFD) studies around fish-shaped bodies. It also shows that RANS can provide sufficient insight into the fish-fluid interactions of a stationary fish to explore the spatially distributed flow fields, and there is no need for the use of higher resolved and therefore more costly methods such as LES or DNS.

RQ 3. The spatial distribution of the flow fields around the fish bodies was found to be correlated with the positioning of the sensory units on the lateral line. In this work, the velocity, pressure, boundary layer thickness, and shear stresses around the surface of a steady gudgeon fish model were calculated using CFD. The approximate positions of the sensory units of the lateral line, CN, and SN were overlaid from [85] on the surface of the simulated model to identify the potential regions of interest. Our observations showed that the flow fields exhibit significant gradients in the regions where the density

of the neuromast was high (Publication III). These findings are consistent with the previous study by [35] that focused on the density distribution of neuromasts along a body of rainbow trout fish that showed that normalized pressure gradients were high in the regions of maximum density of CNs. In our observations, the normalized pressure distribution around the gudgeon also showed secondary gradients resulting from the protuberant pockets around the fish eye. These secondary gradients can play an important role in detecting minute changes in surrounding water fluctuations at relatively lower frequencies ($< 25\text{Hz}$). The boundary layer thickness (δ) in the anterior region was found to be thin compared to the rest of the body, possibly exposing the SN to the fully developed flow outside the boundary layer at all Reynolds numbers. The boundary layer around the surface of the fish plays an imperative role in determining the signal [89] received by the superficial neuromasts. These findings address the research gap (**RG4**) on the physical relationship between spatially distributed flow fields and lateral line sensing units.

The experimental and numerical data presented in this study are openly accessible at the below links, allowing unrestricted access and utilization by the wider research community to accelerate and address the issues related to fish hydrodynamic sensing more effectively. The availability of experimental data addresses the **RG1** related to the lack of metadata for the validation of computational fluid dynamics (CFD) modelling of ecological flows.

Supplementary Data:

- Brown trout data: <https://doi.org/10.24352/UB.OVGU-2022-001>
- Gudgeon data: <https://doi.org/10.5281/zenodo.8142218>

6.1 Limitations of this Work

The current study incorporated both experimental and numerical models, each of which presented distinct limitations. Despite Laser Doppler Anemometry (LDA) demonstrated greater accuracy compared to Acoustic Doppler Velocimetry (ADV) measurements, it faced a substantial decline in the signal-to-noise ratio (SNR) near the walls and the fish's surface within the confined testing space of the swim tunnel. Repetitive measurements showed limited efficacy in improving the SNR. Similar issues were observed by [33, 34] while employing the PIV to a 2D fish body shape where the PIV was unable to measure the velocity close to the body surface. These issues can be resolved using an intrusive technique, i.e. hot film/wire anemometer, which performs well in measuring flow in the boundary layers near the walls [90].

The swim tunnel used in the LDA experiments exhibited high turbulence intensities at upstream and downstream locations within the test sections. Although collective efforts were made to reduce it, such as redesigning the honeycomb structure and closing all air outlets, the high turbulence intensities could not be avoided. This is due to the smaller size of the swim tunnel in which the flow does not get enough space to become homogeneous before and rectilinear after the honeycomb structure. With the use of larger swim tunnels and additional honeycomb structures, the turbulence levels may be reduced.

Lastly, as a preliminary study, it does not incorporate the swimming kinematics of fish into the physical models in both the experiments and the numerical analysis. To date, fish kinematic models have been used in CFD to study the hydrodynamics of a swimming fish [91]. The validated numerical models developed in our study can be refined to incorporate detailed body kinematics, allowing for a comprehensive exploration of flow fields during undulatory fish locomotion.

6.2 Future Outlook

Future studies on fish flow interactions investigating fish's hydrodynamic sensing aim to integrate undulatory motion in physical experiments, through the utilization of a robotic fish such as the one shown in Fig. 23 with optimization of swimming modes. Meanwhile, numerical models employ dynamic meshing techniques that represent the true swimming kinematics of fish. These models can be validated using experimental data and can be employed for further investigation of hydrodynamic sensing both in spatial and temporal resolution. Furthermore, the role of turbulence as a significant factor in fish environmental sensing presents a compelling aspect. Therefore, examining the effects of various turbulence scales on the fish's surface while swimming will provide valuable insights into how instantaneous flow fields relate to the lateral line sensory units.

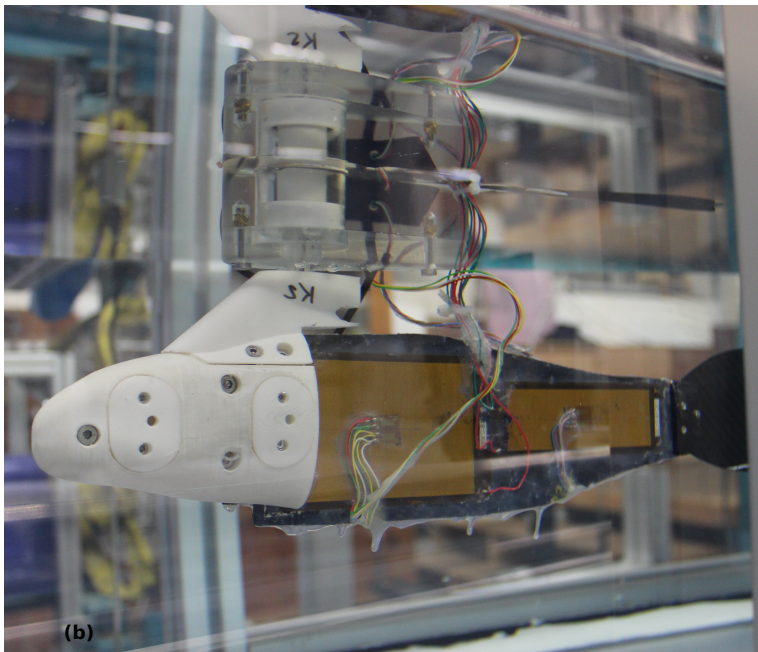


Figure 23: Robotic fish designed and used in the experiments for optimizing swimming modes (Adapted from [92])

List of Figures

1	Self-induced flow fields around fish during the swimming gait cycle.	15
2	Impact of biology, CFD, and engineering on fish flow interactions.....	17
3	Spatial arrangement and cross-sectional view of neuromasts on a trout. ...	19
4	Pasteur's Quadrants: Basic, Use-Inspired, and Applied Research.	23
5	Research methodology overview.	24
6	Functioning principle of Acoustic Doppler Velocimetry (ADV).	25
7	Functioning principle of Laser Doppler Anemometry (LDA).....	26
8	Overview of the ADV experimental setup.....	30
9	Overview of the LDA experimental setup.	31
10	LDA measurement points in the flume.	31
11	Overview of a Loligo swim tunnel.	32
12	LDA setup for swim tunnel measurements.....	32
13	3D models of the Rainbow trout, Gudgeon, and NACA0013 profile.	34
14	Computational domains and boundaries in numerical modelling.	35
15	Velocity distribution in the turbulent boundary layer.....	40
16	Absolute velocity difference for Brown trout, numerical vs experiment.....	41
17	Absolute velocity difference for Gudgeon, numerical vs experiment.	42
18	Bland-Altman plot for velocity difference.....	42
19	Normalised pressure coefficient (C_p) around Gudgeon and velocity profiles upstream of various fish.	44
20	Comparison of simulated vs experimental velocities around a brown trout.	45
21	Dimensionless shear stress vs neuromasts positioning on a gudgeon.....	46
22	Boundary layer thickness around the Gudgeon.....	47
23	Robotic fish designed and used in the experiments	50

List of Tables

1	List of studied fish species	24
2	Experimental setup configurations	29
3	Numerical setups configurations	34
4	Mesh sensitivity analysis through GCI method	37

References

- [1] A. H. Khan, K. R. Hussmann, D. Powalla, S. Hoerner, M. Kruusmaa, and J. A. Tuhtan, "An open 3D CFD model for the investigation of flow environments experienced by freshwater fish," *Ecological Informatics*, vol. 69, p. 101652, 2022.
- [2] K. Bensing, J. A. Tuhtan, G. Toming, A. H. Khan, and B. Lehmann, "Fish body geometry reduces the upstream velocity profile in subcritical flowing waters," *Aquatic Sciences*, vol. 84, no. 3, p. 32, 2022.
- [3] A. H. Khan, S. Hoerner, G. Tomming, M. Kruusmaa, and J. A. Tuhtan, "3D CFD analysis of pressure, boundary layer and shear stresses on a gudgeon (*Gobio gobio*)," *Journal of Ecohydraulics*, pp. 1–15, 2024.
- [4] A. H. Khan, K. R. Hussmann, D. Powalla, S. Hoerner, M. Kruusmaa, and J. A. Tuhtan, "Benchmarking 3D CFD for studies on turbulent flow around fish-shaped bodies," in *Proceedings of the 14th International Symposium on Ecohydraulics*, International Association for Hydro-Environment Engineering and Research, 2022.
- [5] A. H. Khan, G. Toming, S. Hoerner, and J. A. Tuhtan, "Comparison of near-body flow fields of a Gudgeon and NACA0013 profile," in *Advances in Hydraulic Research* (M. B. Kalinowska, M. M. Mrokowska, and P. M. Rowiński, eds.), pp. 231–242, Springer Nature Switzerland, 2024.
- [6] S. Dijkgraaf, "The functioning and significance of the lateral-line organs," *Biological reviews*, vol. 38, no. 1, pp. 51–105, 1963.
- [7] C. B. Braun, S. Coombs, and R. R. Fay, "What is the nature of multisensory interaction between octavolateralis sub-systems?," *Brain, behavior and evolution*, vol. 59, no. 2, pp. 162–76, 2002.
- [8] A. J. Kalmijn, "Hydrodynamic and acoustic field detection," in *Sensory Biology of Aquatic Animals* (J. Atema, R. R. Fay, A. N. Popper, and W. N. Tavolga, eds.), (New York, NY), pp. 83–130, Springer New York, 1988.
- [9] A. T. Silva, M. C. Lucas, T. Castro-Santos, C. Katopodis, L. J. Baumgartner, J. D. Thiem, K. Aarestrup, P. S. Pompeu, G. C. O'Brien, D. C. Braun, N. J. Burnett, D. Z. Zhu, H.-P. Fjeldstad, T. Forseth, N. Rajaratnam, J. G. Williams, and S. J. Cooke, "The future of fish passage science, engineering, and practice," *Fish and Fisheries*, vol. 19, no. 2, pp. 340–362, 2018.
- [10] M. Milardi, A. Iemma, I. R. Waite, A. Gavioli, E. Soana, and G. Castaldelli, "Natural and anthropogenic factors drive large-scale freshwater fish invasions," *Scientific Reports*, vol. 12, 2022.
- [11] A. Kirchhofer and D. Hefti, eds., *Conservation of Endangered Freshwater Fish in Europe*. Advances in Life Sciences, Birkhäuser Verlag Basel, 1996.
- [12] R. A. Brain and R. S. Prosser, "Human induced fish declines in north america, how do agricultural pesticides compare to other drivers?," *Environmental Science and Pollution Research*, vol. 29, no. 44, pp. 66010–66040, 2022.
- [13] C. Seliger and B. Zeiringer, *River Connectivity, Habitat Fragmentation and Related Restoration Measures*, pp. 171–186. Cham: Springer International Publishing, 2018.

- [14] B. Belletti, C. Garcia de Leaniz, J. Jones, S. Bizzi, L. Börger, G. Segura, A. Castelletti, W. van de Bund, K. Aarestrup, J. Barry, K. Belka, A. Berkhuisen, K. Birnie-Gauvin, M. Bussetini, M. Carolli, S. Consuegra, E. Dopico, T. Feierfeil, S. Fernández, P. Fernandez Garrido, E. Garcia-Vazquez, S. Garrido, G. Giannico, P. Gough, N. Jepsen, P. E. Jones, P. Kemp, J. Kerr, J. King, M. Łapińska, G. Lázaro, M. C. Lucas, L. Marcello, P. Martin, P. McGinnity, J. O’Hanley, R. Olivo del Amo, P. Parasiewicz, M. Pusch, G. Rincon, C. Rodriguez, J. Royte, C. T. Schneider, J. S. Tummers, S. Vallesi, A. Vowles, E. Verspoor, H. Wanningen, K. M. Wantzen, L. Wildman, and M. Zalewski, “More than one million barriers fragment europe’s rivers,” *Nature*, vol. 588, 2020.
- [15] S. E. BUNN and A. H. ARTHINGTON, “Basic principles and ecological consequences of altered flow regimes for aquatic biodiversity,” *Environmental Management*, vol. 30, 2002.
- [16] J. F. Webb, *Lateral Line Morphology and Development and Implications for the Ontogeny of Flow Sensing in Fishes*, pp. 247–270. Berlin, Heidelberg: Springer Berlin Heidelberg, 2014.
- [17] P. W. Webb and D. Weihs, “Hydrostatic stability of fish with swim bladders: not all fish are unstable,” *Canadian Journal of Zoology*, vol. 72, no. 6, pp. 1149–1154, 1994.
- [18] N. Rajaratnam, G. V. der Vinne, and C. Katopodis, “Hydraulics of vertical slot fishways,” *Journal of Hydraulic Engineering*, vol. 112, no. 10, pp. 909–927, 1986.
- [19] D. Calluau, V. Cornu, P. Baran, G. Pineau, P. Sagnes, and L. David, “Optimizing flow conditions and fish passage success in vertical slot fishways: Lessons from fish behavior observations,” *Water*, vol. 16, no. 12, 2024.
- [20] J. M. Santos, A. Silva, C. Katopodis, P. Pinheiro, A. Pinheiro, J. Bochechas, and M. T. Ferreira, “Ecohydraulics of pool-type fishways: Getting past the barriers,” *Ecological Engineering*, vol. 48, pp. 38–50, 2012. Ecohydraulic Approaches for Restoring Habitat Connectivity and Suitability.
- [21] H. FA, W. CA, and C. J. Brew A, “Fish responses to flow velocity and turbulence in relation to size, sex and parasite load,” *Journal of the Royal Society, Interface*, vol. 11, no. 91, p. 20130814, 2013.
- [22] T. T. Rodríguez, J. P. Agudo, L. P. Mosquera, and E. P. González, “Evaluating vertical-slot fishway designs in terms of fish swimming capabilities,” *Ecological Engineering*, vol. 27, no. 1, pp. 37–48, 2006.
- [23] J. C. Liao, D. N. Beal, G. V. Lauder, and M. S. Triantafyllou, “Fish exploiting vortices decrease muscle activity,” *Science*, vol. 302, no. 5650, pp. 1566–1569, 2003.
- [24] E. S. Bernhardt and M. A. Palmer, “River restoration: the fuzzy logic of repairing reaches to reverse catchment scale degradation,” *Ecological Applications*, vol. 21, no. 6, pp. 1926–1931, 2011.
- [25] E. Commission and D-G. for Environment, *Biodiversity strategy for 2030 – Barrier removal for river restoration*. Publications Office of the European Union, 2022.
- [26] E. Wohl, S. N. Lane, and A. C. Wilcox, “The science and practice of river restoration,” *Water Resources Research*, vol. 51, no. 8, pp. 5974–5997, 2015.

- [27] M. A. PALMER, H. L. MENNINGER, and E. BERNHARDT, "River restoration, habitat heterogeneity and biodiversity: a failure of theory or practice?," *Freshwater Biology*, vol. 55, no. s1, pp. 205–222, 2010.
- [28] C. F. RABENI and R. B. JACOBSON, "The importance of fluvial hydraulics to fish-habitat restoration in low-gradient alluvial streams," *Freshwater Biology*, vol. 29, no. 2, pp. 211–220, 1993.
- [29] J. C. Liao, "A review of fish swimming mechanics and behaviour in altered flows.," *Philosophical transactions of the Royal Society of London. Series B, Biological sciences*, vol. 362, no. 1487, pp. 1973–93, 2007.
- [30] S. Collin, N. Marshall, C. B. Braun, and S. Coombs, "The overlapping roles of the inner ear and lateral line: the active space of dipole source detection," *Philosophical Transactions of the Royal Society of London. Series B: Biological Sciences*, vol. 355, no. 1401, pp. 1115–1119, 2000.
- [31] E.-S. Hassan, "Mathematical analysis of the stimulus for the lateral line organ," *Biological Cybernetics*, vol. 52, no. 1, pp. 23–36, 1985.
- [32] H. Bleckmann, *Reception of Hydrodynamic Stimuli in Aquatic and Semiaquatic Animals*. Progress in Zoology, Vol 41, Vch Pub, 1994.
- [33] S. P. Windsor, S. E. Norris, S. M. Cameron, G. D. Mallinson, and J. C. Montgomery, "The flow fields involved in hydrodynamic imaging by blind mexican cave fish (*astyanax fasciatus*). part i: open water and heading towards a wall," *Journal of Experimental Biology*, vol. 213, pp. 3819–3831, 11 2010.
- [34] S. P. Windsor, S. E. Norris, S. M. Cameron, G. D. Mallinson, and J. C. Montgomery, "The flow fields involved in hydrodynamic imaging by blind mexican cave fish (*astyanax fasciatus*). part ii: gliding parallel to a wall," *Journal of Experimental Biology*, vol. 213, pp. 3832–3842, 11 2010.
- [35] L. Ristroph, J. C. Liao, and J. Zhang, "Lateral line layout correlates with the differential hydrodynamic pressure on swimming fish," *Phys. Rev. Lett.*, vol. 114, p. 018102, 01 2015.
- [36] S. Dijkgraaf, "Über die reizung des ferntastsinns bei fischen und amphibiien," *Experientia*, vol. 3, no. 5, p. 3, 1947.
- [37] T. B. de Perera, "Spatial parameters encoded in the spatial map of the blind mexican cave fish, *astyanax fasciatus*," *Animal Behaviour*, vol. 68, no. 2, pp. 291–295, 2004.
- [38] T. B. de Perera, "Fish can encode order in their spatial map," *Proceedings of the Royal Society of London. Series B: Biological Sciences*, vol. 271, no. 1553, pp. 2131–2134, 2004.
- [39] R. J. Wubbels, A. B. A. Kroese, and N. A. M. Schellart, "Response properties of lateral line and auditory units in the medulla oblongata of the rainbow trout (*oncorhynchus mykiss*)," *Journal of Experimental Biology*, vol. 179, pp. 77–92, 06 1993.
- [40] J. C. Montgomery, C. F. Baker, and A. G. Carton, "The lateral line can mediate rheotaxis in fish," *Nature*, vol. 389, no. 6654, pp. 960–963, 1997.

- [41] J. C. Liao, "The role of the lateral line and vision on body kinematics and hydrodynamic preference of rainbow trout in turbulent flow," *Journal of Experimental Biology*, vol. 209, pp. 4077–4090, 10 2006.
- [42] E.-S. Hassan, "Mathematical description of the stimuli to the lateral line system of fish derived from a three-dimensional flow field analysis. i the cases of moving in open water and of gliding towards a plane surface," *Biological Cybernetics*, vol. 66, no. 5, pp. 443–452, 1992.
- [43] E.-S. Hassan, "Mathematical description of the stimuli to the lateral line system of fish derived from a three-dimensional flow field analysis. ii the case of gliding alongside or above a plane surface," *Biological Cybernetics*, vol. 66, no. 5, pp. 453–461, 1992.
- [44] L. Prandtl, "Über Flüssigkeitsbewegung bei sehr kleiner Reibung," *Verhandlungen des III. Internationalen Mathematiker Kongresses*, 1904.
- [45] E. Anderson, W. McGillis, and M. Grosenbaugh, "The boundary layer of swimming fish," *Journal of Experimental Biology*, vol. 204, pp. 81–102, 01 2001.
- [46] S. M. van Netten, "Hydrodynamic detection by cupulae in a lateral line canal: functional relations between physics and physiology," *Biological Cybernetics*, vol. 94, pp. 67–85, 01 2006.
- [47] M. A. Rapo, H. Jiang, M. A. Grosenbaugh, and S. Coombs, "Using computational fluid dynamics to calculate the stimulus to the lateral line of a fish in still water," *Journal of Experimental Biology*, vol. 212, pp. 1494–1505, 05 2009.
- [48] S. P. Windsor and M. J. McHenry, "The influence of viscous hydrodynamics on the fish lateral-line system," *Integrative and Comparative Biology*, vol. 49, pp. 691–701, 08 2009.
- [49] M. J. McHenry and J. C. Liao, *The Hydrodynamics of Flow Stimuli*, pp. 73–98. New York, NY: Springer New York, 2014.
- [50] S. M. van Netten and M. J. McHenry, *The Biophysics of the Fish Lateral Line*, pp. 99–119. New York, NY: Springer New York, 2014.
- [51] S. Coombs, J. Janssen, and J. F. Webb, "Diversity of lateral line systems: Evolutionary and functional considerations," in *Sensory Biology of Aquatic Animals* (J. Atema, R. R. Fay, A. N. Popper, and W. N. Tavolga, eds.), (New York, NY), pp. 553–593, Springer New York, 1988.
- [52] J. F. Webb, "Developmental constraints and evolution of the lateral line system in teleost fishes," in *The Mechanosensory Lateral Line* (S. Coombs, P. Görner, and H. Münz, eds.), (New York, NY), pp. 79–97, Springer New York, 1989.
- [53] J. F. Webb, "Gross Morphology and Evolution of the Mechanoreceptive Lateral-Line System in Teleost Fishes (Part 1 of 2)," *Brain Behavior and Evolution*, vol. 33, pp. 34–43, 02 1989.
- [54] S. Coombs, J. Mogdans, M. Halstead, and J. C. Montgomery, "Transformation of peripheral inputs by the first-order lateral line brainstem nucleus," *Journal of Comparative Physiology A*, vol. 182, pp. 609–626, 04 1998.

- [55] J. A. Tuhtan, J. F. Fuentes-Perez, G. Toming, and M. Kruusmaa, "Flow velocity estimation using a fish-shaped lateral line probe with product-moment correlation features and a neural network," *Flow Measurement and Instrumentation*, vol. 54, pp. 1–8, 2017.
- [56] K. Yanase and P. Saarenrinne, "Unsteady turbulent boundary layers in swimming rainbow trout," *Journal of Experimental Biology*, vol. 218, pp. 1373–1385, 05 2015.
- [57] J. F. Fuentes-Pérez, J. A. Tuhtan, R. Carbonell-Baeza, M. Musall, G. Toming, N. Muhammad, and M. Kruusmaa, "Current velocity estimation using a lateral line probe," *Ecological Engineering*, vol. 85, pp. 296–300, 2015.
- [58] N. Strokina, J.-K. Kämäräinen, J. A. Tuhtan, J. F. Fuentes-Pérez, and M. Kruusmaa, "Joint estimation of bulk flow velocity and angle using a lateral line probe," *IEEE Transactions on Instrumentation and Measurement*, vol. 65, no. 3, pp. 601–613, 2016.
- [59] K. Chen, J. A. Tuhtan, J. F. Fuentes-Pérez, G. Toming, M. Musall, N. Strokina, J.-K. Kämäräinen, and M. Kruusmaa, "Estimation of flow turbulence metrics with a lateral line probe and regression," *IEEE Transactions on Instrumentation and Measurement*, vol. 66, no. 4, pp. 651–660, 2017.
- [60] D. Adkins and Y. Yan, "CFD simulation of fish-like body moving in viscous liquid," *Journal of Bionic Engineering*, vol. 3, p. 147–153, 09 2006.
- [61] N. Owsianowski and A. Kesel, *Drag reduction in schooling fish? — A CFD approach-Comparative Biochemistry and Physiology Part A: Molecular & Integrative Physiology*, vol. 150. Elsevier, 07 2008.
- [62] I. Kogan, S. Pacholak, M. Licht, J. W. Schneider, C. Brücker, and S. Brandt, "The invisible fish: hydrodynamic constraints for predator-prey interaction in fossil fish saurichthys compared to recent actinopterygians," *Biology Open*, vol. 4, pp. 1715–1726, 11 2015.
- [63] J. H. Ferziger and M. Perić, *Computational Methods for Fluid Dynamics*. Springer Berlin, Heidelberg, 2012.
- [64] M. Nallasamy, "Turbulence models and their applications to the prediction of internal flows: A review," *Computers & Fluids*, vol. 15, no. 2, pp. 151–194, 1987.
- [65] D. E. Stokes and R. Powell, *Pasteur's Quadrant: Basic Science and Technological Innovation*. Rowman & Littlefield Publishers, 1997.
- [66] R. Lhermitte and R. Serafin, "Pulse-to-pulse coherent doppler sonar signal processing techniques," *Journal of Atmospheric and Oceanic Technology*, vol. 1, no. 4, pp. 293–308, 1984.
- [67] Z. Zhang, *LDA Application Methods*. Experimental Fluid Mechanics, Springer Berlin, Heidelberg, 2010.
- [68] B. Lehmann, K. Bensing, B. Adam, U. Schwevers, and J. A. Tuhtan, *Ethohydraulics*. Springer Wiesbaden, 2022.
- [69] S. Abbaszadeh, R. Leidhold, and S. Hoerner, "A design concept and kinematic model for a soft aquatic robot with complex bio-mimicking motion," *Journal of Bionic Engineering*, vol. 19, no. 1, pp. 16–28, 2022.

- [70] U. Schwevers and B. Adam, "Biometrie einheimischer fischarten als grundlage für die bemessung von fischwegen und fischschutzanlagen," *Wasser Und Abfall*, vol. 01-02, pp. 46–52, 2019.
- [71] M. S. Selig, *UIUC airfoil data site*. Urbana, Illinois: Department of Aeronautical and Astronautical Engineering University of Illinois at Urbana-Champaign, 1996.
- [72] I. B. Celik, U. Ghia, P. J. Roache, C. J. Freitas, H. Coleman, and P. E. Raad, "Procedure for estimation and reporting of uncertainty due to discretization in CFD applications," *Journal of Fluids Engineering*, vol. 130, pp. 078001–4, 07 2008.
- [73] F. G. Schmitt, "About boussinesq's turbulent viscosity hypothesis: historical remarks and a direct evaluation of its validity," *Comptes Rendus Mécanique*, vol. 335, no. 9, pp. 617–627, 2007. Joseph Boussinesq, a Scientist of bygone days and present times.
- [74] W. Jones and B. Launder, "The prediction of laminarization with a two-equation model of turbulence," *International Journal of Heat and Mass Transfer*, vol. 15, no. 2, pp. 301–314, 1972.
- [75] B. E. Launder and B. I. Sharma, "Application of the energy-dissipation model of turbulence to the calculation of flow near a spinning disc," *Letters in heat and mass transfer*, vol. 1, no. 2, pp. 131–137, 1974.
- [76] J. Bardina, P. G. Huang, and T. J. Coakley, "Turbulence modeling validation, testing, and development," *Technical Memorandum (TM)*, 04 1997.
- [77] V. Yakhot and S. A. Orszag, "Development of turbulence models for shear flows by a double expansion technique," *Physics of Fluids A: Fluid Dynamics*, vol. 4, p. 1510, 03 1992.
- [78] D. C. Wilcox, "Reassessment of the scale-determining equation for advanced turbulence models," *AIAA Journal*, vol. 26, pp. 1299–1310, 11 1988.
- [79] F. R. Menter, "Zonal two equation $k-\omega$ turbulence models for aerodynamic flow," *AIAA 24th Fluid Dynamics Conference*, 07 1993.
- [80] F. R. Menter, "Two-equation eddy-viscosity turbulence models for engineering applications," *AIAA Journal*, vol. 32, pp. 1598–1605, 08 1994.
- [81] P. Spalart and S. Allmaras, "A one equation turbulence model for aerodynamic flows," *La Recherche Aérospatiale*, vol. 1, no. 1, pp. 5–21, 1994.
- [82] P. R. Spalart and C. L. Rumsey, "Effective inflow conditions for turbulence models in aerodynamic calculations," *AIAA Journal*, vol. 45, no. 10, pp. 2544–2553, 2007.
- [83] H. Schlichting and K. Gersten, *Boundary-Layer Theory*. Springer-Verlag Berlin Heidelberg, 2000.
- [84] B. J. M. and A. D. G., "Measuring agreement in method comparison studies," *Stat Methods Med Res*, vol. 8, no. 2, pp. 135–160, 1999.
- [85] A. Schmitz, H. Bleckmann, and J. Mogdans, "The lateral line receptor array of cyprinids from different habitats," *Journal of Morphology*, vol. 275, no. 4, pp. 357–370, 2014.

- [86] J. A. Tuhtan, J. F. Fuentes-Perez, G. Toming, M. Schneider, R. Schwarzenberger, M. Schletterer, and M. Kruusmaa, "Man-made flows from a fish's perspective: autonomous classification of turbulent fishway flows with field data collected using an artificial lateral line," *Bioinspiration & Biomimetics*, vol. 13, p. 046006, may 2018.
- [87] C. CC, "Integrated, multi-sensory, behavioral guidance systems for fish diversion," in *Behavioral Technologies for Fish Guidance*, American Fisheries Society Symposium, (Bethesda, MD), pp. 105–113, American Fisheries Society, 2001.
- [88] T. D. Mussen and J. J. Cech, "The roles of vision and the lateral-line system in sacramento splittail's fish-screen avoidance behaviors: Evaluating vibrating screens as potential fish deterrents," *Environmental Biology of Fishes*, vol. 96, no. 8, pp. 971–980, 2013.
- [89] M. J. McHenry, J. A. Strother, and S. M. van Netten, "Mechanical filtering by the boundary layer and fluid-structure interaction in the superficial neuromast of the fish lateral line system," *Journal of Comparative Physiology A*, vol. 194, no. 9, pp. 795–810, 2008.
- [90] F. Jørgensen, V. Chernoray, A. Bakchinov, and L. Löfdahl, "A multi-sensor hot-wire anemometer system for investigation of wall-bounded flow structures," *Experimental Thermal and Fluid Science*, vol. 27, no. 2, pp. 207–214, 2003. 6th International Thermal Anemometry Symposium.
- [91] I. Borazjani and F. Sotiropoulos, "Numerical investigation of the hydrodynamics of carangiform swimming in the transitional and inertial flow regimes," *Journal of Experimental Biology*, vol. 211, pp. 1541–1558, 05 2008.
- [92] S. Abbasazdeh, S. Hoerner, and R. Leidhold, "Experimental optimization of a fish robot's swimming modes – a complex multiphysical problem," *Experiments in Fluids*, vol. 65, pp. 51–68, 3 2024.

Appendix 1

I

A. H. Khan, K. R. Hussmann, D. Powalla, S. Hoerner, M. Kruusmaa, and J. A. Tuhtan, "An open 3D CFD model for the investigation of flow environments experienced by freshwater fish," *Ecological Informatics*, vol. 69, p. 101652, 2022



Contents lists available at ScienceDirect

Ecological Informatics

journal homepage: www.elsevier.com/locate/ecolinf

An open 3D CFD model for the investigation of flow environments experienced by freshwater fish

Ali Hassan Khan^{a,*}, Karla Ruiz Hussmann^b, Dennis Powalla^b, Stefan Hoerner^b,
Maarja Kruusmaa^a, Jeffrey A. Tuhtan^a

^a Department of Computer Systems, Tallinn University of Technology, Tallinn, Estonia

^b Institute of Fluid Dynamics and Thermodynamics, Otto-von-Guericke University Magdeburg, Germany

ARTICLE INFO

Keywords:

Freshwater ecosystems
Fish
CFD
Numerical modelling
Model validation

ABSTRACT

Computational fluid dynamics (CFD) provides a powerful numerical tool to simulate and study many of the complex fluid-body interactions experienced by freshwater fish. However, major gaps remain in the application of CFD to study the fluid-body interactions of fish, including the absence of an openly available reference body geometry, the lack of a detailed study on suitable numerical methods and a deficit of available velocity laboratory measurements for model calibration and validation. To address these gaps, we provide a set of numerical models based on the open-source CFD toolkit OpenFOAM. The contributions of this work are two-fold: First, to provide a validated openly available numerical setup using a realistic fish model geometry including laboratory velocity measurements. Second, to determine the best-performing turbulence models and near-wall treatments using Reynolds-Averaged Navier-Stokes (RANS) numerical simulations. Finally, we conclude with a critical evaluation of the effects and trade-offs of resolving or modelling the boundary layer (BL) in numerical studies of fish-shaped bodies.

1. Introduction

Freshwater ecosystems host one-third of all vertebrate species, and are experiencing a prolonged and rapid decline (Reid et al., 2019). The negatively compounding impacts of climatic and anthropogenic change are reducing freshwater vertebrate populations at more than twice the rate of terrestrial or marine populations (Tickner et al., 2020). To mitigate these negative impacts, advanced integrated modelling approaches are needed. Such methods have shown promising preliminary results when exploring physical hydrological processes and their ecological and socioeconomic interactions (Li et al., 2021). Currently, large-scale physical river processes can be simulated due to advances in computational power, improved algorithms and the rapid growth of high-quality remote sensing data to calibrate and validate numerical simulations (Monegaglia et al., 2018; Vanzo et al., 2021). However, riverine fish habitats naturally encompass a broad spectrum of physical flow conditions (Belletti et al., 2017). Furthermore, the sensory ecology of freshwater fish remains at a nascent stage, where major gaps persist in our knowledge of the hydrodynamic stimuli present in natural flows

(Mogdans, 2019). This is expressed as a persistent lack of established thresholds for abiotic autecological parameters associated with lotic fish habitats, including the flow velocity and water depth (Smialek et al., 2019). Methods to simulate fish-flow interactions under realistic conditions are therefore urgently needed to study, understand, predict and support sustainable freshwater fish populations.

Fish sense the surrounding flow field with their highly specialized lateral line sensory system (Dijkgraaf, 1963). This “touch at a distance” sensing modality allows fish to perceive minute changes in the pressure, velocity and acceleration fields (van Netten and McHenry, 2014). It allows them to orient themselves into the flow, gain information about their spatial environment and plays vital roles in feeding, spawning, migration and predator avoidance (Mogdans, 2019). Measurements and simulations of fish-flow interaction have been used to predict physical habitats (García-Vega et al., 2021) and have the potential to update and improve large-scale fish community distribution models (Cyterski et al., 2020). A fish’s highly streamlined body shape provides minimal resistance while swimming (Lucas et al., 2020) and efficiently modulates the detection of hydrodynamic stimuli in the underwater environment

* Corresponding author.

E-mail addresses: ali.khan@taltech.ee (A.H. Khan), karla.ruiz@ovgu.de (K.R. Hussmann), dennis.powalla@ovgu.de (D. Powalla), stefan.hoerner@ovgu.de (S. Hoerner), maarja.kruusmaa@taltech.ee (M. Kruusmaa), jeffrey.tuhtan@taltech.ee (J.A. Tuhtan).

<https://doi.org/10.1016/j.ecoinf.2022.101652>

Received 17 January 2022; Received in revised form 18 April 2022; Accepted 18 April 2022

Available online 25 April 2022

1574-9541/© 2022 The Authors. Published by Elsevier B.V. This is an open access article under the CC BY license (<http://creativecommons.org/licenses/by/4.0/>).

Table 1.

Dimensions and specifications of the equipment used during physical experiments, including the fish-shaped body, laboratory flume and laser Doppler anemometer.

Dimensions of the fish-shaped body (length x width x height)	366.5 × 49.2 × 75.5 mm
Specifications of the laboratory flume	
Dimensions (length(x) x width(y))	10.0 × 1.2 m
Water level	0.68 m
Mean velocity	0.5382 m/s ± 0.0116 m/s
Mean turbulence intensity	3.1646% ± 0.1798%
Reynolds number	680,000
Froude number	0.21
Specifications of the laser Doppler anemometer	
Model	Dantec Flow Explorer DPSS 300 2D
Laser type	Continuous laser
Wavelength	Horizontal laser: 532 nm Vertical laser: 561 nm
Nominal measurement distance	485 mm with a 500 mm front lens
Measuring volume (length(x) x width(y) x height(z))	0.14 × 0.14 × 2.30mm
Software	BSA Flow Software

(Oteiza et al., 2017). This makes the study of fish-flow interactions a topic of increased interest beyond applied sensory ecology. Indeed, recent technological advances in miniature underwater sensing now include artificial lateral lines (Kottapalli et al., 2014), which can be used for field measurements in rivers and fish passage structures (Tuhtan et al., 2016) as well as in underwater robotics (Liu et al., 2020).

Previous works have shown that fish-flow interactions can be evaluated using computational fluid dynamics (CFD), focusing predominantly on fish swimming kinematics, thrust, drag and the development of complex vortex structures in the wake region (Adkins and Yan, 2006; Macia et al., 2020; Owsianowski and Kesel, 2008). Considering fish sensing, a limited number of studies have investigated the velocity and pressure fields around fish-shaped bodies. A notable contribution to fish sensing using CFD was the pioneering work of Windsor et al. (2010), which applied CFD to study the sensing range of blind Mexican cave fish, estimated as 0.2 fish body lengths. This was done by correlating observations of live fish swimming behavior to the flow field experienced by a CFD simulation of a revolved NACA 0013 profile. A comparison of two-dimensional (2D) and three-dimensional (3D) body geometries by Rapo et al. (2009) showed that 2D CFD simulations were not capable of accurately representing the perturbing effects of the fish-shaped body from a dipole stimulus. This study simulated a flat plate, and highlighted the importance of the numerical treatment used in the boundary layer,

and its impacts on the simulation results of the near-body velocities and strain rates. Herzog et al. (2017) carried out CFD simulations of the flow velocity and pressure fields from a small vibrating sphere interacting with a high-definition 3D scan of the cephalic lateral line from a common carp, (*Leuciscus idus*). The authors of this study recommended that future studies resolve the boundary layer to ensure realistic simulations of the low velocities common to the near-body flow field.

Despite the existing studies using CFD for fish sensing research, substantial gaps remain for the generalized investigation of the fluid-body interactions fish experience outside of the laboratory. Specifically, the absence of an openly available reference numerical model hinders the cross-comparison of numerical studies on fish sensing. This impedes urgently needed improvements to the attraction flows used in fish migration structures (Schütz et al., 2021), which can be investigated with large-scale CFD simulations (Gisen et al., 2017). The significant contribution of this work is the open CFD benchmark study it provides. Future researchers can either make direct use of the model itself, or base new CFD simulations on the best practices established in this work to improve our capacity to represent, understand and predict the flow-body interactions experienced by freshwater fish species.

A critical evaluation of suitable turbulence models and associated boundary layer treatments also remains absent from existing numerical studies of fish-flow interactions, and must be evaluated to ensure robust and repeatable CFD simulation results. This work is the first to assess the effects of boundary layer and turbulence modelling on the stream-wise and lateral velocity components around a fish-shaped body using the Reynolds-averaged Navier-Stokes (RANS) approach. Furthermore, we provide a critical comparison of three different RANS turbulence models as well as modelled and resolved boundary layers. All numerical simulations were carried out on a static fish-shaped body in a rectangular flume, similar to the gliding phase of a freely swimming fish. Planar velocity measurements using a Laser Doppler Anemometer (LDA) were obtained with a physical model situated in an open channel laboratory flume. The LDA measurements were used for numerical model calibration and compared for each turbulence model, considering either modelled or resolved boundary layers.

2. Experimental setup

The laboratory setup was designed for 2D LDA measurements of the flow field around a rigid 3D printed model of a brown trout swimming during the gliding phase of a swimming gait cycle. A summary of the physical model setup and equipment is provided in Table 1. The fish-shaped body geometry is based on the brown trout, (*Salmo trutta*), a

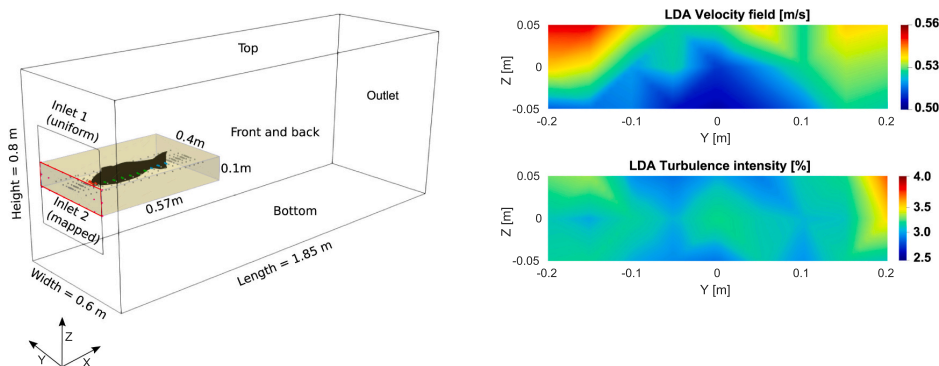


Fig. 1. Overview of the numerical and the experimental domains; (Left) fish-shaped body, spatial distribution of measurement points around the physical model and at the upstream boundary of the CFD model. (Right) Inlet velocity and turbulence distributions at inlet patch (red rectangle in the left panel) measured with LDA and later applied as a mapped inlet condition in the numerical model. (For interpretation of the references to colour in this figure legend, the reader is referred to the web version of this article.)

Table 2.
Summary of the OpenFOAM models investigated in this work.

Numerical solver version	OpenFOAM-v2012
Solver characteristics	Incompressible, transient
Solver algorithm	SIMPLE
Temporal discretization	
Accuracy	First order
Time step	10^{-03} (adjustable)
Spatial discretization*	
Mesh type	Hexahedral
Max cell size	0.0125 m
Min cell size	0.001 m
Total number of cells	$N_{fine} = 4.2 \text{ M}$
Turbulence models	$k - \epsilon$, $k - \omega$ SST, Spalart Allmaras
Wall treatment	Wall functions (unresolved) Calculated (resolved)
Convergence criteria	
Residuals	$U = 10^{-04}$, $P = 10^{-05}$
Relaxation factors	$U = 0.7$, $P = 0.6$
Simulation time	$\approx 384 \text{ CPUh}$

* corresponding to the final mesh grid chosen after completing the grid sensitivity analysis.

common freshwater rheophile fish species. A detailed overview of the body geometry is provided in a separate work on the development of a bio-inspired robotic fish (Abbaszadeh et al., 2021) which has an identical geometry to the fish-shaped body investigated in this work. All physical experiments were conducted in the open-channel laboratory flume at the Otto-von-Guericke University (OVGU) in Magdeburg, Germany. The flume is 10 m long, 1.2 m wide and the mean water depth for all experiments was fixed at 0.68 m. The LDA system was placed underneath the flume, with optical access from the bottom to a 0.6 m long, 0.53 m wide and 0.26 m high measurement volume. All measurements were taken with a mean streamwise velocity of 0.5382 m/s, corresponding to a fully turbulent flow with a Reynolds number of $Re = 6.8 \times 10^5$ after Eq. 1:

$$Re = \frac{\rho \cdot U \cdot d_h}{\mu} \quad (1)$$

where ρ is the density of water, U is the streamwise mean velocity, d_h is the hydraulic diameter of the flume and μ the dynamic viscosity. The hydraulic diameter was calculated for open channel flows (Eq. 2), following Surek and Stempin (2017), where b is the flume width and h is the mean water depth:

$$d_h = \frac{4 \cdot b \cdot h}{b + 2 \cdot h} \quad (2)$$

The Froude number was calculated as $Fr = 0.21$, (Eq. 3), assuming a gravitational constant of $g = 9.81 \text{ m/s}^2$, indicating that the flow is subcritical, and near-surface perturbations in the flume will therefore propagate in the upstream direction.

$$Fr = \frac{U}{\sqrt{g \cdot h}} \quad (3)$$

The LDA velocity point measurements were carried out at 253 locations with increasing sample density in the vicinity of the body of the fish (Fig. 1). Measurement locations included the undisturbed section upstream of the fish-shaped body, as well as the wake region immediately after the tail fin. In the vicinity of the fish-shaped body the closest measurement probes were located at a distance of 3 mm, and at the tail 2.5 mm from the body surface. At each location, the planar 2D velocity (U_x and U_y) was measured, and the turbulence intensity was calculated. The measurement were grouped into the head, body and tail regions of interest, to compare the performance of the different wall treatments and turbulence models. In order to ensure reproducibility over multiple days of measurement, a grid of 18 points in the upstream section was measured at the beginning of each experiment. The mean streamwise

velocity of the laboratory flume was 0.538 m/s, resulting in a standard deviation of 0.0116 m/s. At each location, 2000 (U_y) to 10,000 (U_x) measurements were recorded over a maximum time interval of 200 s. The LDA data was post-processed and stored with the commercial software BSA Flow using a Dantec Flow Explorer DPSS 300 2D, which allowed for the acquisition of raw data at a single measurement location. The same equations applied by the commercial software were used to compare the results from each of the numerical simulation setups. The software calculates the signal quality for each measurement based on the signal to noise ratio (SNR), which was used to qualitatively assess all LDA measurements before comparison with the CFD models. The lowest SNR value of 70.1% was obtained for LDA points close to the surface. Additional information regarding the LDA velocities, turbulence intensity and data validity are provided in the supplementary material, and the LDA measurements are included as part of this work's open data repository.

The upstream flow boundary immediately preceding the fish-shaped body used a mapped inlet condition and is indicated with a red outline in the left panel of Fig. 1. This was due to the non-symmetric velocity and turbulence intensity distributions within the laboratory flume, as illustrated in the right panels of Fig. 1. The planar LDA measurement point locations also served as the reference coordinates for the CFD probes, which retrieved the simulated model velocity at the closest cell to the given LDA measurement location.

3. Numerical model

Numerical modelling was performed using the OpenFOAM toolkit, an open source collection of C++ libraries and applications for continuum mechanics and multi-physics simulations (Jasak and Uroić, 2020). OpenFOAM was chosen because it is well-established in both the academic and commercial CFD communities, and provides a freely available model setup for ongoing and future studies. An overview of the numerical setup established in OpenFOAM environment for current case study is illustrated in Table 2, stating the range and selection of parameters. For the current case study, RANS modelling was preferred due to the trade-off between robustness and computational efficiency, where the turbulence is modelled, in contrast to more advanced approaches which partially or fully resolve turbulence effects, such as Large-Eddy Simulations (LES) or Direct Numerical Simulations (DNS).

A single-phase simulation was selected as the planar velocity measurements can be assumed to be largely unaffected by perturbations induced by the free surface at the LDA measurement locations. This assumption was further validated after comparison with the LDA point measurements, and are presented in the results section of this work. A segregated, single-phase algorithm (*pimpleFoam*) was used to solve the general momentum equation for incompressible, unsteady flow. It implements both the Pressure-Implicit-Split-Operator (PISO) and Semi-Implicit-Method-Of-Pressure Linked Equations (SIMPLE) algorithms for the treatment of the velocity and pressure fields. An advantage of using the SIMPLE algorithm is that it can be applied to simulations with high Courant–Friedrichs–Lewy (CFL) numbers (Deng and Tang, 2002). Due to the complexity of the problem, the CFL number in this study was set to a maximum of 20. All model setups evaluated in this work, required the use of an adjustable time step to preserve the CFL number under unsteady flow conditions. Within each time step, multiple outer loops of iterations were run for the pressure-momentum correction, with a residual tolerance of 10^{-05} for pressure and 10^{-04} for the velocity.

3.1. Geometry and mesh

The simulation domain was uniformly discretized along the x (streamwise), y (lateral) and z (vertical) directions. And the volume of domain was constrained to $1850 \times 800 \times 600 \text{ mm}^3$, to reduce the computational cost to the greatest extent feasible (Fig. 1). The model domain was defined using a hybrid mesh using two separate open source

Table 3. Overview of the numerical model setups investigated in this work as combinations of near-wall treatments and RANS turbulent models.

Near-wall treatment	RANS turbulence model		
	Standard $k - \epsilon$	$k - \omega$ SST	Spalart Allmaras
Boundary Layer Unresolved	BL modelled through wall functions ($30 < y^+ < 300$)	BL modelled through wall functions ($30 < y^+ < 300$)	-
Boundary Layer Resolved	BL fully resolved ($y^+ < 1$)	BL fully resolved ($y^+ < 1$)	BL fully resolved ($y^+ < 1$)

meshing tools. The OpenFOAM utility *blockMesh* was first applied to generate the flume domain, with the exception of a rectangular block cavity which contained the fish geometry. This first mesh also encompasses all of the domain’s outer boundaries. The *blockMesh* utility allows for the control of the grid with a block-oriented, structured meshing approach using hexahedral elements, but it is generally unsuitable for complex geometries (Greenshields, 2021). The second mesh region contained the fish-shaped body geometry, and was generated with the open source version of *cfMesh* (Juretić, 2015). The body geometry was imported as an *.stl* file in a Cartesian hexahedral mesh and then recursively refined into a structured mesh around fish body surface, including the boundary mesh layers. Three near-body mesh layers were added around fish body, starting from the first layer having a thickness of 1 mm and an expansion ratio of 1.5. An advantage of this tool is the improved handling of complex geometries. In a final meshing step, both meshes were merged and stitched together. For more complex geometries, e.g. more detailed shapes of real fish with fins, a tetrahedral mesh can be generated in the cavity and merged with the structured block oriented hexahedral mesh generated with *blockMesh*. An advantage of our approach is that it uses only open source mesh generation tools which are largely automated, making it especially suitable for future fish-shaped bodies with different geometries.

3.2. Boundary conditions and initial values

In the numerical simulations carried out in this work, all walls were considered with a slip boundary condition, except the fish body, which was assigned a no-slip boundary condition. The effects of the free surface were therefore neglected in this work. Accounting for the free surface would require computationally expensive multi-phase calculations without a significant change in the flow field around the fish-shaped body. Even a simplified but computationally efficient volume-of-fluid model would require the calculation of additional terms for the air phase, and at a finer spatial discretization of the phase interface at the free surface. Furthermore, the temporal discretization required to satisfy

the condition that $CFL < 1$ would increase substantially to ensure numerical stability. Considering a trade-off between computational cost and the need for only near-body velocity and pressure fields, a single phase flow model was employed in this study.

The inlet boundary included an outer sub-patch, which was assigned a uniform velocity of 0.55 m/s, as well as an inner sub-patch, which was mapped using the LDA measurements (Fig. 1). The mapping was made using a second order polynomial derived from the LDA velocity vectors U_x and U_y , interpolated as the inner sub-patch using the expressions-based boundary conditions utility in OpenFOAM-v2012. It is important to note that U_z was not included in our study, and was considered to

Table 4. Calculation of discretization error for current study.

Parameter	Drag coefficient (c_d)
N_1, N_2, N_3, N_4, N_5	47K, 107K, 700K, 4.2M, 5.5M
$Y_1^+, Y_2^+, Y_3^+, Y_4^+, Y_5^+$	3.9, 2.7, 1.4, 0.7, 0.5
$\phi_1, \phi_2, \phi_3, \phi_4, \phi_5$	0.0417, 0.0367, 0.0320, 0.0282, 0.0285
P_{ave}	1.49
$\psi_{ext}^{21}, \psi_{ext}^{32}, \psi_{ext}^{43}, \psi_{ext}^{54}$	0.0467, 0.0414, 0.0358, 0.1116
$e_a^{21}, e_a^{32}, e_a^{43}, e_a^{54}$	11.99%, 12.80%, 11.87%, 1.06%
$GC_{c_d}^{21, coarse}$	14.98%
$GC_{c_d}^{32}$	16.00%
$GC_{c_d}^{43}$	14.84%
$GC_{c_d}^{54, fine}$	5.30%

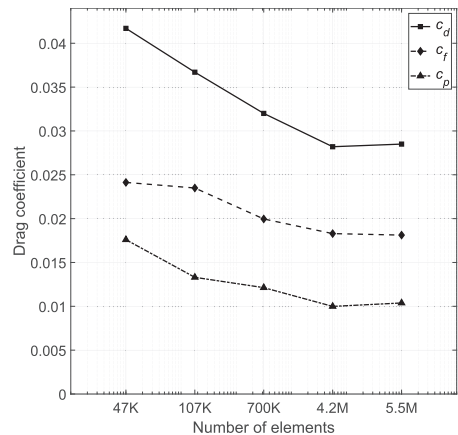


Fig. 3. Evolution of drag (c_d), friction drag (c_f) and pressure drag (c_p) coefficients for increasing mesh resolution and number of cells (abscissa in logarithmic scale).

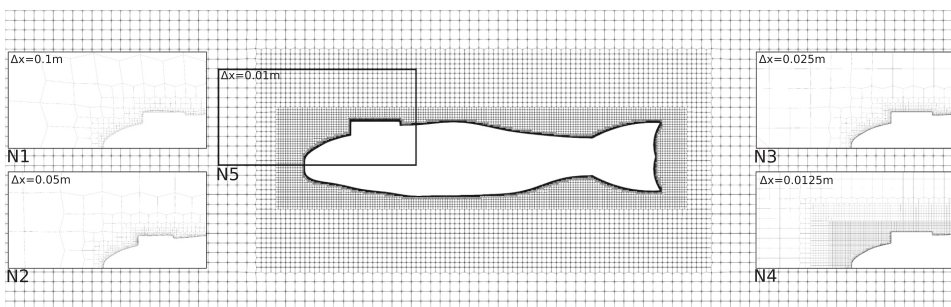


Fig. 2. Mesh discretization of the flume domain from coarse to fine (N1–N5), with cell sizes ranging from from 0.1 m to 0.01 m, including step-wise mesh refinement regions and boundary layers around the fish surface.

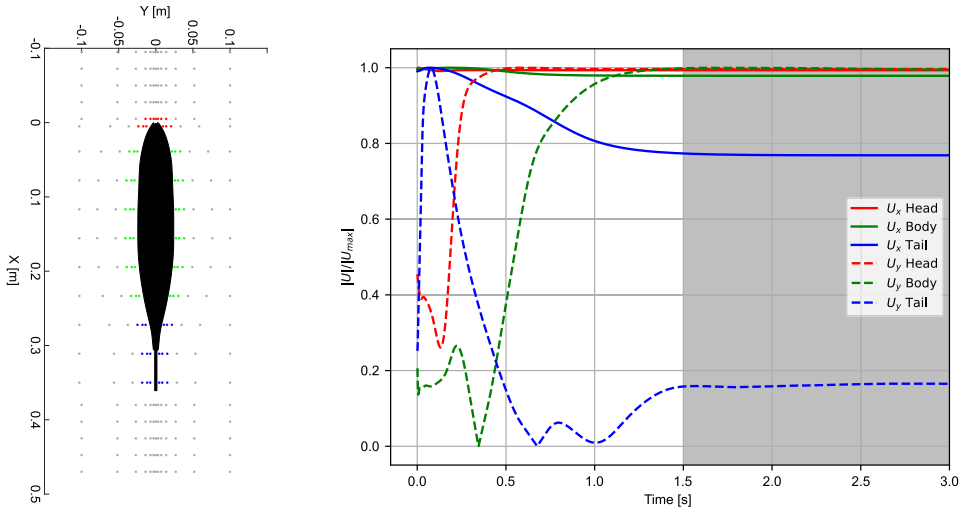


Fig. 4. Left: Velocity measurements and numerical probes around fish body in three regions: head (red), body (green) and tail (blue). Gray points further away from body surface correspond to LDA measurement locations not used in the mesh sensitivity analysis. Right: Convergence of the streamwise and lateral velocity components in the head, body and tail regions over a simulation time of 3 s. (For interpretation of the references to colour in this figure legend, the reader is referred to the web version of this article.)

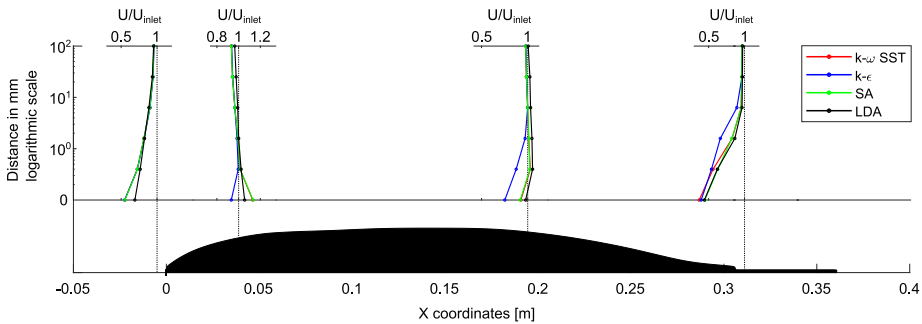


Fig. 5. Normalized streamwise velocity profiles at three different regions along the fish-shaped body for all turbulence models and LDA measurements. At some locations, the $k - \omega$ SST model overlaps the *Spalart Allmaras* model and is not visible.

be negligible. The inlet boundary was kept 0.1 m upstream of the head of the fish, to most closely match the mapped inner sub-patch interpolated from the LDA experiments. This short distance allowed for a close matching of the flow pattern directly upstream of the body. This choice was justified based on the comparison of the mapped inlet boundary condition with a uniform inlet condition placed 0.4 m distance to the fish, where it was observed that the mapped inner sub-patch resulted in an average reduction of the deviation in the streamwise velocity of 7.3%. Considering pressure, a Neumann boundary condition ($\nabla P = 0$) was specified at the inlet patch and a Dirichlet boundary condition ($P = 0$) was applied at the outlet patch. The side and bottom walls were specified with Neumann boundary conditions ($\nabla P = 0$) for the pressure.

As velocity and turbulence intensity (TI) were acquired from the LDA experiments, an average turbulence intensity field from the experiments ($TI = 3.07\%$) was also implemented at the inlet patch implicitly by assigning the turbulence kinetic energy (k) and dissipation using (ϵ) and (ω), respectively. Mathematical expressions used for the calculation of turbulent kinetic energy (k) and dissipation rate (ϵ) and (ω) were

adapted from [Launder and Sharma \(1974\)](#):

$$k = \frac{3}{2}(U \times TI)^2, \quad \epsilon = c_\mu^{\frac{3}{4}} k^{\frac{3}{2}} l^{-1}, \quad \omega = \sqrt{k} / l \quad (4)$$

where, U is the velocity, c_μ is the model constant with a value of 0.09 and l is the turbulent length scale of $0.22 h_0$, where $h_0 \approx 0.1$ m is the height of fish-shaped body.

Different wall functions for k , ϵ , ω and μ_t depending upon the type of mesh discretization (e.g. for setups where the boundary layer was either resolved or unresolved) were applied as initial conditions. A detailed table of the numerical model setups is provided in the supplementary material. The roughness at the surface of the fish model and walls was considered to be uniform with a roughness height of 100×10^{-6} , and remained as the default value for all model setups evaluated in this study. This roughness value was chosen as it is commonly applied in CFD studies of hydraulically smooth surfaces ([Adams et al., 2012](#)). The adaptation of the surface roughness allows for a fine tuning of the flow separation zone. However for this study, it was not required to be

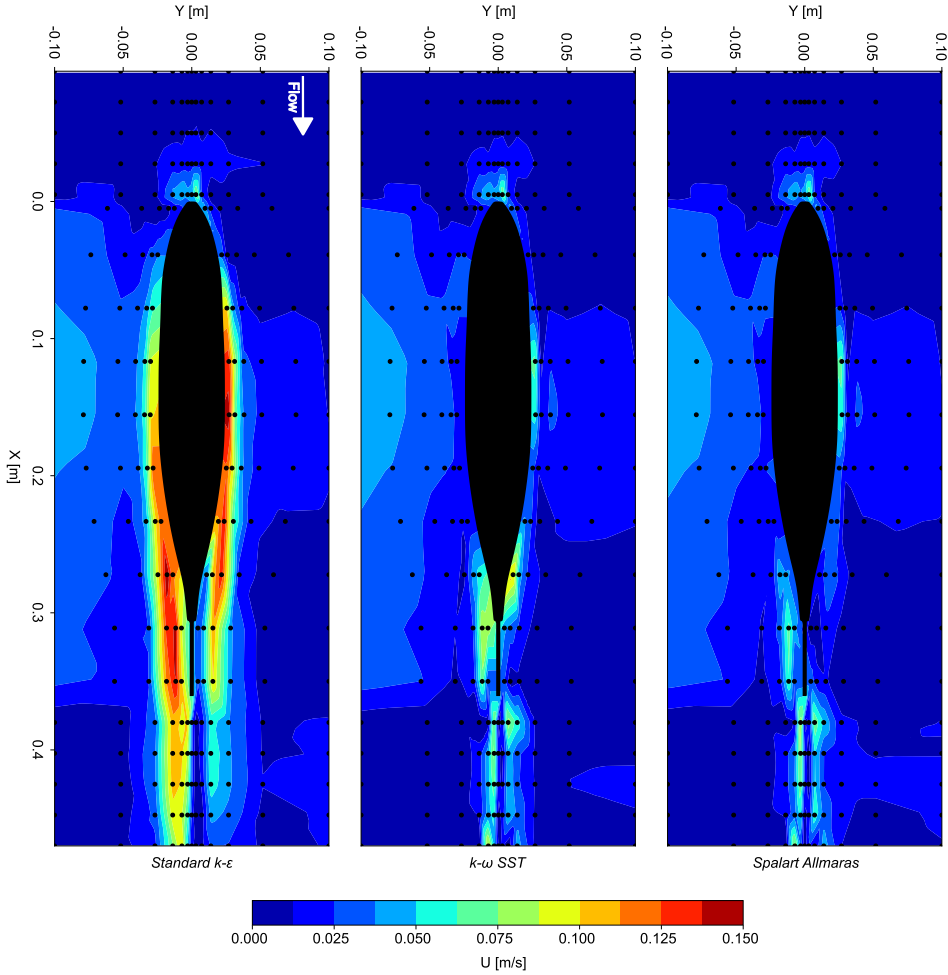


Fig. 6. Contour plots of the absolute difference in streamwise velocity between LDA measurements and the standard $k - \epsilon$ (left), $k - \omega$ SST (center) and Spalart Allmaras (right) turbulence models.

adjusted as the default value was found suitable when compared to the LDA measurements. It is also interesting to point out that previous research on the roughness at the surface of trout has found that the presence of scales and mucus did not substantively alter the boundary layer (Gorb et al., 2017).

3.3. Turbulence models

The RANS approach used in this work allows for a sufficient representation of the physical model flow conditions, but required further assessment to determine the best performing turbulence model. The turbulence models evaluated in this study were based on the Boussinesq hypothesis, in which the Reynolds stresses are proportional to the mean rates of deformation (Schmitt, 2007). Using Reynolds decomposition, the Navier-Stokes momentum equation is given as (Batchelor, 2000):

$$\rho \frac{\partial u_i}{\partial t} + \rho \frac{\partial}{\partial x_j} (u_i u_j) = - \frac{\partial p}{\partial x_i} + \frac{\partial}{\partial x_j} (2\mu S_{ij} - \rho \overline{u'_i u'_j}) \quad (5)$$

where u is velocity, t is time, p is pressure, μ is the dynamic viscosity, S_{ij} is the mean strain rate tensor, u' is the fluctuating velocity component and $\overline{u'_i u'_j}$ are the mean velocity gradients. The Boussinesq approach fundamentally relates the Reynolds stresses to the mean velocity gradients which are expressed as:

$$-\rho \overline{u'_i u'_j} = \mu_t \left(\frac{\partial u_i}{\partial x_j} + \frac{\partial u_j}{\partial x_i} \right) - \frac{2}{3} \left(\rho k + \mu_t \frac{\partial u_k}{\partial x_k} \right) \delta_{ij} \quad (6)$$

where δ_{ij} is the Kronecker delta with orthogonal coordinate indices i and j . An advantage of modelling the Reynolds stresses with the Boussinesq hypothesis is the decrease in computational cost associated with using a turbulent viscosity μ_t . The Boussinesq hypothesis fundamentally assumes μ_t to be a scalar quantity, and the turbulent kinetic energy (k) produced within the flow is then estimated as:

$$k = \frac{1}{2} \overline{u'_i u'_i} \quad (7)$$

Three well-established RANS turbulence models, $k - \epsilon$, $k - \omega$ SST

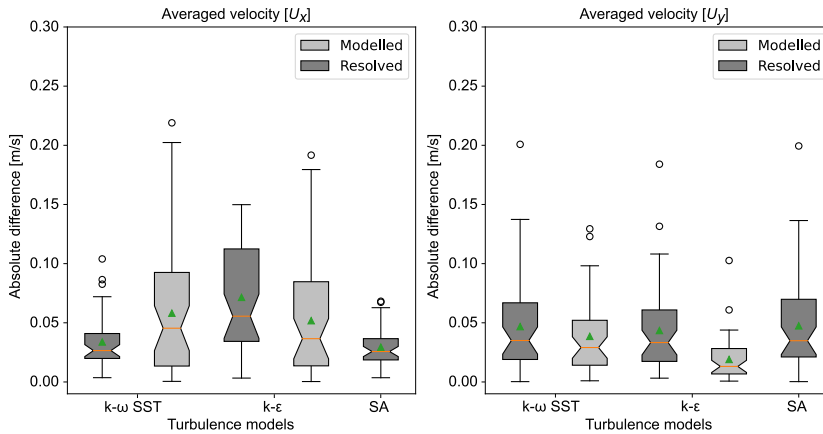


Fig. 7. Box-plots of the absolute difference between the time-averaged velocities (U_x and U_y) for the three turbulence models, compared to the LDA measurements. The box-plot indicates the inter-quartile range, mean (green triangle), median (orange line) and outliers are shown as black circles. The fill colour indicates either resolved or modelled boundary layers. (For interpretation of the references to colour in this figure legend, the reader is referred to the web version of this article.)

and Spalart-Allmaras models were selected based on their general suitability for the case study. They were compared with the experimental LDA measurements to determine the best-performing model for flow around fish-shaped bodies. A summary of the turbulence models and near-wall treatments investigated in this work is provided in Table 3.

3.3.1. Standard $k - \epsilon$ model

The standard $k - \epsilon$ model is one of the most widely used for RANS simulations. It is a two-equation model which solves the turbulent kinetic energy k and turbulent dissipation ϵ , approximating turbulence in the averaged flow field as calculated by the RANS approach (Jones and Launder, 1972). The $k - \epsilon$ model is known to perform well far from surfaces, where pressure gradients tend to be small (Bardina et al., 1997; Launder and Sharma, 1974) and thus its performance was not anticipated to be the best considering the near-body flows of interest in this study. There are multiple extensions of the standard model available, including the realizable $k - \epsilon$ model and *Re*-Normalisation Group (RNG) $k - \epsilon$ model (Yakhot and Orszag, 1992). Differences between the standard model and its extensions concern the calculation of model constants for the turbulent viscosity (μ_t) and the inclusion of different scales of motion. This results in improved predictions of jet spreading rates, a stronger capacity to capture the mean flow around structures, and for complex flows including rotation and boundary layers under high adverse pressure.

3.3.2. $k - \omega$ SST model

To resolve some of the issues when applying the standard $k - \epsilon$ model, the hybrid turbulence model $k - \omega$ SST model was also chosen in this work. It is a two-equation model which combines the advantages of the $k - \omega$ model (Wilcox, 1988) and $k - \epsilon$ model. The $k - \omega$ SST model is especially well-suited for wall-bounded and unbounded flows (Menter, 1993), where the transport of shear stress is included in the turbulent viscosity to improve the prediction of flow separation on smooth surfaces with adverse pressure gradients. Menter (1994) added a turbulent prediction limiter to avoid over-prediction of turbulent kinetic energy in stagnation regions without influencing the shear layers. Due to the importance of the near-wall flow field for fish sensing, this model was chosen as it incorporates a blended function which determines the position and activates the required turbulence model. The function becomes zero far from the wall, applying $k - \epsilon$, and remains unity within the boundary layer where $k - \omega$ is used. In the present study, all model constants were executed with the default values presented in Menter (1994).

3.3.3. Spalart-Allmaras model

The Spalart-Allmaras model is a single equation approach which implements linear eddy viscosity. The model was first introduced by Spalart and Allmaras (1994) and developed for modelling airfoils with adverse pressure gradients, which are geometrically similar to fish-shaped bodies. In this model, the turbulence kinetic energy is not readily available. Instead, while estimating the Reynolds stresses the last term in Eq. 6 is ignored and the kinematic eddy viscosity is calculated through the use of closure functions (Spalart and Rumsey, 2007).

3.4. Boundary layer and near-wall treatment

The flow inside the flume is fully turbulent ($Re_{channel} = 6.8 \times 10^5$) and strongly influenced by the presence of the fish-shaped body, primarily due to the large velocity gradients resulting from the no-slip condition on the body surface. As the distance from the surface increases, turbulence increases due to the increased production of turbulent kinetic energy, generated principally due to the presence of large gradients in the mean streamwise and lateral velocities. Modelling the flow field accurately in the vicinity to the fish-shaped body thus required special attention to the combinations of turbulence models and near-wall treatments, as summarized in Table 3. Furthermore, a comprehensive overview table of the wall functions used in conjunction with the investigated turbulence models and near-wall treatments is provided in the supplementary material to this work.

The exploration of the sensing range of a fish through numerical modelling requires simulations of the near-body flow fields. Close to the surface of fish, the flow is dominated by viscous effects, where the near-body velocity depends on the distance from the surface of the fish, the fluid density, viscosity and shear stress. The viscous forces inside the viscous region of the boundary layer dominate over the inertial forces, creating a no slip boundary condition ($U = 0$) at the surface of the fish's body. This region is extremely thin, and the mean velocity is assumed to increase linearly with increasing radial distance from the body surface (wall). The dimensionless wall distance (y^+) was calculated as:

$$y^+ = \frac{y u_\tau}{\mu} \quad (8)$$

where y is the absolute distance from the wall, u_τ is the frictional velocity and μ is dynamic viscosity. Simulating the boundary layer can be challenging for biologically inspired geometries such as the fish-shaped body investigated in this work, as it depends on the finest regions of the mesh.

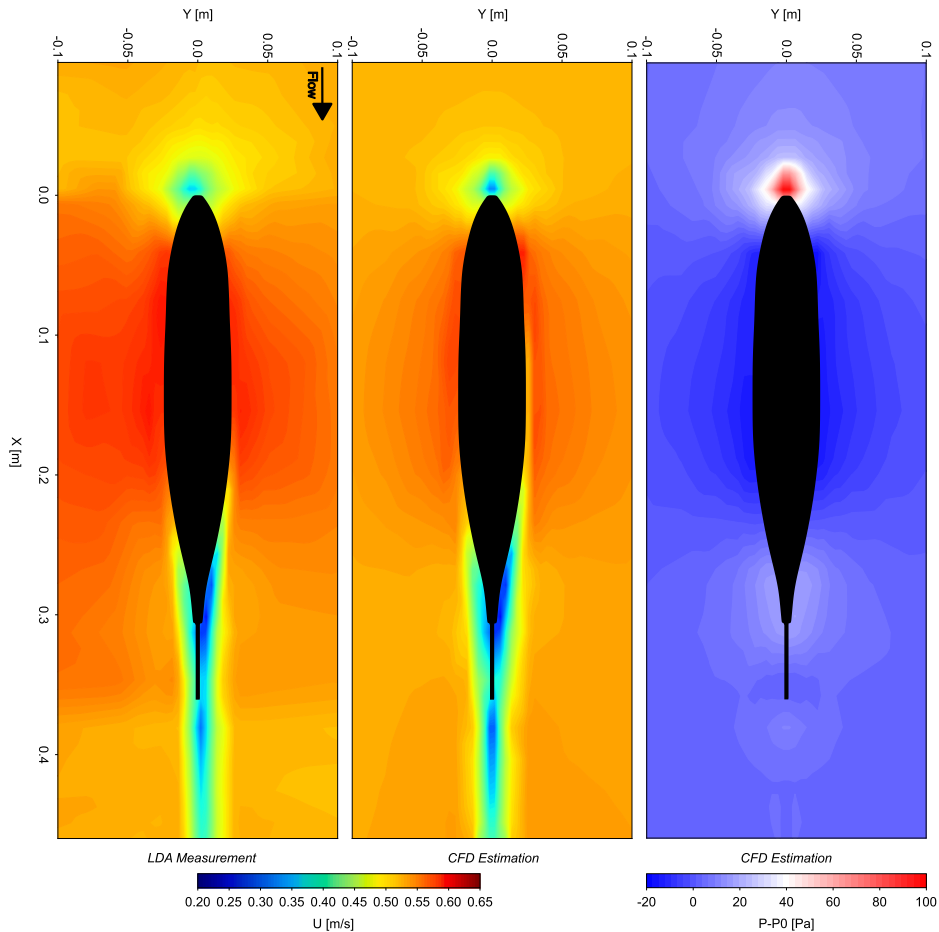


Fig. 8. Comparison of the 2D velocity fields at the midsection plane $z = 0$, showing the LDA measurements and best-performing RANS simulation using a resolved boundary layer. Left: LDA measurements. Center: *Spalart Allmaras* turbulence model. Right: Contour plot of the dynamic pressure field around the fish-shaped body from the *Spalart Allmaras* model at $z = 0$. The pressure values are reported as P-P0, where P0 corresponds to the hydrostatic pressure at the stagnation point of the body.

Specifically, the near-body mesh must adequately capture the geometry, and the chosen simulation approach depends on the Reynolds number and wall roughness. There are two general numerical simulation approaches used to simulate flow around complex geometries. The first is a more simplified approach where the boundary layer is modelled using a wall function ($30 < y^+ < 300$). A more sophisticated approach resolves the boundary layer with a fine mesh discretization ($y^+ < 1$), which generally improves the accuracy but is correspondingly more computationally demanding. As one of the research objectives of this work was to address the lack of a comparison of near-wall treatments for CFD studies on fish-shaped bodies, we compared the unresolved and resolved boundary layers in conjunction with the three RANS turbulence models $k - \epsilon$, $k - \omega SST$ and *Spalart Allmaras*. To accomplish this, it was necessary to create two different types of mesh to achieve y^+ values within the desired range of $y^+ < 1$ for the resolved, and $30 < y^+ < 300$ for a modelled boundary layer (Table 3).

4. Mesh and time sensitivity analyses

Mesh and time sensitivity analyses were performed to ensure the consistency of the numerical simulation performance and in preparation for the numerical model comparison with the LDA measurements. The numerical settings were first verified through a mesh refinement process (from coarse to fine) to identify the appropriate spatial discretization, as presented in Fig. 2. The mesh sensitivity results for the five different resolutions tested are summarized in Table 4. Subsequently, a time sensitivity analysis was also performed to determine the time for a fully developed flow field at which the streamwise and lateral near-body velocities for each of the head, body and tail regions stabilize.

The mesh sensitivity analysis was carried out with a setup employing the $k - \omega SST$ turbulence model. For the mesh sensitivity analysis, the drag coefficient was chosen as an evaluation metric, because it considers the pressure and shear forces over the entire surface of the fish-shaped body, providing an integrated overview of both the velocity and pressure fields as a single value. Mathematical expression for the calculation of drag coefficient is as follows (Heddleson et al., 1957):

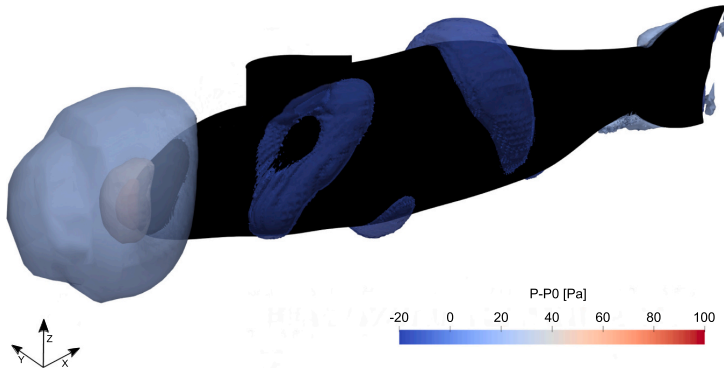


Fig. 9. 3D isosurfaces of the dynamic pressure around the fish-shaped body. The illustration neglects the effect of the sting, providing a qualitative depiction of the highly complex pressure surface topology in the vicinity of the body. The pressure values are reported as P–P0, where P0 corresponds to the hydrostatic pressure at the stagnation point of the body.

$$c_d = \frac{2F_d}{\rho U^2 A} \tag{9}$$

Where F_d is the drag force on the reference area A of fish (which is approximately 0.01448 m^2 for current fish model) moving with velocity U inside a fluid of density ρ . The mesh sensitivity analyses followed the ASME criteria (Celik et al., 2008) using five different base-mesh cell sizes: 0.1 m, 0.05 m, 0.025 m, 0.0125 m and 0.01 m with a global refinement ratio r of 10 ($r = h_{\text{course}}/h_{\text{fine}}$ where h = mesh cell size). The y^+ values for all meshes were restricted to remain in the viscous range (i.e. up to $y^+ = 5$). This was due to the functional requirements of the resolved wall functions, and was required to achieve comparable near-body velocities and pressure fields. These quantities are of particular interest for future studies on the spatial extents of the active sensory space that includes the velocity, acceleration and pressure fields in the immediate vicinity of a fish-shaped body. The numerical uncertainty was assessed using the grid convergence index (GCI) method. First, the approximate relative error (e_d^i) in the numerical model results between two successive mesh grids was evaluated. Afterwards, the grid convergence index (Roache, 1994) between consecutive meshes was calculated. For each of the five mesh sizes, the drag coefficient (c_d), which is composed of the sum of friction (c_f) and pressure drag (c_p), was calculated at the surface of the fish model for comparison. Table 4 represents the mean variable ϕ_n – in our case the drag coefficient – which denotes its value on the n th grid and the local order of accuracy p_a of the method for each respective mesh, which was calculated as:

$$p_a = \frac{1}{\ln(r_{ji})} \left| \ln \left[\frac{\epsilon_{kj}}{\epsilon_{ji}} \right] + q(p_a) \right| \tag{10}$$

where $\epsilon_{kj} = \phi_k - \phi_j$ and $\epsilon_{ji} = \phi_j - \phi_i$.

$$q(p_a) = \ln \left[\frac{r_{ji}^{p_a} - s}{r_{kj}^{p_a} - s} \right] \tag{11}$$

$$s = 1. \text{sgn}(\epsilon_{kj} / \epsilon_{ji}) \tag{12}$$

The extrapolated values of the variable were calculated as:

$$\phi_{\text{ext}}^i = (r_{ji}^{p_a} \phi_i - \phi_j) / (r_{ji}^{p_a} - 1) \tag{13}$$

And the approximate relative error (e_d^i) between each consecutive mesh was calculated along with the grid convergence index (GCI) using following expressions:

$$e_a^i = \left| \frac{\phi_i - \phi_j}{\phi_i} \right| \tag{14}$$

$$GCI_{\text{fine}}^i = \frac{1.25 e_a^i}{r_{ji}^{p_a} - 1} \tag{15}$$

The relative difference in simulated results between consecutive meshes (i.e. for refinements between meshes of $\Delta x = 0.1$ and 0.01), had a maximum value of 31.65%. The average order of accuracy p_{avg} , defined as the lowest order term in the truncation error, was found to be 1.49. This value is in good agreement with the formal order of the numerical schemes applied, which were chosen to be first order. Therefore, the mesh sizes used in this case study lie within the asymptotic range. The results of the mesh sensitivity analyses based on the drag coefficient are presented in Fig. 3, which illustrate the drag coefficient convergence occurring between meshes N4 and N5 with a 1.06% reduction of the relative percentage error. To optimize numerical model efficiency and reduce the computational time, the N4 mesh was selected based on the mesh sensitivity analyses for all further model setups used in this work.

The time sensitivity analyses were performed for three distinct near body regions around the model geometry corresponding to the head, body and tail regions as shown in Fig. 4 and are denoted by the red, green and blue points, respectively. Considering a fish’s lateral line sensing system, the bulk flow intensity and its direction are encoded by the upstream (head) flow, swimming kinematics are regulated by the forces acting laterally (body) and the energy consumption used during swimming is reflected in the momentum deficit present in the wake (tail). For this reason, the time sensitivity as well as the results for the numerical model setups are presented for these three regions in the remainder of this work. The streamwise and lateral velocities were monitored over a 3 s interval. The flow field becomes fully developed after 1.5 s, as indicated in the gray hatched region of Fig. 4. The velocities U_x , U_y corresponded to locations where the LDA measurements were obtained and were ensemble averaged for all points within each of the three regions at each time step. In the head region, the velocities were averaged from 13 points at each time step, 36 for the body and 18 in the tail region (the locations of all points is shown in Fig. 4). As expected, the convergence of U_x occurred in the head region first, followed by the body and finally the tail region. The delayed convergence of the streamwise U_x velocity in the tail region is due to the flow separation. Similar behavior was observed for the U_y velocity. A time step sensitivity analysis was also conducted for the velocity field by using three different time steps, i.e. $\Delta t = 0.1, 0.01$ and 0.001 resulted in negligible differences.

5. Results and discussion

5.1. Turbulence model assessment

The normalized streamwise velocity profiles for all three turbulence models were plotted against the LDA profiles in the near-body region, and are shown in Fig. 5. The profiles in the head region, beginning 5 mm upstream of the body, exhibited the largest relative error of 20% when compared with the LDA measurement, decreasing rapidly to 0.4% as the profile extended into the freestream.

All turbulence models performed nearly equally at the stagnation point, which features an especially rapid velocity gradient (Fig. 6). Laterally along the fish-shaped body, it can be seen that the $k - \epsilon$ model failed to adequately capture the adverse velocity profile at the head. The $k - \omega$ SST and *Spalart Allmaras* models performed nearly equally at the head with minor exceptions. Similar trends were observed in the body region profile, where the $k - \omega$ SST and *Spalart Allmaras* models had a 6% deviation, whereas the $k - \epsilon$ model exhibited a 23% deviation from the LDA measurements.

The tail region includes boundary layer separation and vortex shedding, and therefore represents one of the most challenging regions for accurate numerical simulation. Within the tail region, the *Spalart Allmaras* model using a resolved boundary layer predicted the streamwise velocity profile with the highest overall accuracy, both near the body surface and extending into the freestream flow. In addition to the near-body velocity profiles, contour plots of the absolute difference in streamwise velocity for all three turbulence models and LDA measurements are presented in Fig. 6. The results provide a spatially distributed quantitative assessment of regions with higher and lower absolute errors. In the vicinity of the fish body, a significant difference of up to 0.15 m/s in the absolute streamwise velocity was observed when using the $k - \epsilon$ model. In contrast, the $k - \omega$ SST model exhibited far lower deviations with a maximum of 0.1 m/s, and the *Spalart Allmaras* had a maximum of 0.05 m/s absolute deviation from the LDA measurements.

5.2. Resolved and modelled boundary layer comparison

To assess the impact of modelling or resolving the boundary layer, a comparative study between the subset of LDA measurements points within the maximum distance of 0.0139 m at the surface of fish were chosen for evaluation. The absolute difference between the time-averaged velocities from the CFD models and the LDA measurements was obtained for both streamwise (U_x) and lateral velocity (U_y), at the probe locations within the range. It is worth pointing out that the *Spalart Allmaras* model only operates with a resolved boundary layer case. The results of the near-wall treatments for all turbulence models are given in Fig. 7 as box-plots. From the plots, it was found that considering the streamwise velocity, the *Spalart Allmaras* model had the lowest observed absolute difference but there were no substantive differences observed across model setups considering the lateral velocity. Overall the resolved boundary layer cases showed less absolute difference in velocity as compared to the modelled one for streamwise velocity component, whereas it was marginal in case of lateral velocity component.

5.3. Validation with LDA measurements

Among the three turbulence models, the *Spalart Allmaras* model performed best overall, closely followed by the $k - \omega$ SST model, which was found to have both streamwise and lateral velocity errors with similar distributions. A comparison of the velocity contour plots using the *Spalart Allmaras* model with resolved boundary layer as compared to the experimental LDA data is shown in Fig. 8. The CFD model and LDA measurements are in good agreement, especially considering the strong velocity gradients in the upstream head region. The experimental results had a slightly larger time-averaged mean freestream velocity of 0.52 m/s, whereas the numerical model had an average of 0.50 m/s. The spatial

distribution of the high velocity region around the body found in the LDA contour plot illustrates a broader spatial extent than the numerical model. This may have been caused by wall effects in the laboratory flume. The highly turbulent tail region shows that the CFD model accurately captured the flow separation, which occurred at 2/3 of the total body length. The wake region shows good agreement in the streamwise velocity between both the measured and simulated results.

6. Summary and conclusions

This work was motivated by the lack of an openly available laboratory measurements and fish body model. Addressing this gap will improve the ability of researchers to systematically study turbulent flow fields around fish-shaped bodies. The major contributions of this work are the laboratory LDA velocity measurements, and the critical evaluation of the most suitable turbulence model considering the boundary layer numerical treatment.

In this study, RANS turbulence models were selected due to the trade-off between robustness and computational efficiency. Correspondingly, we chose the standard $k - \epsilon$, the $k - \omega$ SST and *Spalart Allmaras* models. The numerical model was validated with LDA measurement data, where it was found that a resolved boundary layer and *Spalart Allmaras* had the lowest overall error, followed by $k - \omega$ SST and finally $k - \epsilon$ with respect to the streamwise velocity. Although minor differences were found, the three turbulence models performed nearly equally well for the near-body, lateral averaged velocity. In this study, the *Spalart Allmaras* performed the best over the whole length of the fish-shaped body, when compared with the $k - \omega$ SST and $k - \epsilon$ models. The average deviations of the streamwise velocity when compared with the LDA measurements were 7.8%, 11.4% and 15.17%, respectively, in the near-surface region. Thus the *Spalart Allmaras* model was found to be the most suitable RANS turbulence model for future CFD studies on the active sensory space of fish.

Streamwise velocity gradients are used by the fish's superficial neuromast flow sensing system, and previous works have shown that flow-sensitive receptors are highly concentrated in the head region (Ristroph et al., 2012). The density of sensory receptors was found to have high densities around the eye socket, with a maximum receptor density at 10% of the total body length, decreasing rapidly and tailing off at 20%, where sparsely located lateral canal neuromasts remain. Motivated by these biological observations, future analyses of the near-body flow field should also include an assessment of the spatial sensitivity of velocity gradients and pressure.

The boundary layer around the surface of fish was resolved to a thickness of 0.014 m, following the work of Yanase and Saarenrinne (2016) who measured it on a swimming trout with PIV. The absolute difference between the near-body streamwise velocity for modelled and resolved boundary layers was consistently lower for the resolved boundary layer setup (21%–52.5%), when comparing the $k - \epsilon$ and $k - \omega$ SST models. Considering the lateral velocity, the absolute differences between modelled and resolved setups were found to be marginal. This is partially due to the presence of wall effects in the laboratory flume, which resulted in a significant reduction of the lateral velocity component. The *Spalart Allmaras* turbulence model resolved boundary layer case exhibited the least absolute difference among the three turbulence models tested in this study. Based on these findings, we recommend resolving the boundary layer to ensure an accurate representation of the near-body streamwise and lateral velocities, which is in agreement with the recommendations from Rapo et al. (2009) and Herzog et al. (2017).

The pressure gradients around the fish body were not the major focus of this work. This was primarily because the LDA velocity measurements served as the measured reference for model tuning and validation. However, since the canal-based lateral line system does indeed rely on the near-body pressure distribution, it was also of interest to plot the pressure isosurfaces as shown in Fig. 9. As first illustrated by Kogan et al. (2015), the pressure isosurfaces provide an interesting view of the

highly complex “touch at a distance” sensing modality. It is worth pointing out that the pressure isosurfaces can be easily recovered from CFD models. Interesting observations may be obtained where the fish-shaped body is positioned downstream of obstacles or near walls, to further study how changes in the near-body pressure field relate to a wider range of freshwater fish body geometries and realistic flow environments.

Future works are ongoing to investigate the effects of synthetic turbulence of known length and correlation time scales on the pressure and velocity fields in the boundary layer of fish-shaped bodies. We will also study additional body geometries from nine different common European freshwater fish species. These studies will include bottom-oriented, weak and strong swimmers, and the results of the ongoing research will provide new insights as to how a fish’s body geometry interacts with a broader range of turbulent flows. These insights can be used to improve our basic understanding of how fish may use or avoid flow fields which they commonly encounter in Nature during feeding, for predator avoidance, as well as for spawning and migration. The findings and recommendations in this work are meant to inspire and encourage a more rapid adoption of CFD to improve our understanding of freshwater fish’s advanced sensing abilities as well as the complex flows they inhabit and rely on for survival. Although our initial contribution is a single fish model, we are optimistic that a far wider range of freshwater “CFD fish” are soon to follow.

6.1. Data availability

Additional data supporting the findings of this study and supplementary materials including the open numerical model and measurement data are available from the Open Science data repository of the Otto-von-Guericke University Magdeburg at doi:[10.24352/UB.OVGU-2022-001](https://doi.org/10.24352/UB.OVGU-2022-001)

Declaration of Competing Interest

None.

Acknowledgements

The research work presented in this paper has received funding from European Union Horizon 2020 Research and Innovation Programme under the Marie Skłodowska-Curie Actions, Grant Agreement No. 860800. Laboratory measurements were conducted as part of the RETERO project, sponsored by the German Federal Ministry of Education and Research Grant no. 161L0152A. Jeffrey A. Tuhtan’s contribution was funded by the Estonian Research Council Grant PRG1243 and Maarja Kruusmaa was funded by EXCITE supported by the Estonian Centre of Excellence in IT, funded by the European Regional Development Fund Project nr 2014-2020.4.01.15-0018. The authors are grateful to M. Yanneck Kiiski for the design and 3D printing of the fish geometry and the CAD model of the laboratory flume.

References

Abbaszadeh, S., Leidhold, R., Hoerner, S., 2021. A design concept and kinematic model for a soft aquatic robot with complex bio-mimicking motion. *J. Bionic Eng.* <https://doi.org/10.1007/s42235-021-00126-4>.

Adams, T., Grant, C., Watson, H., 2012. A simple algorithm to relate measured surface roughness to equivalent sand-grain roughness. *Int. J. Mech. Eng. Mechatron.* **1**, 66–71. <https://doi.org/10.11159/ijmem.2012.008>.

Adkins, D., Yan, Y., 2006. CFD simulation of fish-like body moving in viscous liquid. *J. Bionic Eng.* **3**, 147–153. [https://doi.org/10.1016/S1672-6529\(06\)60018-8](https://doi.org/10.1016/S1672-6529(06)60018-8).

Bardina, J., Huang, P.G., Coakley, T.J., 1997. Turbulence modeling validation, testing, and development. Technical Memorandum (TM) 1, 1–100, 19970017828.

Batchelor, G.K., 2000. An Introduction to Fluid Dynamics. Cambridge Mathematical Library, Cambridge University Press. <https://doi.org/10.1017/CBO9780511800955>.

Belletti, B., Rinaldi, M., Bussetti, M., Comiti, F., Gurnell, A.M., Mao, L., Nardi, L., Vezza, P., 2017. Characterising physical habitats and fluvial hydromorphology: a

new system for the survey and classification of river geomorphic units. *Geomorphology* **283**, 143–157. <https://doi.org/10.1016/j.geomorph.2017.01.032>.

Celik, I.B., Ghia, U., Roache, P.J., Freitas, C.J., Coleman, H., Raad, P.E., 2008. Procedure for estimation and reporting of uncertainty due to discretization in CFD applications. *J. Fluids Eng.* **130**, 078001–078004. <https://doi.org/10.1115/1.2960953>.

Cyterski, M., Barber, C., Galvin, M., Parmar, R., Johnston, J.M., Smith, D., Ignatius, A., Prieto, L., Wolfe, K., 2020. Pisces: P(i)scine stream community estimation system. *Environ. Model. Softw.* **127**, 104703 <https://doi.org/10.1016/j.envsoft.2020.104703>.

Deng, Q.H., Tang, G.F., 2002. Special treatment of pressure correction based on continuity conservation in a pressure-based algorithm. *Numerical Heat Transfer, Part B: Fundamentals* **42**, 73–92. <https://doi.org/10.1080/10407790190053842>.

Dijkstra, S., 1963. The functioning and significance of the lateral-line organs. *Biol. Rev.* **38**, 51–105. <https://doi.org/10.1111/j.1469-185x.1963.tb00654.x>.

García-Vega, A., Fuentes-Pérez, J.F., Fukuda, S., Kruusmaa, M., Sanz-Ronda, F.J., Tuhtan, J.A., 2021. Artificial lateral line for aquatic habitat modelling: an example for lefua echigonia. *Ecol. Informat.* **65**, 101388 <https://doi.org/10.1016/j.ecoinf.2021.101388>.

Gisen, D.C., Weichert, R.B., Nestler, J.M., 2017. Optimizing attraction flow for upstream fish passage at a hydropower dam employing 3d detached-eddy simulation. *Ecol. Eng.* **100**, 344–353. <https://doi.org/10.1016/j.ecoleng.2016.10.065>.

Gorb, S., Gorb, E., Vignolini, S., Steiner, L., Onelli, O., 2017. Functional Surfaces in Biology III-Diversity of the Physical Phenomena. Springer. <https://doi.org/10.1007/978-3-319-74144-4>.

Greenshields, C.J., 2021. OpenFOAM user guide: Document version 9. OpenFOAM Foundation Ltd. URL: <http://foam.sourceforge.net/docs/Guides-a4/OpenFOAMUserGuide-A4.pdf>.

Heddeson, C.F., Brown, D.L., Cliffe, R.T., 1957. Summary of Drag Coefficients of Various Shaped Cylinders. General Electric Company, p. 56. <https://doi.org/10.21239/ADA388540>.

Herzog, H., Klein, B., Ziegler, A., 2017. Form and function of the teleost lateral line revealed using three-dimensional imaging and computational fluid dynamics. *J. R. Soc. Interface* **14**, 20160898. <https://doi.org/10.1098/rsif.2016.0898>.

Jasak, H., Uroić, T., 2020. Practical Computational Fluid Dynamics with the Finite Volume Method-Modeling in Engineering Using Innovative Numerical Methods for Solids and Fluids. Springer, pp. 103–161. https://doi.org/10.1007/978-3-030-37518-8_4.

Jones, W., Launder, B., 1972. The prediction of laminarization with a two-equation model of turbulence. *Int. J. Heat Mass Transf.* **15**, 301–314. [https://doi.org/10.1016/0017-9310\(72\)90076-2](https://doi.org/10.1016/0017-9310(72)90076-2).

Juretić, F., 2015. cfMesh User Guide: Document version 1.1. Creative Fields, Ltd. URL: http://cfmesh.com/wp-content/uploads/2015/09/User_Guide-cfMesh_v1.1.pdf.

Kogan, I., Pacholak, S., Licht, M., Schneider, J.W., Brücker, C., Brandt, S., 2015. The invisible fish: hydrodynamic constraints for predator-prey interaction in fossil fish saurichthys compared to recent actinopterygians. *Biol. Open* **4**, 1715–1726.

Kottapalli, A.G.P., Asadnia, M., Miao, J., Triantafyllou, M., 2014. Touch at a distance sensing: lateral-line inspired MEMS flow sensors. *Bioinspiration Biomimetics* **9**, 046011. <https://doi.org/10.1088/1748-3182/9/4/046011>.

Lauder, B.E., Sharma, B.I., 1974. Application of the energy-dissipation model of turbulence to the calculation of flow near a spinning disc. *Lett. Heat Mass Transf.* **1**, 131–137. [https://doi.org/10.1016/0094-4548\(74\)90150-7](https://doi.org/10.1016/0094-4548(74)90150-7).

Li, X., Zhang, L., Zheng, Y., Yang, D., Wu, F., Tian, Y., Han, F., Gao, B., Li, H., Zhang, Y., Ge, Y., Cheng, G., Fu, B., Xia, J., Song, C., Zheng, C., 2021. Novel hybrid coupling of ecophysiology and socioeconomy at river basin scale: a watershed system model for the Heihe river basin. *Environ. Model. Softw.* **141**, 105058 <https://doi.org/10.1016/j.envsoft.2021.105058>.

Liu, G., Wang, M., Xu, L., Inceciik, A., Sotelo, M.A., Li, Z., Li, W., 2020. A new bionic lateral line system applied to pitch motion parameters perception for autonomous underwater vehicles. *Appl. Ocean Res.* **99**, 102142 <https://doi.org/10.1016/j.apor.2020.102142>.

Lucas, K.N., Lauder, G.V., Tytell, E.D., 2020. Airfoil-like mechanics generate thrust on the anterior body of swimming fishes. *Proc. Natl. Acad. Sci.* **117**, 10585–10592. <https://doi.org/10.1073/pnas.1919055117>.

Macia, M.M., Souza, F., Junior, A.C.B., Oliveira, T.F., 2020. Three-dimensional viscous wake flow in fish swimming - a CFD study. *Mech. Res. Commun.* <https://doi.org/10.1016/j.mechrescom.2020.103547>.

Menter, F.R., 1993. Zonal two equation $k-\omega$ turbulence models for aerodynamic flow. In: AIAA 24th Fluid Dynamics Conference. <https://doi.org/10.2514/6.1993-2906>.

Menter, F.R., 1994. Two-equation eddy-viscosity turbulence models for engineering applications. *AIAA J.* **32**, 1598–1605. <https://doi.org/10.2514/3.12149>.

Mogdans, J., 2019. Sensory ecology of the fish lateral-line system: morphological and physiological adaptations for the perception of hydrodynamic stimuli. *J. Fish Biol.* **95**, 53–72. <https://doi.org/10.1111/jfb.13966>.

Monegaglia, F., Zolezzi, G., Güneralp, I., Henshaw, A.J., Tubino, M., 2018. Automated extraction of meandering river morphodynamics from multitemporal remotely sensed data. *Environ. Model. Softw.* **105**, 171–186. <https://doi.org/10.1016/j.envsoft.2018.03.028>.

Oteiza, P., Odrisil, I., Lauder, G., Portugues, R., Engert, F., 2017. A novel mechanism for mechanosensory-based rheotaxis in larval zebrafish. *Nature* **547**, 445–448. <https://doi.org/10.1038/nature23014>.

Owsianowski, N., Kesel, A., 2008. Drag reduction in schooling fish? — a CFD approach. *Comp. Biochem. Physiol. A Mol. Integr. Physiol.* **150** (3) <https://doi.org/10.1016/j.cbpa.2008.04.148>. Elsevier.

- Rapo, M.A., Jiang, H., Grosenbaugh, M.A., Coombs, S., 2009. Using computational fluid dynamics to calculate the stimulus to the lateral line of a fish in still water. *J. Exp. Biol.* 212, 1494–1505. <https://doi.org/10.1242/jeb.026732>.
- Reid, A.J., Carlson, A.K., Creed, I.F., Eliason, E.J., Gell, P.A., Johnson, P.T.J., Kidd, K.A., McCormack, T.J., Olden, J.D., Ormerod, S.J., Smol, J.P., Taylor, W.W., Tockner, K., Vermaire, J.C., Dudgeon, D., Cooke, S.J., 2019. Emerging threats and persistent conservation challenges for freshwater biodiversity. *Biol. Rev.* 94, 849–873. <https://doi.org/10.1111/brv.12480>.
- Ristrop, L., Liao, J.C., Zhang, J., 2012. Lateral line layout correlates with the differential hydrodynamic pressure on swimming fish. *Phys. Rev. Lett.* 114, 0181021–0181025. <https://doi.org/10.1103/PhysRevLett.114.018102>.
- Roache, P.J., 1994. Perspective: a method for uniform reporting of grid refinement studies. *J. Fluids Eng.* 116, 405–413. <https://doi.org/10.1115/1.2910291>.
- Schmitt, F.G., 2007. About boussinesq's turbulent viscosity hypothesis: historical remarks and a direct evaluation of its validity. *Comptes Rendus Mécanique* 335, 617–627. <https://doi.org/10.1016/j.crme.2007.08.004>.
- Schütz, C., Henning, M., Czerny, R., Herbst, M., Pitsch, M., 2021. Addition of auxiliary discharge into a fishway – a contribution to fishway design at barrages of large rivers. *Ecol. Eng.* 167, 106257. <https://doi.org/10.1016/j.ecoleng.2021.106257>.
- Smialek, N., Pander, J., Mueller, M., van Treeck, R., Wolter, C., Geist, J., 2019. Do we know enough to save European riverine fish?—a systematic review on autecological requirements during critical life stages of 10 rheophilic species at risk. *Sustainability* 11. <https://doi.org/10.3390/su11185011>.
- Spalart, P., Allmaras, S., 1994. A one equation turbulence model for aerodynamic flows. *La Recherche Aérospatiale* 1, 5–21. <https://doi.org/10.2514/6.1992-439>.
- Spalart, P.R., Rumsey, C.L., 2007. Effective inflow conditions for turbulence models in aerodynamic calculations. *AIAA J.* 45, 2544–2553. <https://doi.org/10.2514/1.29373>.
- Surek, D., Stempin, S., 2017. *Technische Strömungsmechanik*. Springer Fachmedien Wiesbaden. <https://doi.org/10.1007/978-3-658-18757-6>.
- Tickner, D., Opperman, J.J., Abell, R., Acreman, M., Arthington, A.H., Bunn, S.E., Cooke, S.J., Dalton, J., Darwall, W., Edwards, G., Harrison, I., Hughes, K., Jones, T., Leclère, D., Lynch, A.J., Leonard, P., McClain, M.E., Muruvu, D., Olden, J.D., Ormerod, S.J., Robinson, J., Tharme, R.E., Thieme, M., Tockner, K., Wright, M., Young, L., 2020. Bending the curve of global freshwater biodiversity loss: an emergency recovery plan. *BioScience* 70, 330–342. <https://doi.org/10.1093/biosci/biaa002>.
- Tuhtan, J.A., Fuentes-Pérez, J.F., Strokina, N., Toming, G., Musall, M., Noack, M., Kämäräinen, J.K., Kruusmaa, M., 2016. Design and application of a fish-shaped lateral line probe for flow measurement. *Rev. Sci. Instrum.* 87, 045110. <https://doi.org/10.1063/1.4946765>.
- van Netten, S.M., McHenry, M.J., 2014. *The Biophysics of the Fish Lateral Line*. Springer, New York, New York, NY, pp. 99–119. https://doi.org/10.1007/2506_2013_14.
- Vanzo, D., Peter, S., Vonwiller, L., Bürgler, M., Weberndorfer, M., Siviglia, A., Conde, D., Vetsch, D.F., 2021. Basement v3: a modular freeware for river process modelling over multiple computational backends. *Environ. Model. Softw.* 143, 105102. <https://doi.org/10.1016/j.envsoft.2021.105102>.
- Wilcox, D.C., 1988. Reassessment of the scale-determining equation for advanced turbulence models. *AIAA J.* 26, 1299–1310. <https://doi.org/10.2514/3.10041>.
- Windsor, S.P., Norris, S.E., Cameron, S.M., Mallinson, G.D., Montgomery, J.C., 2010. The flow fields involved in hydrodynamic imaging by blind mexican cave fish (*Astyanax fasciatus*). Part i: open water and heading towards a wall. *J. Exp. Biol.* 213, 3819–3831. <https://doi.org/10.1242/jeb.040741>.
- Yakhot, V., Orszag, S.A., 1992. Development of turbulence models for shear flows by a double expansion technique. *Phys. Fluids A: Fluid Dynam.* 4, 1510. <https://doi.org/10.1063/1.858424>.
- Yanase, K., Saarenrinne, P., 2016. Boundary layer control by a fish: unsteady laminar boundary layers of rainbow trout swimming in turbulent flows. *Biol. Open* 5, 1853–1863. <https://doi.org/10.1242/bio.020008>.

Appendix 2

II

K. Bensing, J. A. Tuhtan, G. Toming, A. H. Khan, and B. Lehmann, "Fish body geometry reduces the upstream velocity profile in subcritical flowing waters," *Aquatic Sciences*, vol. 84, no. 3, p. 32, 2022



Fish body geometry reduces the upstream velocity profile in subcritical flowing waters

Katharina Bensing¹ · Jeffrey A. Tuhtan² · Gert Toming² · Ali Hassan Khan² · Boris Lehmann¹

Received: 22 November 2021 / Accepted: 24 March 2022
© The Author(s) 2022

Abstract

Fish body geometry is highly variable across species, affecting the fluid-body interactions fish rely on for habitat choice, feeding, predator avoidance and spawning. We hypothesize that fish body geometry may substantially influence the velocity experienced by fish swimming. To test this hypothesis, we built nine full-scale physical prototypes of common freshwater fish species. The prototypes were placed in a large laboratory flume and upstream time-averaged velocity profiles were measured with increasing distance from the anterior-most location of each body. The measurements revealed that the body geometry can have a significant influence on the velocity profile, reducing the flow field at a distance of one body length upstream of the fish. Furthermore, it was found that the upstream velocity profiles from the nine fish species investigated in this study can be normalized to a single fit curve based on the freestream velocity and fish body length under subcritical flow conditions. These findings are significant, because they show that conventional point velocity measurements overlook the reducing effect of the fish body on the upstream flow field, creating a systematically biased representation of the velocity experienced by fish in subcritical flowing waters. This bias is illustrated by velocity field maps created with and without the presence of the physical models for three different fish species. Finally, we provide an example of how point velocity measurements can be recalculated to provide upstream velocity field maps closer to “the fish’s perspective”.

Keywords Ethohydraulics · Fish habitat · Fish body morphology · Flow velocity · Spatial scales

Introduction

Successful ecosystem management requires effective analytical approaches based on physical descriptors to estimate the spatial–temporal distributions of fish and their habitats (Brownscombe et al. 2021). A key physical descriptor in lotic habitats is the flow velocity (García-Vega et al. 2021), which facilitates drift feeding (O’Brien and Showalter 1993) and gravel spawning (Kondolf et al. 2008) and is also the main parameter used to study and classify fish swimming performance (Katopodis and Gervais 2016).

Historically, fish habitats are surveyed by in situ sampling of the fish’s location and surrounding physical environment

(Nestler et al. 2019). The parameters most frequently used to describe the physical environment are the average water depth, time-averaged velocity, substrate composition, vegetation and cover (Wheaton et al. 2010). These data are often recorded as point values, where it has been pointed out that the scale dependency of physical habitat parameters remain largely unexplored (Crook et al. 2001). Additionally important to the study of fish habitats is improving the understanding of their variability across space, identifying the physical conditions causing this variation, and determining the extent to which these conditions are scale dependent or may be considered as independent (Gido et al. 2006).

Locally, fish microhabitat conditions are dynamically driven by the river flow regime, and can be used to explain and predict fish community attributes in unregulated and regulated rivers (Senay et al. 2017). These community attributes are needed to better reflect the size-dependent needs of the distribution of fish species life stages across multiple spatial scales (Santos et al. 2011). In addition to the fish size, recent studies have begun to explore more complex relationships between fish body geometry (morphometrics) on attempt rate

✉ Katharina Bensing
k.bensing@wb.tu-darmstadt.de

¹ Chair for Hydraulic Engineering, Department of Civil and Environmental Engineering, Technical University of Darmstadt, Darmstadt, Germany

² Department of Computer Systems, Tallinn University of Technology, Tallinn, Estonia

and passage success through culverts (Goerig et al. 2020), including the development and application of automated image analysis software (Navarro et al. 2016). These studies are some of the first to explore how fish body geometry relates to conventional assessments of the critical swimming speed of fish outside of laboratory settings, and are important, because the swimming speed is a widely used metric to classify fish swimming performance (Cano-Barbacid et al. 2020). To classify swimming performance, tests are carried out in swim tunnel respirometers based on the highest velocity at which fish can maintain speed for predetermined time intervals over which the velocity is incrementally increased until fatigue is observed (Webb 1971). In contrast to habitat models, which use the velocity's physical units (m/s), the swimming speeds are often considered scaled to the fish's body length (L_{fish}/s). This is an important distinction, as it directly includes the size of the organism as the characteristic length scale. The use of the body length thus provides a normalized velocity to investigate fish swimming capabilities as a function of their body geometry.

Advancing our ability to understand the relevance of measured physical flow parameters in lotic ecosystems and their relations to fish body geometry has valuable implications for environmental research and management. By improving our knowledge of the underlying physics of fish and flow interactions, we expect advances across multiple domains, including improving the cross-study transferability of fish habitat, swimming, behavioural and energetics research findings, all of which play significant roles in improving fish species distribution predictions.

Freshwater fish species exhibit a broad range of morphological traits (Brosse et al. 2021) and experience a wide range of velocities in ambient flows. Previous works have shown that fish use their lateral line system to sense near-body changes in the velocity field (Bleckmann 1994) and correspondingly, the major findings of the presented work highlight the need to consider that fish body geometry may impact the velocity upstream of a fish. The magnitude of the distortion a fish's body causes on the flow field is not commonly included in either laboratory or field assessments, and is also highly likely to influence the fish's flow sensing ability. To address this, we recommend the use of a body length-dependent velocity correction. Once applied, the corrected measurements can provide a standardized reference velocity for the further investigation and cross-comparison of the upstream flow conditions experienced by fish swimming freely in lotic systems.

Materials and methods

Laboratory flume and hydraulic setups

All measurements in this study were conducted in a large glass-walled laboratory flume at the Technical University of Darmstadt, Germany. The flume has a constant width of 2 m, a wall height of 1.2 m and a total length of 40 m, as shown in Fig. 1. The flume bottom has zero slope, where both the upstream and downstream ends are at the same vertical elevation, and is supplied with water by two elevated tanks and one additional pump, with a maximum flow rate of $1 \text{ m}^3/\text{s}$. The flume water supply was equipped with electromagnetic flow meters (PROMAG 33F, Endress + Hauser Group Services AG, Switzerland; 10 D 1425 A; Fischer & Porter, Germany) which continuously displayed the discharge during experimentation. The water level in the flume was adjusted and maintained throughout the experiments by manually operating a sluice gate at the end of the flume. Three different hydraulic setups (H1, H2, H3—Table 1) were chosen for the experiments. The velocities were set by adjusting the discharge while maintaining a fixed water depth ranging from 0.7 to 0.75 m. The highest velocity in the flume was 0.63 m/s, measured at the centroid of the cross-section 14.5 m downstream of the inlet. We chose velocities at which fish show clear rheotactic alignment with the flow, and therefore the minimum velocity was set to be above 0.3 m/s and the middle velocity was set to 0.48 m/s.

Fish-shaped bodies

To evaluate the impact of fish body geometry on the upstream velocity profile, nine different fish body shapes (FS), of eight common freshwater fish species were manufactured (Table 2, Fig. 1). Each fish body was designed using the computer aided drafting software SolidWorks 2019 (Dassault Systems, France) and the model of each fish was based on the 3D models of fish donated by Dosch Design Kommunikationsagentur GmbH (Marktheidenfeld, Germany) from imagery collected of live fish, and modified to fit the morphometric ratios presented in Schwevers and Adam (2019). For all physical prototypes, the anterior 1/3 of the bodies were kept rigid for mounting purposes, while the remaining posterior 2/3 was made from cast flexible silicon with a Shore hardness of 8. The rigid parts were

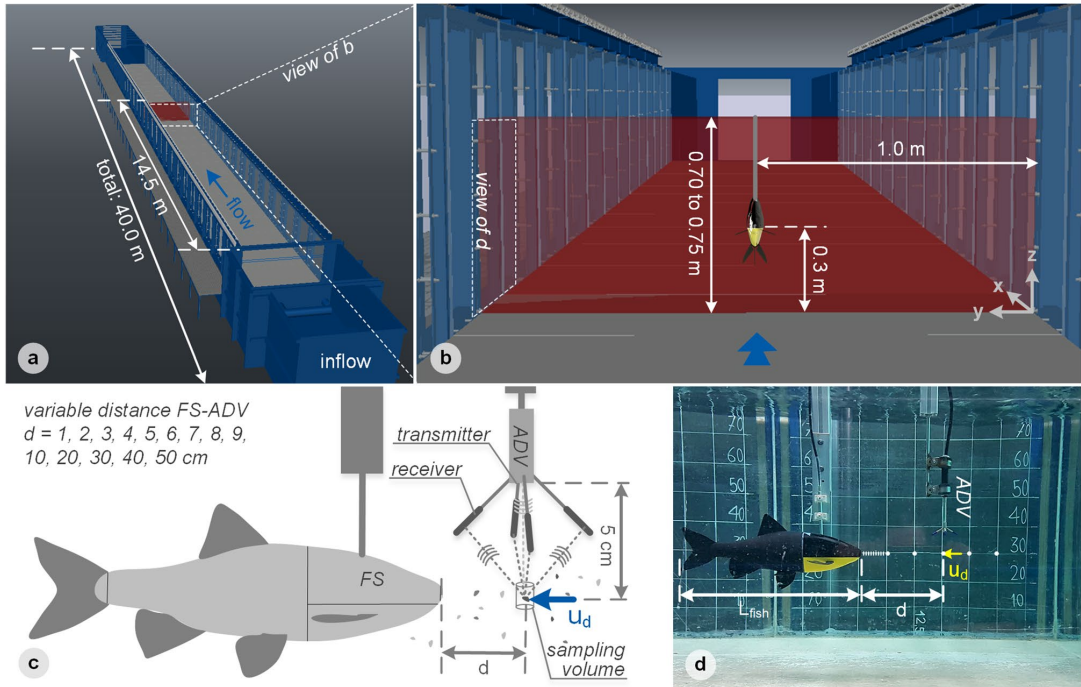


Fig. 1 Laboratory flume and measurement setup used in this study: **a** location of the flume sampling area (red); **b** position and orientation of the fish-shaped physical model (FS) in the flume cross-section; **c** measuring principle of the ADV in front of the fish’s nose: ultrasonic waves are transmitted, reflected at in the flow transported particles









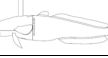









in a small sampling volume and received again by the ADV. Due to the Doppler phase shift between two signals, the water velocity can be estimated; **d** measurement setup using a chub-shaped body in the hydraulic flume

Table 1 Overview of the hydraulic conditions during the laboratory flume experiments

Hydraulic setup no.	Water supply	Flow rate [m ³ /s] Mean (min–max)	Water depth [m] Mean (min–max)	Mean freestream velocity at investigated location [m/s] Mean (\pm stdev, min–max)	Reynolds/Froude number of freestream [-]
H1	Gallery tank	0.490 (0.485–0.495)	0.7 (0.68–0.72)	0.35 (\pm 0.041, 0.19–0.49)	575,538/0.13
H2	Gallery tank	0.700 (0.693–0.707)	0.75 (0.73–0.77)	0.48 (\pm 0.060, 0.26–0.69)	814,096/0.17
	Roof tank	0.070 (0.069–0.071)			
H3	Gallery tank	0.700 (0.693–0.707)	0.72 (0.69–0.75)	0.63 (\pm 0.065, 0.41–0.87)	1,055,072/0.24
	Roof tank	0.087 (0.086–0.088)			
	Additional pump	0.173 (0.172–0.174)			

Where applicable, values are reported as the time-average \pm standard deviation as well as the range of values (minimum–maximum). Similar to a natural flow environment, the hydraulic conditions in the large laboratory flume varied over time and space due to local turbulence and discharge fluctuations in the water supply pipes caused by the pumps. The investigated location of the mean freestream velocity was in the centroid of a cross-section 14.5 m downstream of the inlet

Table 2 Species and main geometric properties of the nine fish-shaped bodies (FS) used in this work

Sample name - ID	Species	Side view	Front view	Body length [cm]	Body height [cm]	Body width [cm]
FS1	Gudgeon <i>Gobio gobio</i>			15	2.70	1.95
FS2	Perch <i>Perca fluviatilis</i>			20	5.80	3.20
FS3	Roach <i>Rutilus rutilus</i>			20	6.00	2.80
FS4	Nase <i>Chondrostoma nasus</i>			25	5.50	3.00
FS5	Burbot <i>Lota lota</i>			25	4.25	4.25
FS6	Chub <i>Squalius cephalus</i>			25	6.00	3.75
FS7	Barbel <i>Barbus barbus</i>			30	5.70	3.60
FS8	Bream <i>Abramus brama</i>			30	10.20	3.00
FS9	Chub <i>Squalius cephalus</i>			40	9.60	6.00

The model for FS6 and FS9 are identical, the only difference being that they are scaled to represent Chub with different total body lengths

3D printed, using the Form 3 commercial stereolithography printer (Formlabs Inc, USA) using the Formlabs Durable resin. The posterior (tail) portions of the bodies, molds were 3D printed using the same technique and material. The bodies, including fins were cast using a non-toxic duplication silicone Elite Double 8 (Zhermack SpA, Italy).

Acoustic Doppler velocimetry

All velocity measurements in this study were performed using a commercial Acoustic Doppler Velocimeter (ADV, Vectrino Standard, Nortek AS, Norway) which was mounted in the flume directly upstream of the fish-shaped body and was configured to record with a sampling rate of 25 Hz (Fig. 1c, d). The transmitter at the ADV centre emits two ultrasonic pulses with a known time offset. The pulses are reflected from particles in a small, cylindrical sampling volume at a distance of 5 cm below the transmitter, and are received at four small bar-shaped receivers. The

configuration of the device is depending on the quantity of transported particles, the flow velocity and the positioning of the probe in relation to solid boundaries and had been adjusted individually depending on the quality parameters correlation and SNR (signal to noise ratio). The final ADV velocity data consisted of the three Cartesian velocity vector components (u , v , w).

Laboratory open channel flume tests

The full study consists of three tests that build on one another, in which the ADV probe head was placed at a distance, d upstream of each FS. This allowed for the point-wise comparison between the undistorted freestream velocity, u_{∞} and the distorted velocity, u_d at different distances, d upstream of the fish-shaped body.

Test (1): pre-analyses

A pilot study using all three hydraulic setups H1, H2, H3 (Table 1) was first undertaken to determine the measurement protocol for the detailed experiments carried out in Test 2. It, therefore, did not require the use of all probes, but rather a subset of them (FS1, FS4 and FS9) which were representative of the range of physical scales (small, medium, large) and fish swimming types included in this study. The results of Test 1 were used to determine the time duration required for stationary statistical analysis and the distances at which the ADV should be mounted upstream of the fish shapes anterior-most point for all measurement. This was done by recording velocities upstream of each of the three fish-shaped bodies, and determining the sampling duration required to provide a stable mean value and standard deviation. The protocol established for ADV measurements upstream of fish-shaped bodies is as follows: at each measurement point of the upstream velocity profile, five minutes of ADV measurements at 25 Hz were recorded. It was determined that a minimum duration of 1.5 min was required, as this resulted in a constant time-averaged mean and constant standard deviation. These durations were checked against the literature, and were found to be similar to previous investigations of ADV sampling rates and durations in laboratory flumes (Springer et al. 1999; Díaz Lozada et al. 2021). Furthermore, it was found that a value of 1 cm was the minimum distance between the fish shape and the ADV without creating signal reflections from the body surface. The upper distance limit of 50 cm was defined as it was the maximum distance at which clearly no distortion in the upstream flow profile was detected using the largest fish-shaped body (FS9). The distance increments from 1 to 10 cm from the body were made in 1 cm steps to capture the rapid decrease of the upstream flow velocity approaching the anterior-most point.

Test (2): velocity profiles upstream of fish-shaped bodies

Based on Test 1, a cross-section 14.5 m downstream of the inlet was chosen for Test 2 as the sampling location as it corresponded to the most stable region of steady, uniform flow (Fig. 1a, b). The ADV and fish-shaped bodies were mounted on a robotic gantry, controlled by an electric motor to user-defined coordinates. The position was chosen as the middle of the cross-section to minimize the influence of the walls, ensuring a symmetric flow around the bodies (Fig. 1b–d). The distance between the nose (anterior-most point) of the fish-shaped body and the measurement volume of the ADV ranged between one and fifty centimetres as established in Test 1 (Fig. 1).

This second series of measurements were conducted for all nine fish-shaped bodies, using hydraulic setup H2 (Table 1) and following the protocol established in Test 1 using 5-min ADV measurement durations at 25 Hz and recording distorted velocity in several distances upstream of the fish. Here, we opted to maintain the 5-min duration measurements for future research use to compare turbulence levels upstream of the fish body. To assess the potential effects of alternative freestream velocities on the flow distortion, the results of Test 1 using FS1, FS4 and FS9 in other hydraulic conditions with higher and lower velocities (H1 and H3) were added for the full experiment. These data of Test 1 and 2 were evaluated as upstream velocity profiles and used to generate a fit curve which can be used to correct the distortion of the upstream velocity caused by the presence of the body (“Data post-processing”, Fig. 4, Eq. 1).

Test (3): planar velocity field measurements

Test 3 was intended as a proof-of-concept application of the flow distortion function, which was established in Test 2. We tested the efficacy of the correction using three common European fish species (FS1, FS3 and FS9), again choosing

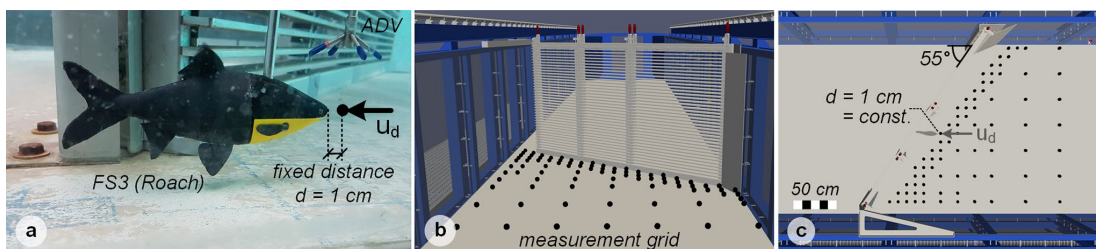


Fig. 2 Laboratory flume setup used for the planar velocity field measurements: **a** FS3 and ADV in front of the 1:1 scale fish protection rack with horizontal bars and a vertical slot bypass opening extending from the flume bottom to the water surface, facing into the flow direction; **b** 3D model of the bar rack showing ADV grid measurement

points ($n=79$) as black dots 6 cm above the flume bottom; **c** top view of the planar grid measurements for FS3. Each dot represents a position of the ADV sampling volume during measurement at a fixed distance 1 cm upstream from the anterior-most point of the fish-shaped body. The mean velocity was 0.48 m/s (hydraulic setup H2)

them to span the range of length scales, and obtained ADV measurements of 1.5-min duration at 25 Hz using hydraulic setup H2. To choose a more complex flow environment, a series of four planar velocity measurements (ADV-only, and ADV with the bodies FS1, FS3 and FS9) was conducted upstream of a 1:1 scale horizontal fish protection rack, where the velocities due to the structure of the rack and for selecting hydraulic setup H2 varied in a similar range to that covered by the tested velocities in Test 2. Subsequently, this allowed a limited application of the established correction equation to these field measurements. The rack was angled at 55° to the main streamwise flow direction, and included a vertical bypass slot extending from the flume bottom to the water surface, as illustrated in Fig. 2. This hydraulic model setup was chosen as it represents a controlled environment physically similar to those wild fish encounter during downstream passage around hydropower plants. Goulet et al. (2008) highlight that “only the near flow field can communicate outside information to the lateral line”. We were interested in investigating how the presence of the three different fish-shaped bodies changes the corresponding flow velocity maps. During the experiments with the three fish-shaped bodies FS1, FS3 and FS9, the ADV point measurements were made at a fixed upstream distance of 1 cm from the anterior-most point of each body, which was determined in Test 1 to be the closest point. The number of point measurements obtained for each of the planar velocity field measurements differed for each body due to their minimal possible distance to the rack: FS1 ($n = 85$), FS3 ($n = 79$) and for FS9 ($n = 55$). The measurement locations for FS3 are shown in Fig. 2b–c, and for FS1 and FS9 in the appendix (Figs. 9a, 10a). A second set of 85 ADV-only point measurements was taken under the same flow setup, but without the presence of a fish-shaped body, which were used as the control data set (undistorted velocity field). It was observed in previous experiments in the same flume with fish at an angled rack that fish often move close to the bottom. Therefore, we chose our measurement volume at 6 cm above the bottom of the flume (Fig. 2a). As in Test 2, the velocity measurements were time-averaged for every point to create maps of (a) the spatial distribution of the undistorted velocity field without the presence of the fish-shaped body, and (b) the potentially distorted velocity field 1.0 cm upstream of the fish-shaped body (Figs. 5, 9, 10). These maps are commonly used in laboratory and field studies to evaluate habitat and bioenergetics models of freshwater fish in lotic ecosystems. Here, again, it is important to clarify that Test 3 was carried out to verify the practical application of the flow distortion function established from Test 2.

Data post-processing

All ADV velocity data were post-processed to remove spikes using the software WinADV (Wahl 2004) applying the phase-space threshold despiking method of Goring and Nikora (2002), modified by Wahl (2003), and the time-series were edited using Python (Version 3.7.11) to provide the time-averaged, streamwise velocity as well as the standard deviation at each single measurement point. Subsequently, curve fitting was applied for the data of Test 1 and 2 to obtain functions that describe the course of the point data the best as (a) a function of distorted velocity, u_d over distance, d (Figs. 3b, 6, 7, and 8), and (b) a normalised function of distorted velocity, u_d to freestream velocity, u_∞ over distance, d to fish body length, L_{fish} (Fig. 4).

Fit curve performance was evaluated using non-linear least squares, and a hyperbolic function was found as the best fit using the SciPy library (`scipy.optimize.curve_fit`). To examine further relations between fish geometry and the distortion of the upstream velocity field, the body geometries were classified as either belonging to fish which typically inhabit the “freestream” or are “bottom oriented”, and according to the swim types of “weak”, “intermediate” or “strong”. The cross sections for each body were estimated as the product of the width and height and plotted over the fish length, as shown in Fig. 3a.

The mean velocity data of Test 3 were compiled with the corresponding Cartesian coordinates of the flume system to map the field data two-dimensionally for all four measurement series (ADV-only, ADV-FS1, ADV-FS3, ADV-FS9) using the ParaView (Version 5.7.0) software. Additionally, the general distortion function presented in the result “Effect of fish body type on the upstream velocity profile” was applied to the ADV-only measurements to model the effect of different fish shape on the flow field. The results were subsequently used to contrast modelled and measured ADV-FS maps and therefore validate the gained function (“Application of flow distortion function”).

Results

Effect of fish body type on the upstream velocity profile

The results of both the upstream velocity profiles and planar velocity measurements upstream of the fish protection rack support the main hypothesis of this work, that a fish-shaped body can distort the upstream velocity field. This finding is illustrated by a visual comparison of the different upstream velocity profiles in Fig. 3b and the planar velocity field maps with and without a fish-shaped body in Fig. 5a, b. The upstream velocity profiles, including the measurement

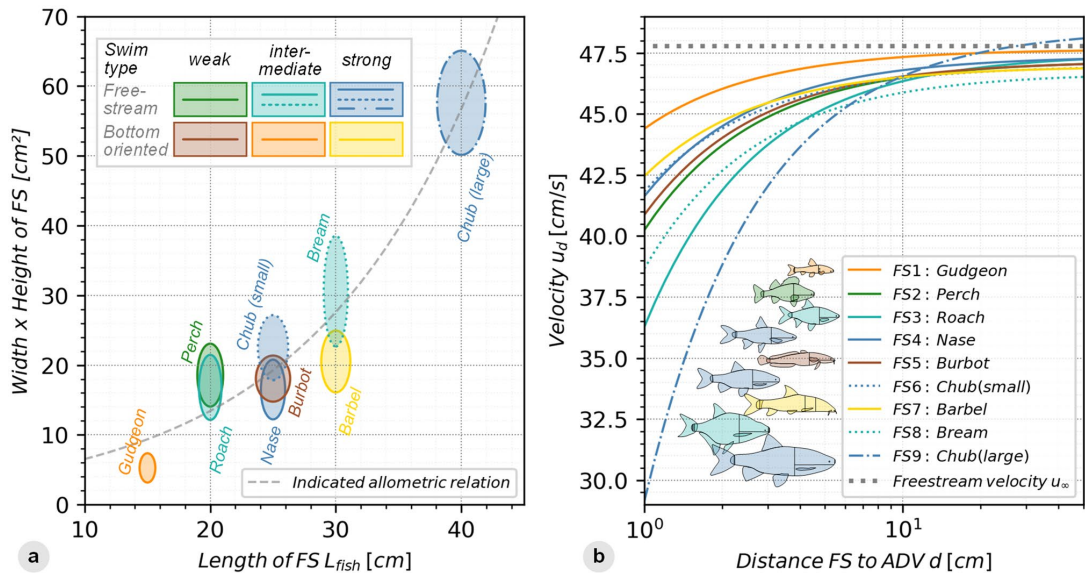


Fig. 3 Distortion of the upstream velocity profile by fish-shaped bodies: **a** comparison of the area to total body length relationship, the scaled ellipses correspond to the maximal body dimension (width and height), colored for each fish-shaped body by hydraulic preference and swim type. The dashed grey line indicates the allometric relation

between the different fish species; **b** measured flow velocity profiles upstream of the fish-shaped bodies, shown with a logarithmic scaling of the horizontal axis. The velocity u_d is the streamwise velocity at each measurement point along the profile, and d is the streamwise distance from the most anterior point of the fish

uncertainty expressed as the standard deviation for each fish-shaped body are provided in the appendix (Figs. 6, 7, 8).

The cross-section areas of the different fish species reflect interspecific similarities, or allometric relations, which are dependent on the fish total body length (Fig. 3a). This characterization follows a trend, where increasing body length corresponds to larger cross-section areas. Due to this relation, we chose the total length of the fish-shaped body as a geometric scaling factor for further investigations. The graph indicates that bottom-oriented fish species tend to lie under the indicated allometric curve, while freestream swimmers tend to lie above it. Considering the individual velocity profiles for each fish shape and its geometry, it was found that the highest flow distortion occurs for the longest body and the lowest distortion by the shortest body (Fig. 3b).

To compare the systematic reduction of the upstream velocity caused by the fish-shaped body, normalized functions of the streamwise velocity were fit for each hydraulic setup (Table 1). This resulted in a total of three fit curves (Fig. 4a–c) where it was observed that the individual curves were not found to differ substantially. Due to this similarity, the data from all three hydraulic setups were fit to a single hyperbolic curve. This resulted in a fit equation of the measured velocity, u_d , based on the freestream velocity, u_∞ , the distance from the anterior-most point

to the ADV measurement location, d , and the total body length of the fish-shaped body, L_{fish} (Fig. 4d):

$$\frac{u_d}{u_\infty} = 1 - \frac{L_{fish}}{158 \cdot d} \tag{1}$$

We stress here that the fit curve established in this work has been verified only for the tested ranges of velocities, from 0.35 to 0.63 m/s, for fish with total body lengths of 15–40 cm and the subcritical flow conditions present in the large open channel laboratory flume. It is worth noting that for small d/L_{fish} ratios, the uncertainty of the equation increases due to a smaller number of measurements. The above function is suitable for use at low Froude numbers (Fr) corresponding to subcritical flows where $Fr < 1$. This is because for critical or supercritical flows where $Fr \gg 1$, large flow distortions are not propagated upstream of a submerged body (Bureau of Reclamation 2001).

The reduction of the upstream velocity profile was observed for all fish-shaped bodies, reaching a value of around only 0.6% of the freestream velocity at one body length ($d/L_{fish} = 1$). This is considered as the distance of negligible effect, and is highlighted as the grey region in Fig. 4.

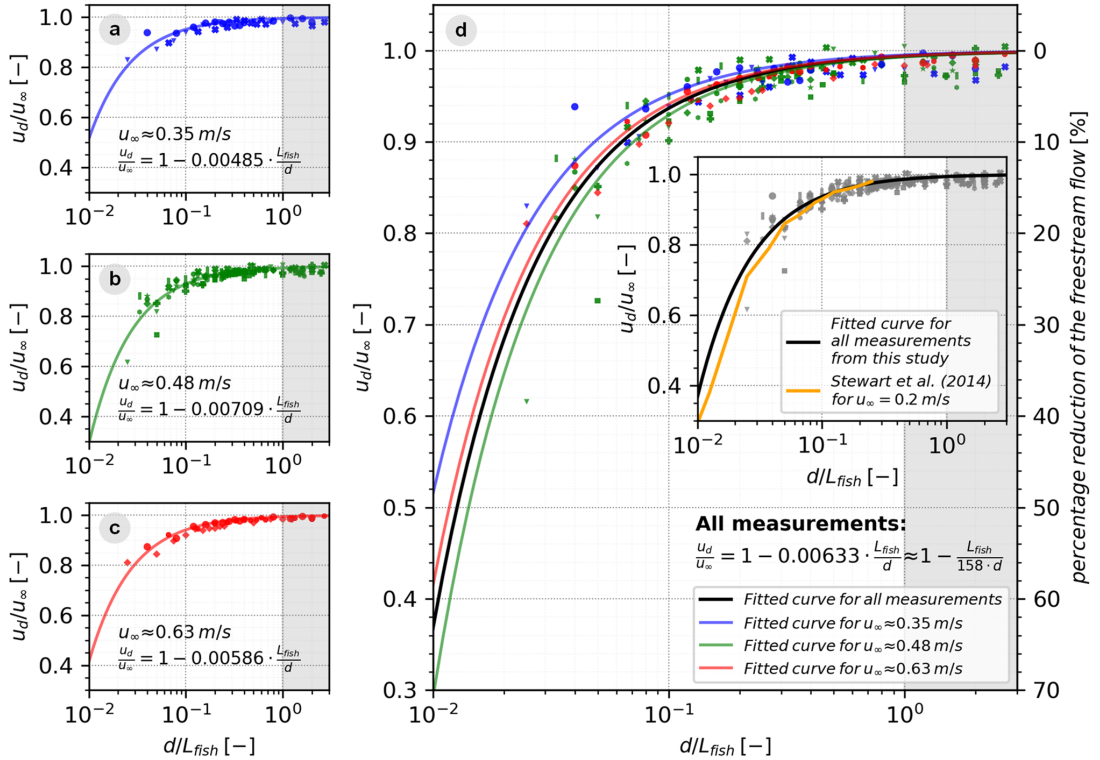


Fig. 4 Upstream velocity profile plots and fit curves for all setups and fish-shaped bodies. The normalized streamwise velocity u_d/u_∞ is plotted against the dimensionless length scale d/L using a logarithmic scaling of the horizontal axis. **a** The upstream profile for a freestream velocity, u_∞ of 0.35 m/s (FS 1, 4 and 9); **b** upstream profile for 0.48 m/s (all FS); **c** upstream profile for 0.63 m/s (FS 1, 4 and

9); **d** measurements from all experiments summarized as a single plot, the insert figure compares the results of this study with a replotting of the results found in Stewart et al. (2014). In the tests of Stewart et al. (2014), the fish was propelled (0.2 m/s shown) through still water. The right axis of **d** indicates the percentage reduction of the freestream flow velocity

Application of flow distortion function

Based on the results shown in “Effect of fish body type on the upstream velocity profile”, a clear workflow for velocity correction using Eq. (1) was established and applied in Test 3 using the planar ADV-only velocity measurements:

1. Evaluate the undistorted freestream velocity, u_∞ without the presence of a fish-shaped body by measurement or CFD;
2. Verify if the velocities are within the limits of applicability of the flow distortion function ($0.35 \text{ m/s} < u_\infty < 0.63 \text{ m/s}$);
3. Choosing the distance, d , and the length of the fish, L_{fish} , which are of interest for a certain investigation but within the here given limits ($15 \text{ cm} < L_{\text{fish}} < 40 \text{ cm}$) and determining the distortion (reduction) of the freestream velocity in Eq. (1);

4. Apply the flow distortion function (Eq. 1) to the undistorted flow field to create velocity maps for the distorted flow field, u_d , as experienced by the fish-shaped body.

This method was carried out in Test 3 for three different fish-shaped bodies (FS1: $L_{\text{fish}} = 15 \text{ cm}$, FS3: $L_{\text{fish}} = 20 \text{ cm}$, FS9: $L_{\text{fish}} = 40 \text{ cm}$) at a distance of 1 cm upstream of the fish, whereby based on step 3 the following fit equations were derived from Eq. (1):

$$\text{FS1 } (L_{\text{fish}} = 0.15 \text{ m}) : u_d = \left(1 - \frac{0.15[\text{m}]}{158 \cdot 0.01[\text{m}]} \right) u_\infty = 0.905 \cdot u_\infty \tag{2}$$

$$\text{FS3 } (L_{\text{fish}} = 0.20 \text{ m}) : u_d = \left(1 - \frac{0.20[\text{m}]}{158 \cdot 0.01[\text{m}]} \right) u_\infty = 0.873 \cdot u_\infty \tag{3}$$

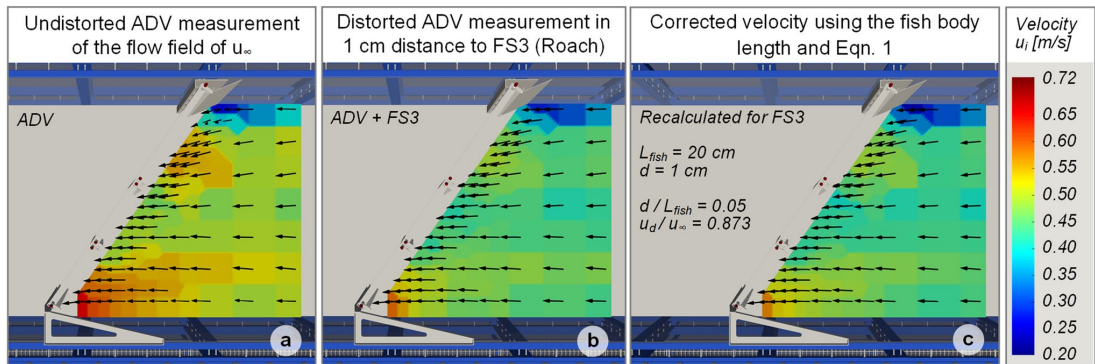


Fig. 5 Planar velocity fields of ADV-only, ADV-FSS and after correction: **a** measured planar velocity field for ADV-only; **b** measured planar velocity field in 1 cm distance to FS3; **c** velocity field map based on the flow distortion function. The orientation of the vectors

in the ADV-only flow field in **a** do not deviate strongly from those observed upstream of the fish-shaped bodies in **b**, indicating that the orientation of the flow field was not highly altered by the presence of the body

$$FS9(L_{\text{fish}} = 0.40 \text{ m}) : u_d = \left(1 - \frac{0.40[\text{m}]}{158 \cdot 0.01[\text{m}]}\right) u_{\infty} = 0.747 \cdot u_{\infty} \quad (4)$$

In the above equations, the ADV-only point measurements correspond to the values for u_{∞} . After applying the flow distortion function, the distorted velocities, u_d (Fig. 5c) were verified by comparing the values with direct measurements taken 1 cm upstream of the fish-shaped body (Fig. 5b). The results are shown for FS3 in Fig. 5, and additional figures are provided for FS1 and FS9 in the appendix (Figs. 9, 10). It should be noted that some of the freestream velocities are slightly above and below the tested range of $0.35 \text{ m/s} < u_{\infty} < 0.63 \text{ m/s}$ in this work.

A comparison between the different fish sizes also in general shows that larger fish experience a more pronounced reduction of the freestream velocity, and that the spatial extent of this reduction is also greater for larger bodies than for smaller bodies (Fig. 4, Eq. 1).

Discussion

The results of the measurements clearly showed that for all eight species investigated, a systematic reduction of the upstream velocity profile was observed. Although our work used distinct fish-shaped bodies, the general findings are in substantial agreement with those performed on hydrofoils, submerged cylinders or similar streamlined shapes (Deng et al. 2021; Lake 1971). The major advantage of the flow distortion function is that the undistorted flow field can be measured or even simulated using computational fluid dynamics (CFD) and the corresponding distorted velocity field may be easily estimated using the fish's body length.

Our work differs from previous fish related studies because they focus largely on the velocity, pressure and vorticity fields and their development downstream of the submerged bodies, few works have specifically investigated the upstream flow. We compared our findings with the results of Stewart et al. (2014), who analyzed the upstream flow field via PIV (Particle Image Velocimetry) and CFD (Computational Fluid Dynamics) and were found to be a good agreement with our work, as presented in Fig. 4d. Stewart et al. (2014) observed a reduction of the upstream velocity profile for a moving fish-shaped object towed through still water. The cause of the reduction in their study was attributed to the presence of a bow wake, similar to that found upstream of large vessels traveling at low speed. Thus, if a swimming fish is considered in a moving fluid, the relative velocity between the fish and the flow should be taken for further analysis. As discussed in Montgomery et al. (1997), fish may use the flow around their body to detect stationary objects which distort the self-produced field. Other previous works have proposed the detection length scale of fish's lateral line-sensing system (Coombs 1999) by using the total body length as the scaling factor. Our study supports these results by providing physical evidence that the extent of the active sensory space is strongly correlated with the fish total body length and the relative velocity between the fish and the flow. It should be noted that previous works have also found that the total body length can be a key factor for evaluating the swimming speed (Adam and Lehmann 2011; Nikora et al. 2003; Katopodis and Gervais 2016).

Despite the conclusive evidence provided in this investigation using replicated experiments under a range of flow conditions, we wish to point out that several limitations remain.

First, due to varying flow conditions for each measurement and slight positioning differences (sub-centimeter) of the measurement device in front of the fish shapes, the time-averaged upstream velocity profiles should be considered including standard measurement uncertainty, expressed as the standard deviation of the velocity of each point. Second, although this work covered both lotic and benthic freshwater species as physical models, the measurements were made only using static fish-shaped bodies, and thus do not cover the entire spectrum of freshwater fish body morphologies, and do not consider swimming kinematics. For example, we did not consider the yawing motion of the fish’s head during swimming, and therefore, the major findings of our work should be considered as physically analogous to the gliding phase of fish swimming. Third, we wish to point out that our experimental investigation was focused solely on determining the effect of the time-averaged upstream velocity profile with increasing distance from the anterior-most point. This choice was purposeful, as the time-averaged velocity is the most common flow measurement for studies of fish habitats, behaviour and swimming speed. Finally, it should be noted that the effects of the fish body shape on the upstream turbulence profile were not considered in this work. This particular topic has been investigated in the course of our investigation, and will be presented as a technical publication based on rapid distortion theory as a follow-up to this work.

The results of this study provide key insights needed to refine both lab and field flow velocity measurements investigating fish habitat usage, swimming speed and in situ observations of feeding and spawning activities.

Considering fish swimming, the observed reduction of the upstream velocity profile is significant because current field methods typically assume that the measured undisturbed velocity remains the same for all fish species and life stages. The experimental evidence gathered in this work shows that this assumption is largely unwarranted when considering the subcritical flows fish experience in nature.

Future works will use the same body shapes and computational fluid mechanics simulations of turbulent flows to explore the three-dimensional velocity fields around the different body geometries, covering a wider range of flow velocities, body orientations and the presence of obstacles. We have also begun conducting field investigations with ADV and fish-shaped bodies in rivers and nature-like fishways to compare the findings of the laboratory study with the types of highly turbulent flows fish encounter in nature.

The major finding of this work, that fish body geometry reduces the upstream velocity profile, may have wide-ranging implications for monitoring and improving fish passage designs. We hope that our work encourages the aquatic sciences community to critically consider flowing waters from “the fish’s perspective” in future laboratory and field investigations, and in the evaluation of previous works based on point measurements of the time-averaged velocity.

Appendix

See Figs. 6, 7, 8, 9 and 10.

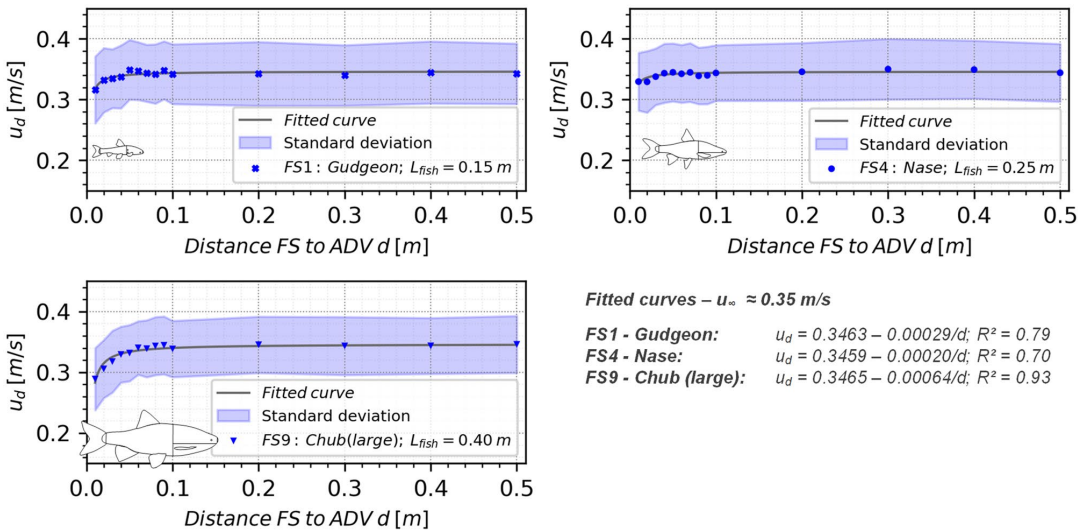


Fig. 6 Individual plots of the upstream velocity profile for each of the fish-shaped bodies with increasing distance from the anterior-most point, for hydraulic setup H1. The lower rightmost panel includes the results of the fit curves for each body

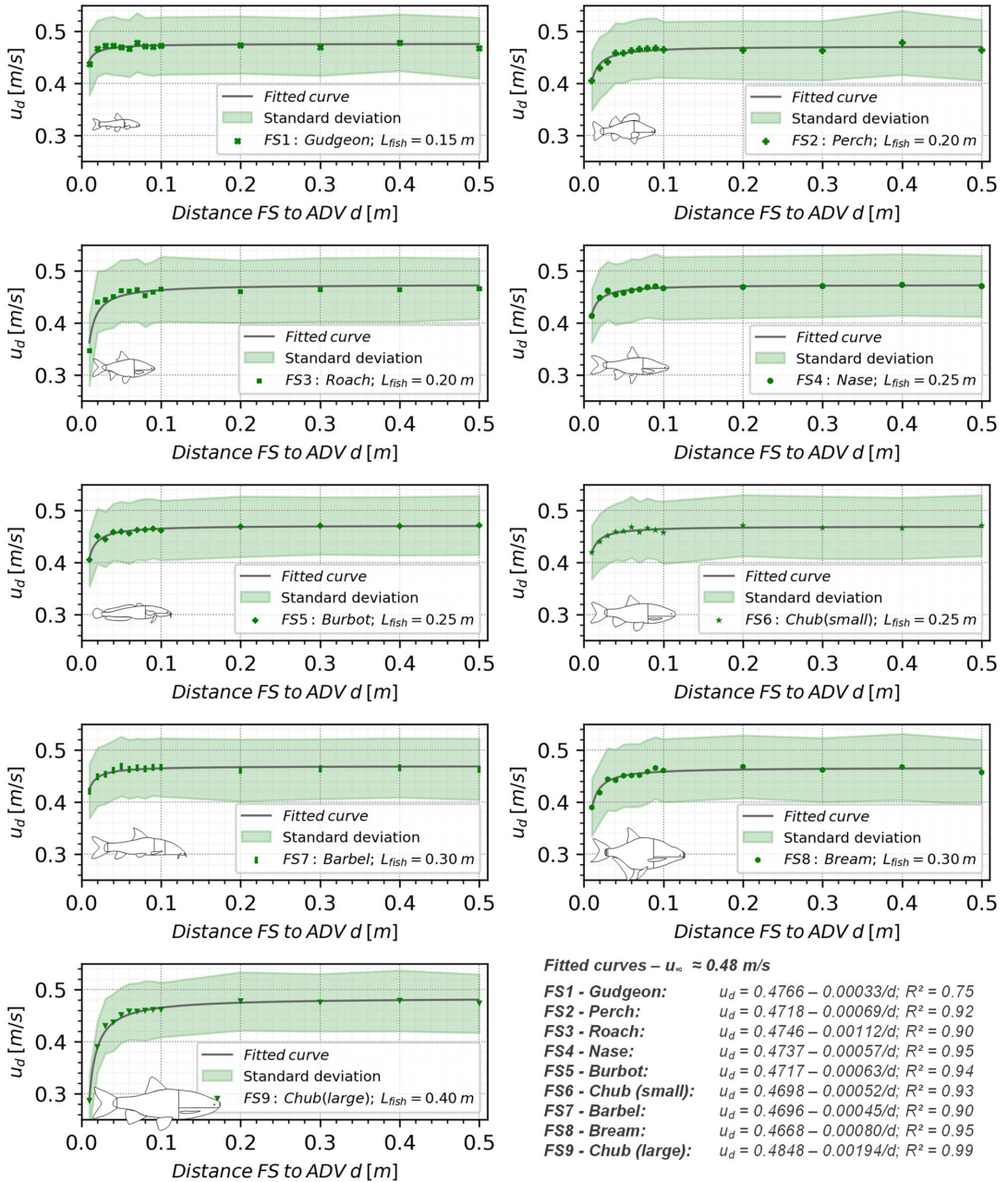


Fig. 7 Individual plots of the upstream velocity profile for each of the fish-shaped bodies with increasing distance from the anterior-most point, for hydraulic setup H2. The lower rightmost panel includes the results of the fit curves for each body

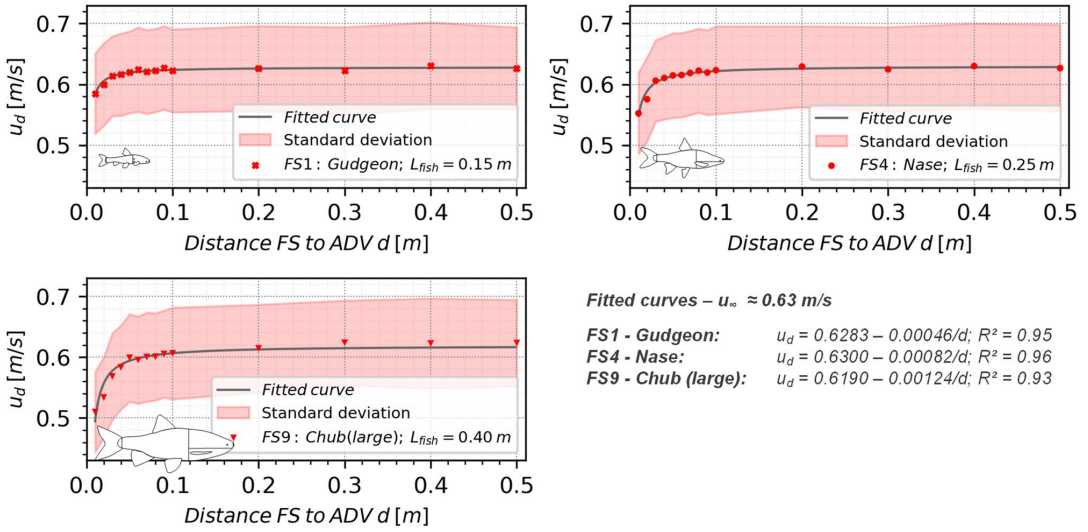


Fig. 8 Individual plots of the upstream velocity profile for each of the fish-shaped bodies with increasing distance from the anterior-most point, for hydraulic setup H3. The lower rightmost panel includes the results of the fit curves for each body

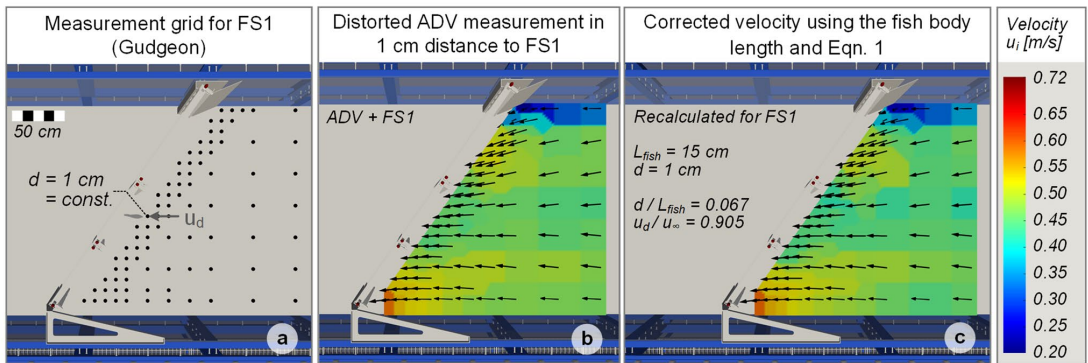


Fig. 9 Planar velocity field measurements for FS1: **a** measurement grid of 85 points in front of a fish protection rack angled at 55°; **b** measured planar velocity fields in 1 cm distance to FS1; **c** velocity

field map based on point velocity measurements without the presence of a fish-shaped body after applying the flow distortion function. The freestream velocity has been distorted using Eq. (2)

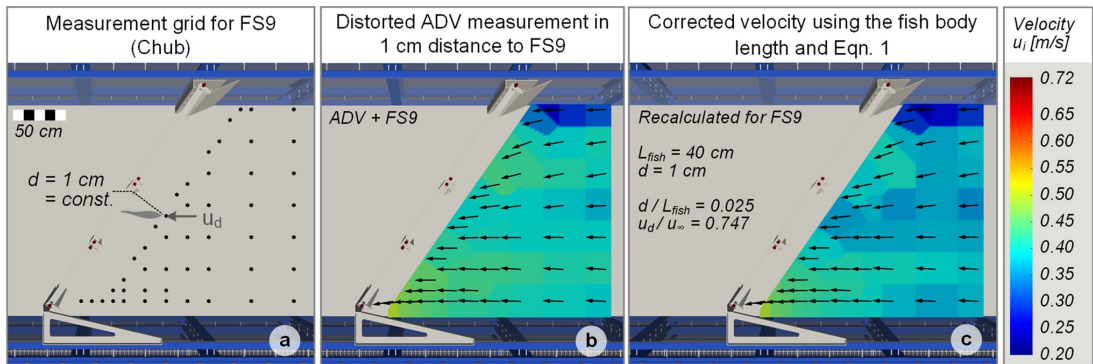


Fig. 10 Planar velocity field measurements for FS9: **a** measurement grid of 55 points in front of a fish protection rack angled at 55°; **b** measured planar velocity fields in 1 cm distance to FS9; **c** velocity

field map based on point velocity measurements without the presence of a fish-shaped body after applying the flow distortion function. The freestream velocity has been distorted using Eq. (4)

Funding Open Access funding enabled and organized by Projekt DEAL. This project has been primarily funded from The German Federal Environmental Foundation (Deutsche Bundesstiftung Umwelt DBU), Az. 33867/01. Ali Hassan Khan's contribution has received funding from the European Union Horizon 2020 Research and Innovation Programme under the Marie Skłodowska-Curie Actions, Grant Agreement No. 860800 RIBES. Jeffrey Tuhtan's contribution was supported by the Estonian Research Council grant PRG1243 and EXCITE.

Data availability The datasets generated during and/or analysed during the study are available from the corresponding author on reasonable request.

Code availability Code availability is not applicable to this study, as no software application or custom code was created or used in this project.

Declarations

Conflict of interest The authors declare that no conflicts or competing interests exist.

Open Access This article is licensed under a Creative Commons Attribution 4.0 International License, which permits use, sharing, adaptation, distribution and reproduction in any medium or format, as long as you give appropriate credit to the original author(s) and the source, provide a link to the Creative Commons licence, and indicate if changes were made. The images or other third party material in this article are included in the article's Creative Commons licence, unless indicated otherwise in a credit line to the material. If material is not included in the article's Creative Commons licence and your intended use is not permitted by statutory regulation or exceeds the permitted use, you will need to obtain permission directly from the copyright holder. To view a copy of this licence, visit <http://creativecommons.org/licenses/by/4.0/>.

References

Adam B, Lehmann B (2011) Ethohydraulik. Springer, Berlin, Heidelberg

- Bleckmann H (1994) Reception of hydrodynamic stimuli in aquatic and semiaquatic animals. In: Rathmayer W (ed). Prog. Zool. Vol 41. Gustav Fischer, Stuttgart, Jena, New York
- Brosse S, Charpin N, Su G, Toussaint A, Herrera-R GA, Tedesco PA, Villéger S (2021) FISHMORPH: a global database on morphological traits of freshwater fishes. Glob Ecol Biogeogr 30(12):2330–2336. <https://doi.org/10.1111/geb.13395>
- Brownscombe JW, Midwood JD, Cooke SJ (2021) Modeling fish habitat: model tuning, fit metrics, and applications. Aquat Sci 83:44. <https://doi.org/10.1007/s00027-021-00797-5>
- Bureau of Reclamation (2001) Water Measurement Manual. 3rd ed rev repr, Tech rep. Water Resources Research Laboratory, US Department of the Interior.
- Cano-Barbacid C, Radinger J, Argudo M, Rubio-Gracia F, Vila-Gispert A, García-Berthou E (2020) Key factors explaining critical swimming speed in freshwater fish: a review and statistical analysis for Iberian species. Sci Rep 10:18947. <https://doi.org/10.1038/s41598-020-75974-x>
- Coombs S (1999) Signal detection theory, lateral-line excitation patterns and prey capture behaviour of mottled sculpin. Anim Behav 58(2):421–430. <https://doi.org/10.1006/anbe.1999.1179>
- Crook DA, Robertson AI, King AJ, Humphries P (2001) The influence of spatial scale and habitat arrangement on diel patterns of habitat use by two lowland river fishes. Oecologia 129:525–533. <https://doi.org/10.1007/s004420100750>
- Deng R, Wang S, Luo W, Wu T (2021) Experimental study on the influence of bulbous bow form on the velocity field around the bow of a trimaran using towed underwater 2D–3C SPIV. J Mar Sci Eng 9(8):905. <https://doi.org/10.3390/jmse9080905>
- Díaz Lozada JM, García CM, Scacchi G, Oberg KA (2021) Dynamic selection of exposure time for turbulent flow measurements. J Hydraul Eng 147(10):04021035. [https://doi.org/10.1061/\(asce\)hy.1943-7900.0001922](https://doi.org/10.1061/(asce)hy.1943-7900.0001922)
- García-Vega A, Fuentes-Pérez JF, Fukuda S, Kruusmaa M, Sanz-Ronda FJ, Tuhtan JA (2021) Artificial lateral line for aquatic habitat modelling: An example for *Lefua echigonia*. Ecol Inform 65:101388. <https://doi.org/10.1016/j.ecoinf.2021.101388>
- Gido KB, Falke JA, Oakes RM, Hase KJ (2006) Fish-habitat relations across spatial scales in prairie streams. Am Fish Soc Symp 48:265–285
- Goerig E, Wasserman BA, Castro-Santos T, Palkovacs EP (2020) Body shape is related to the attempt rate and passage success of brook

- trout at in-stream barriers. *J Appl Ecol* 57(1):91–100. <https://doi.org/10.1111/1365-2664.13497>
- Goring DG, Nikora VI (2002) Despiking acoustic Doppler velocimeter data. *J Hydraul Eng* 128(1):117–126. [https://doi.org/10.1061/\(asce\)0733-9429\(2002\)128:1\(117\)](https://doi.org/10.1061/(asce)0733-9429(2002)128:1(117))
- Goulet J, Engelmann J, Chagnaud BP, Franosch J-MP, Suttner MD, van Hemmen JL (2008) Object localization through the lateral line system of fish: theory and experiment. *J Comp Physiol A* 194:1–17. <https://doi.org/10.1007/s00359-007-0275-1>
- Katopodis C, Gervais R (2016) Fish swimming performance database and analyses. DFO Can Sci Advis Sec Res 2016/002
- Kondolf GM, Williams JG, Horner TC, Milan D (2008) Assessing physical quality of spawning habitat. *Am Fish Soc Symp* 48
- Lake BM (1971) Velocity measurements in regions of upstream influence of a body in aligned-fields MHD flow. *J Fluid Mech* 50(2):209–231. <https://doi.org/10.1017/S0022112071002544>
- Montgomery JC, Baker CF, Carton AG (1997) The lateral line can mediate rheotaxis in fish. *Nature* 389:960–963. <https://doi.org/10.1038/40135>
- Navarro A, Lee-Montero I, Santana D, Henríquez P, Ferrer MA, Morales A, Soula M, Badilla R, Negrín-Báez D, Zamorano MJ, Afonso JM (2016) IMAFISH_ML: A fully-automated image analysis software for assessing fish morphometric traits on gilthead seabream (*Sparus aurata* L.), meagre (*Argyrosomus regius*) and red porgy (*Pagrus pagrus*). *Comput Electron Agric* 121:66–73. <https://doi.org/10.1016/j.compag.2015.11.015>
- Nestler JM, Milhous RT, Payne TR, Smith DL (2019) History and review of the habitat suitability criteria curve in applied aquatic ecology. *River Res Appl* 35(8):1155–1180. <https://doi.org/10.1002/rra.3509>
- Nikora VI, Aberle J, Biggs BJB, Jowett IG, Sykes JRE (2003) Effects of fish size, time-to-fatigue and turbulence on swimming performance: a case study of *Galaxias maculatus*. *J Fish Biol* 63(6):1365–1382. <https://doi.org/10.1111/j.1095-8649.2003.00241.x>
- O'Brien WJ, Showalter JJ (1993) Effects of current velocity and suspended debris on the drift feeding of arctic grayling. *Trans Am Fish Soc* 122(4):609–615. [https://doi.org/10.1577/1548-8659\(1993\)122%3c0609:eocvas%3e2.3.co;2](https://doi.org/10.1577/1548-8659(1993)122%3c0609:eocvas%3e2.3.co;2)
- Santos JM, Reino L, Porto M, Oliveira J, Pinheiro P, Almeida PR, Cortes R, Ferreira MT (2011) Complex size-dependent habitat associations in potamodromous fish species. *Aquat Sci* 73:233–245. <https://doi.org/10.1007/s00027-010-0172-5>
- Schwevers U, Adam B (2019) Biometrie einheimischer Fischarten als Grundlage für die Bemessung von Fischwegen und Fischschutzzanlagen. *Wasser Und Abfall* 01–02:46–52. <https://doi.org/10.1007/s35152-019-0003-5>
- Senay C, Taranu ZE, Bourque G, Macnaughton CJ, Lanthier G, Harvey-Lavoie S, Boisclair D (2017) Effects of river scale flow regimes and local scale habitat properties on fish community attributes. *Aquat Sci* 79:13–26. <https://doi.org/10.1007/s00027-016-0476-1>
- Springer B, Friedrichs M, Graf G, Nittikowski J, Queisser W (1999) A high-precision current measurement system for laboratory flume systems: a case study around a circular cylinder. *Mar Ecol Prog Ser* 183:305–310. <https://doi.org/10.3354/meps183305>
- Stewart WJ, Nair A, Jiang H, McHenry MJ (2014) Prey fish escape by sensing the bow wave of a predator. *J Exp Biol* 217(24):4328–4336. <https://doi.org/10.1242/jeb.111773>
- Wahl TL (2004) Analyzing ADV data using WinADV. Joint Conference on Water Resource Engineering and Water Resources Planning and Management 2000: July 30–August 2. ASCE, Minneapolis, Minnesota, US. [https://doi.org/10.1061/40517\(2000\)300](https://doi.org/10.1061/40517(2000)300)
- Wahl TL (2003) Discussion of “Despiking Acoustic Doppler Velocimeter Data” by Derek G. Goring and Vladimir I. Nikora. *J Hydraul Eng* 129(6):484–487. [https://doi.org/10.1061/\(asce\)0733-9429\(2003\)129:6\(484\)](https://doi.org/10.1061/(asce)0733-9429(2003)129:6(484))
- Webb PW (1971) The swimming energetics of trout. II. Oxygen consumption and swimming efficiency. *J Exp Biol* 55(2):521–540. <https://doi.org/10.1242/jeb.55.2.521>
- Wheaton JM, Brasington J, Darby SE, Merz J, Pasternack GB, Sear D, Vericat D (2010) Linking geomorphic changes to salmonid habitat at a scale relevant to fish. *River Res Appl* 26(4):469–486. <https://doi.org/10.1002/rra.1305>

Publisher's Note Springer Nature remains neutral with regard to jurisdictional claims in published maps and institutional affiliations.

Appendix 3

III

A. H. Khan, S. Hoerner, G. Tomming, M. Kruusmaa, and J. A. Tuhtan, "3D CFD analysis of pressure, boundary layer and shear stresses on a gudgeon (*Gobio gobio*)," *Journal of Ecohydraulics*, pp. 1-15, 2024

3D CFD analysis of pressure, boundary layer and shear stresses on a gudgeon (*Gobio gobio*)

Ali Hassan Khan^a, Stefan Hoerner^{b,c}, Gert Toming^a, Maarja Kruusmaa^a and Jeffrey A. Tuhtan^a

^aDepartment of Computer Systems, Tallinn University of Technology, Tallinn, Estonia; ^bLaboratory of Geophysical and Industrial Flows (LEGI), CNRS, G-INP, University Grenoble-Alpes, Grenoble, France; ^cLaboratory of Fluid Dynamics & Technical Flows (LSS), Otto-von-Guericke University Magdeburg/ISUT, Magdeburg, Germany

ABSTRACT

The fish's mechanosensory lateral line system detects non-acoustic hydrodynamic stimuli required for feeding, schooling, predator avoidance and underwater object detection. Biological investigations have established that flow stimuli are detected through the boundary layer as pressure gradients by canal neuromasts and as shear stresses acting on the superficial neuromasts. Previous works have also shown that the spatial distribution of neuromasts is strongly correlated with the pressure coefficient. Despite these fundamental insights, substantial knowledge gaps persist in understanding how fish body geometry influences the boundary layer, the pressure distribution and shear stresses. To address these gaps, we provide a set of numerical models based on the open-source CFD toolkit *OpenFOAM* which are experimentally validated using velocity measurements obtained in a laboratory fish swim tunnel. Specifically, we investigate the mid dorsal-ventral planar flow fields around a 3D fish-shaped body of gudgeon (*Gobio gobio*), a common freshwater bottom-dwelling fish. The contributions of this work are two-fold: First, we provide a comparison of the boundary layer thicknesses and velocity profiles at flow velocities ranging from 0.25 to 1.25 m/s. Second, we qualitatively compare the spatial distributions of the pressure coefficient, dynamic pressure and shear stresses to biological observations of the neuromast locations of adult gudgeon.

ARTICLE HISTORY

Received 9 October 2023
Revised 28 July 2024
Accepted 9 September 2024



KEYWORDS


Fish sensing; lateral line; boundary layer; pressure coefficient; shear stress

1. Introduction

Ray-finned fishes represent a highly diverse group of vertebrates, comprising half of all extant species (Helfman et al. 2009). Their highly evolved lateral line flow sensing system consists of neuromasts, specialized receptor organs distributed along the head and body of the fish. The lateral line is involved in multiple behaviors including feeding, navigation, predator avoidance, and rheotaxis (Montgomery et al. 2014). Although the biological lateral line has been extensively researched, the hydrodynamic properties of natural flow stimuli are rarely considered or characterized in the literature, especially the spatio-temporal patterns of small-scale water motion (Bleckmann 2023). This makes it especially challenging for ecohydraulic researchers to relate flow stimuli recorded in laboratory or field studies to fish sensory system morphology, function and responses (Mogdans 2019). Indeed, in 1963 Dijkgraaf postulated that the hydrodynamic environment influences the peripheral lateral line system morphology

(Dijkgraaf 1963). Since then, several reports and studies have shown that the lateral line system morphology can be linked to natural habitats (Zauner and Eberstaller 1999). In general, limnophilic fish tend to have larger counts of superficial neuromasts, widened canals, or canal loss (Bassett et al. 2006), whereas rheophilic fish have well-developed canals and lower counts of superficial neuromasts (Schellart 1991). Furthermore, differences in the peripheral lateral line sensory responses to identical flow stimuli have been observed between still water fish (*Carassius auratus*) and riverine fish (*Oncorhynchus mykiss*), hypothesized as an adaptation to habitats with higher water velocities (Engelmann et al. 2002). Biological studies also provide further evidence that riverine fish species exhibit phenotypic lateral line specialization adapted to divergent habitat types (Wark and Peichel 2010; Vanderpham et al. 2016). A detailed literature review of the sensory ecology of the lateral line sensory system is provided by Mogdans (Mogdans 2019).

CONTACT Ali Hassan Khan  ali.khan@taltech.ee  Department of Computer Systems, Tallinn University of Technology, Tallinn, Estonia

 Supplemental data for this article can be accessed online at <https://doi.org/10.1080/24705357.2024.2426809>.

© 2024 The Author(s). Published by Informa UK Limited, trading as Taylor & Francis Group

This is an Open Access article distributed under the terms of the Creative Commons Attribution License (<http://creativecommons.org/licenses/by/4.0/>), which permits unrestricted use, distribution, and reproduction in any medium, provided the original work is properly cited. The terms on which this article has been published allow the posting of the Accepted Manuscript in a repository by the author(s) or with their consent.

The sensory units of lateral line system, i.e. neuromasts, can be classified into two types: shear-sensitive superficial neuromasts (SN), which are exposed on the skin surface, and pressure-sensitive canal neuromasts (CN), embedded within small canals in the upper layer of the epidermis. Thus both types of lateral line neuromasts contain hair cells specialized to respond to hydromechanical stimuli. The near-body flow field is dominated by viscous effects over the typical range of the Reynolds number ($100 < Re < 100,000$) fish experience during swimming. These viscous effects generate a thin layer of fluid over the body surface, known as the boundary layer (Windsor and McHenry 2009). The boundary layer acts as a high-pass filter for the SN, attenuating the low-frequency stimuli (McHenry et al. 2008). Previous studies have shown that the pressure across the boundary layer remains largely constant (White 2006). This implies that the stimuli experienced by CN are largely determined by the body geometry, which governs the pressure distribution and boundary layer thickness. In addition, the boundary layer thickness over a streamlined body tends to decrease with increasing Reynolds number (Windsor and McHenry 2009). The shear stress exerted on SN cupula cause deflection due to minute changes in the fluid-body flow field fluctuations (Dijkgraaf 1963; Bleckmann 2008) and tend to be most sensitive to frequencies ranging from ≤ 1 to 150 Hz.

Superficial neuromasts are especially well-suited to detect low-frequency oscillations (≤ 20 Hz) common to flowing waters, and are especially sensitive to near-body velocity gradients (Tuhtan and Fuentes-Perez 2018). The local skin friction coefficient (C_f), boundary layer thickness (δ) and the freestream flow velocity largely determine the local oscillations in the boundary layer (Anderson et al. 2001). It is also known that the boundary layer thickness varies along a fish's body length, further complicating the relationship between the freestream flow and superficial neuromast stimuli (McHenry and Liao 2014). Previous works have reported a strong positive correlation between the density of superficial neuromasts in the anteriormost region of the fish's body (Coombs et al. 2014). These findings indicate that the location of superficial neuromasts may correspond to regions where both the local shear stresses and pressure gradients are the highest, caused by rapid deceleration and flow stagnation at the fish's head.

The pores of the canal neuromasts penetrate the upper epidermis, and are thus most sensitive to the pressure differences across the pores. Considering canal neuromasts, the variation in the cupular size,

sliding stiffness, canal density and fluid viscosity determine the resonant response of CN to flow stimuli (Van Netten 2006). This complex mechano-sensory filtering allows canal neuromasts to be more robust to local pressure gradients, enhancing the fish's ability to orient and detect obstacles (Bleckmann 2008). Knowledge of the boundary layer profile for fish hydrodynamic sensing is also important because previous works have established that near-body velocity fluctuations can be modulated due to the damping properties of the boundary layer (Teyke 1988). In the absence of undulatory motion during swimming, the near-body flow field around a stationary fish exhibits steady conditions without an oscillatory boundary layer (Anderson et al. 2001). The boundary layer velocity is zero at the body surface and reaches 99% of the freestream velocity at the outermost edge of the log region (Schlichting and Gersten 2000). Although the boundary layer is known to play different roles in the hydrodynamic sensing capabilities of fish, there remain few studies which have specifically taken it into account, largely due to the difficulty of obtaining data on live fish or fish-shaped bodies.

Due to the wide variety and complexity of the biological lateral line and the general lack of studies into natural flow stimuli, Computational Fluid Dynamics (CFD) can aid in the investigation of the near-body flow fields experienced by the fish's lateral line sensing system. Previous CFD studies have focused on fish swimming kinematics, thrust and drag, and vortex structures generation in the wake (Adkins and Yan 2006; Owsianowski and Kesel 2008). The authors of this work have shown in a previous CFD study on a trout-shaped body (Khan et al. 2022) that the Reynolds-averaged Navier-Stokes (RANS) and Spalart Allmaras turbulence models can be applied to assess near-body flow fields with good agreement with measured velocities, however this work did not investigate the boundary layer velocity profiles or shear stresses on the body. A small number of works have applied CFD to specifically investigate the hydrodynamic sensing capabilities of the lateral line. Notable contributions are (Windsor et al. 2008, 2010) which carried out three-dimensional numerical modelling of a fish-shaped body of a blind Mexican cave fish (*Astyanax fasciatus*), comparing it to a NACA0013 profile. These works are based on simplified fish-like body geometries, which allow for a substantially simplified CFD model setup, reducing the computational effort and overall time required for post-processing and analysis.

In addition to CFD, full-scale physical models have been used to investigate the pressure

distribution around a rainbow trout (*Oncorhynchus mykiss*) at yaw angle orientations of 5° , 10° and 20° as well as pressure fluctuations induced by a foil placed immediately upstream of the physical model (Ristroph et al. 2015). A major finding of that work was that the sensitivity (stimulation per degree) and canal neuromast density were strongly correlated along the trout's anteroposterior axis. Despite the important advances presented in previous works, major gaps persist in quantifying and understanding the boundary layer on fish bodies and the specific effects it has on the lateral line sensing capabilities. In this work, our analysis is focused on the boundary layer of the gudgeon (*Gobi gobio*, TSN: 163658), a common freshwater fish species which often remains stationary in the flow (Schmitz et al. 2014). The typical body length of gudgeon found in European rivers ranges between 9–21 cm (Maitland and Campbell 1992; Kottelat and Freyhof 2007), and the body length was chosen to be 15 cm, reflecting a typical size of wild specimens. The dimensions of the gudgeon model are provided in Figure 1.

The contributions of this work are two-fold: First, we provide a high-resolution open numerical model of the gudgeon fish, including a fully resolved boundary layer as well as an analysis of the pressure and shear fields. Specifically, we assess the thickness and velocity profiles of the boundary layer around the gudgeon body at four different Reynolds numbers corresponding to typical velocity ranges in rivers inhabited by the gudgeon (0.25, 0.55, 0.85 and 1.25 m/s). Secondly, we evaluate the spatial distribution of the pressure coefficient and shear stresses to biological observations of the canal and superficial neuromast locations on a gudgeon body. The pressure coefficient exhibited the largest gradients in the anterior 20%

of the body and the shear stress distribution was found to have two distinct peaks in the anterior-most 10% of the body, above the eye orbit.

2. Experimental methods

2.1. Gudgeon body geometry and swim tunnel setup

The gudgeon's geometry shown in Figure 1 is based on the 3D gudgeon model of fish donated by Dosch Design Kommunikationsagentur GmbH (Marktheidenfeld, Germany) from imagery collected of live fish, and modified to fit the total body length of 15 cm using the Computer-Aided Design (CAD) software SolidWorks (V27, Dassault Systèmes, France). All physical experiments were conducted in the laboratory of fluid dynamics and technical flows at Otto-von-Guericke University, Magdeburg, Germany.

The model was 3D printed and placed into (Form 3 L, Formlabs Inc., USA) a commercial swim tunnel (185 L, Loligo Systems, Denmark). The tunnel was chosen as they are widely used in studying fish swimming kinematics, energy expenditure and swimming performance (Jones et al. 2020) and has been used in a study of gudgeon swimming performance on fish of a similar size (Egger et al. 2021). The planar two-dimensional velocity measurements around the fish were then recorded *via* optical access from the bottom of the swim tunnel. These velocity measurements are necessary and sufficient for calibrating and validating the CFD model. However, in order to obtain velocity, shear and pressure values over the entire surface of the gudgeon body to evaluate fluid-body interactions and the placement of neuromasts, a numerical model is needed. Prior to the measurements, the flow inside

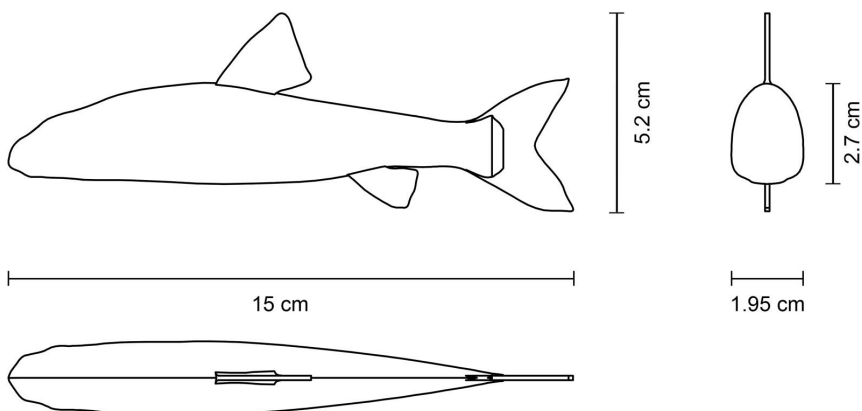


Figure 1. Physical dimensions of the gudgeon fish-shaped physical model. The pectoral fins were removed from the model as they are primarily responsible for hovering, turning and braking (Lauder and Drucker 2004) which are swimming activities not investigated in this work.

Table 1. Overview of the dimensions, specifications, settings and equipment used in the commercial swim tunnel, including the gudgeon-shaped physical model and laser Doppler anemometer.

Dimensions of the gudgeon-shaped body (length x width x height)	15 × 1.95 × 2.7 cm
Specifications of the swim tunnel	
Length × width × height	28 × 7.5 × 7.5 cm
Water depth	7.5 cm
Mean inlet velocity	0.238 ± 0.06 m/s, 0.543 ± 0.06 m/s
Mean turbulence intensity	15.21 ± 4 %, 11.38 ± 10 %
Reynolds number	37,436, 82,360
Froude number	0.21, 0.45
Specifications of the Laser Doppler Anemometer (LDA)	
Model	Dantec Flow Explorer DPSS
Laser type	300 2D
Wavelength	Continuous laser
Nominal measurement distance	485 mm with 500 mm bottom lens
Measuring volume (length(x) × width(y) × height(z))	24 × 6 × 6 cm
Software	BSA Flow Software

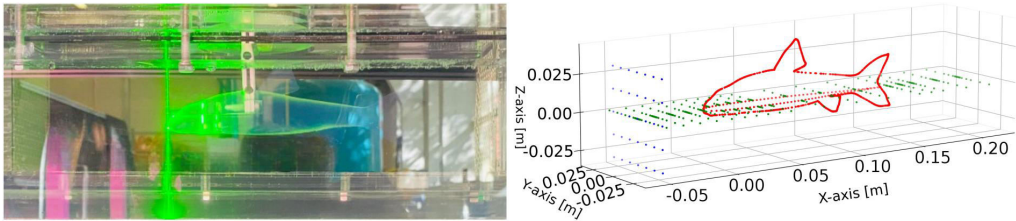


Figure 2. Swim tunnel physical velocity measurement experimental setup used for the gudgeon body, the flow direction is from left to right. Left: Side view of the swim tunnel working section showing the 3D printed body, mounting assembly during an LDA measurement at the anteriormost observation location. Right: Planar velocity measurement locations inside the swim tunnel working section, the outline of the fish-shaped gudgeon body is marked in red. Blue markers represent the vertical plane used for the upstream boundary conditions and green markers indicate the probe locations of the horizontal plane used for numerical model tuning and validation.

the swim tunnel was run for a minimum of five minutes before activating the laser to ensure the measurements occurred during fully developed turbulence. A summary of the swim tunnel experiments is given in Table 1, and a detailed overview of the velocity measurements are provided in the following subsection.

2.2. LDA velocity measurements

Velocity measurements were carried out using a Dantec FlowExplorer (Dantec Dynamics, Denmark) two-dimensional (2D) laser Doppler anemometer (LDA). Two planar test sections were measured. First, at a vertical plane located 0.048 m upstream of the physical model body to establish the inlet boundary conditions. Second, at a horizontal plane taken at mid-body elevation (assigned as 0 m), to obtain the planar flow field around the gudgeon body which was required for numerical model calibration and validation (Figure 2).

The two-dimensional horizontal velocity field was measured as streamwise, U_x and lateral, U_y components. The LDA data were post-processed and saved using the BSA Flow software (Dantec Dynamics, Denmark). The parameters and settings applied in post-processing are provided in the supplementary material. The lowest signal-to-noise ratio (SNR) of

63.11% was found at measurement points located closest to the surface of the fish. Polyamide seed particles with a mean diameter of 5 μm were added to the swim tunnel to maintain a high SNR for all measurements. The measurement locations within the swim tunnel test section were determined after calculating the focal length and adjusting it to account for refraction through the tunnel's acrylic walls and through the water. A custom *Python* script was created to calculate the vertical displacement of the laser inside the test section, and is included in the supplementary material.

At each of the two flow velocities measured (0.25 and 0.55 m/s), the first set of measurements were recorded in the vertical plane (YZ) at 0.048 m upstream of the gudgeon body. The vertical plane data were used to define the inlet flow boundary conditions of the numerical model. Each vertical plane consisted of 35 measurement points at a distance of 7.5 mm from the walls. The distance between each measurement point along the y-axis was 10 mm and 15 mm along the z-axis. The second set of measurements was obtained in the horizontal (XY) plane around the gudgeon body at 264 measurement points, where the neutral axis of $Z=0$ was established as the anteriormost point of the body (Figure 2). At each measurement location, 2000 U_x and 2000 U_y samples were recorded over a time duration of 300 s. The density of LDA velocity measurements in the immediate vicinity of the fish-shaped

body was higher than in the freestream region. The streamwise distance between points was reduced in the head region, corresponding to the anterior 40% of the total body length, to ensure a smooth interpolation of the large velocity gradients caused by stagnation. The closest points to the surface of the body were located at a distance of 0.5 mm, and resided inside of the boundary layer. The physical experiments in this work provided 2D velocity measurements required to tune and validate numerical Model I (swim tunnel) and to define the inlet boundary condition and numerical model divergence criteria Figure 3.

3. Numerical model

The open source framework *OpenFOAM-v2112* was used in this work for numerical modelling of the flow around the fish-shaped body. Validation of the numerical model was carried out at Reynolds numbers of 3.74×10^4 and 8.23×10^4 , which correspond to standard operational conditions in the commercial swim tunnel with freestream velocities of 0.25 and 0.55 m/s, respectively. All numerical simulations were based on the 3D incompressible steady-state Navier-Stokes equations using the Finite

Volume Method (FVM). As the gudgeon model is a rigid body and does not move within the domain, the steady-state solver *simpleFoam* was chosen. A comprehensive summary of the numerical method, spatial and temporal discretization, turbulence model and boundary conditions used in this work is shown in Table 2. The flow within the swim tunnel test section (Model I) was found to be dominated by lateral wall effects, which lead to high turbulence

Table 2. Overview of the OpenFOAM simulations for Model I and Model II setups investigate in this work.

Numerical framework	OpenFOAM-v2112
Solver	simpleFoam
Characteristics	Incompressible, steady-state, turbulence
Algorithm	SIMPLE
Spatial discretization	
Mesh type	Polyhedral
Max cell size	0.004 m
Minimum cell size	0.00004 m
Total number of cells	5.8 M
Steady-state	
Max. no of iterations	5000
Timestep	1
Turbulence model	RANS-Spalart Allmaras
Wall treatment	Calculated (fully resolved)
Convergence criteria	
Residuals	10^{-6}
Relaxation factors	$U = 0.7, p = 0.7$
Total simulation time	80 CPUh

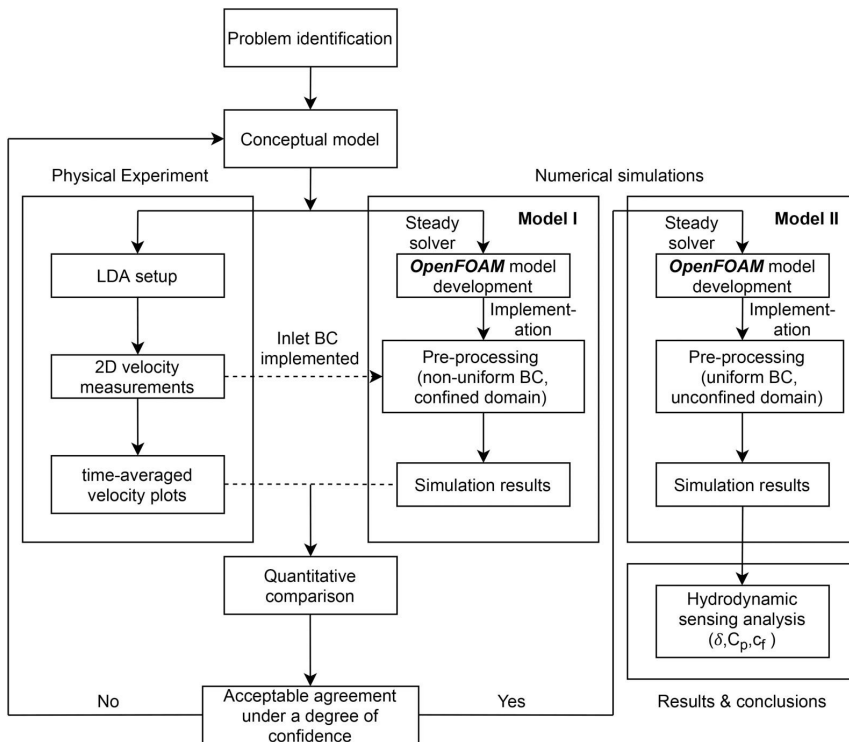


Figure 3. Flowchart of the physical experiments and two numerical model setups (model I and model II) applied in this work. Model I was used for numerical model tuning and validation based on the physical experiments in the commercial swim tunnel, and numerical model II (widened mesh, unconstrained by the tunnel geometry) provided the main results of this work investigating fish hydrodynamic sensing based on the boundary layer, and anteroposterior pressure coefficient and shear stress distributions.

intensities (TI). Due to this limitation, and after validating the Model I setup based on the LDA measurements, a second model domain (Model II) was widened to 0.3 m, which removed the lateral wall effects. An overview of the physical model setup and corresponding numerical model validation and application to evaluate the fish-shaped body hydrodynamic sensing analysis is provided in Figure 3. The results of the widened domain model were subsequently used in the investigation of the boundary layer, the pressure coefficient and shear stresses over the gudgeon body. The two model domains including the boundary conditions and dimensions are shown in Figure 4.

3.1. Boundary conditions

The inlet flow conditions in numerical Model I were assigned in the form of a second-order polynomial interpolated using the vertical planar LDA measurements with the expression-based boundary condition (*exprFixedValue*) in *OpenFOAM*. The interpolated inlet velocity was measured and modelled at an upstream distance of 0.048 m from the anteriormost point of the fish-shaped body. Model II was assigned a uniform inlet velocity distribution. The domain walls for both numerical setups were specified with a *noSlip* boundary condition as well as for the gudgeon body. A zero gradient Neumann inlet pressure boundary condition of both numerical setups was specified as $\nabla p = 0$, and the outlets were defined using Dirichlet boundary conditions with zero pressure, $p = 0$. In this study, the influence of wall roughness was neglected, and the default value of the wall roughness parameter ($E = 9.0253$) in *OpenFOAM* was adopted within the wall boundary condition for turbulent viscosity ν_t (Spalding 1961).

3.2. Mesh discretization

A 3D rectangular test section of the swim tunnel ($28 \times 7.5 \times 7.5$ cm) was modelled in an open-source tool: *Salome*. The CAD model of gudgeon along

with the test section were imported as *.stl* files in *OpenFOAM* and discretized using the open-source utilities: *surfaceFeatureEdges* and *cfMesh*. The result was an unstructured mesh composed of hexahedral and polyhedral elements. Near the surface of the gudgeon within the boundary layer, polyhedral cells of size $40 \mu\text{m}$ were created. To ensure a fine mesh resolution at the surface of the gudgeon, five boundary mesh layers were added around the surface resulting in the first node of the mesh in the viscous region with an average y^+ value of 0.7. Moreover, different mesh regions were defined around the gudgeon body with varying cell sizes depending upon the distance from the gudgeon. The outer boundaries of the test section were meshed with hexahedral elements of a larger size, approximately 0.4 mm. The final simulations were run with a total of 5.8 M elements (Mesh N4 in Table 3).

3.3. Turbulence modelling

Previous works on near-body flow fields around fish-shaped bodies have assumed laminar flows, neglecting the effects of turbulence (Rapo et al. 2009; Li et al. 2022). (Windsor et al. 2010) applied the Arbitrary Lagrangian-Eulerian (ALE) CFD code, solving the incompressible Navier-Stokes equation on an unstructured Voronoi finite volume mesh, to investigate the flow fields around a blind Mexican cavefish approaching a wall and validated the numerical models using Particle Image Velocimetry (PIV) data. To address the lack of turbulence

Table 3. Discretization error for various meshes around gudgeon model.

Parameter	Drag force coefficient (C_d)
N_1, N_2, N_3, N_4, N_5	172K, 0.65 M, 1.0 M, 5.8 M, 7.9 M
$Y_1^+, Y_2^+, Y_3^+, Y_4^+, Y_5^+$	4.0, 0.40, 0.46, 0.65, 0.09
$C_{d1}, C_{d2}, C_{d3}, C_{d4}, C_{d5}$	0.07087, 0.07431, 0.06947, 0.06389, 0.06354
P_{ave}	3.632
$C_{d_{int}}^{21}, C_{d_{int}}^{32}, C_{d_{int}}^{43}, C_{d_{int}}^{54}$	0.07546, 0.05011, 0.05831, 0.06319
$e_a^{21}, e_a^{32}, e_a^{43}, e_a^{54}$	4.63%, 6.96%, 8.73%, 0.55%
GC^{21}_{fine}	1.92%
GC^{32}_{coarse}	34.83%
GC^{43}	10.91%
GC^{54}_{fine}	0.68%

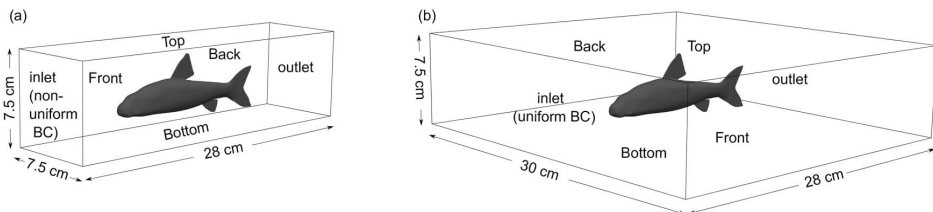


Figure 4. Schematic showing the numerical model domain dimensions, the location of the gudgeon body and boundary condition labels. The gudgeon model dimensions are given in Figure 1. (a) Numerical model I, used for model tuning and validation with the same geometry as the swim tunnel with LDA measurements. (b) Numerical model II, widened domain used for the analysis of the boundary layer, pressure coefficient, dynamic pressure and shear stress distributions over the gudgeon-shaped body.

modelling for fish sensory ecology CFD studies, the authors compared several Reynolds Averaged Navier Stokes (RANS) turbulence models in a previous work (Khan et al. 2022), where it was found that the Spalart-Allmaras model yielded superior results when considering flows with a fully resolved boundary layer ($y^+ < 1$). Based on these findings, the Spalart-Allmaras turbulence model was implemented in this work.

The RANS-Spalart Allmaras (SA) model, also known as a linear eddy viscosity model, is widely used for simulating turbulent flows, particularly in aerospace applications (Matsui et al. 2021). Unlike other Reynolds-averaged Navier-Stokes (RANS) models, the Spalart-Allmaras model distinguishes itself by omitting the inclusion of an auxiliary set of equations to facilitate turbulence closure. Instead, it focuses solely on solving the transport equation governing the turbulent eddy viscosity. The turbulent eddy viscosity is intricately linked to the mean flow properties, and as a consequence, it does not explicitly encompass the spatial attributes of turbulence. Similar to other RANS models the Spalart Allmaras model is also based on the Boussinesq hypothesis which takes the assumption that the Reynolds stress tensor (τ_{ij}) is proportional to the traceless mean strain rate tensor S_{ij} (Spalart and Allmaras 1992).

$$\tau_{ij} = 2\mu_t S_{ij}^* - \frac{2}{3}\rho k\delta_{ij} \quad (1)$$

The model can be reasonably applied to predict turbulent flows with adverse pressure gradients. A further advantage of the model is that it is local, which means the transport equation being solved remains independent of the solution at other locations.

3.4. Grid convergence study

In order to define the mesh resolution at which the numerical simulation is no longer affected by the spatial discretization of the computational mesh, a grid convergence study was conducted following the guidelines of Celik et al. (2008). The analysis is based on the accuracy of the numerical solution by calculating the discretization error between meshes with increasing levels of refinement. In this work, the numerical domain was discretized using five different meshes ($N_1 - N_5$) with base cell sizes (h), 4 cm, 1 cm, 0.8 cm, 0.4 cm and 0.2 cm respectively. Following the (Celik et al. 2008) criteria, the global refinement ratio, r ($r = h_{course}/h_{fine}$) was chosen as 10, which remained above the suggested minimal threshold value of 1.3. The targeted discretization error parameter used in this work was the drag coefficient (C_d). It was chosen as it integrates pressure and shear forces over the entire surface of the fish-shaped body based on the following expression:

$$C_d = \frac{2F_d}{\rho U^2 A} \quad (2)$$

where F_d is the drag force acting on the fish body, ρ is the density of water, U is the freestream velocity (here taken at 0.50 cm upstream of the fish) and A is the projected surface area of the body in the vertical plane perpendicular to the freestream velocity. The discretization errors between two meshes as a function of C_d is reported in Table 3. In addition, the apparent order of the method (p_{avg}), extrapolated values ($C_{d,ext}^{j_i}$) between the successive meshes, the approximate relative error ($e_a^{j_i}$) and the grid convergence index (GCI) were also calculated to establish the final mesh resolution. The formulas and variables used to calculate the grid convergence parameters are provided in the supplementary material.

The second finest mesh with 5.8M cells was found to provide a stable estimation of the drag coefficient with a suitable relative error (Table 3). The summed fluxes over all elements stabilized to a constant minimum after 456 iterations, and data were obtained from this time step for further analysis of the boundary layer, pressure coefficient and shear stress distributions.

3.5. Numerical model validation

The swim tunnel model (numerical Model I) was validated based on the planar time-averaged velocity fields obtained from LDA measurements at 0.25 and 0.55 m/s. The velocity difference between the LDA measurements and simulated values was evaluated based on the standard deviation, which yielded a mean difference value of around 1 cm/s. Outliers were detected and removed using Bland-Altman plots (see supplementary material) with maximum deviations of up to 0.08 m/s, primarily in the anteriormost region of the tunnel working section. The measured and simulated streamwise velocities are illustrated in Figure 5 and the relative differences are shown in Figure 6.

4. Results

In this study, a numerical model of a gudgeon fish subject to steady flow was developed to investigate the near-body flow fields relevant to the superficial and canal lateral line sensing modalities. The physical fish-shaped body was placed within a commercial swim tunnel, and 2D LDA velocity measurements of the streamwise and lateral velocity distributions at the mid dorsal-ventral plane were used to tune and validate the numerical model. This section presents the results of the numerical analysis, focusing on the boundary layer velocity profile and thickness, as well as the pressure distribution and shear stresses, including their relationship to biological observations of the superficial and canal neuromast distributions on a gudgeon.

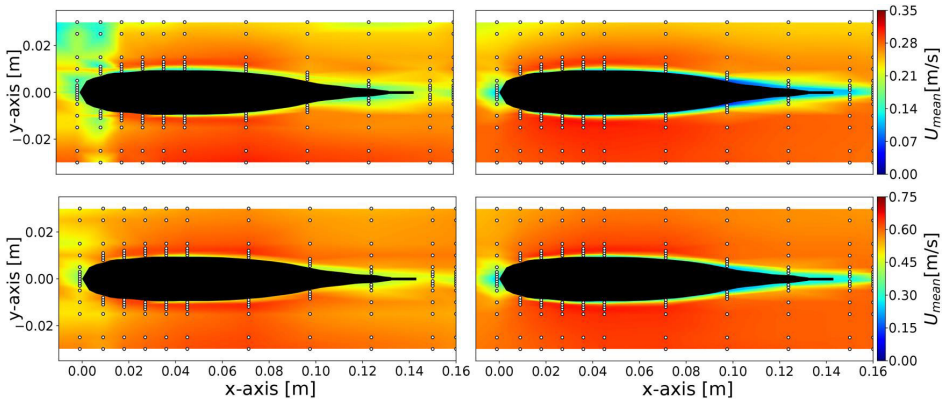


Figure 5. Mean streamwise velocity fields at the $z=0$ plane from the swim tunnel. Left panels: LDA measured velocity at $U=0.25$ m/s (upper) and $U=0.55$ m/s (lower). Right panels: Simulation results of the time-averaged streamwise velocity at $U=0.25$ m/s (upper) and $U=0.55$ m/s (lower).

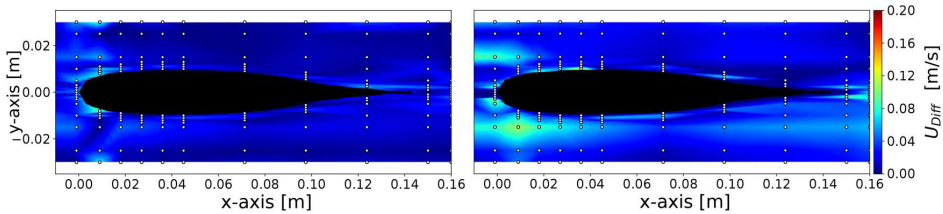


Figure 6. Relative velocity difference between swim tunnel LDA measurements and numerical simulations (Model I) around the gudgeon. Left: Relative velocity differences at $U=0.25$ m/s. Right: Relative velocity difference at $U=0.55$ m/s.

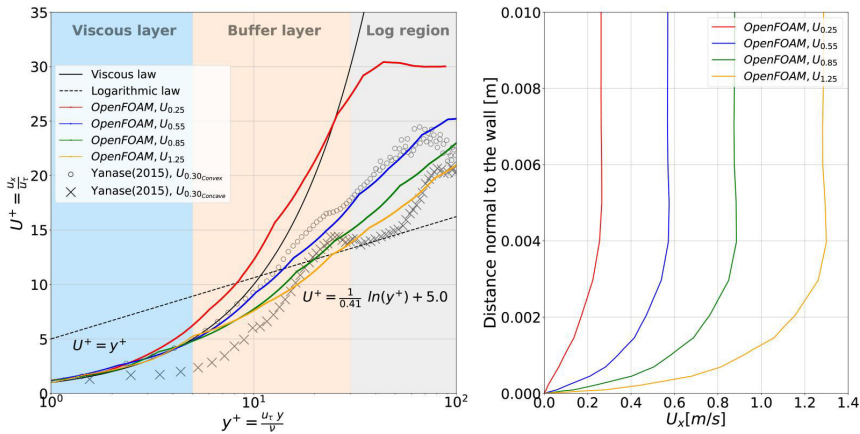


Figure 7. Left: Steady, dimensionless boundary layer profile envelopes in the posterior region (65% BL), highlighting the viscous sublayer (blue background), buffer layer (orange background) and log region (gray background color). The black circles (convex during gait) and crosses (concave during gait) of a swimming rainbow trout after (Yanase and Saarenrinne 2015), which were also obtained at 65% BL to provide a qualitative comparison between a static gudgeon and a swimming trout. The solid black line represents the viscous law and the dashed black line the classic logarithmic law of the wall. Right: Boundary layer velocity profiles of the four streamwise velocities (0.25, 0.55, 0.85, and 1.25 m/s) obtained perpendicular to the body at 65% BL.

4.1. Fish boundary layer

The boundary layer was resolved *via* numerical simulations using a RANS model by employing low Reynolds number wall functions to provide a wall

constraint on the turbulent viscosity ($\nu_t = 0$). The boundary layer simulation results were first evaluated (at 65% BL) by plotting (Figure 7) the dimensionless velocities, (U^+) and distances, (y^+) and

comparing the velocity profiles for each of the four flow rates evaluated in this work (0.25, 0.55, 0.85 and 1.25 m/s).

The model results of the boundary layer profiles indicate that inside the viscous sub-layer (i.e. $y^+ < 5$), the velocity is linearly increasing with the normal distance to the wall irrespective of the flow velocity. The flow inside the viscous sublayer is dominated by viscous forces and exhibits significant shear. The boundary layer profiles in the buffer layer increase in slope with decreasing freestream velocity. Within the buffer region, the turbulence production is maximum due to the outward ejection of low-speed flow near the body, which transport low-momentum fluid from the wall into the main flow. The buffer layer thus serves as an intermediary, establishing a link between the region characterized by prevailing viscous effects and the transport region, where inertial forces dominate. The flow behavior in the transport region exhibits a pronounced dependency on the Reynolds number, Re . In the case of a fully turbulent flow ($Re > 10^6$) over a flat plate, the velocity profile follows the classic law of wall, where the transport region is proportional to the logarithmic distance from the surface (Chen and Doi 2002). However in this study, the flow at the surface of the gudgeon is not yet fully turbulent, but rather transient i.e. $Re = 10^4$, for all four velocities investigated. Therefore the profiles do not strictly follow the logarithmic law on a significant part of the body. Despite all velocities laying in transitional state, with an increase in inlet velocity, the mean velocity tends to converge towards the classical curve shapes in the log-law region. Furthermore, the averaged velocity profiles shown here correspond to a streamwise location of 65% BL of the fish, where the flow is not fully developed. Further downstream, for example, close to the tail, the flow gets fully developed and the boundary layer exhibit turbulent behavior, as shown in Khan et al. (2024).

The authors were also interested in the potential effects of a steady swimming gait on the boundary layer velocity profile (65% BL), and overlaid observations (Figure 7) obtained from a swimming rainbow trout during the concave and convex portions of the gait cycle from (Yanase and Saarenrinne 2015). Although this data provides a rough and qualitative comparison, the (U^+) trend from the numerical model closely matched that obtained during the trout's convex body orientation during a swimming gait but was found to overestimate the (U^+) trend for the concave portion of the gait cycle.

Canal neuromasts, embedded in the upper dermal layer, and superficial neuromasts, originating from the surface and suspended in the flow, both

tend to reside within the boundary layer (McHenry and Liao 2014). The authors illustrate the boundary layer thickness at various locations along the body length of gudgeon Figure 8. Following the nomenclature and visualizations of Yanase and Saarenrinne (2015), the boundary layer regions are classified as anterior, pectoral, pelvic and posterior. The boundary layer thickness in each region was calculated using the classical approach of Schlichting and Gersten (2000). The results of the numerical model show that regardless of the flow rate, the boundary layer thickness is observed to be thinner in the anteriormost region of the gudgeon body, while it increases along the body and reaches its maximum thickness in the tail region. For instance, at 0.25 m/s velocity, the boundary layer was found to grow the most rapidly from 26% BL anterior region to 80% BL posterior region, reaching a local maximum of 6.04 mm near the tail. This trend was generally observed for all flow velocities. The boundary layer remained laminar in the anterior head region until reaching 67% BL. Corresponding to the known height of superficial neuromasts, assuming a standard value of 50 μm (Coombs et al. 2014), the boundary layer thickness in the head region is notably higher at all Reynolds numbers than the height of superficial neuromasts at the fish's surface. These observations align with the findings of the study conducted by McHenry et al. (2008), which suggests that the viscous drag within the boundary layer induces deflection of the elastic hair cells within the cupula of a superficial neuromast, and not the near-body velocity itself.

4.2. Pressure distribution

The spatial distribution of gudgeon canal neuromasts is concentrated in the anterior head region, where it diverges into multiple branches and extends as a single main branch laterally along the body (Schmitz et al. 2014). The distribution of the majority of canal neuromasts are illustrated in Figure 9 and overlaid with the normalized pressure coefficient C_p for the four velocities investigated in this work in order to qualitatively assess the sensitivity of the pressure-sensitive canal neuromast receptors for the gudgeon.

The individual positions of the superficial and canal neuromasts were obtained from a biological study of gudgeon (Schmitz et al. 2014), and each neuromast location was manually extracted from the reference work using WebPlotDigitizer. Subsequently, these points were superimposed onto the reconstructed 3D model surface of the gudgeon body used in this work, keeping the original vertical and horizontal aspect ratios of the neuromast

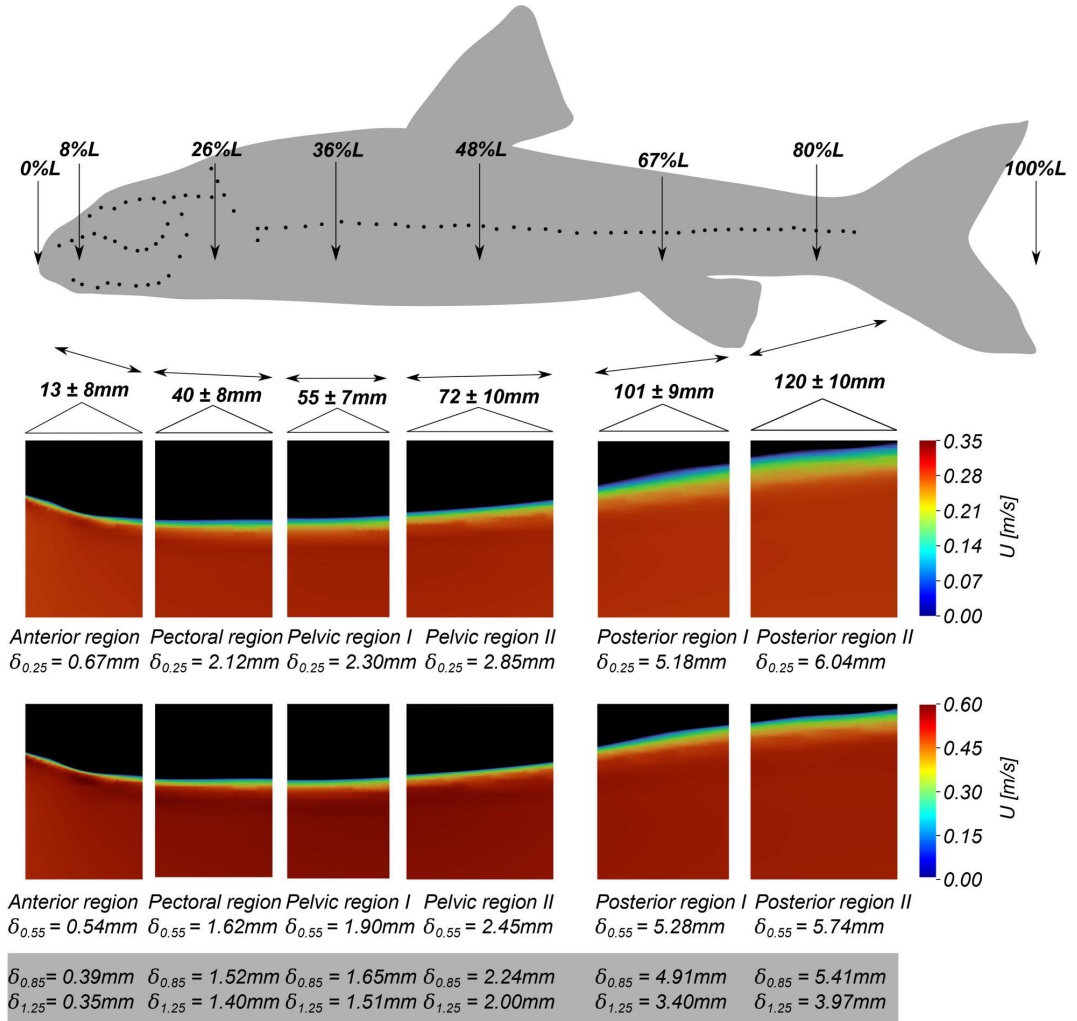


Figure 8. Near-body velocity fields around the stationary gudgeon model. The boundary layer thickness is reported at the anterior, pectoral, pelvic, and posterior regions at $U = 0.25, 0.55, 0.85,$ and 1.25 m/s velocity. The boundary layer thickness was obtained by determining the normal distance from the body at which the flow velocity is 99% U_∞ (Schlichting and Gersten 2000).

distribution as close to the original work as possible. The precise locations of the presented neuromasts are therefore reasonable approximations of a live gudgeon and are evaluated in terms of their relative position along the total body length to reduce position errors to the greatest extent possible.

It was observed that the most rapid change in C_p , corresponding to the region of highest pressure sensitivity occurs within the first 20% of the gudgeon body. These results are in good agreement with those presented in previous works which investigated the C_p distribution over a slender hydrofoil (Hassan 1992), a blind Mexican cave fish (Windsor et al. 2010) and a rainbow trout (Ristroph et al. 2015). Noticeable deviation in C_p from these works is the presence of a large secondary peak for all investigated velocities on the

gudgeon body between 6 % and again at 14 % of the body length. These peaks correspond to the regions immediately anterior to, and aligned with the gudgeon's eye, and are associated with the highest density of canal neuromasts. The Ristroph model (Ristroph et al. 2015) also included a detailed body geometry including the trout eye, and exhibits a similar secondary depression of the C_p at nearly the same location along the normalized body length, as shown in Figure 9.

The normalized pressure coefficient C_p describing the pressure to inertial forces around the gudgeon body remain identical for all flow rates. Whereas the dynamic pressure at the surface of the fish changes with respect to the Reynolds number (see Figure 10). The maximum dynamic pressure is observed to be at the stagnation region (at the nose) of fish and recedes

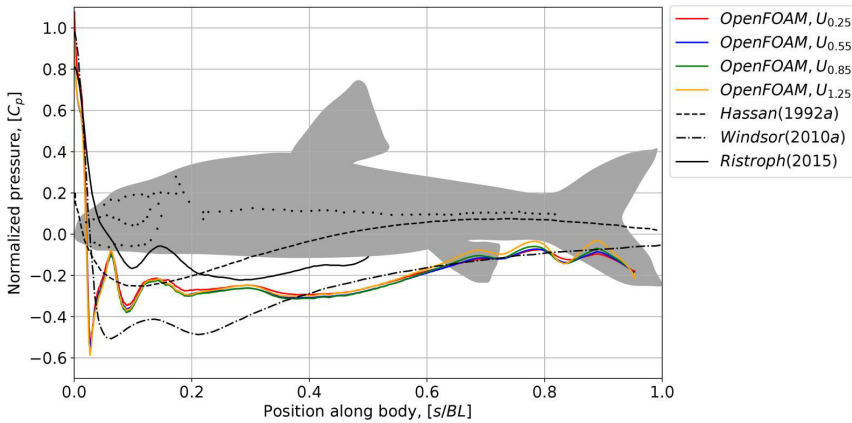


Figure 9. Pressure coefficient, C_p along the body length of the gudgeon fish model in comparison with previous studies. The C_p measurements are compared at the vertical plane ($s/BH = 0$) as of the normalized fish geometry. Black dots represent the estimated locations of the canal neuromasts, distributed on the surface of gudgeon adopted from the biological study of Schmitz et al. (2014).

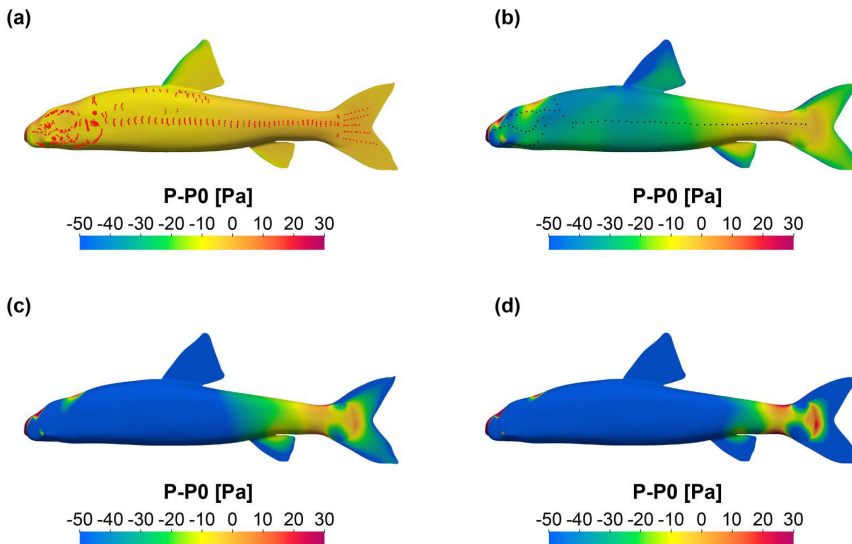


Figure 10. Comparison of the dynamic pressure ($P - P_0$) distribution over the gudgeon body at four freestream velocities. (a–d) Dynamic pressure on the surface of the gudgeon model body at 0.25, 0.55, 0.85 and 1.25 m/s. Top left: ($P - P_0$) distribution overlaid with the approximate positions of the lateral line receptors of a biological gudgeon specimen. Black dots represent the canal neuromasts and red dots the superficial neuromasts, adapted from (Schmitz et al. 2014).

around the head region along the body until it reaches 80% BL where it eventually rises due to the retardation of the flow velocity in the posterior tail region because of the streamlined body shape. The pressure coefficient is normalized by the kinetic energy of the fluid, and is therefore insensitive to changes in the freestream velocity. In order to better assess the regions of higher sensitivity to near-body pressure changes, the dynamic pressure (difference between freestream pressure and the pressure acting at a point on the body) was also plotted for all four velocities, as shown in Figure 10. An interesting finding emerged from this visualization, as it can be seen that the sensitivity of the dynamic pressure varies widely, depending on the freestream

flow velocity, where the anteriormost (head) and posterior regions around the caudal peduncle had the highest gradients for all flows investigated in this work. The increased density of superficial neuromasts in the posterior regions correspond well with the increased dynamic pressure in this region, indicating that they may benefit from the increased pressure gradients in these regions in addition to fluid shear stresses.

4.3. Shear stress distribution

As the boundary layer develops along the body, its thickness increases, and the wall shear stress decreases (Schlichting and Gersten 2000). Water

motion around the surface of fish exerts a constant drag force produced as a result of shear forces acting on the surface. Fish perceive the flow caused by the deflection of the cupulae through the depolarization of the membrane potential of hair cells within the cupulae. To better understand how a fish perceives its surroundings, we evaluated the net variation of the shear along the body in juxtaposition to the total percentage of superficial and canal neuromasts. A dimensionless shear stress coefficient at the surface of the gudgeon model along the mid dorsal-ventral plane was calculated and plotted with the percentage of neuromasts along the body of the gudgeon in Figure 11. The shear stress inside of the viscous sub-layer are a function of the viscosity and velocity gradient, and is driven by the velocity profiles resulting from changes in the freestream velocity, as shown in the rightmost panel of Figure 7.

In our observations, the concentration of both the canal and superficial neuromasts in gudgeon is found to be primarily situated within the anterior 20% of the total body length. The approximate locations of these neuromasts on the surface of the fish are adapted from (Schmitz et al. 2014). The plot depicting the total count of superficial and canal neuromasts in each 2.5 mm segment of the fish's body length is presented as a function of the percentage of each respective neuromast in Figure 11.

Along the gudgeon body, the distribution of both types of neuromasts was observed to concentrate in the the anteriormost region, where the coefficient of skin friction (C_f) was the highest. The anterior 20% BL contains above 47% of the total number of superficial neuromasts. Analogous to the pressure coefficient, the coefficient of skin friction (C_f) in this region also exhibited notable gradients. These findings suggest that the arrangement of superficial and canal neuromasts on the body of the gudgeon are not solely associated with near-body pressure

gradients, but may also correlate to regions with elevated shear stress and gradients thereof.

5. Discussion

Whether migrating, feeding, schooling, or avoiding predators, fish must contend with an extensive range of natural flow conditions for survival. The flow conditions encountered by fish are necessary but not sufficient to understand the fish's response to its physical environment. Due to this, we must also investigate how fish perceive and adapt to the dynamically changing flow environment *via* their sensory systems. However, measuring the near-body flow fields under laboratory conditions remains a persistent challenge. To address this difficulty, CFD can be used in some cases to provide fully-resolved and highly detailed information to better understand fish-flow interactions. However, this requires the development, testing, and validation of numerical models capable of accurately simulating boundary layers, pressure fields and shear stresses.

In this work, we propose numerical methods suitable for exploring the variability of near-body velocity profiles as well as the boundary layer thickness on a gudgeon-shaped body. In addition to the boundary layer, the pressure and shear stress distributions can be obtained from numerical simulations and compared with the locations of superficial and canal lateral line receptors. A major contribution of this work for future studies are the openly available LDA near-body velocity measurements required for the validation of the simulation as well as an open-body geometry, mesh, and numerical modelling setup which can be replicated in studies of other near-body flow fields. Although there were significant differences at some probe locations within the swim tunnel due to the measurement artifacts, the mean velocity difference between the measured and

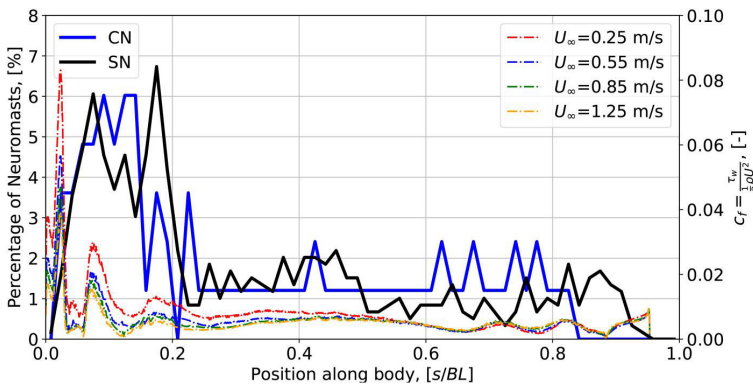


Figure 11. Dimensionless shear stress along the body of the gudgeon (right vertical axis) in relation to the distribution of neuromasts (left vertical axis) expressed as the percentage of canal neuromasts (CN) and superficial neuromasts (SN). The percentages were calculated based on biological observations from (Schmitz et al. 2014).

simulated gudgeon model after removing outliers remained at a suitably low level ($U_{diff} = 0.01$ m/s), substantiating the proposed numerical model setup. In general, the numerical approach used in this work can be considered suitable for any fish-shaped body where the boundary layer mesh region is refined such that $y^+ < 1$.

The resolved boundary layer model was evaluated for four flow velocities (0.25, 0.55, 0.85 and 1.25 m/s). Inside the boundary layer at all investigated Reynolds numbers, the flow within the known length scales of the superficial neuromasts (approx. 30 μm (Coombs et al. 2014)) remained laminar. The boundary layer thickness varies around the gudgeon body ranges from 0.67 mm in the anterior region (head region) to 6.04 mm in the posterior region (tail region) for the 0.25 m/s velocity. The variation of the boundary layer thickness along the fish's body length could be the source of perceiving the velocity gradients from the bulk flow. Based on these biological observations which report the notable features of the boundary layer, we encourage future studies to consider the potential effects of the boundary layer on fish lateral line sensing.

Pressure gradients are perceived by the canal neuromasts distributed on the fish surface. Previous studies have shown that the lateral line receptors are highly concentrated in the anterior head region 20% of the total body length and tails off further along the body (Ristroph et al. 2015). For the current study, the pressure distribution was analysed by plotting the pressure coefficient, C_p along the body length of the gudgeon model at the mid dorsal-ventral plane relative to the previous biological observation of neuromasts layout. The C_p along the body largely agree with the previous literature, and exhibits large gradients in the anterior head region at up to 20% of BL. Furthermore, the pressure coefficient plots illustrate that because C_p is normalized by the freestream kinetic energy, lateral distributions of C_p do not provide information related to potential changes in pressure-related lateral line sensitivity as a function of the freestream velocity. Instead, we recommend evaluating the dynamic pressure distribution over the body, which is highly sensitive to changes in the freestream flow velocity.

The variation in the dimensionless shear stress, C_f along the fish's body at different Reynolds numbers over the gudgeon body was found to correlate with higher percentages of both types of neuromasts, the majority of which were found within the first 20% of the fish's body length. This indicates that similar to the pressure coefficient, C_p the highest sensitivity to shear stresses likely occurs in the anteriormost region of the gudgeon head, corresponding to the location of the fish's eye. However,

in contrast to the pressure coefficient, C_f exhibited a greater degree of variability as a function of the flow velocity, where it was found that C_f tended to increase in magnitude with decreasing Reynolds numbers (and correspondingly, at lower flow velocities). Models of superficial neuromasts have indicated that their sensitivity is also dependent on their morphology, where increased flexural stiffness leads to a decrease in sensitivity (McHenry and van Netten 2007). These findings warrant further investigation by evaluating CFD-based shear stress distributions with biological observations of the placement and morphological characteristics of superficial neuromasts obtained in previous studies (Coombs and Montgomery 1994). Such investigations could plausibly evaluate if individual superficial neuromasts' sensitivity or groupings thereof are specifically tuned for fixed ranges of shear stresses. If the properties of superficial neuromasts of a given fish species and life stage were well-defined, it would then be possible to infer the flow conditions at which the fish are most sensitive.

A limitation of this work was the use of a stationary numerical approach. Although the time-averaged velocity, pressure and shear stress can provide valuable insights into the magnitude of lateral line stimuli, further work using time-resolved numerical models is required to explore spatio-temporal stimuli experienced by live fish. In addition, the authors wish to point out that the walls of the flume were smooth and modelled without any surface relief, which represents a highly synthetic flow environment. Stationary flow simulations including realistic bedforms with cobbles and woody debris can be used to model more complex hydrodynamic environments, and may lead to further insights into the lateral line sensing abilities of freshwater fish, even under stationary flow conditions.

6. Conclusion

This work is one of very few to provide open numerical models of a fish-shaped body, including laboratory-validated simulations for near-body flows under stationary conditions. Specifically, the open velocity data, mesh, and simulation setup from this work can be utilized by other researchers to improve the understanding of how fish perceive turbulent flows in natural and laboratory setups. The investigation of boundary layer thickness around the gudgeon revealed consistent variations along the body length across all Reynolds numbers. The anterior head region showed a thin, laminar boundary layer, while the posterior tail region exhibited a relatively thicker, turbulent boundary layer. Within the viscous region of the boundary layer at 65% BL,

velocity profiles remained linear with the normal distance from the wall at all incoming flow velocities. The velocity profiles varied in the logarithmic region generally conformed to the logarithmic law. The pressure coefficient evaluated at the mid dorsal-ventral plane of the gudgeon exhibits large gradients in the anterior 20% of the body length, and was found to agree with previous studies by Windsor et al. (2010) and Ristroph et al. (2015). The dynamic pressure was most sensitive in the anteriormost (head) and posterior (caudal) regions. Similarly, the shear stress coefficient exhibited the largest gradients in the anterior head region, near the eye. These findings suggest that the high-density distribution of SNs and CNs in the anteriormost head region are likely to correspond to the pressure gradients and local shear stresses experienced by a stationary gudgeon oriented into the principal flow direction.

Acknowledgement(s)

We are thankful for the donation of the gudgeon 3D fish geometry for scientific research by Dosch Design Kommunikationsagentur GmbH (Marktheidenfeld, Germany). The authors are very grateful to Dr. Arvo Tuvikene from the Estonian University of Life Sciences for providing the Loligo swim tunnel used in this study.

Disclosure statement

No conflict of interest has been reported by the authors.

Funding

The research work presented in this paper has received funding from European Union's Horizon 2020 research and innovation programme under the Marie Skłodowska-Curie grant agreement No [860800]. Maarja Kruusmaa's contribution was funded by EXCITE supported by the Estonian Centre of Excellence in IT, funded by the European Regional Development Fund Project No 2014-2020.4.01.15-0018. The laboratory work at Otto-von-Guericke-University Magdeburg was supported by means of the RETERO Project, funded by the German Ministry of Research and Education with funding No 16LW0169K.

Data availability statement

Additional data supporting the findings of this study and supplementary materials including the open numerical model and measurement data are available at Zenodo open repository: 10.5281/zenodo.8142218.

References

Adkins D, Yan Y. 2006. CFD simulation of fish-like body moving in viscous liquid. *J Bionic Eng.* 3(3):147–153. doi: 10.1016/S1672-6529(06)60018-8.

- Anderson E, McGillis W, Grosenbaugh M. 2001. The boundary layer of swimming fish. *J Exp Biol.* 204(Pt 1): 81–102. doi: 10.1242/jeb.204.1.81.
- Bassett DK, Carton AG, Montgomery JC. 2006. Flowing water decreases hydrodynamic signal detection in a fish with an epidermal lateral-line system. *Mar Freshwater Res.* 57(6):611–617. doi: 10.1071/MF05193.
- Bleckmann H. 2008. Peripheral and central processing of lateral line information. *J Comp Physiol A Neuroethol Sens Neural Behav Physiol.* 194(2):145–158. doi: 10.1007/s00359-007-0282-2.
- Bleckmann H. 2023. Life along the fish lateral line and beyond. *J Acoust Soc Am.* 154(2):1274–1286. doi: 10.1121/10.0020661.
- Celik IB, Ghia U, Roache PJ, Freitas CJ, Coleman H, Raad PE. 2008. Procedure for estimation and reporting of uncertainty due to discretization in CFD applications. *Trans ASME J Fluids Eng.* 130(7):078001.
- Chen Z, Doi Y. 2002. Numerical study on relaminarization in fish-like locomotion. *J SNAJ, Nihon Zousen Gakkai Ronbunshu.* 2002(191):9–16. doi: 10.2534/jjas-naoe1968.2002.9.
- Coombs S, Bleckmann H, Fay RR, Popper AN. 2014. The lateral line system. Vol. 48. New York (NY): Springer New York.
- Coombs S, Montgomery J. 1994. Function and evolution of superficial neuromasts in an Antarctic notothenioid fish. *Brain Behav Evol.* 44(6):287–298. doi: 10.1159/000113590.
- Dijkgraaf S. 1963. The functioning and significance of the lateral-line organs. *Biol Rev Camb Philos Soc.* 38(1): 51–105. doi: 10.1111/j.1469-185X.1963.tb00654.x.
- Egger B, Wiegler J, Seidel F, Burkhardt-Holm P, Emanuel Hirsch P. 2021. Comparative swimming performance and behaviour of three benthic fish species: the invasive round goby (*Neogobius melanostomus*), the native bullhead (*Cottus gobio*), and the native gudgeon (*Gobio gobio*). *Ecol Freshwater Fish.* 30(3):391–405. doi: 10.1111/eff.12592.
- Engelmann J, Hanke W, Bleckmann H. 2002. Lateral line reception in still-and running water. *J Comp Physiol A Neuroethol Sens Neural Behav Physiol.* 188(7):513–526. doi: 10.1007/s00359-002-0326-6.
- Hassan ES. 1992. Mathematical description of the stimuli to the lateral line system of fish derived from a three-dimensional flow field analysis. *Biol Cybern.* 66(5):443–452. doi: 10.1007/BF00197725.
- Helfman G, Collette BB, Facey DE, Bowen B. 2009. The diversity of fishes: biology, evolution, and ecology. New York: John Wiley & Sons.
- Jones PE, Svendsen JC, Börger L, Champneys T, Consuegra S, Jones JA, Garcia de Leaniz C. 2020. One size does not fit all: inter-and intraspecific variation in the swimming performance of contrasting freshwater fish. *Conserv Physiol.* 8(1):coaa126. doi: 10.1093/conphys/coaa126.
- Khan AH, Hussmann KR, Powalla D, Hoerner S, Kruusmaa M, Tuhtan JA. 2022. An open 3D CFD model for the investigation of flow environments experienced by freshwater fish. *Ecol Inf.* 69:101652. doi: 10.1016/j.ecoinf.2022.101652.
- Khan AH, Toming G, Hoerner S, Tuhtan JA. 2024. Comparison of near-body flow fields of a gudgeon and naca0013 profile. In Kalinowska MB, Mrokowska MM, Rowiński PM, editors, *Advances in hydraulic research*. Cham: Springer Nature Switzerland; p. 231–242.

- Kottelat M, Freyhof J. 2007. Handbook of European freshwater fishes. Berlin: Publications Kottelat, Cornol and Freyhof.
- Lauder GV, Drucker EG. 2004. Morphology and experimental hydrodynamics of fish fin control surfaces. *IEEE J Oceanic Eng.* 29(3):556–571. doi: [10.1109/JOE.2004.833219](https://doi.org/10.1109/JOE.2004.833219).
- Li G, Kolomenskiy D, Liu H, Thiria B, Godoy-Diana R. 2022. Hydrodynamical fingerprint of a neighbour in a fish lateral line. *Front Robot AI.* 9:825889. doi: [10.3389/frobt.2022.825889](https://doi.org/10.3389/frobt.2022.825889).
- Maitland P, Campbell R. 1992. Freshwater fishes of the British Isles. London: HarperCollins Publishers.
- Matsui K, Perez E, Kelly RT, Tani N, Jemcov A. 2021. Calibration of Spalart-Allmaras model for simulation of corner flow separation in linear compressor cascade. *J Glob Power Propuls Soc.* 1–16. doi: [10.33737/jgpps/135174](https://doi.org/10.33737/jgpps/135174).
- McHenry MJ, Liao JC. 2014. The hydrodynamics of flow stimuli, chapter 3. New York (NY): Springer; p. 73–98.
- McHenry MJ, Strother JA, van Netten SM. 2008. Mechanical filtering by the boundary layer and fluid-structure interaction in the superficial neuromast of the fish lateral line system. *J Comp Physiol A Neuroethol Sens Neural Behav Physiol.* 194(9):795–810. doi: [10.1007/s00359-008-0350-2](https://doi.org/10.1007/s00359-008-0350-2).
- McHenry MJ, van Netten SM. 2007. The flexural stiffness of superficial neuromasts in the zebrafish (*Danio rerio*) lateral line. *J Exp Biol.* 210(Pt 23):4244–4253. doi: [10.1242/jeb.009290](https://doi.org/10.1242/jeb.009290).
- Mogdans J. 2019. Sensory ecology of the fish lateral-line system: morphological and physiological adaptations for the perception of hydrodynamic stimuli. *J Fish Biol.* 95(1):53–72. doi: [10.1111/jfb.13966](https://doi.org/10.1111/jfb.13966).
- Montgomery J, Bleckmann H, Coombs S. 2014. Sensory ecology and neuroethology of the lateral line. In: Coombs S, Bleckmann H, Fay RR, Popper AN, editors. The lateral line system. Cham: Springer; p. 121–150.
- Owsianowski N, Kesel A. 2008. Drag reduction in schooling fish?—a CFD approach-comparative. *Biochem Physiol A Mol Integr Physiol. Bionik: Patente aus der Natur – Session Oberflächen/Haftung.* 150(3):S85. doi: [10.1016/j.cbpa.2008.04.148](https://doi.org/10.1016/j.cbpa.2008.04.148).
- Rapo MA, Jiang H, Grosenbaugh MA, Coombs S. 2009. Using computational fluid dynamics to calculate the stimulus to the lateral line of a fish in still water. *J Exp Biol.* 212(Pt 10):1494–1505. doi: [10.1242/jeb.026732](https://doi.org/10.1242/jeb.026732).
- Ristroph L, Liao JC, Zhang J. 2015. Lateral line layout correlates with the differential hydrodynamic pressure on swimming fish. *Phys Rev Lett.* 114(1):018102. doi: [10.1103/PhysRevLett.114.018102](https://doi.org/10.1103/PhysRevLett.114.018102).
- Schellart NA. 1991. Interrelations between the auditory, the visual and the lateral line systems of teleosts; a mini-review of modelling sensory capabilities. *Neth J Zool.* 42(2-3):459–477. doi: [10.1163/156854291X00450](https://doi.org/10.1163/156854291X00450).
- Schlichting H, Gersten K. 2000. Boundary-layer theory. Berlin Heidelberg: Springer-Verlag.
- Schmitz A, Bleckmann H, Mogdans J. 2014. The lateral line receptor array of cyprinids from different habitats. *J Morphol.* 275(4):357–370. doi: [10.1002/jmor.20219](https://doi.org/10.1002/jmor.20219).
- Spalart P, Allmaras S. 1992. A one-equation turbulence model for aerodynamic flows, chapter 1. *Aerosp Res Cent.* 1:5–21. pagesdoi: [10.2514/6.1992-439](https://doi.org/10.2514/6.1992-439).
- Spalding DB. 1961. A single formula for the “law of the wall”. *J Appl Mech.* 28(3):455–458. doi: [10.1115/1.3641728](https://doi.org/10.1115/1.3641728).
- Teyke T. 1988. Flow field, swimming velocity and boundary layer: parameters which affect the stimulus for the lateral line organ in blind fish. *J Comp Physiol A.* 163(1):53–61. doi: [10.1007/BF00611996](https://doi.org/10.1007/BF00611996).
- Tuhtan JA, Fuentes-Perez JF. 2018. How do fish sense flow?. 12th International Symposium of Echohydraulics, Tokyo-Japan.
- Van Netten SM. 2006. Hydrodynamic detection by cupulae in a lateral line canal: functional relations between physics and physiology. *Biol Cybern.* 94(1):67–85. doi: [10.1007/s00422-005-0032-x](https://doi.org/10.1007/s00422-005-0032-x).
- Vanderpham J, Nakagawa S, Senior A, Closs G. 2016. Habitat-related specialization of lateral-line system morphology in a habitat-generalist and a habitat-specialist New Zealand eleotrid. *J Fish Biol.* 88(4):1631–1641. doi: [10.1111/jfb.12912](https://doi.org/10.1111/jfb.12912).
- Wark A, Peichel C. 2010. Lateral line diversity among ecologically divergent threespine stickleback populations. *J Exp Biol.* 213(1):108–117. doi: [10.1242/jeb.031625](https://doi.org/10.1242/jeb.031625).
- White FM. 2006. Viscous fluid flow. London: McGraw-Hill.
- Windsor SP, McHenry MJ. 2009. The influence of viscous hydrodynamics on the fish lateral-line system. *Integr Comp Biol.* 49(6):691–701. doi: [10.1093/icb/icip084](https://doi.org/10.1093/icb/icip084).
- Windsor SP, Norris SE, Cameron SM, Mallinson GD, Montgomery JC. 2010. The flow fields involved in hydrodynamic imaging by blind Mexican cave fish (*Astyanax fasciatus*). Part I: open water and heading towards a wall. *J Exp Biol.* 213(Pt 22):3819–3831. doi: [10.1242/jeb.040741](https://doi.org/10.1242/jeb.040741).
- Windsor SP, Tan D, Montgomery JC. 2008. Swimming kinematics and hydrodynamic imaging in the blind Mexican cave fish (*Astyanax fasciatus*). *J Exp Biol.* 211(Pt 18):2950–2959. doi: [10.1242/jeb.020453](https://doi.org/10.1242/jeb.020453).
- Yanase K, Saarenrinne P. 2015. Unsteady turbulent boundary layers in swimming rainbow trout. *J Exp Biol.* 218(Pt 9):1373–1385. doi: [10.1242/jeb.108043](https://doi.org/10.1242/jeb.108043).
- Zauner G, Eberstaller J. 1999. Klassifizierungsschema der österreichischen flußfischfauna in bezug auf deren lebensraumsprüche. *Österreichs Fischerei.* 52(8/9):198–205.

Appendix 4

IV

A. H. Khan, K. R. Hussmann, D. Powalla, S. Hoerner, M. Kruusmaa, and J. A. Tuhtan, "Benchmarking 3D CFD for studies on turbulent flow around fish-shaped bodies," in *Proceedings of the 14th International Symposium on Ecohydraulics*, International Association for Hydro-Environment Engineering and Research, 2022

BENCHMARKING 3D CFD FOR STUDIES ON TURBULENT FLOW AROUND FISH-SHAPED BODIES

ALI HASSAN KHAN^{*1}, KARLA RUIZ HUSSMANN², DENNIS POWALA², STEFAN HOERNER²,
MAARJA KRUSMAA¹, JEFFREY A. TUHTAN¹

¹*Department of Computer Systems, Tallinn University of Technology, Ehitajate tee 5, 19086 Tallinn, Estonia*

²*Institute for Fluid Mechanics and Thermodynamics, Otto-von-Guericke Universität, Universitätsplatz 2, 39106 Magdeburg, Germany*

Abstract

Fish use their lateral line flow sensing system to locate food, avoid predators and to navigate in turbulent, dark and turbid waters. Biophysical studies of the lateral line indicate that fish are capable of sensing pressure, velocity, and acceleration of the near-body flow field, as well as their gradients at rates between 20 and 400 Hz. This allows fish to perceive minute changes in the hydrodynamic environment, referred to as “touch at a distance”. Previous investigations on near-body flows around fish have illustrated that basic fish-flow interactions can be evaluated using computational fluid dynamics (CFD). Despite these promising findings, there remains a gap in applying CFD to lateral line studies, largely because it is not known which turbulence models are suitable to simulate flows around fish-shaped bodies. To address this, RANS turbulence models are used to simulate a benchmark turbulent flow ($Re=6.8 \times 10^5$) around the body of a 3D printed brown trout in an open channel flume. Three different RANS models, the standard $k-\epsilon$, $k-\omega$ SST, and Spalart Allmaras were selected based on their applicability. The RANS model assessment was validated in a 1:1 physical open channel flume from laser doppler anemometer (LDA) measurements taken at 250 points distributed around the fish-shaped body, as near as 3 mm from the surface. Furthermore, the effects of modelled and resolved boundary layers were also evaluated. The results of this open source and open data benchmark study provide a numerical model can be used by others for further CFD research on fish flow interactions in fishways, rivers and possibly even to study turbine passage.

Keywords: *Fish habitat, turbulence models, boundary layer*

1 INTRODUCTION

A rapid decline in freshwater fish populations across Europe are caused in part by anthropogenic effects and climate change, forming a persistent threat to river ecology [1]. Understanding how fish perceive flow parameters such as velocity, pressure, and acceleration to navigate through the complex habitats is a critical, but poorly understood component of aquatic habitat preservation [2]. Fish have evolved a mechanosensory system to navigate through complex turbulent flows. This sensory system is comprised of tiny hair-like structures on the surface of fish known as superficial neuromasts, and is capable of detecting as low as 20 Hz of water fluctuations, and canal neuromasts can detect higher frequencies up to 400 Hz [3]. Fish can sense upstream and in the lateral direction up to 20% of their body length, efficiently navigating through highly turbulent flows [4].

Turbulence in natural river habitats can be characterized by four major elements: intensity, periodicity, orientation, and scale [5]. Woody material, boulders, vegetation and local bedforms generate turbulence in the form of eddies which cascade from large to small in space and time [6], [7]. The spatial scales of these eddies can be up to several meters and the time scale of turbulence eddies over which it interrupts the mean flow, ranges from a small i.e., Kolmogorov microscale to large convective time scales. In addition, the riverbeds in natural environments are highly heterogeneous and non-uniform which disrupts the mean flow resulting in a non-uniform boundary layer and turbulent eddies which affects the fish’s swimming efficiency. A fish’s response to unpredictable turbulence can therefore also be unpredictable. Fish may take advantage of the turbulence during the normal swimming gait cycle to improve their swimming efficiency. However, it is also possible that turbulent eddies decrease the overall swimming performance [8], [9]. A recent study shows that even if there are similar turbulence levels in different locations, the fish responses will not be the same [2]. This is likely because in addition to turbulence, other factors can play a crucial role in the fish’s behavioral response to flow, including illumination, sound and scent. Multiple studies focus on quantifying fish habitats from the observer’s perspective

do not typically consider how a fish perceives its environment [10]. To begin to address this issue, studies of flow fish interactions are required which describe the flow fields around fish-shaped bodies including the velocity, pressure and their gradients.

Recent advancement in computer technology and the up-gradation of computational resources, has increased the possibility to model such complex flows through numerical approximations. Computational fluid dynamics (CFD) has shown promising results in the past modelling river flows on large scales [11]. But at the microscale, the boundary layer contributes towards flow separation on the body, as well as vortex generation in the wake [12]. Previous studies have emphasized fish swimming kinematics as well as the propulsion and drag forces [13]–[15]. However, very few studies have discussed how these may relate to a fish’s sensing capabilities. For example, [16] tested a blind Mexican fish (*Astyanax fasciatus*) facing a wall laterally or approaching a wall and found that it can sense up to 20% of its body length (BL) at normal swimming speeds. Similarly [12] showed that 3D simulations can be used to detect the spatial patterns of pressure gradients around fish bodies generated by a dipole source. Both studies highlighted the significance of the boundary layer at the body surface to detect the near-body pressure gradients stimulating the lateral line.

In this work, a 3D CFD study around a fish-shaped body provides a benchmark using Reynolds Averaged Navier-Stokes (RANS) turbulence models to estimate the velocity and pressure fields. Furthermore, we present fish and flow interaction in the presence of a boundary layer and the investigate the significance of resolving the boundary layer in perceiving the flow fluctuations on the fish body surface. The significant contribution of this work is the open-source numerical model it provides, which can be applied by future researchers in new CFD studies. This work is significant because it is the first to assess the effects of boundary layer and turbulence modelling on flow fields around fish-shaped bodies using the RANS approach.

2 METHODOLOGY

2.1 Numerical Modelling

An open-source numerical model was developed in the OpenFOAM framework, modelling the flow around a steady fish in an open channel flume. OpenFOAM is a C++ toolbox for solving continuum mechanics problems with the efficacy of customizing the numerical solvers, and pre-and post-processing utilities. Modelling a section of a flume, with a particular interest in the spatial flow parameters, reduces the computational cost and time. Therefore, a section of flume with dimensions $1850 \times 800 \times 600 \text{ mm}^3$ was modelled in this study (Fig 1). In this work, only RANS turbulence models are taken into account for a single-phase flow due to their robustness and low computational costs. A numerical model using Large Eddy Simulation (LES) or Direct Numerical Simulation (DNS) would require a very fine mesh discretization of the flume, which intuitively requires more computational resources and time. We tested three different RANS turbulence models; the *Standard k- ϵ* model, *k- ω SST* model, and the *Spalart Allmaras* model. Modelling physical flow problems in the finite volume method (FVM) assures that the pressure velocity coupling at the center of each cell. The pressure velocity coupling is solved through an iterative solution strategy, ‘Semi-implicit method of pressure linked equations (SIMPLE)’ [17]. An advantage of using this iterative solution strategy is that it can be applied to simulations with high Courant-Friedrichs-Lewy (CFL) numbers. As the primary focus of this study is to simulate the boundary layer (BL) around the surface of fish, with a very fine mesh (with cell size up to a few mm). Simulating the boundary layer is an important consideration for fish sensing because within the BL, the viscous forces dominate over inertial forces and large pressure gradients permeate the flow field. These flow field gradients are key factors in determining the fish’s active sensory space. Thus, five different model setups are purposed in this study corresponding to the turbulence models with the possibility of both resolving and modelling the boundary layer at the surface of fish. All five model setups were validated later with the experimental data obtained. The summary of these model setups is provided in Tab 1.

Tab 1. Overview of the numerical model setups investigated in this work as combinations of near-wall treatments and RANS turbulent models.

Near-wall treatment	RANS turbulence models		
	Standard $k-\epsilon$	$k-\omega$ SST	Spalart Allmaras
Boundary layer Unresolved	BL modelled Wall treatment through wall functions ($30 < y^+ < 300$)	BL modelled Wall treatment through wall functions ($30 < y^+ < 300$)	-
Boundary layer Resolved	BL fully resolved ($y^+ < 1$)	BL fully resolved ($y^+ < 1$)	BL fully resolved ($y^+ < 1$)

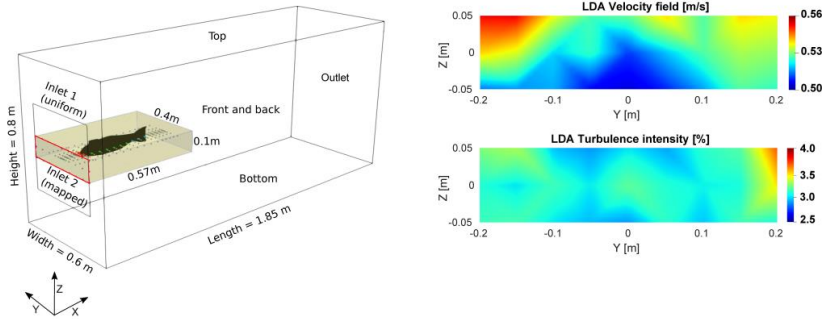


Fig 1. Overview of the numerical and the experimental domains; (Left) fish-shaped body, the spatial distribution of measurement points around the physical model and at the upstream boundary of the CFD model. (Right) Inlet velocity and turbulence distributions at the inlet patch (red rectangle in the left panel) were measured with LDA and later applied as a mapped inlet condition in the numerical model.

For resolved boundary layer cases, mesh discretization in the vicinity of fish is very fine ($y^+ < 1$). In these model cases, low Reynolds wall functions are used to model the flow within the boundary layer. Whereas for modelled boundary layer cases, high Reynolds wall functions are enacted in OpenFOAM.

2.1.1 Geometry and mesh

A three-dimensional model of a brown trout (*Salmo trutta*) was generated in computer-aided design (CAD) software. This model was imported into OpenFOAM as an *stl* file which was later snapped into the domain and meshed with hexahedral cells of different sizes. The mesh cell size increases from the surface of fish to outer domain boundaries. The meshing strategy followed a two-step approach, in the first step the flume domain was generated with a *blockMesh* utility and discretized with hexahedral cells around a cavity, in the second step the fish was snapped and discretized with hexahedral cells through *cfMesh* utility which was later merged into that cavity and stitched with the existing mesh (Fig 2). The whole meshing algorithm was automated through a bash file in the Linux system to save time. For a grid independence study, five different mesh sizes were generated with the cell size ranging between 0.1 m to 0.01 m.

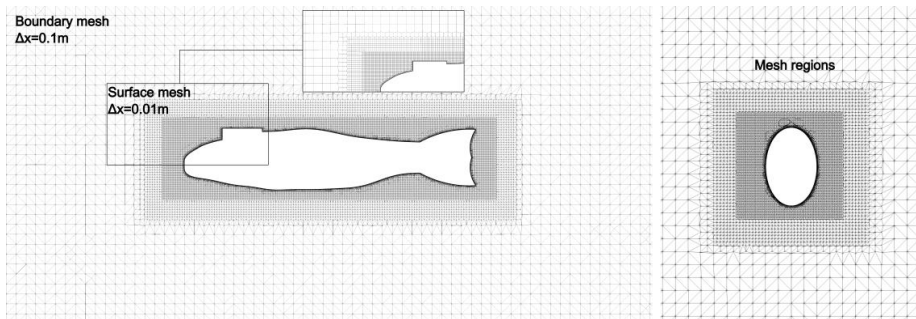


Fig 2. Mesh discretization of the domain: (Left) frontal section showing the boundary mesh and fine discretization of mesh boundary layers around the surface of fish (zoomed section illustrates the boundary layers around the fish body). (Right) Lateral discretization of mesh with different mesh regions around the fish body.

2.1.2 Boundary conditions

Specification of the boundary conditions as well as the initial values at the inlet and outlet patches in a numerical setup for simulating physical flow problems is the first step of CFD analysis. Flow within the flume is highly turbulent ($Re = 6.8 \times 10^5$ at the fish surface), with a time-averaged velocity of 0.54 ms^{-1} and turbulent intensity of 3.16 %. For the development of a numerical model representing similar flow characteristics, the inlet patch is divided into two sub-patches. The inlet patch upstream of the fish head is specified with the flow velocity mapped from the LDA experiments through a second-order polynomial else the mean velocity was enacted in the free stream surrounding region. A no-slip boundary condition was applied to all the patches except the atmospheric patch where a slip boundary was applied.

2.2 Experimental Setup

A lab experimental facility was designed at Otto-von-Guericke University Germany in which 2D LDA measurements were recorded around a rigid 3D printed fish model for velocity and turbulence intensity in a 10 m long and 1.2 m wide flume. The water depth inside the flume was kept constant at a height of 0.68 m. The LDA system was projected from underneath the flume with optical access to 0.6 m in length, 0.53 m in width, and 0.26 m in height. The LDA velocity measurements were recorded at 253 locations in total with an increasing sample density closer to the surface of the fish. This includes the measurements taken upstream, near the body, and in the wake region. To ascertain the velocities in the vicinity of the fish body within the boundary layer the closest distance was set to 3mm along the body and 2.5mm along the tail. Single plane measurements (at $z = 0$) were taken into account to demonstrate the velocity tendency around the fish body. Within the scope of this study, only U_x and U_y velocities are considered (neglecting the U_z). The measurements are grouped into head, body, and tail regions of interest to compare the performance of wall treatments and turbulence models. To ensure the reproducibility over several multiple days of measurements, a grid of 18 measurement points upstream of fish was analyzed at the beginning of each experiment. The LDA data was post-processed and stored with a commercial software BSA Flow using a Dantec Flow Explorer DPSS 300 2D which allowed for the acquisition of raw data at a single measurement location. It also calculates the signal quality for each measurement based on the signal-to-noise ratio (SNR) which was used for LDA qualitative assessment before actual measurements.

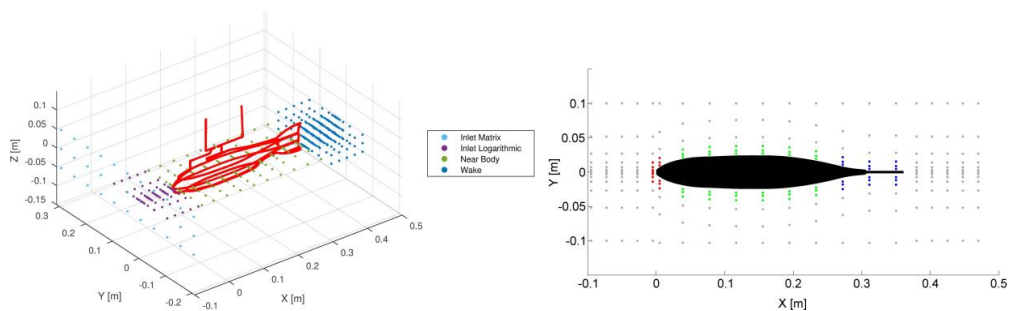


Fig 3. Left: Position of all measurement points in the 3D experimental domain indicated by each targeted group. Right: Velocity measurements and numerical probes around the fish body in the 2D plane with three regions: head (red), body (green), and tail (blue) inside the boundary layer. Gray points further away from the body surface correspond to LDA measurement locations not taken into account for boundary layer measurement.

2.3 Results and discussions

2.3.1 Mesh and time sensitivity analysis

The mesh sensitivity analysis was achieved through ASME criteria [18]. The evaluation factor chosen for mesh sensitivity analysis was, 'drag coefficient (c_d)'. It is convenient to consider the drag coefficient as an evaluation metric because it manifests the pressure and shear forces over the entire surface of the fish body. Five different setups with varying mesh sizes were tested for the calculation of drag coefficient and analyzed through grid convergence index (GCI). It is worth mentioning here that for all setups it was ensured that the y^+ remained in the viscous range.

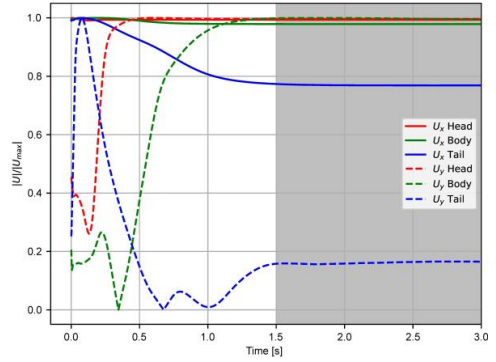
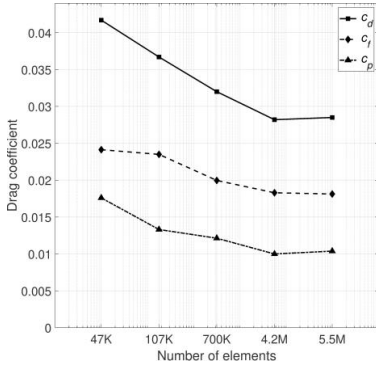


Fig 4. Left: Evolution of drag (c_d), friction drag (c_f), and pressure drag (c_p) coefficients for increasing mesh number of cells (abscissa in logarithmic scale). Right: Convergence of the streamwise and lateral velocity components within the boundary layer (Fig 3) over a simulation time of 3 s.

The drag coefficient (c_d) decreases with the increase in the number of mesh and converges at 4.2M. Thus, the model setup with 4.2M cells was opted for final simulation for validation purposes. A time-sensitivity analysis was performed to analyze the fluctuation of velocities in the vicinity of the fish surface. The total time of simulation was set to 3.0 s but the velocities (streamwise U_x and lateral U_y) converged after 1.5 s. Therefore, all validations were carried out after 1.5 s of the time interval.

2.3.2 Resolved and modelled boundary layer

Flow characteristics are mainly dependent upon the type of flow. Studies with fluid-low interactions generally require the boundary layer to be resolved with a fine resolution mesh. Different RANS turbulence models have different approaches for model wall-bounded flows. The streamwise and lateral velocity measured through LDA measurements and simulations models for Standard $k-\epsilon$, $k-\omega$ SST, and Spalart Allmaras, are compared for probe points within a distance of 0.06 m from the boundary layer. Fig 5. shows a comparison of absolute velocity difference within the boundary layer between the simulated models (both resolved and unresolved) and LDA measurements. From the comparison, we found that the Spalart Allmaras model was capable of simulating the boundary layer effectively with a maximum velocity difference of 0.07m for streamwise velocity (U_x). Whereas for lateral velocities, the results did not show a substantive difference across the model setups. Overall, the resolved boundary layer cases showed less absolute difference than the modelled cases.

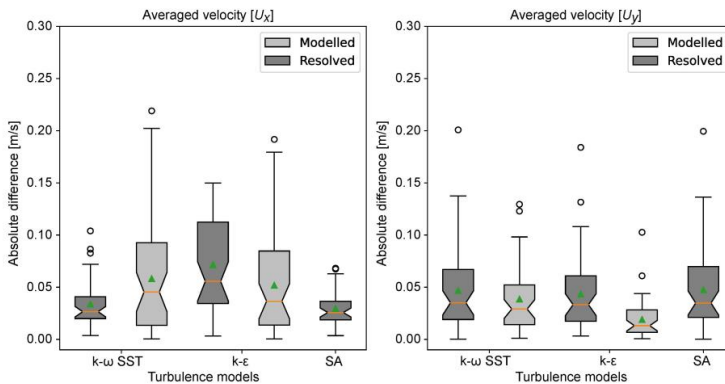


Fig 5. Box plots of the absolute difference between the time-averaged velocities (U_x and U_y) for the three turbulence models, compared to the LDA measurements. The boxplot indicates the inter-quartile range, mean (green triangle), median (orange line), and outliers are shown as black circles. The fill color indicates either resolved or modelled boundary layers.

2.3.3 Turbulence models and wall modelling

All turbulence models have performed equally in the free stream, but major differences emerge at the surface of fish where $k-\omega$ SST and Spalart Allmaras performed better as compared to the Standard $k-\epsilon$ model. The $k-\omega$ SST and Spalart Allmaras had minor divergence to the LDA measurements between streamwise velocity. Among all three turbulence models, Spalart Allmaras performed best. Fig 6. illustrates the normalized streamwise velocity

profiles in three different regions along the body of fish. Within the boundary layer, the performance of the *Standard k-ε* model turbulence model around the head region was not satisfactory.

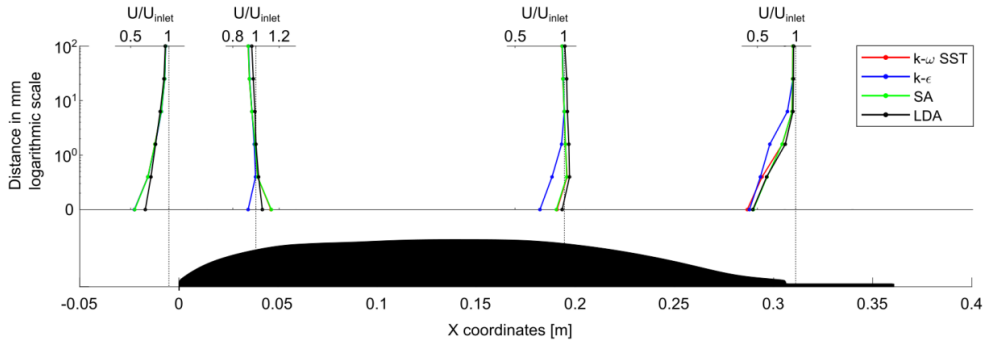


Fig 6. Normalized streamwise velocity profiles at three different regions along the fish-shaped body for all turbulence models and LDA measurements. At some locations, the *k-ω SST* model overlaps the *Spalart Allmaras* model and is not visible.

2.4 Conclusion

Modelling turbulent flows around fish-shaped bodies require special care in handling the boundary layer. Using wall functions to modify the wall shear stress empirically and satisfy the physics of flow across the boundary layer, adeptly bridges the flow between the inner region and the fully turbulent flow. An alternative way to determine the wall shear stress is by resolving the gradient near the wall by fine resolution of the mesh. In turbulent flows with a high Reynolds number, the boundary layer gets thinner resulting in a gradient at the wall steeper which needs smaller cells to resolve the gradient. In this study, a fine resolution of mesh with mesh size up to 1mm at the surface of fish was generated to get the first mesh node inside the viscous layer ($y^+ < 1$) with additional layers at a thickness ratio of 1.15. Subsequently, a coarser mesh with the first node ($30 < y^+ < 300$) in the logarithmic layer was generated for the modelled boundary layer case. Simulation results for streamwise and lateral velocity for both modelled and resolved cases support the argument that resolving the boundary layer provides better results in analyzing flow characteristics for all turbulence models. It is worth mentioning that the *Spalart Allmaras* model can only be applied for the resolved cases. The modelled cases in general show more divergence from the LDA measurements as compared to resolved cases. Thus, for future studies, we recommend resolving the boundary layer while simulating turbulent flow around fish-shaped bodies.

Among the tested RANS turbulence models, the *Spalart Allmaras* model performance was the best. The *k-ω SST* model also performed well, except in the tail region where it did not accurately estimate the position of flow separation. The *Standard k-ε* model performance was substandard in the regions of high-pressure gradients.

This research is significant because it spotlights the implication of resolving the boundary layer for simulating fish in a highly turbulent environment. Fish senses minute fluctuations inside the boundary layer through superficial neuromasts and studies show that they are predominantly concentrated inside the head region [19]. Thus, it is important to simulate the flow across the boundary layer by resolving it and deploying the *Spalart Allmaras* turbulence model for modelling turbulent flows around fish-shaped bodies [20].

Future studies can implement these modalities on more diverse species of fish with inclusion of fish undulatory motion to explore the flow parameters of the fish body. Understanding flow characteristics velocity or pressure on the 3D complex surface of fish would help us to find how fish perceive its environment in nature.

3 ACKNOWLEDGMENTS

The research work presented in this paper has received funding from European Union Horizon 2020 Research and Innovation Programme under the Marie Skłodowska-Curie Actions, Grant Agreement No. 860800. Laboratory measurements were conducted as part of the RETERO project, sponsored by the German Federal Ministry of Education and Research Grant no. 161L0152A. Jeffrey A. Tuhtan's contribution was funded by the Estonian Research Council Grant PRG1243 and Maarja Kruusmaa was funded by EXCITE supported by the Estonian Centre of Excellence in IT, funded by the European Regional Development Fund Project nr 2014.2020.4.01.15-0018. The authors are grateful to M. Yanneck Kiiski for the design and 3D printing of the fish geometry and the CAD model of the laboratory flume.

REFERENCES

- [1] A. Marion *et al.*, “Aquatic interfaces: a hydrodynamic and ecological perspective,” <http://dx.doi.org/10.1080/00221686.2014.968887>, vol. 52, no. 6, pp. 744–758, Nov. 2014, doi: 10.1080/00221686.2014.968887.
- [2] D. L. Smith, R. A. Goodwin, J. M. Nestler, and R. Andrew Goodwin, “Relating Turbulence and Fish Habitat: A New Approach for Management and Research,” *Rev. Fish. Sci. Aquac.*, vol. 22, no. 2, pp. 123–130, 2014, doi: 10.1080/10641262.2013.803516.
- [3] J. F. Fuentes-Pérez *et al.*, “Current velocity estimation using a lateral line probe,” *Ecol. Eng.*, vol. 85, pp. 296–300, Dec. 2015, doi: 10.1016/J.ECOLENG.2015.10.008.
- [4] S. P. Windsor, S. E. Norris, S. M. Cameron, G. D. Mallinson, and J. C. Montgomery, “The flow fields involved in hydrodynamic imaging by blind Mexican cave fish (*Astyanax fasciatus*). Part II: gliding parallel to a wall,” *J. Exp. Biol.*, vol. 213, no. 22, pp. 3832–3842, Nov. 2010, doi: 10.1242/JEB.040790.
- [5] R. W. J. Lacey, V. S. Neary, J. C. Liao, E. C. Enders, and H. M. Tritico, “The ipos framework: Linking fish swimming performance in altered flows from laboratory experiments to rivers,” *River Res. Appl.*, vol. 28, no. 4, pp. 429–443, May 2012, doi: 10.1002/RRA.1584.
- [6] J. B. Allen and D. L. Smith, “Characterizing the Impact of Geometric Simplification on Large Woody Debris Using CFD,” *Int. J. Hydraul. Eng.*, vol. 2012, no. 2, pp. 1–14, 2012, doi: 10.5923/j.ijhe.20120102.01.
- [7] D. W. Crowder and P. Diplas, “Vorticity and circulation: spatial metrics for evaluating flow complexity in stream habitats,” <https://doi.org/10.1139/f02-037>, vol. 59, no. 4, pp. 633–645, 2011, doi: 10.1139/F02-037.
- [8] A. I. Lupandin, “Effect of Flow Turbulence on Swimming Speed of Fish,” *Biol. Bull. 2005 325*, vol. 32, no. 5, pp. 461–466, Sep. 2005, doi: 10.1007/S10525-005-0125-Z.
- [9] J. C. Liao, “A review of fish swimming mechanics and behaviour in altered flows,” *Philos. Trans. R. Soc. B Biol. Sci.*, vol. 362, no. 1487, pp. 1973–1993, Nov. 2007, doi: 10.1098/RSTB.2007.2082.
- [10] G. Trinci, G. L. Harvey, A. J. Henshaw, W. Bertoldi, and F. Hölker, “Turbulence, instream wood and fish: Ecohydraulic interactions under field conditions,” *Ecohydrology*, vol. 13, no. 5, p. e2211, Jul. 2020, doi: 10.1002/ECO.2211.
- [11] M. Nones, M. Guerrero, N. Ruther, and S. Baranya, “CFD modelling of Po River morphodynamics affected by bridge piers,” *Geophys. Res. Abstr.*, vol. 19, pp. 2017–2269, 2017.
- [12] M. A. Rapo, H. Jiang, M. A. Grosenbaugh, and S. Coombs, “Using computational fluid dynamics to calculate the stimulus to the lateral line of a fish in still water,” *J. Exp. Biol.*, vol. 212, no. 10, pp. 1494–1505, May 2009, doi: 10.1242/JEB.026732.
- [13] D. Adkins and Y. Y. Yan, “CFD Simulation of Fish-like Body Moving in Viscous Liquid,” *J. Bionic Eng.*, vol. 3, no. 3, pp. 147–153, Sep. 2006, doi: 10.1016/S1672-6529(06)60018-8.
- [14] N. Thekkethil, A. Sharma, and A. Agrawal, “Unified hydrodynamics study for various types of fishes-like undulating rigid hydrofoil in a free stream flow,” *Phys. Fluids*, vol. 30, no. 7, p. 077107, Jul. 2018, doi: 10.1063/1.5041358.
- [15] M. M. Macias, I. F. Souza, A. C. P. Brasil Junior, and T. F. Oliveira, “Three-dimensional viscous wake flow in fish swimming - A CFD study,” *Mech. Res. Commun.*, vol. 107, p. 103547, Jul. 2020, doi: 10.1016/J.MECHRESCOM.2020.103547.
- [16] S. P. Windsor, S. E. Norris, S. M. Cameron, G. D. Mallinson, and J. C. Montgomery, “The flow fields involved in hydrodynamic imaging by blind Mexican cave fish (*Astyanax fasciatus*). Part I: open water and heading towards a wall,” *J. Exp. Biol.*, vol. 213, no. 22, pp. 3819–3831, Nov. 2010, doi: 10.1242/JEB.040741.
- [17] A. Outhwaite, “Numerical Solutions for Pressure-Velocity Coupling in Steady Flow Systems using the SIMPLE Algorithm,” pp. 1–24, 2007.
- [18] I. B. Celik, U. Ghia, P. J. Roache, C. J. Freitas, H. Coleman, and P. E. Raad, “Procedure for estimation and reporting of uncertainty due to discretization in CFD applications,” *J. Fluids Eng. Trans. ASME*, vol. 130, no. 7, pp. 0780011–0780014, Jul. 2008, doi: 10.1115/1.2960953/444689.
- [19] L. Ristroph, J. C. Liao, and J. Zhang, “Lateral line layout correlates with the differential hydrodynamic pressure on swimming fish,” *Phys. Rev. Lett.*, vol. 114, no. 1, p. 018102, Jun. 2015, doi: 10.1103/PHYSREVLETT.114.018102/FIGURES/4/MEDIUM.
- [20] A. H. Khan, K. Ruiz Hussmann, D. Powalla, S. Hoerner, M. Kruusmaa, and J. A. Tuhtan, “An open 3D CFD model for the investigation of flow environments experienced by freshwater fish,” *Ecol. Inform.*,

vol. 69, p. 101652, Jul. 2022, doi: 10.1016/J.ECOINF.2022.101652.

Appendix 5

V

A. H. Khan, G. Toming, S. Hoerner, and J. A. Tuhtan, "Comparison of near-body flow fields of a Gudgeon and NACA0013 profile," in *Advances in Hydraulic Research* (M. B. Kalinowska, M. M. Mrokowska, and P. M. Rowiński, eds.), pp. 231–242, Springer Nature Switzerland, 2024

Comparison of Near-Body Flow Fields of a Gudgeon and NACA0013 Profile



Ali Hassan Khan, Gert Toming, Stefan Hoerner, and Jeffrey A. Tuhtan

Abstract Hydrodynamic sensing using the lateral line system allows fish to detect, localize and classify minute flow field fluctuations filtered through the boundary layer. These near-body flow fields provide valuable information about the current state of the flow environment during a swimming gait cycle and at rest. Previously, fish-like sensors have been developed for ecological studies using a simplified NACA0013 axisymmetric streamlined profile, which is a considerable simplification compared to the geometry of fish. To investigate potential differences in the near-body flow field resulting from the differences in body geometry, a comparison of the flow fields around a NACA0013 profile and a digital model of a bottom-dwelling gudgeon (*Gobio gobio*) fish (length = 15 cm) was performed. The time-averaged velocity fields around a gudgeon body and NACA0013 profile were obtained numerically using the open-source tool OpenFOAM at 0.25 and 0.55 ms⁻¹. The results show that the streamwise velocity distribution in the lateral direction around the gudgeon body has minor deviations from those observed around the NACA profile. Specifically, near the surface of the fish-shaped body and NACA, a well-developed boundary layer was observed, with turbulent behavior in the posterior region near the tail fin. The results of this study indicate that the use of the NACA profile for boundary layer studies in ecologically relevant flows would be a suitable approximation of the gudgeon.

A. H. Khan (✉) · G. Toming · J. A. Tuhtan
Department of Computer Systems, Tallinn University of Technology, Ehitajate Tee 5, 19086
Tallinn, Estonia
e-mail: ali.khan@taltech.ee

S. Hoerner
Institute for Fluid Mechanics and Thermodynamics, Otto-von-Guericke Universität,
Universitätplatz 2, 39106 Magdeburg, Germany

1 Introduction

Hydrodynamic sensing is common to many aquatic vertebrates and is used to navigate through complex environments, locate prey, and avoid predators. It is also essential for social interactions such as schooling behavior in fish by allowing individuals to locate their fellows (Bleckmann and Zelick 2009). The lateral line sensory system in fish detects the relative movement between the fish's body and the surrounding water (Dijkgraaf 1963). The neuromast sensory organs of the lateral line system are further classified as superficial neuromasts and canal neuromasts. Superficial neuromasts are present at the body surface and are sensitive to the velocity of the surrounding fluid. In contrast, canal neuromasts make use of tunnel-like structures beneath the fish's skin and are sensitive to pressure gradients (Mogdans 2019). Ecological studies on fish sensing primarily focus on the lateral line system and the flow field quantities of velocity, pressure, acceleration, and their gradients to investigate the hydrodynamic sensing capabilities of fish.

Previous works have made use of simplified fish body geometries to investigate the sensory capabilities of the lateral line. Fish behavioral studies revealed that a blind fish is capable of detecting and recognizing objects at a distance. These empirical derivations are based on a fish of disc-like shape with large flat sides (Hassan 1985). Following this study, a range of different fish-shaped analogies was investigated to determine the spatial and temporal distribution of stimuli to the lateral line system from flow fields (Hassan 1992a, 1992b, 1993). With the advancement in computational power and resources, the flow fields around fish-shaped bodies can now be simulated through computational fluid dynamics (CFD). One of the earliest three-dimensional models (3D) of fish-shaped bodies was simulated including the dorsal and pectoral fins to investigate the flow fields in the presence of stimuli (Rapo et al. 2009). The fish model used in these simulations was a simplified body of a Mottled Sculpin. The author of this study recommended considering the effect of the boundary layer (BL) at the surface of fish for fish-sensing studies. More recent contributions to fish sensing using CFD (Windsor et al. 2010a, 2010b) focused on the fish sensing range of a blind Mexican cavefish and employed a NACA0013 profile to validate the experimental results.

One challenge in using simplified fish-like body geometries is that each fish species at various life stages possess inter and intra-species morphological variations. The distinctive layout of the lateral line system varies among species which to some extent are subject to developmental and morphological constraints (Webb 1989). Thus, each fish species has a specific flow field pattern based on its body morphology, creating a unique hydrodynamic image used in detecting stimuli at a distance.

Despite the existing studies using CFD for fish sensing research, substantial gaps persist in the evaluation and the quantification of flow fields around realistic fish-like body geometries. The major contribution of this work is to conduct a comparative analysis between a realistic fish-like body geometry and a NACA0013 model. Although the authors recognize that a fish's lateral line system is highly sensitive

to the instantaneous flow fields, we assume that major differences between fish-like and simplified body geometries can be evaluated based on time-averaged flow fields. Therefore, Reynolds Averaged Navier Stokes (RANS) modelling was performed to estimate the time-averaged flow velocity around the gudgeon fish and the NACA model. The boundary layer along the surface of the fish and NACA was assessed through the mean velocity to investigate the potential difference between the BL characteristics. This work is the first to assess the boundary layer of a realistic fish-like body (gudgeon) to a simplified streamlined body geometry (NACA0013) to determine if and where major differences in the boundary layer between body geometry types occur.

2 Methods

In this study, a numerical model is developed to investigate flow fields around a freshwater fish gudgeon and a common fish analogy, i.e., axisymmetric NACA0013 model, at two different Reynolds numbers (Table 1). The gudgeon is an elongated bottom-dwelling fish commonly found in a rapidly flowing freshwater (Schmitz et al. 2014). Morphometric analysis of gudgeon in European rivers shows that common body length ranges between 9 and 21 cm (Maitland and Campbell 1992; Page 2008). Thus, in this study, the gudgeon model with an average body length of 15 cm was taken into consideration. Simultaneously, the chord length of the NACA0013 profile was 15 cm for comparison purposes. To achieve a three-dimensional symmetrical configuration, the surface of the NACA0013 airfoil was revolved along its chord length axis, transforming it into a hydrofoil shape. The simulation model was set up for a test section of a swim tunnel in which the gudgeon and NACA0013 models were placed. Due to the viscous effects, the boundary layer attenuates the amplitude of velocity fluctuations across it, thus making it a damping layer to the flow stimulus (Rapo et al. 2009). The NACA0013 profile is designed to generate a thin boundary layer attached to the surface providing the most favorable ratio of lift to drag in aerodynamic applications, whereas fish in wild are known to possess a thicker boundary layer (Yanase and Saarenrinne 2015). Therefore, in this study, the boundary layer around the surface of the fish model and the NACA profile was fully resolved to simulate the flow in the near-wall regions. The boundary layer thickness, i.e., a normal distance from the wall where the velocity was taken as 99% U_∞ (Schlichting and Gersten 2016) was calculated at different regions along the body length to provide a comparison of the boundary layer thickness between the fish-like and simplified body geometries.

Table 1 Channel specifications and inlet flow velocities for the gudgeon fish and NACA0013 hydrofoil

Channel dimensions	Mean flow velocity \bar{U} (ms ⁻¹)	Flow rate Q (ms ⁻³)	Reynold number Re	Froude number Fr
L × W × H	0.25	1.41 × 10 ⁻³	3.74 × 10 ⁴	0.21
28 cm × 7.5 cm × 7.5 cm	0.55	3.09 × 10 ⁻³	8.24 × 10 ⁴	0.45

2.1 Numerical Modelling

An open-source numerical model was developed using the OpenFOAM framework based on the test section of a Loligo swim tunnel (Fig. 1). OpenFOAM is a C++ toolbox for solving continuum mechanics problems. The rectangular test section of the swim tunnel with a dimension of 28 cm × 7.5 cm × 7.5 cm was modelled with the fish at a distance of 6.4 cm from the inlet upstream. The flow is assumed to be highly turbulent at the inlet, thus the turbulence inside the test section was modelled by using a RANS turbulence model, i.e., Spalart Allmaras (SA), commonly used for aerodynamics applications (Spalart and Allmaras 1994). The SA model has previously shown good results in modelling flow fields around fish-shaped bodies with a resolved boundary layer near the surface of fish (Khan et al. 2022). Spalart Allmaras (SA) is a one-equation model that solves the transport equation for the kinematic turbulent eddy viscosity. For the steady fish case, RANS provides time-averaged flow fields which are sufficient to compare the boundary layer thicknesses used in this study. Considering unsteady cases with undulatory motion of fish, the authors recommend Detached Eddy Simulation (DES) or Large Eddy Simulation (LES), as these methods will provide more detailed information (i.e., time-resolved flow fields) at a substantially higher computational cost.

The numerical model employed the Finite Volume Method (FVM) to ensure sufficient resolution of pressure–velocity coupling inside each cell center, solved using the iterative solution strategy, ‘Semi-implicit method of pressure linked equations

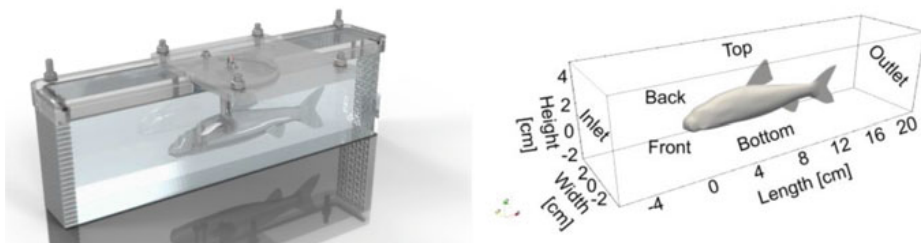


Fig. 1 Overview of the gudgeon model inside the swim tunnel respirometer; (Left) Cross-sectional view of three-dimensional gudgeon model inside the test section. (Right) Numerical model for OpenFOAM defining the computational domain along with boundaries

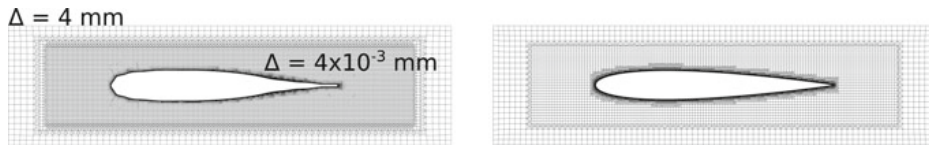


Fig. 2 2D planar view ($z = 0$) of mesh discretization within the domain along with gudgeon and hydrofoil; (Left) Planar view of the mesh discretization with additional mesh regions around the gudgeon body and the boundary layer. (Right) Planar view of the mesh discretization around the NACA0013 hydrofoil

(SIMPLE)' (Versteeg and Malalasekera 2005). For FVM problems, this iterative solution is useful for simulating flows at higher Courant-Friedrichs-Lewy (CFL) numbers by converging the pressure and velocity within each time step.

2.2 Geometry and Mesh

The three-dimensional body geometry of the gudgeon and the NACA profile modelled in computer-aided design (CAD) software, i.e., SolidWorks were imported into OpenFOAM as *.stl* files which were snapped into the domain and meshed with hexahedral and polyhedral cells of different sizes. A common meshing strategy adopted for gudgeon and NACA was to decrease the mesh cell size near the surface ($\Delta \sim 0.004$ mm) and gradually increase it towards the outer boundaries ($\Delta \sim 4$ mm). For snapping and meshing within the domain, an OpenFOAM built-in utility called *cfMesh* was used. *cfMesh* is an automated utility within the OpenFOAM framework that generates hybrid mesh, i.e., unstructured mesh around the complex geometries and structured mesh in the free domain. To reduce discretization errors, a grid independence study was conducted with the generation of five different meshes with different cell sizes ranging between 0.04 and 0.004 m, from coarse to fine. The ultimate mesh used for comparison studies was containing 5.8 M cells with a fish's surface cell size of 4×10^{-3} mm and a domain boundary cell size of 4 mm (Fig. 2).

2.3 Boundary Conditions

The inlet flow conditions were provided through a non-uniform velocity at the inlet patch. At the top, bottom, front, and back patches a '*noSlip*' wall condition was applied to assure the physical wall-bounded flow inside the channel. Similarly, at the surface of the gudgeon and NACA profile, the '*noSlip*' wall condition was applied. For pressure, the Neumann boundary condition was applied at the inlet patch, along with a '*fixedFluxpressure*' condition at boundaries, i.e., setting the pressure gradient to the provided value such that the velocity boundary condition specifies the flux on the boundary. For the current study, the wall roughness at the surface of fish was

neglected and the OpenFOAM default value for the wall roughness is used implicitly by specifying the turbulent viscosity as zero at the walls.

3 Results and Discussions

3.1 Mesh and Time Sensitivity Analysis

The mesh sensitivity was analyzed using ASME criteria (Celik et al. 2008). The evaluation of the meshes was based on the drag coefficient, c_d . The drag coefficient was chosen because it is an integrated metric that includes the pressure over the entire surface of the profile. To perform a grid independence study, the drag coefficient was measured for five different mesh resolutions (N1–N5). The convergence of c_d was analyzed using the Grid Convergence Index (GCI) and the reduction of relative error e_a^{ji} between the successive meshes (Table 2). For all meshes, the first node cell was ensured to be inside the viscous region ($y^+ < 5$).

With the increase in the number of mesh elements, the drag coefficient gradually decreases, but the relative error between successive meshes, e_a^{ji} , remained nearly constant between N1 and N2. Thus, the model setup with N2 = 5.8 M cells was opted for the final simulation for comparative studies. The time sensitivity analysis was ensured by selecting the total time of simulation enough for the fluid to transit through the channel. Considering the total length of the channel (i.e., 0.28 m), the total time of the simulation was selected to 2 s which lies within the asymptotic range.

Table 2 Calculation of discretization error between different mesh sizes for the current study.

Parameter	Drag force coefficient (c_d)
N ₁ , N ₂ , N ₃ , N ₄ , N ₅	7.9 M, 5.8 M, 1.0 M, 0.65 M, 172 K
$y^+_1, y^+_2, y^+_3, y^+_4, y^+_5$	0.09, 0.65, 0.46, 0.40, 4.0
$c_{d1}, c_{d2}, c_{d3}, c_{d4}, c_{d5}$	0.06354, 0.06389, 0.06947, 0.07432, 0.07087
p_{avg}	3.632
$c_{dext}^{21}, c_{dext}^{32}, c_{dext}^{43}, c_{dext}^{54}$	0.06319, 0.05831, 0.05011, 0.07546
$e_a^{21}, e_a^{32}, e_a^{43}, e_a^{54}$	0.55%, 8.73%, 6.96%, 4.63%
GCI^{21}_{fine}	0.68%
GCI^{32}	10.91%
GCI^{43}	34.83%
GCI^{54}_{coarse}	1.92%

where y^+ is the non-dimensional distance from the wall, p_{avg} is the averaged apparent order of the mesh, and c_{dext}^{ji} are the extrapolated drag coefficient values; other symbols explained in the text

3.2 *Boundary Layer Thickness (δ)*

Streamlined bodies subjected to fluid flow possess a boundary layer due to the viscous effects which causes the fluid to resist surface shear. The boundary layer is a thin layer of fluid around the surface of fish formed by the fluid flowing along the surface. The fluid interaction with the fish surface induces a no slip boundary condition ($U = 0$ at the surface). But with the increase in the normal distance from the surface, the fluid velocity gradually increases and reaches $99\%U_\infty$ at the edge of the boundary layer. Superficial neuromasts present at the surface of the fish are therefore principally embedded within the boundary layer itself (Bleckmann and Zelick 2009; Kroese and Schellart 1992; Liao 2007). The presence of the boundary layer around the fish's surface further attenuates the amplitude of the velocity fluctuations across it due to its damping properties, i.e., flow gradients (McHenry et al. 2008). This is primarily caused by the laminar behavior of the fluid in the immediate vicinity of fish's surface, which undergoes high momentum diffusion and low momentum convection. Thus, the boundary layer is a significant, but largely uninvestigated factor in lateral line research.

The known distribution of the lateral line mechanoreceptors on the surface of fish demonstrates that the anterior head region (20% BL) is densely populated with the canals and superficial neuromasts making the anterior region more sensitive to the approaching events (Ristoph et al. 2015).

Although previous studies correlate the distribution of the neuromasts along the surface of fish to the pressure coefficient (C_p), the evaluation of boundary layer along the surface of fish is also essential in the exploration of fish's sensory ecology.

The boundary layer thickness varies along the surface of fish with the increase or decrease in local Reynolds number (Yanase and Saarenrinne 2015). To investigate the boundary layer thickness along the surface, the digital model of gudgeon fish as well as the NACA0013 profile was classified into multiple regions, i.e., anterior, pectoral, pelvic, and posterior, as shown in Figs. 3 and 4. The boundary layer thickness (δ) was measured as a normal distance from the surface at which the velocity becomes $99\% U_\infty$ (Schlichting and Gersten 2016).

The boundary layer vastly depends upon the surface roughness of the fish. Though the presence of mucus on the surface affects the boundary layer but the study in hand considered the qualitative assessment of boundary layer rather than the quantitative assessment. Therefore, both numerical setups were built with similar roughness effects. The numerical model depicts that the fish model possesses a relatively thin boundary layer in the anterior region as compared to the NACA0013. However, continuing along the body length, it is found that the fish body exhibits a slightly thicker boundary layer (upto $\Delta\delta = 0.5$ mm) in the pectoral and pelvic regions. A turbulent behavior of boundary layer was observed in the posterior region which persists till the wake region. Velocity profiles at the representative streamwise locations showing the velocity distribution across the boundary layer are shown for both models (see Fig. 5).

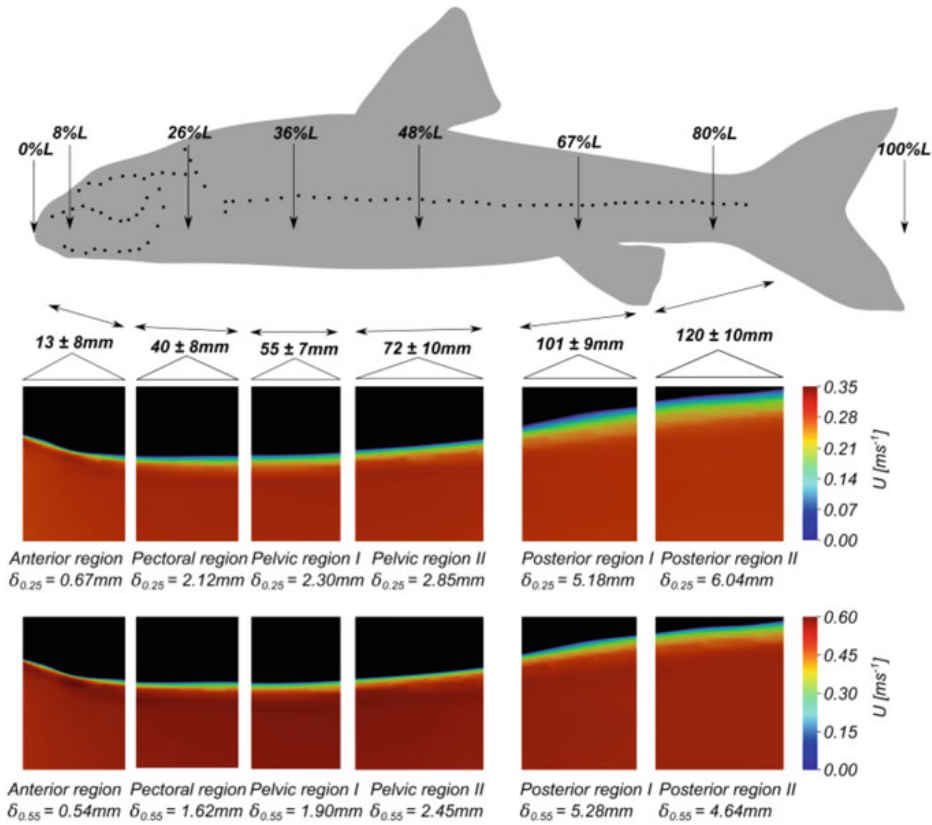


Fig. 3 Top: The layout of canal neuromasts along the body of a gudgeon fish (after Schmitz et al. 2014). The fish body is classified into multiple regions i.e., anterior, pectoral, pelvic and posterior. Bottom: 2D planar view ($z = 0$) of velocity fields around the gudgeon fish model at both free stream velocities representing the boundary layer thickness in respective regions

Within the fish's anterior region, the velocity becomes relatively high due to the slight curvature on the surface of the fish. The steep gradient of velocity corresponds to the thick boundary layer at the surface of fish and the NACA0013 model in the pectoral and pelvic regions. The boundary layer at the surface of both models was observed to be laminar except for the posterior region.

4 Summary and Conclusion

The lateral line mechanoreceptors are distributed along the body length of fish and are sensitive to minute fluctuations of hydrodynamic fields in the range of 1–150 Hz (Mogdans 2019; Schmitz et al. 2014). These receptors are primarily distributed in the anterior region (20% BL) of fish and act as a “hydrodynamic antenna” during rheotaxis. Fish sensory systems can be investigated using simplified geometrical

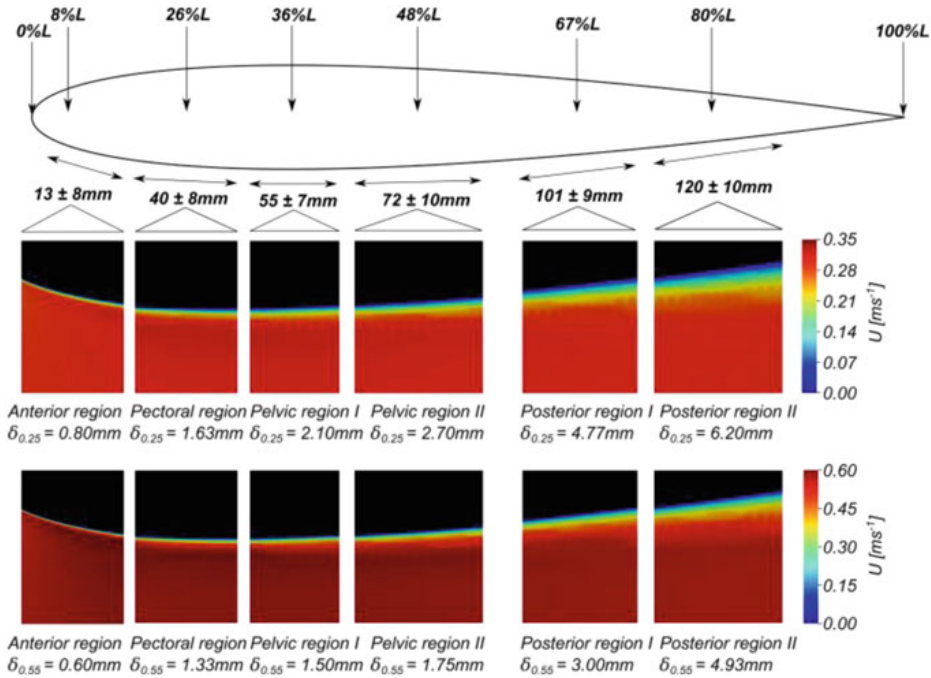


Fig. 4 Top: Axisymmetric body of the NACA0013 model classified into representative regions. Bottom: 2D planar view ($z = 0$) of velocity fields around the NACA0013 axisymmetric model at both free stream velocities in the specified regions representing the boundary layer thickness

configurations such as hydrofoils. Numerical models of these bodies provide estimates of the near-body flow field in cases where realistic fish-like body geometries are unavailable.

The boundary layer acts as a medium allowing the stimulus perturbations to reach the superficial and canal neuromasts at the surface of fish. The boundary layer thickness of a gudgeon fish marginally differentiates from that of the NACA0013 model. In general, it was found that both models exhibited a thinner boundary layer in the anterior region. A thinner boundary layer in the anterior head region was also observed in earlier studies of rainbow trout (Yanase and Saarenrinne 2015). The presence of a thinner boundary layer is also correlated with an increased density of neuromasts. Furthermore, previous works have shown a similar correlation with the pressure coefficient (C_p) (Ristroph et al. 2015).

Around the fish’s head region, the mean flow velocity is slightly higher than the NACA0013 model due to the protuberant organs (eyes and mouth). Similar behavior was observed in the pectoral and pelvic regions where the mean flow velocity around fish remains moderately higher than the NACA0013 model. The minor differences in the flow field around both geometries indicate that using simplified fish-like bodies would be a suitable approximation of the fish for boundary layer studies.

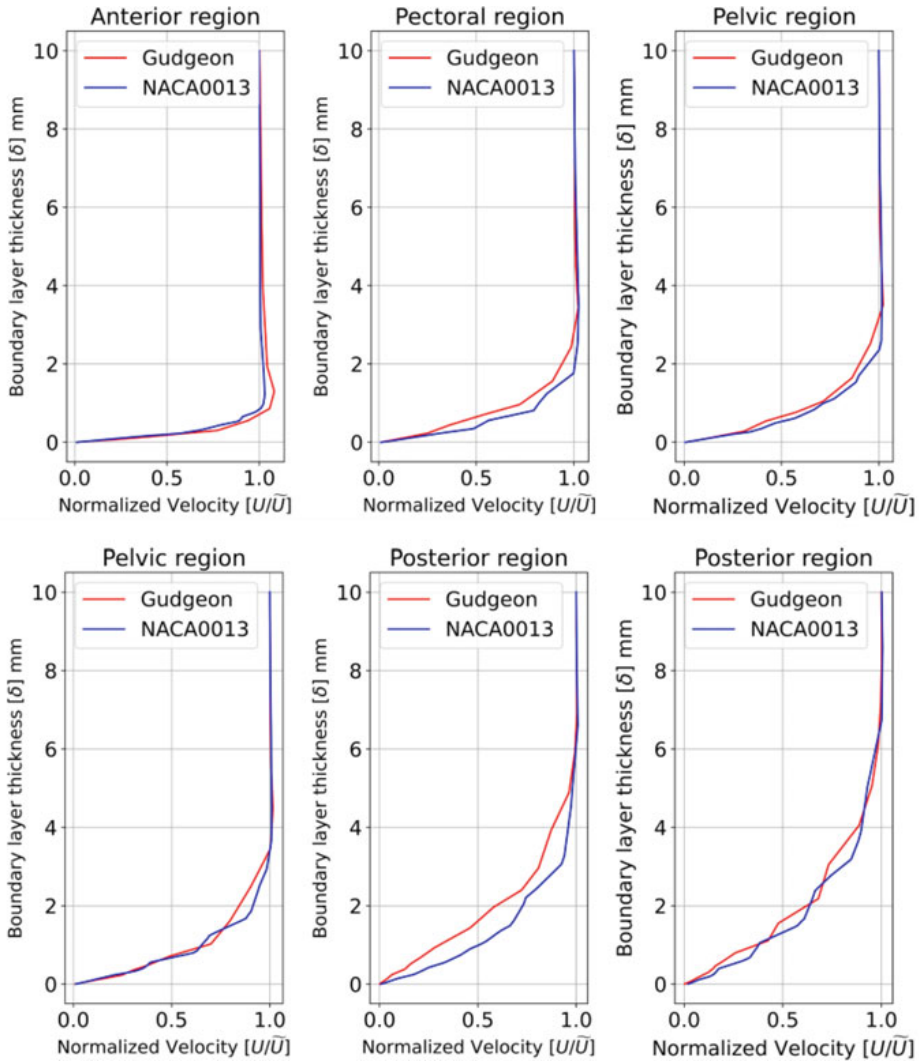


Fig. 5 Comparison of velocity profiles at the representative locations on the surface of gudgeon and NACA0013 model representing the boundary layer thickness in each location. The velocity at each location normal to the surface is normalized with the potential flow velocity \tilde{U}

Acknowledgements The research work presented in this paper has received funding from European Union Horizon 2020 Research and Innovation Programme under the Marie Skłodowska-Curie Actions, Grant Agreement No. 860800. Jeffrey A. Tuhtan's contributions were funded by EXCITE supported by the Estonian Centre of Excellence in IT, funded by the European Regional Development Fund Project nr 2014.2020.4.01.15-0018.

References

- Bleckmann H, Zelick R (2009) Lateral line system of fish. *Integr Zool* 4(1):13–25. <https://doi.org/10.1111/J.1749-4877.2008.00131.X>
- Celik IB, Ghia U, Roache PJ, Freitas CJ, Coleman H, Raad PE (2008) Procedure for estimation and reporting of uncertainty due to discretization in CFD applications. *J Fluids Eng Trans ASME* 130(7):0780011–0780014. <https://doi.org/10.1115/1.2960953/444689>
- Dijkgraaf S (1963) The functioning and significance of the lateral-line organs. *Biol Rev* 38(1):51–105. <https://doi.org/10.1111/J.1469-185X.1963.TB00654.X>
- Hassan ES (1985) Mathematical analysis of the stimulus for the lateral line organ. *Biol Cybern* 52(1):23–36. <https://doi.org/10.1007/BF00336932>
- Hassan ES (1992a) Mathematical description of the stimuli to the lateral line system of fish derived from a three-dimensional flow field analysis—I The cases of moving in open water and of gliding towards a plane surface. *Biol Cybern* 66(5):443–452. <https://doi.org/10.1007/BF00197725/METRICS>
- Hassan ES (1992b) Mathematical description of the stimuli to the lateral line system of fish derived from a three-dimensional flow field analysis—II The case of gliding alongside or above a plane surface. *Biol Cybern* 66(5):453–461. <https://doi.org/10.1007/BF00197726/METRICS>
- Hassan E-S (1993) Mathematical description of the stimuli to the lateral line system of fish, derived from a three-dimensional flow field analysis. III. The case of an oscillating sphere near the fish. *Biol Cybern* 69(5):525–538. <https://doi.org/10.1007/BF00199452>
- Khan AH, Ruiz Hussmann K, Powalla D, Hoerner S, Kruusmaa M, Tuhtan JA (2022) An open 3D CFD model for the investigation of flow environments experienced by freshwater fish. *Eco Inform* 69:101652. <https://doi.org/10.1016/J.ECOINF.2022.101652>
- Kroese ABA, Schellart NAM (1992) Velocity- and acceleration-sensitive units in the trunk lateral line of the trout. *J Neurophysiol* 68(6):2212–2221. <https://doi.org/10.1152/JN.1992.68.6.2212>
- Liao JC (2007) A review of fish swimming mechanics and behavior in altered flows. *Philos Trans Royal Soc B Biol Sci* 362(1487):1973–1993. <https://doi.org/10.1098/RSTB.2007.2082>
- Maitland PS, Campbell RNB (1992) *Freshwater fishes of the British Isles*, p 368
- McHenry MJ, Strother JA, Van Netten SM (2008) Mechanical filtering by the boundary layer and fluid-structure interaction in the superficial neuromast of the fish lateral line system. *J Comp Physiol A Neuroethol Sens Neural Behav Physiol* 194(9):795–810. <https://doi.org/10.1007/S00359-008-0350-2/FIGURES/12>
- Mogdans J (2019) Sensory ecology of the fish lateral-line system: morphological and physiological adaptations for the perception of hydrodynamic stimuli. *J Fish Biol* 95(1):53–72. <https://doi.org/10.1111/JFB.13966>
- Page LM (2008) *Handbook of European freshwater fishes*, vol 2008(3). The American Society of Ichthyologists and Herpetologists. <https://doi.org/10.1643/OT-08-098A.1>
- Rapo MA, Jiang H, Grosenbaugh MA, Coombs S (2009) Using computational fluid dynamics to calculate the stimulus to the lateral line of a fish in still water. *J Exp Biol* 212(10):1494–1505. <https://doi.org/10.1242/JEB.026732>
- Ristroph L, Liao JC, Zhang J (2015) Lateral line layout correlates with the differential hydrodynamic pressure on swimming fish. *Phys Rev Lett* 114(1):018102. <https://doi.org/10.1103/PHYSREVLETT.114.018102>
- Schlichting H, Gersten K (2016) Boundary-layer theory. In: *Boundary-layer theory*, pp 1–799. <https://doi.org/10.1007/978-3-662-52919-5/COVER>
- Schmitz A, Bleckmann H, Mogdans J (2014) The lateral line receptor array of cyprinids from different habitats. *J Morphol* 275(4):357–370. <https://doi.org/10.1002/JMOR.20219>
- Spalart PR, Allmaras SR (1994) One-equation turbulence model for aerodynamic flows. *Recherche Aerospaciale* 1:5–21. <https://doi.org/10.2514/6.1992-439>
- Versteeg HK, Malalasekera W (2005) An introduction to parallel computational fluid dynamics. *IEEE Concurrency* 6(4). <https://doi.org/10.1109/mcc.1998.736434>

- Webb JF (1989) Gross morphology and evolution of the mechanoreceptive lateral-line system in teleost fishes (Part 1 of 2). *Brain Behav Evol* 33(1):34–43. <https://doi.org/10.1159/000115896>
- Windsor SP, Norris SE, Cameron SM, Mallinson GD, Montgomery JC (2010a) The flow fields involved in hydrodynamic imaging by blind Mexican cave fish (*Astyanax fasciatus*). Part I: open water and heading towards a wall. *J Exp Biol* 213(22):3819–3831. <https://doi.org/10.1242/JEB.040741>
- Windsor SP, Norris SE, Cameron SM, Mallinson GD, Montgomery JC (2010b) The flow fields involved in hydrodynamic imaging by blind Mexican cave fish (*Astyanax fasciatus*). Part II: gliding parallel to a wall. *J Exp Biol* 213(22):3832–3842. <https://doi.org/10.1242/JEB.040790>
- Yanase K, Saarenrinne P (2015) Unsteady turbulent boundary layers in swimming rainbow trout. *J Exp Biol* 218(9):1373–1385. <https://doi.org/10.1242/JEB.108043>

Curriculum Vitae

1. Personal data

Name	Ali Hassan Khan
Date and place of birth	11 June 1991 Jhang, Pakistan
Nationality	Pakistani

2. Contact information

Address	Centre for Environmental Intelligence and Sensing, Department of Computer Systems, Tallinn University of Technology, Akadeemia tee 15a, 12618 Tallinn, Estonia
Phone	+372 58345606
E-mail	ali.khan@taltech.ee

3. Education

2020–2024	Tallinn University of Technology, School of Information Technologies, Computer Systems and Engineering, [Ph.D.]
2016–2019	University of Rostock, Faculty of Computer Science and Electrical Engineering, Computational Science and Engineering, [M.Sc.]
2010–2014	University of Wah, Faculty of Mechanical Engineering, Mechanical Engineering, [B.Sc.]

4. Language competence

English	Fluent
Deutsch	Working proficiency
Estonian	Basic

5. Professional employment

2020–2023	Tallinn University of Technology, Early Stage Researcher
2018–2019	University of Rostock, Student Assistant
2015–2015	National Automotive Components Pvt. Ltd., Junior Mechanical Engineer

6. Computer skills

- Operating systems: Microsoft Windows, Linux
- Document preparation: Microsoft Office, Libre Office, Latex, Overleaf
- Programming languages: Python, C++, R
- Scientific packages: SOLIDWORKS, Pro-E Creo Elements, FreeCAD, AutoCAD, Open-FOAM, Ansys Fluent, Salome, Gmsh, MeshLab, PrePoMax, OpenFAST

7. Awards and Scholarships

- 2020, Marie Skłodowska-Curie Actions, [Ph.D.]
- 2020, Estonian National Scholarship, [Ph.D.]

8. Field of research

- Fluid Dynamics
- Numerical Modelling
- Ecohydraulics
- Hydrodynamics

9. Scientific work

Journal Articles

1. A. H. Khan, K. R. Hussmann, D. Powalla, S. Hoerner, M. Kruusmaa, and J. A. Tuhtan, "An open 3D CFD model for the investigation of flow environments experienced by freshwater fish," *Ecological Informatics*, vol. 69, p. 101652, 2022
2. K. Bensing, J. A. Tuhtan, G. Toming, A. H. Khan, and B. Lehmann, "Fish body geometry reduces the upstream velocity profile in subcritical flowing waters," *Aquatic Sciences*, vol. 84, no. 3, p. 32, 2022
3. A. H. Khan, S. Hoerner, G. Tomming, M. Kruusmaa, and J. A. Tuhtan, "3D CFD analysis of pressure, boundary layer and shear stresses on a gudgeon (*Gobio gobio*)," *Journal of Ecohydraulics*, pp. 1–15, 2024

Conference contributions

1. A. H. Khan, K. R. Hussmann, D. Powalla, S. Hoerner, M. Kruusmaa, and J. A. Tuhtan, "Benchmarking 3D CFD for studies on turbulent flow around fish-shaped bodies," in *Proceedings of the 14th International Symposium on Ecohydraulics*, International Association for Hydro-Environment Engineering and Research, 2022
2. A. H. Khan, G. Toming, S. Hoerner, and J. A. Tuhtan, "Comparison of near-body flow fields of a Gudgeon and NACA0013 profile," in *Advances in Hydraulic Research* (M. B. Kalinowska, M. M. Mrokowska, and P. M. Rowiński, eds.), pp. 231–242, Springer Nature Switzerland, 2024
3. Ali Hassan Khan, Stefan Hoerner, Maarja Kruusmaa and Jeffrey A. Tuhtan. *Fish flow fields in Loligo swim tunnel*, Vattendagar med Fiskmarknad, 5–7 October 2022, Karlstad, Sweden

Elulookirjeldus

1. Isikuandmed

Nimi	Ali Hassan Khan
Sünniaeg ja -koht	11.06.1991, Jhang, Pakistan
Kodakondsus	Pakistani

2. Kontaktandmed

Address	Keskonnaseire Tehnoloogiate Keskus, Arvutisüsteemide Instituut, Tallinna Tehnikaülikool, Akadeemia tee 15a, 12618 Tallinn, Estonia
Telefon	+372 58345606
E-post	ali.khan@taltech.ee

3. Haridus

2020–2024	Tallinna Tehnikaülikool, Infotehnoloogia teaduskond, Arvutisüsteemid ja Tehnika, [Ph.D.]
2011–2013	Universitat Rostock, Arvutiteaduse ja elektrotehnika teaduskond, Arvutusteadus ja Tehnika, [M.Sc.]
2008–2011	University of Wah, Masinaehituse teaduskond, Masinaehitus, [B.Sc.]

4. Keelteoskus

inglise keel	korgtase
saksa keel	toooskus
eesti keel	algaja

5. Teenistuskaik

2020– 2023	Tallinna Tehnikaülikool, teadur
2018–2019	Universitat Rostock, opilase abiline
2015–2015	National Automotive Components Pvt. Ltd., nooremmehaanikainsener

6. Computer skills

- Operatsioonisüsteemid: Microsoft Windows, Linux
- Kontoritarkvara: Microsoft Office, Libre Office, Latex, Overleaf
- Programmeerimiskeeled: Python, C++, R
- Teadustarkvara paketid: Solidworks, Pro-E Creo Elements, FreeCAD, AutoCAD, Open-FOAM, Ansys Fluent, Salome, Gmsh, MeshLab, PrepoMay, OpenFAST

7. Auhinnad ja stipendiumid

- 2020, Marie Sklodowska-Curie Actions, [Ph.D.]
- 2020, Eesti riiklik stipendium, [Ph.D.]

8. Teadustöö põhisuunad

- Vedeliku dünaamika
- Numbriline modelleerimine
- Ökohüdraulika
- Hüdrodünaamika

9. Teadustegevus

Teadusartiklite, konverentsiteeside ja konverentsietekannete loetelu on toodud ingliskeelse elulookirjelduse juures.

ISSN 2585-6901 (PDF)
ISBN 978-9916-80-254-0 (PDF)